

**STRUCTURE, MORPHOLOGY, OPTICAL AND
ELECTROCHEMICAL PROPERTIES OF INDIUM- AND
ALUMINUM-BASED NITRIDE THIN FILMS DEPOSITED BY
PLASMA-ASSISTED REACTIVE EVAPORATION**

MAHDI ALIZADEH KOUZEH RASH

**FACULTY OF SCIENCE
UNIVERSITY OF MALAYA
KUALA LUMPUR**

2016

**STRUCTURE, MORPHOLOGY, OPTICAL AND
ELECTROCHEMICAL PROPERTIES OF INDIUM- AND
ALUMINUM-BASED NITRIDE THIN FILMS
DEPOSITED BY PLASMA-ASSISTED REACTIVE
EVAPORATION**

MAHDI ALIZADEH KOUZEH RASH

**THESIS SUBMITTED IN FULFILMENT OF THE
REQUIREMENTS FOR THE DEGREE OF DOCTOR OF
PHILOSOPHY**

**FACULTY OF SCIENCE
UNIVERSITY OF MALAYA
KUALA LUMPUR**

2016

UNIVERSITY OF MALAYA
ORIGINAL LITERARY WORK DECLARATION

Name of Candidate: **Mahdi Alizadeh Kouzeh Rash**

Registration/Matric No: **SHC120022**

Name of Degree: **Doctor of Philosophy**

Title of Thesis:

**STRUCTURE, MORPHOLOGY, OPTICAL AND ELECTROCHEMICAL
PROPERTIES OF INDIUM- AND ALUMINUM-BASED NITRIDE THIN
FILMS DEPOSITED BY PLASMA-ASSISTED REACTIVE EVAPORATION**

Field of Study: **III-Nitride semiconductors**

I do solemnly and sincerely declare that:

- (1) I am the sole author/writer of this Work;
- (2) This Work is original;
- (3) Any use of any work in which copyright exists was done by way of fair dealing and for permitted purposes and any excerpt or extract from, or reference to or reproduction of any copyright work has been disclosed expressly and sufficiently and the title of the Work and its authorship have been acknowledged in this Work;
- (4) I do not have any actual knowledge nor do I ought reasonably to know that the making of this work constitutes an infringement of any copyright work;
- (5) I hereby assign all and every rights in the copyright to this Work to the University of Malaya ("UM"), who henceforth shall be owner of the copyright in this Work and that any reproduction or use in any form or by any means whatsoever is prohibited without the written consent of UM having been first had and obtained;
- (6) I am fully aware that if in the course of making this Work I have infringed any copyright whether intentionally or otherwise, I may be subject to legal action or any other action as may be determined by UM.

Candidate's Signature

Date:

Subscribed and solemnly declared before,

Witness's Signature

Date:

Name:

ABSTRACT

A plasma-assisted reactive evaporation system was developed for the growth of indium- and aluminum-based nitride thin films. The effects of the most influential growth parameters were investigated with respect to the structure, elemental composition, morphology and optical properties of these films. Decreasing the filament-to-substrate distance resulted in AlN thin films with reduced presence of metallic phase. The morphology of the films shifted from cauliflower-like to micro grain structure when the distance was reduced. RF power showed strong influence on the crystallinity, nitrogen incorporation and oxygen contamination in the InN film structure. An optimized RF power resulted in highly crystalline InN thin films with high nitrogen incorporation and lower oxygen contamination. The unavoidable presence of oxygen impurity in the InN film structure resulted in higher band gap energy values of 2.0 – 2.5 eV for films grown at various RF powers. This value is much higher than reported values of band gap energy for InN films. In-rich and Al-rich $\text{Al}_x\text{In}_{1-x}\text{N}$ films were prepared by simply varying the AC voltage applied to the filament holding the indium wire. The band gap energy of the films increased from 1.08 to 2.50 eV when the Al composition (x) varied from 0.10 to 0.64. Nitrogen flow rate also showed significant influence on the structure, morphology and optical properties of In-rich and Al-rich $\text{Al}_x\text{In}_{1-x}\text{N}$ films. Increasing the nitrogen flow rate resulted in enhancement of the agglomeration of the particles in the film structure. Increasing the nitrogen flow rate also decreased the Al composition in the films and this led to the decrease in the band gap energy of the films. The electrochemical properties of the deposited InN was studied and it was found that the films deposited at lower RF power showed better electrochemical behavior. The photoelectrochemical behavior of $\text{Al}_x\text{In}_{1-x}\text{N}$ thin films was also investigated. Thin films grown at high nitrogen flow rates with Al composition between 0.45 and 0.6 showed good photoelectrochemical behavior.

ABSTRAK

Satu sistem penyejatan reaktif dengan bantuan plasma telah dibangun untuk pertumbuhan filem nipis nitrida berasaskan indium dan aluminium. Kesan parameter pertumbuhan yang paling berpengaruh telah dikaji merujuk kepada struktur, komposisi unsur, morfologi dan ciri-ciri optik filem-filem ini. Pengurangan jarak di antara filamen dan substrat menghasilkan penurunan kehadiran fasa logam di dalam filem nipis AlN. Morfologi filem beralih daripada bentuk seperti kubis bunga kepada struktur bijian mikro apabila jarak dikurangkan. Kuasa RF menunjukkan pengaruh yang kuat ke atas penghabluran, penggabungan nitrogen dan pencemaran oksigen dalam struktur filem InN. Kuasa RF yang optimum menghasilkan filem nipis InN yang tinggi penghablurannya dengan penggabungan nitrogen yang tinggi dan pencemaran oksigen yang lebih rendah. Kewujudan pencemaran oksigen yang tidak dapat dielakkan di dalam struktur filem InN yang tumbuh pada pelbagai kuasa RF menghasilkan jalur tenaga yang lebih tinggi di dalam lingkungan di antara 2.0 hingga 2.5 eV. Nilai ini adalah jauh lebih tinggi daripada nilai yang dilaporkan bagi jalur tenaga filem InN. Filem $\text{Al}_x\text{In}_{1-x}\text{N}$ yang kaya-In dan kaya-Al dapat disediakan dengan hanya mengubah voltan AC dikenakan kepada filamen yang memegang dawai indium. Jalur jurang tenaga filem meningkat daripada 1.08 kepada 2.50 eV apabila kandungan Al (x) berubah daripada 0.10 kepada 0.64. Kadar aliran nitrogen juga menunjukkan pengaruh yang signifikan pada struktur, morfologi dan sifat optik bagi filem-filem $\text{Al}_x\text{In}_{1-x}\text{N}$ yang kaya-In dan kaya-Al. Peningkatan kadar aliran nitrogen meningkatkan aglomerasi partikel dalam struktur filem. Peningkatan kadar aliran nitrogen juga menurunkan komposisi Al dalam filem dan ini menyebabkan penurunan jalur jurang tenaga filem. Sifat elektrokimia InN yang dimendapkan telah dikaji dan didapati yang filem yang dimendapkan pada kuasa RF yang rendah menunjukkan perilaku elektrokimia yang lebih baik. Perilaku fotoelektrokimia filem nipis $\text{Al}_x\text{In}_{1-x}\text{N}$ juga dikaji. Pertumbuhan filem nipis pada kadar aliran nitrogen yang tinggi dengan

komposisi Al di antara 0.45 hingga 0.6 menunjukkan perilaku fotoelektrokimia yang baik.

University of Malaya

ACKNOWLEDGEMENTS

In the name of ALLAH, the Most Gracious, the Most Merciful.....

All praises to Allah for His blessing and granting me the straight and ability to complete this thesis. First and foremost, I offer my deepest gratitude to my supervisor, Professor Datin Dr. Saadah Abdul Rahman for providing me the opportunity to conduct my PhD. I would like to thank immensely for her support, advice and patience during this research work. Without her recommendations and efforts, this thesis would have never been possible to be completed. Special thanks to my co-supervisor Dr. Goh Boon Tong for guiding me in laboratory works, giving positive feedbacks on result troubleshooting and also providing all the materials that are needed in this research.

Many thanks to my colleague Dr. Vottikondala Ganesh for his help and encouragements in all this period. I extend my thanks to all my teammates for their endless assistance throughout my experimental work.

I would like to acknowledge government of Malaysia for the grants including Fundamental Research Grant Scheme (FP009-2013B), University of Malaya, High Impact Research (HIR, grant: UM.C/HIR/MOHE/SC/06) and University of Malaya Postgraduate Research (PPP, grant: PG081-2012B) for financial support of my PhD work.

Last but not least, I would like to thank my family and all my friends who made even my little free time highly enjoyable during these intense three years in Malaysia, for their moral support and encouragements.

TABLE OF CONTENTS

| | |
|--|----------|
| Abstract | iii |
| Abstrak | iv |
| Acknowledgements | vi |
| Table of Contents | vii |
| List of Figures | xi |
| List of Tables..... | xviii |
| List of Symbols and Abbreviations..... | xix |
| | |
| CHAPTER 1: INTRODUCTION..... | 1 |
| 1.1 Important Properties of Indium- and Aluminum-Based Nitrides | 1 |
| 1.2 Application of Indium- and Aluminum-Based Nitrides | 3 |
| 1.3 Growth Techniques of Indium- and Aluminum-Based Nitrides | 4 |
| 1.4 Research Problems..... | 5 |
| 1.5 Research Objectives..... | 6 |
| 1.6 Outline of Thesis..... | 7 |
| | |
| CHAPTER 2: LITERATURE REVIEW..... | 9 |
| 2.1 Introduction..... | 9 |
| 2.2 Crystal Structure of Indium- and Aluminum-Based Nitrides..... | 9 |
| 2.3 Band gap and Band Alignment..... | 11 |
| 2.4 Photoelectrochemical Water Splitting Application | 13 |
| 2.5 Growth Methods of Indium- and Aluminum-Based Nitride Thin Films..... | 19 |
| 2.5.1 Metalorganic Chemical Vapor Deposition (MOCVD) | 20 |
| 2.5.2 Sputtering | 26 |
| 2.5.3 Molecular Beam Epitaxy (MBE)..... | 31 |

| | | |
|-------|--|----|
| 2.5.4 | Pulsed Laser Deposition (PLD)..... | 37 |
| 2.5.5 | Plasma-Enhanced Chemical Vapor Deposition (PECVD)..... | 41 |

CHAPTER 3: SAMPLE PREPARATION AND CHARACTERIZATION

TECHNIQUES44

| | | |
|-------|--|----|
| 3.1 | Introduction..... | 44 |
| 3.2 | Research Methodology | 44 |
| 3.3 | Deposition of the Thin Films..... | 47 |
| 3.3.1 | Deposition System..... | 47 |
| 3.3.2 | Pre-heating of Filament | 50 |
| 3.3.3 | Preparation of Substrates | 51 |
| 3.3.4 | Pre-deposition Process | 51 |
| 3.3.5 | Deposition of AlN Thin Films..... | 53 |
| 3.3.6 | Deposition of InN Thin Films | 53 |
| 3.3.7 | Deposition of Al _x In _{1-x} N Thin Films | 54 |
| 3.3.8 | Annealing Process | 56 |
| 3.4 | Characterization Techniques | 57 |
| 3.4.1 | X-ray Diffraction (XRD)..... | 58 |
| 3.4.2 | Fourier Transform Infrared (FTIR) Spectroscopy..... | 60 |
| 3.4.3 | Micro-Raman Scattering Spectroscopy..... | 62 |
| 3.4.4 | Field Emission Scanning Electron Microscopy (FESEM) and Energy-Dispersive X-ray (EDX) Spectroscopy | 65 |
| 3.4.5 | X-ray Photoelectron Spectroscopy (XPS)..... | 66 |
| 3.4.6 | Surface Profilometry | 68 |
| 3.4.7 | Ultra-Violet Visible Near-Infrared Spectroscopy | 69 |
| 3.5 | Electrochemical Study of Al _x In _{1-x} N and InN Thin Films..... | 71 |
| 3.5.1 | Electrochemical Measurement for Al _x In _{1-x} N Thin Films..... | 71 |

| | | |
|-------|---|----|
| 3.5.2 | Electrochemical Measurement for InN Thin Films..... | 72 |
|-------|---|----|

CHAPTER 4: ALUMINUM NITRIDE AND INDIUM NITRIDE THIN FILMS BY PLASMA-ASSISTED REACTIVE EVAPORATION 73

| | | |
|-----|---|----|
| 4.1 | Introduction..... | 73 |
| 4.2 | Effects of Filament-to-Substrate Distance on the Structure, Morphology and Optical Properties of Aluminum Nitride Thin Films..... | 73 |
| 4.3 | Effects of RF Power on Crystallinity, Morphology, Composition and Optical Properties of Indium Nitride Thin Films | 83 |
| 4.4 | Summary..... | 93 |

CHAPTER 5: ALUMINUM INDIUM NITRIDE THIN FILMS: STRUCTURE, MORPHOLOGY AND OPTICAL PROPERTIES 94

| | | |
|-----|---|-----|
| 5.1 | Introduction..... | 94 |
| 5.2 | The Role of Filament Temperature on the Growth of Aluminum Indium Nitride Thin Films..... | 94 |
| 5.3 | Effects of Nitrogen Flow Rate on Structure, Morphology, Composition and Optical Properties of In-rich and Al-rich Aluminum Indium Nitride Thin Films..... | 107 |
| 5.4 | Effects of Annealing Temperature on the Composition, Structure and Optical Properties of Aluminum Indium Nitride Thin Films..... | 121 |
| 5.5 | Summary..... | 127 |

CHAPTER 6: ELECTROCHEMICAL BEHAVIOR OF INDIUM- AND ALUMINUM-BASED NITRIDE THIN FILMS GROWN BY PLASMA-ASSISTED REACTIVE EVAPORATION..... 128

| | | |
|-----|-------------------|-----|
| 6.1 | Introduction..... | 128 |
|-----|-------------------|-----|

| | | |
|-----|---|-----|
| 6.2 | Effects of RF Power on the Electrochemical Properties of Indium Nitride Thin Films..... | 128 |
| 6.3 | Electrochemical and Photoelectrochemical Behaviors of Aluminum Indium Nitride Thin Films Grown by Plasma-Assisted Dual Source Reactive Evaporation..... | 138 |
| 6.4 | Summary..... | 147 |

CHAPTER 7: CONCLUSION AND SUGGESTIONS FOR FUTURE WORKS..148

| | | |
|-----|--|-----|
| 7.1 | Overview..... | 148 |
| 7.2 | Conclusion..... | 149 |
| 7.3 | Suggestions for Future Work..... | 152 |
| | References..... | 154 |
| | List of Publications and Papers Presented..... | 171 |

University of Malaya

LIST OF FIGURES

| | |
|---|----|
| Figure 2.1: Schematic diagram of wurtzite AlN structure (Kuang et al., 2012c). | 11 |
| Figure 2.2: Valence band position and offsets for group III-nitrides alloys. From Ref. (Ramon Collazo & Dietz, 2013). | 13 |
| Figure 2.3: Photoelectrochemical water splitting systems using n-type semiconductor photoanode (a), p-type semiconductor photocathode (b), and tandem system (c) (Abe, 2010). | 15 |
| Figure 2.4: The SEM results of AlInN films grown by MOCVD method under various MO gas flow rates of (a) 0.5, (b) 1, and (c) 1.4 standard liters per minute (SLM). The characters 1, 2, and 3 refer to the substrate positions 92, 118, and 144 mm from MO entrance. The length of white scale bar is 5 μm (Kang, Yamamoto, Tanaka, Hashimoto, & Yamamoto, 2009)..... | 24 |
| Figure 2.5: Raman spectra AlInN thin films grown by MOCVD at various MO gas flow rates. From Ref. (Kang, Yamamoto, Tanaka, Hashimoto, & Yamamoto, 2009). | 25 |
| Figure 2.6: Transmittance spectra (a) and squared absorption coefficient (b) of sputtered $\text{In}_x\text{Al}_{1-x}\text{N}$ films with different In content (x). From Ref. (He et al., 2010). | 30 |
| Figure 2.7: HRXRD spectra of InN thin films grown by PA-MBE at the RF powers of (a) 350 W and (b) 450 W. From Ref. (M. Kumar et al., 2012)..... | 34 |
| Figure 2.8: The SEM image of cross-section (a) and surface (b) of InN films grown by PA-MB. From Ref. (Kamimura et al., 2007) | 36 |
| Figure 2.9: SEM image of AlN thin films grown by PLD method at different N_2 pressures; (a) 100 Torr; (b) 50 Torr; (c) 10 Torr; (d) 1 Torr; (e) 10^{-1} Torr; (f) 5×10^{-2} Torr. From Ref. (Shukla & Khare, 2008). | 39 |
| Figure 3.1: Flowchart of research methodology involved in this work. | 46 |
| Figure 3.2: A photograph of plasma-assisted reactive evaporation system. | 48 |
| Figure 3.3: Schematic diagram of plasma-assisted reactive evaporation system for growth of AlN and InN thin films. A single tungsten filament holding the In or Al wires are clamped to stainless steel rods filament holders. | 49 |
| Figure 3.4: Schematic diagram of plasma-assisted reactive evaporation system for growth of $\text{Al}_x\text{In}_{1-x}\text{N}$ thin films. The tungsten filaments holding the In and Al wires are clamped perpendicular to each other (see the inset image) to stainless steel rod filament holders. The former is placed above the latter. | 50 |

| | |
|---|----|
| Figure 3.5: A photograph of the tube furnace used for the annealing process..... | 57 |
| Figure 3.6: (a) The principle of X-ray diffraction and (b) X-ray diffracted beam path in $\theta/2\theta$ mode. From Ref (Goh, 2012). | 59 |
| Figure 3.7: A photograph of SIEMENS D5000 X-ray diffractometer..... | 60 |
| Figure 3.8: A photograph of FTIR Perkin-Elmer System 2000..... | 61 |
| Figure 3.9: Schematic diagram of Raman principle. From Ref. (Othman, 2012)..... | 63 |
| Figure 3.10: A photograph of Renishaw inVia Raman Microscope..... | 63 |
| Figure 3.11: A photograph of JEOL JSM-7600F microscope. | 66 |
| Figure 3.12: A photograph of PHI Quantera II XPS system..... | 68 |
| Figure 3.13: A photograph of KLA-Tencor P-6 surface profiler system..... | 69 |
| Figure 3.14: A photograph of Lambda 750 UV/Vis/NIR spectrometer..... | 70 |
| Figure 3.15: Schematic diagram of three-electrode photoelectrochemical cell..... | 71 |
| Figure 3.16: A photograph of PAR-VersaSTAT 3 electrochemical work station with 150-W Xenon arc lamp. | 72 |
| Figure 4.1: The XRD spectra of AlN thin films grown at different filament-substrate distances (d_{f-s}). Decrease in d_{f-s} shows significant decrease of intensity of metallic peaks along with preferential AlN growth orientation along the c-axis perpendicular to the substrate..... | 75 |
| Figure 4.2: FESEM image of AlN films grown at different filament-substrate distances (d_{f-s}) (a) $d_{f-s} = 2.2$, (b) $d_{f-s} = 1.8$, (c) $d_{f-s} = 1.4$ and (d) $d_{f-s} = 1.0$ cm with $\times 5000$ magnification. Decreasing the distance the filament distance results in agglomeration of smaller grains to form cauliflower-shaped grains..... | 76 |
| Figure 4.3: EDX spectra of AlN films deposited at different filament-substrate distances (a) $d_{f-s} = 2.2$, (b) $d_{f-s} = 1.8$, (c) $d_{f-s} = 1.4$ and (d) $d_{f-s} = 1.0$ cm. By decreasing d_{f-s} , intensity of Al decreases whereas that of N increases..... | 77 |
| Figure 4.4: (a) Dependence of the elemental percentage of the AlN films on filament-substrate distance (d_{f-s}); (b) dependence of N/Al ratio of AlN films on d_{f-s} . The atomic concentration of N and Al are greatly affected with respect to d_{f-s} ; Decrease in d_{f-s} from 2.2 to 1.0 cm, increases the N/Al ratio to a stoichiometric value of 1. (Note: The lines joining the points are only used as a guide to the eye.) | 79 |

| | |
|---|----|
| Figure 4.5: FTIR spectra of AlN films grown at various filament-substrate distance (d_{f-s}). A strong absorption peak corresponding to a feature of AlN films is observed at $d_{f-s} = 1.0$ cm. | 81 |
| Figure 4.6: Curve-fitting results for the AlN films grown at various filament-substrate distance (a) $d_{f-s} = 1.8$, (b) $d_{f-s} = 1.4$ and (c) $d_{f-s} = 1.0$ cm. The sub-peaks 1, 2, 4, 5 are attributed to $A_1(\text{TO})$, $E_1(\text{TO})$, $A_1(\text{LO})$ and $E_1(\text{LO})$ vibration modes of AlN, respectively. The sub-peak 3 is due to bond stretching vibration of Al–N bonds. The intensity of sub-peak 3 (bond stretching vibration of Al–N bonds) is increased by decreasing d_{f-s} | 82 |
| Figure 4.7: Dependence of intensity of bond stretching vibration of Al–N bonds on filament-substrate distance (d_{f-s}). The intensity of bond stretching vibration of Al–N bonds is increased by decreasing d_{f-s} | 83 |
| Figure 4.8: XRD patterns of the InN films grown at different RF powers. The crystallinity of InN films is improved by increasing the RF power up to 200 W. | 84 |
| Figure 4.9: Raman spectra of the InN thin films that were deposited at different applied RF powers. B_2 (low), E_2 (high) and A_1 (LO) phonon modes of InN are observed from the Raman spectra. | 86 |
| Figure 4.10: FESEM images of the InN thin films grown at the applied RF powers of 50 W (a), 100 W (b), 150 W (c), 200 W (d) and 250 W(e) with $\times 20000$ magnification. FESEM results of all the samples showed agglomeration of InN grains. | 88 |
| Figure 4.11: (a) Dependence of the elemental percentage of the InN films on RF power; (b) dependence of N/In ratio of AlN films on RF power. The atomic concentration of N and Al are greatly affected with respect to RF power. Increase in RF power from 50 to 250 W, increases the N/In ratio to a stoichiometric value of 1. (Note: The lines joining the points are only used as a guide to the eye.) | 90 |
| Figure 4.12: Plots of $(\alpha hv)^2$ versus hv for the InN thin films grown at various applied RF powers. The value of the optical band gap is determined by extrapolating the linear part of the curve to energy axis | 92 |
| Figure 5.1: In $3d_{5/2}$ core-level photoelectron spectra of $\text{Al}_x\text{In}_{1-x}\text{N}$ films deposited at $V_{\text{In}} = 65$ (a), 70 (b), 75 (c) and 80 V (d). The inset of (a), (b), (c) and (d) are the corresponding Al $2p$ core-level photoelectron spectra. A significant increase in the intensity of In $3d_{5/2}$ core-level is observed when V_{In} is increased. | 96 |
| Figure 5.2: Dependence of Al composition in the $\text{Al}_x\text{In}_{1-x}\text{N}$ films and F_{In} temperature on the applied AC voltage to the filament holding indium wire. The increase in temperature of the filament holding In wire results in decrease in Al incorporation in the $\text{Al}_x\text{In}_{1-x}\text{N}$ films. (Note: The lines joining the points are only used as a guide to the eye.). | 97 |

- Figure 5.3: XRD pattern of the $\text{Al}_x\text{In}_{1-x}\text{N}$ thin films grown at different applied AC voltage to the filament holding (V_{In}). No diffraction peaks assigned to crystalline $\text{Al}_x\text{In}_{1-x}\text{N}$ is observed for the films deposited at $V_{\text{In}} = 65, 70$ and 75 V..... 98
- Figure 5.4: Raman spectra of the grown $\text{Al}_x\text{In}_{1-x}\text{N}$ (a) and AlN (b) thin films. (c) Fitted curve of Raman spectrum of $\text{Al}_{0.64}\text{In}_{0.36}\text{N}$ films in the range of $650 - 900 \text{ cm}^{-1}$. The $E_2(\text{high})$ and $A_1(\text{LO})$ phonon modes are blue-shifted when the aluminum incorporation is increased. The $A_1(\text{LO})$ phonon mode of Al-rich $\text{Al}_x\text{In}_{1-x}\text{N}$ films shows two-mode behavior..... 101
- Figure 5.5: FESEM images of the $\text{Al}_x\text{In}_{1-x}\text{N}$ films with Al compositions of $x = 0.64$ (a), 0.60 (b), 0.18 (c) and 0.10 (d) with $\times 30000$ magnification. Agglomeration of grains are observed from the FESEM image of Al-rich $\text{Al}_x\text{In}_{1-x}\text{N}$ films. 102
- Figure 5.6: Transmittance (a) and Reflectance spectra (b) of $\text{Al}_x\text{In}_{1-x}\text{N}$ films with different Al compositions. The inset of (a) and (b) are transmittance and reflectance spectra of AlN ($x = 1$), respectively. As x is increased toward Al-rich region, the absorption edge and the reflectance minimum of the films shifts toward shorter wavelength..... 104
- Figure 5.7: Plots of $(\alpha hv)^2$ versus hv for $\text{Al}_x\text{In}_{1-x}\text{N}$ films with different x . The inset is the plot of $(\alpha hv)^2$ versus hv for AlN films. The band gap energy values of the films are shifted from 1.08 to 2.50 as the x is increased from 0.10 to 0.64 , respectively..... 105
- Figure 5.8: Band gap energy of $\text{Al}_x\text{In}_{1-x}\text{N}$ film as a function of Al composition, x . A bowing parameter of 4.3 was obtained by fitting the obtained band gap values with the theoretical ones..... 106
- Figure 5.9: $\text{In}3d_{5/2}$ core-level photoelectron spectra of the In-rich $\text{Al}_x\text{In}_{1-x}\text{N}$ films deposited at N_2 flow rate of 40 sccm (a), 60 sccm (b), 80 sccm (c) and 100 sccm (d). The inset of (a), (b), (c) and (d) are the corresponding $\text{Al}2p$ core-level photoelectron spectra. The Al incorporation in the In-rich $\text{Al}_x\text{In}_{1-x}\text{N}$ decreases from 0.11 to 0.03 as the nitrogen flow rate is increased from 40 to 100 sccm. 108
- Figure 5.10: $\text{In}3d_{5/2}$ core-level photoelectron spectra of the Al-rich $\text{Al}_x\text{In}_{1-x}\text{N}$ films deposited at N_2 flow rate of 40 sccm (a), 60 sccm (b), 80 sccm (c) and 100 sccm (d). The inset of (a), (b), (c) and (d) are the corresponding $\text{Al}2p$ core-level photoelectron spectra. The Al incorporation in the Al-rich $\text{Al}_x\text{In}_{1-x}\text{N}$ decreases from 0.66 to 0.48 as the nitrogen flow rate is increased from 40 to 100 sccm. 109
- Figure 5.11: $\text{N}1s$ core-level photoelectron spectra of the In-rich $\text{Al}_x\text{In}_{1-x}\text{N}$ samples deposited at N_2 flow rate of 40 sccm (a), 60 sccm (b), 80 sccm (c) and 100 sccm (d). The presence of N-In and N-Al components further confirms growth of $\text{Al}_x\text{In}_{1-x}\text{N}$ films. 111
- Figure 5.12: $\text{N}1s$ core-level photoelectron spectra of the Al-rich $\text{Al}_x\text{In}_{1-x}\text{N}$ samples deposited at N_2 flow rate of 40 sccm (a), 60 sccm (b), 80 sccm (c) and 100 sccm (d).

| | |
|---|-----|
| The presence of N–In and N–Al components further confirms growth of $\text{Al}_x\text{In}_{1-x}\text{N}$ films. | 112 |
| Figure 5.13: FESEM images of the In-rich $\text{Al}_x\text{In}_{1-x}\text{N}$ samples deposited at N_2 flow rate of 40 sccm (a), 60 sccm (b), 80 sccm (c) and 100 sccm (d) with $\times 30000$ magnification. Agglomeration of the grains is enhanced by increasing nitrogen gas flow rate. | 114 |
| Figure 5.14: FESEM images of the Al-rich $\text{Al}_x\text{In}_{1-x}\text{N}$ films deposited at N_2 flow rate of 40 sccm (a), 60 sccm (b), 80 sccm (c) and 100 sccm (d) with $\times 30000$ magnification. Cauliflower-shaped grains are observed from FESEM image of Al-rich $\text{Al}_x\text{In}_{1-x}\text{N}$ films grown at higher N_2 flow rate. | 115 |
| Figure 5.15: Micro-Raman spectra of the In-rich $\text{Al}_x\text{In}_{1-x}\text{N}$ samples. The structure of the In-rich $\text{Al}_x\text{In}_{1-x}\text{N}$ thin films tend to turn into amorphous state at high nitrogen flow rate. | 117 |
| Figure 5.16: (a) Raman spectra of the Al-rich $\text{Al}_x\text{In}_{1-x}\text{N}$ thin films grown at different N_2 flow rates. (b) and (c) Fitted curves of Raman spectrum of Al-rich $\text{Al}_x\text{In}_{1-x}\text{N}$ films deposited at $\text{N}_2 = 80$ and 100 sccm, respectively in the range of $700 - 950 \text{ cm}^{-1}$. Raman features of all Al-rich $\text{Al}_x\text{In}_{1-x}\text{N}$ are very broad possibly due to unstable nature of $\text{Al}_x\text{In}_{1-x}\text{N}$ thin films in Al-rich composition range. | 118 |
| Figure 5.17: Plots of $(\alpha h\nu)^2$ versus $h\nu$ for the In-rich $\text{Al}_x\text{In}_{1-x}\text{N}$ samples grown at various N_2 flow rates. The band gap energy of the films decreases from 1.08 to 0.90 eV as the flow rate is increased from 40 to 100 sccm. | 120 |
| Figure 5.18: Plots of $(\alpha h\nu)^2$ versus $h\nu$ for Al-rich $\text{Al}_x\text{In}_{1-x}\text{N}$ films grown at different N_2 flow rates. The band gap energy of the films decreases from 2.33 to 1.92 eV as the flow rate is increased from 40 to 100 sccm. | 121 |
| Figure 5.19: $\text{In}3d_{5/2}$ core-level photoelectron spectra of the as-grown In-rich $\text{Al}_x\text{In}_{1-x}\text{N}$ films (a) and the films annealed at 200 °C (b), 300 °C (c), 400 °C (d) and 500 °C (e). Intensity of the peak corresponding to In–O bond increases as the annealing temperature is increased. | 123 |
| Figure 5.20: $\text{N}1s$ core-level photoelectron spectra of the as-grown In-rich $\text{Al}_x\text{In}_{1-x}\text{N}$ films (a) and the films annealed at 200 °C (b), 300 °C (c), 400 °C (d) and 500 °C (e). At all annealing temperatures, the $\text{N}1s$ spectra of $\text{Al}_x\text{In}_{1-x}\text{N}$ films are disappeared and the intensity of N–In dramatically decreases. | 124 |
| Figure 5.21: Micro-Raman spectra of the $\text{Al}_x\text{In}_{1-x}\text{N}$ samples annealed at various temperatures. The annealing process completely collapses all the films' structures into a totally amorphous state. | 125 |
| Figure 5.22: Plots of $(\alpha h\nu)^{1/2}$ versus $h\nu$ for the $\text{Al}_x\text{In}_{1-x}\text{N}$ samples annealed at various temperature. After the $\text{Al}_x\text{In}_{1-x}\text{N}$ thin film with band gap energy of 0.90 eV was annealed | |

at 200, 300, 400 and 500 °C, the E_g value increases to 1.17, 1.40, 1.70 and 1.70 eV, respectively. 126

Figure 6.1: Mott–Schottky plots of the measured capacitance of the Si substrate (a) and the InN thin films grown at RF powers of 50 W (b), 100 W (c), 150 W (d), 200 W (e) and 250 W (f). 129

Figure 6.2: Dependence of donor density (N_d) and flat band potential (V_{fb}) of the InN thin films on the applied RF power. At lower RF powers the N_d of the films is higher while the V_{fb} is more negative at higher RF power. (Note: The lines joining the points are only used as a guide to the eye.). 131

Figure 6.3: Linear sweep voltammograms of the InN thin films grown at different RF powers. The films grown at lower RF power show higher anodic current. 132

Figure 6.4: Nyquist plots of the Si substrate (a) and the InN thin films deposited at the RF powers of 50 W (b), 100 W (c), 150 W (d), 200 W (e) and 250 W (f). 133

Figure 6.5: Dependence of current and resistance of the InN thin films on the applied RF powers. By increasing the power to a certain value the resistance increases while the current decreases. (Note: The lines joining the points are only used as a guide to the eye.). 134

Figure 6.6: Bode angle phase plots of the InN thin films grown at different RF power in the presence of 0.1 M KOH. The phase angles for the InN thin films grown at different RF powers are all less than 90° 135

Figure 6.7: Dependence of Bode phase angle and electron recombination lifetime (τ_n) of the InN thin films on the applied RF powers. (Note: The lines joining the points are only used as a guide to the eye.). 137

Figure 6.8: Linear sweep voltammograms (LSV) of the $\text{Al}_x\text{In}_{1-x}\text{N}$ thin films grown at different N_2 flow rates without (a) and under (b) simulated AM 1.5 G illumination. The films grown at the N_2 flow rates of 60 and 80 sccm show significant photocurrent.... 140

Figure 6.9: Amperometric $i-t$ curve of the $\text{Al}_x\text{In}_{1-x}\text{N}$ thin films grown at nitrogen flow rate of 80 sccm under simulated AM 1.5 G illumination. A rapid rise in the current upon illumination is seen from the cycles confirming considerable PEC behavior of the sample. 140

Figure 6.10: Nyquist plots of the $\text{Al}_x\text{In}_{1-x}\text{N}$ thin films deposited at the N_2 flow rates of 40 sccm (a), 60 sccm (b), 80 sccm (c) and 100 sccm (d). The film deposited $\text{N}_2 = 80$ sccm shows the lowest quartercircle-like diameter (the lowest resistance). 142

Figure 6.11: Bode angle phase plots of the $\text{Al}_x\text{In}_{1-x}\text{N}$ thin films grown at different N_2 flow rates in the presence of 0.1 M PBS. The obtained Bode phase angles of all $\text{Al}_x\text{In}_{1-x}\text{N}$ films are less than 90° suggesting that these thin films can be easily permeated by ions. 144

Figure 6.12: Mott–Schottky plots of the measured capacitance of the $\text{Al}_x\text{In}_{1-x}\text{N}$ thin films grown at N_2 flow rates of 40 sccm (a), 60 sccm (b), 80 sccm (c) and 100 sccm (d). Donor densities (N_d) and flat band potentials (V_{fb}) of all the films were calculated using this plots and Equations (6.1) and (6.2). 146

University of Malaya

LIST OF TABLES

| | |
|---|-----|
| Table 3.1: Deposition parameters used for deposition of AlN and InN thin films. A set of four AlN films was deposited at filament-substrate distances of 2.2, 1.8, 1.4 and 1.0 cm and a set of five InN films was deposited different RF powers of 50, 100, 150, 200 and 250 W..... | 55 |
| Table 3.2: Growth parameters used for deposition $Al_xIn_{1-x}N$ thin films. A set of four $Al_xIn_{1-x}N$ films was initially deposited at various AC voltages applied to the filament holding In wire (set 1). Two sample were selected from set 1 and two sets (set 2&3) of four $Al_xIn_{1-x}N$ thin films were deposited at N_2 flow rate of 40, 60, 80, 100 sccm..... | 56 |
| Table 3.3: Raman-active optical modes of AlN and InN and their positions (Junqiao Wu, 2009). | 64 |
| Table 4.1: The thickness and band gap energy values of InN films deposited at various RF powers. The band gap values (E_g) are close to that of polycrystalline InN..... | 92 |
| Table 6.1: Calculated compositional, optical and electrical values of $Al_xIn_{1-x}N$ films grown at various N_2 flow rates..... | 143 |

LIST OF SYMBOLS AND ABBREVIATIONS

| | | |
|-----------------|---|---|
| A | : | Interfacial area |
| AFM | : | Atomic force microscopy |
| AlGaN | : | Aluminum gallium nitride |
| AlInN | : | Aluminum indium nitride |
| AlN | : | Aluminum nitride |
| BAW | : | Bulk acoustic wave |
| C | : | Capacitance of the space charge region |
| °C | : | Degree centigrade |
| CBM | : | Conduction band minimum |
| CO | : | Carbon monoxide |
| CO ₂ | : | Carbon dioxide |
| d_{f-s} | : | Filament-to-substrate distance |
| DUV | : | Deep ultra-violet |
| ϵ | : | Static dielectric constant |
| ϵ_0 | : | Permittivity of free space |
| E_g | : | Band gap energy |
| EC | : | Electrochemical |
| EDX | : | Energy-dispersive X-ray spectroscopy |
| EIS | : | Electrochemical impedance spectroscopy |
| F _{Al} | : | Filament holding (heating) Al wire |
| F _{In} | : | Filament holding (heating) In wire |
| FESEM | : | Field emission scanning electron microscopy |
| FTIR | : | Fourier transform infrared spectroscopy |
| FWHM | : | Full width at half maximum |

| | | |
|--------------------------------|---|--|
| GaN | : | Gallium nitride |
| H ₂ | : | Hydrogen |
| HAADF | : | High angle annular dark field |
| HEMT | : | High-electron-mobility transistor |
| HRTEM | : | High-resolution transmission electron microscopy |
| HRXRD | : | High-resolution x-ray diffraction |
| InAs | : | Indium arsenide |
| InGaN | : | Indium gallium nitride |
| InN | : | Indium nitride |
| In ₂ O ₃ | : | Indium oxide |
| ISBT | : | Inter-subband electron transition |
| k | : | Boltzmann's constant |
| LED | : | Light-emitting diode |
| LD | : | Laser diode |
| LO | : | Longitudinal optical |
| LSV | : | Linear sweep voltammogram |
| LT | : | Low temperature |
| MB | : | Moss-Burstein |
| MBE | : | Molecular beam epitaxy |
| MFC | : | Mass flow controller |
| MOCVD | : | Metalorganic chemical vapor deposition |
| MQW | : | Multiple quantum well |
| MS | : | Mott-Schottky |
| N ₂ | : | Nitrogen |
| N _d | : | Electron donor density |
| NHE | : | Normal hydrogen electrode |

| | | |
|-----------------|---|--|
| NIR | : | Near-infrared |
| O ₂ | : | Oxygen |
| PBS | : | Phosphate buffer solution |
| PEC | : | Photoelectrochemical |
| PECVD | : | Plasma-enhanced chemical vapor deposition |
| PL | : | Photoluminescence |
| PLD | : | Pulsed laser deposition |
| q | : | Elementary electron charge |
| R_{ct} | : | Charge-transfer resistance |
| RF | : | Radio frequency |
| RHEED | : | Reflection high-energy electron diffraction |
| RMS | : | Root mean square |
| RTA | : | Rapid thermal annealing |
| SAW | : | Surface acoustic wave |
| sccm | : | Standard cubic centimeters per minute |
| Si | : | Silicon |
| SiC | : | Silicon carbide |
| T_f | : | Filament temperature |
| τ_n | : | Electron recombination lifetime |
| T_s | : | Substrate temperature |
| TMAI | : | Trimethyl aluminum |
| TMGa | : | Trimethyl gallium |
| TMIn | : | Trimethyl indium |
| TO | : | Transversal optical |
| V _{AC} | : | AC voltage |
| V _{Al} | : | AC voltage applied to the filament holding Al wire |

| | | |
|-------------------|---|--|
| V_{bias} | : | Applied voltage |
| V_{fb} | : | Flat band potential |
| V_{In} | : | AC voltage applied to the filament holding In wire |
| VBM | : | Valence band maximum |
| Vis | : | Visible |
| WO_3 | : | Tungsten oxide |
| XPS | : | X-ray photoelectron spectroscopy |
| XRD | : | X-ray diffraction |
| XRF | : | X-ray fluorescence |

University of Malaya

CHAPTER 1:

INTRODUCTION

1.1 Important Properties of Indium- and Aluminum-Based Nitrides

In the last few years the group III-nitrides have emerged as one of the most important compound semiconductor materials and have attracted much attention. This is due to their superior physical properties (G. Li, Wang, Yang, & Wang, 2015; Junqiao Wu, 2009; Yang et al., 2014) which can be employed in many electronic and opto-electronic devices. The large differences in the ionic radii and bonding energies of the group III metal cations give rise to different lattice constants, electron affinities and band gap energies which challenge the epitaxial deposition of the III-nitrides and their alloys. The most notable of the group III-nitrides are aluminum nitride (AlN), indium nitride (InN) and their ternary alloy (aluminum indium nitride, AlInN) which have found applications in various devices.

AlN has many outstanding properties such as wide band gap energy (6.2 eV), excellent chemical stability, high hardness, high thermal conductivity, high volume resistivity and low dielectric constant (Kuang et al., 2012a). Due to strong chemical bonding, AlN has outstanding physical (high melting point and mechanical strength) and chemical stability. Since this semiconductor does not have ferroelectric behavior, it is not required to pole it for piezoelectric sensors/actuators which possess excellent advantages of low power consumption as compared to capacitive and magnetomotive ones (Tran et al., 2013). AlN thin films can exist in various crystal orientation and band gap values depending on the impurity incorporation and the growth parameters such as deposition temperature and pressure. Investigation of the properties of AlN (and $\text{In}_x\text{Al}_{1-x}\text{N}$) films under different growth conditions is of importance for application of these films in the

electro-acoustic devices as well as for understanding defect mechanism and the origin of the band gap modulation.

Among the group III-nitrides, InN has the smallest effective mass, smallest band gap energy (0.64 eV) and highest electron drift velocity which make it particularly suitable for opto-electronic devices (Ooi et al., 2011; Xu & Yoshikawa, 2003). Up to late 90s, sputtering method had been mostly used for the growth of InN and the fundamental band gap energy of the semiconductor was assumed to be 1.9 eV. In fact, A breakthrough stemmed from the improvement of InN films deposited by molecular beam epitaxy (MBE) (J. Wu et al., 2002), has led to the revision of InN band gap energy from 1.9 eV to a much smaller value of 0.64 eV (J. Wu et al., 2003). The new value has been confirmed theoretically as well (Bechstedt et al., 2003). As a result, it can be concluded that the full-color spectrum can be achieved by the devices. The dissociation temperature of InN is quite low (around 600 °C) (X. Wang & Yoshikawa, 2004), hence, to avoid re-evaporation of nitrogen adatoms the low temperature is required for growth of InN thin films.

$\text{Al}_x\text{In}_{1-x}\text{N}$ has the widest band gap energy range among all of the group III-nitrides and has been extensively utilized in opto-electronic field of applications. The increasing interest is due to its tunable band gap varying remarkably in the range of 0.7-6.2 eV depending on the amount of indium (or aluminum) constituent (V Yu Davydov et al., 2002). Hence, varying the composition of $\text{Al}_x\text{In}_{1-x}\text{N}$ film makes it possible to customize the electronic structures of the alloy films for specific applications. $\text{Al}_x\text{In}_{1-x}\text{N}$ provides considerable wider band gap energy and lower refractive indices than those of gallium nitride (GaN) resulting in improved confinement of carriers and photons compared to gallium-rich aluminum gallium nitride (Ga-rich AlGaN) (Ferhat & Bechstedt, 2002). However, from the thermodynamic point of view, it is difficult to grow high quality

$\text{Al}_x\text{In}_{1-x}\text{N}$ thin film due to the large difference between thermal stability of AlN and InN. Therefore, few works have been reported so far on the growth of high quality $\text{Al}_x\text{In}_{1-x}\text{N}$ compound.

1.2 Application of Indium- and Aluminum-Based Nitrides

Due to the excellent properties of indium and aluminum based nitrides, these semiconductors have been utilized in numerous applications. AlN is a promising material for many applications such as bulk acoustic wave (BAW) and surface acoustic wave (SAW) devices, deep ultra-violet (DUV) light-emitting diodes (LEDs), laser diodes (LDs), field emission displays and thermoelectric devices (García-Gancedo et al., 2011; L. a. Guo, Chen, Zhu, Duan, & Ye, 2015; Jeong, Jeon, Lee, & Kim, 2015; Rodríguez-Madrid et al., 2012). InN has emerged as a potential candidate for many applications including high-efficiency solar cells, opto-electronic, high speed and high-power electronic devices (Bhuiyan, Hashimoto, & Yamamoto, 2003). Furthermore, InN has received remarkable interest for the development of chemical sensors and biosensors due to its high surface donor density and the corresponding surface electron accumulation, chemical inertness, and chemical recognition capabilities (Naveed ul Hassan et al., 2013; Sofikiti et al., 2010). $\text{Al}_x\text{In}_{1-x}\text{N}$ has attracted so much attention for various applications such as distributed Bragg reflector, field effect transistors, facilitation layers in pseudomorphic epitaxy and solar cells (Berger, Dadgar, Bläsing, & Krost, 2013; Monemar, Paskov, & Kasic, 2005; Saidi, Mejri, Baira, & Maaref, 2015; Watson et al., 2005). In-rich $\text{In}_x\text{Al}_{1-x}\text{N}$ thin films with tunable band gap of 0.7-2.4 eV can be used for multi-junction solar cell devices since this band gap energy range almost covers solar spectrum (Yamamoto, Islam, Kang, & Hashimoto, 2010).

1.3 Growth Techniques of Indium- and Aluminum-Based Nitrides

Nowadays, according to the applications, various epitaxial growth techniques have been specifically employed for the synthesis of high quality AlN, InN and AlInN semiconductors under controlled conditions. The most common methods are Metalorganic Chemical Vapor Deposition (MOCVD), Molecular Beam Epitaxy (MBE), Pulsed Laser Deposition (PLD), reactive sputtering and Plasma-Enhanced Chemical Vapor Deposition (PECVD). The deposition process of each method will be described in detail in chapter 2. Among these methods, sputtering is undoubtedly the most inexpensive and convenient technique. This technique is versatile in preparing highly crystalline films economically, which is beneficial for lowering the cost of the device fabrication. MOCVD and MBE are well-established techniques and are widely utilized for both research and device production such as LED.

The first AlN and InN compounds were prepared as early as 1907 (Fichter, 1907) and 1932 (Johnson & Parsons, 1931), respectively. However, no remarkable progress was reported until the end of 1960s. In the late 1960s and early 1970s, development of new epitaxial deposition methods caused to significant interest in III-nitrides (Manasevit, Erdmann, & Simpson, 1971; Maruska & Tietjen, 1969; Yoshida, Misawa, & Itoh, 1975) though quality of the materials was not sufficient for device development. The optical properties of AlInN/sapphire films were initially investigated in the Al-rich composition regime in order to use the properties in potential applications (Kubota, Kobayashi, & Fujimoto, 1989). In the mid-1990s, performance of the nitride devices was improved very rapidly and commercial attention toward III-nitrides was established by fabrication of LEDs in the blue and the green regions of the spectrum using MOCVD method. Nakamura and his colleagues at Nichia Laboratory have improved quality of the fabricated blue and green LEDs to a level that the devices could be commercialized in the mid-1990s (Pearson, Zolper, Shul, & Ren, 1999). Following that, numerous works on the

fabrication of the optically pumped lasers with high performance were reported (Akasaki et al., 1995; Schmidt et al., 1996). In recent years, MOCVD technique has been employed to fabricate high frequency and high power AlInN high-electron-mobility transistors (HEMTs) with different buffer layers (Kelekci et al., 2012). It has been shown that the device performance is much better than AlGaIn/GaN structures due to enhancement of spontaneous polarization as a result of AlInN intrinsic properties (Medjdoub et al., 2006).

1.4 Research Problems

Despite the fact that most of the above-mentioned methods led to the growth of high quality group III-nitride nanostructures, some unwanted drawbacks seem to be unavoidable using the methods. For instance, in MOCVD process group III-nitride films are obtained at high substrate temperatures on specified substrates (e.g., sapphire and GaN) by using a toxic gas such as NH_3 . Therefore, this method is restricted by the type and temperature of substrate. The properties of crystalline AlN thin films grown by using a PLD system are undesirably affected by the repetition frequency of the applied laser pulses (Sumitani et al., 2010). The sputtered AlN, InN and AlInN films suffer from low deposition rate which dramatically increases time and cost of device production.

Also, in most cases larger band gap energy values (much higher than 0.7 eV) for InN and In-rich AlInN films are obtained by sputtering (He et al., 2010; H. F. Liu, Tan, Dalapati, & Chi, 2012; Valdueza-Felip et al., 2012) although the sputtered films are highly crystalline. This limits the sputter-deposited InN and In-rich AlInN films for solar cell applications since the films with narrow band gaps are highly desirable as the base materials in the solar cell devices. In addition, there have been remarkable disagreements among the band gap energies measured for AlInN films grown by MOCVD, MBE and sputtering-based methods. One reason may be that some of the measurements were

carried out before the new value of 0.7 eV was established for band gap energy of indium nitride (InN).

Moreover, in most of the deposition methods listed above, external heating of substrate with high temperature is required which may cause degradation of the substrate (H. Cheng et al., 2003) as the whole wafer is exposed to the heating source. Also, these non-self-heating methods of depositions are costly in terms of energy consumption, increase thermal budget of manufacture procedure and require long time for heating prior to the deposition. In other words, preparation of thin films by using a technique that provides self-heating of substrates during the deposition simplifies the deposition system, shortens time of the process and as a result makes it possible to gain higher throughput at low cost.

On the other hand, less works have been devoted to the electrochemical (EC) and photoelectrochemical (PEC) properties of indium and aluminum based nitride thin films. The unavoidable surface donor density and the corresponding surface electron accumulation of InN can be effectively employed for the charge transfer in EC water splitting application. Also, it has been theoretically shown that Al-rich $\text{Al}_x\text{In}_{1-x}\text{N}$ with a minimum Al composition (x) of ~ 0.45 and band gap energy of 1.8 eV is suitable for PEC water splitting. Therefore, tuning the band gap energy of $\text{Al}_x\text{In}_{1-x}\text{N}$ in the range that meets water splitting requirement may offer an alternative approach for production of H_2 fuel with PEC water splitting technique.

1.5 Research Objectives

This work focuses on the structure, morphology, optical and electrochemical properties of indium and aluminum based nitride thin films grown by plasma-assisted reactive evaporation method. The objectives of this research work are stated below:

1. To investigate the effects of radio-frequency (RF) power and filament-to-substrate distance towards the structure, morphology and composition of InN and AlN thin films, respectively.
2. To investigate the effects of voltage applied onto filament holding the In wire on the structure, morphology, composition and optical properties of $\text{Al}_x\text{In}_{1-x}\text{N}$ films towards tuning the band gap of the films.
3. To investigate the effects of nitrogen gas flow rate on the structure, morphology and composition of In-rich and Al-rich $\text{Al}_x\text{In}_{1-x}\text{N}$ films.
4. To investigate the effects of annealing on the properties of selected $\text{Al}_x\text{In}_{1-x}\text{N}$ films for determining the stability of the films for applications in devices.
5. To investigate the EC and PEC performance of InN and Al-rich $\text{Al}_x\text{In}_{1-x}\text{N}$ films, respectively.

1.6 Outline of Thesis

The thesis is structured as follows. In chapter 2, a literature review based on the different growth methods of indium- and aluminum-based nitride thin films, their benefits, drawbacks and the related works are presented. The experimental details and characterization methods are discussed in chapter 3. This chapter consists of two main sections. In the first section the sample preparation, the deposition system and process are described. The second part of the chapter focuses on the analytical apparatus used for characterization of the grown samples. Also, the corresponding calculations for analysis of the results are included in the second section of chapter 3. Chapter 4, 5 and 6 are devoted to obtained results and the corresponding discussions. In chapter 4 the results and discussions related to growth of AlN and InN thin films are presented in two separated parts. The first part of chapter 4 focuses on the results and discussions of deposition of AlN thin films at different filament-to-substrate distances, whereas the second part is devoted to the results and discussions of growth of InN thin films at different RF powers.

Chapter 5 presents the results and discussions corresponding to growth of $\text{Al}_x\text{In}_{1-x}\text{N}$ thin films. This chapter includes three main sections. The results of the effect of indium-contained filament (F_{In}) temperature on the properties of $\text{Al}_x\text{In}_{1-x}\text{N}$ thin films are presented and discussed in the first part of chapter 5. The second section focuses on the results and discussions for the deposition of Al-rich and In-rich $\text{Al}_x\text{In}_{1-x}\text{N}$ thin films under various nitrogen flow rates. The last part of the chapter is devoted to the results and discussions associated to the annealing $\text{Al}_x\text{In}_{1-x}\text{N}$ thin films at various temperatures. Chapter 6 of this thesis presents the electrochemical (EC) and photoelectrochemical (PEC) properties of InN and $\text{Al}_x\text{In}_{1-x}\text{N}$ thin films, respectively. The EC behavior of the InN films grown under different RF powers is presented in the first part of chapter 6, whereas the PEC behavior of the Al-rich $\text{Al}_x\text{In}_{1-x}\text{N}$ thin films deposited under various nitrogen gas flow rates is described in the second part of the chapter. Finally, this thesis is concluded in chapter 7 which includes summary of the findings and suggestions for future works.

CHAPTER 2:

LITERATURE REVIEW

2.1 Introduction

In chapter 1, the properties of indium- and aluminum-based nitrides, the potential applications of the semiconductors and the proceeding growth methods for deposition of these materials were described. A comprehensive review on the previous studies on the growth and properties of AlN, InN and $Al_xIn_{1-x}N$ may help us to get familiar with these material in order to deposit them by using plasma-assisted reactive evaporation technique.

This chapter begins with a description on the crystal structure of the indium and aluminum based nitride semiconductors. The next sections gives a detailed information about the optical properties of the studied semiconductors including the band gap and band alignment. This leads to an understanding of band positions of $Al_xIn_{1-x}N$ at the whole composition range. Electrochemical (EC) and photoelectrochemical (PEC) Water Splitting processes, the corresponding requirements for a semiconductor to be used as a photoelectrode as well as the potential properties of InN and $Al_xIn_{1-x}N$ thin films for EC and PEC water applications will be explained in the fourth section of this chapter. The chapter ends with a review on the current growth methods of AlN, InN and $Al_xIn_{1-x}N$ thin films.

2.2 Crystal Structure of Indium- and Aluminum-Based Nitrides

Under ambient conditions these two nitrides tend to crystallize into two different structures: wurtzite (hexagonal) and zincblende (cubic). This is an advantage for group III-nitrides semiconductors over conventional semiconductors such as Si or GaAs, which have only a diamond or zincblende structure with cubic symmetry. The wurtzite structure with the space group of $P6_3mc$ (C_{6v}^4) is thermodynamically stable. Due to the strong ionic

bond between the group-III metal cations and nitrogen anions, the unit cell of the III-nitrides is distorted from the ideal wurtzite structure causing to a large spontaneous polarization along the c-axis. In fact, the group III-nitrides are polar crystals because they do not have a center of symmetry (Daudin, Rouvière, & Arlery, 1996). Due to this advantage, III-nitrides possess many properties such as pyroelectricity, piezoelectricity (Kucera et al., 2014; Yalavarthi, Gaddipati, & Ahmed, 2011) and second harmonic generation (Ivanov, Shubina, Komissarova, & Jmerik, 2014; H. Y. Zhang et al., 1996). However, the zincblende phase with the space group $F4\bar{3}m (T_d^2)$ has been stabilized by epitaxial growth of thin films. It has been reported that at a hydrostatic pressure of ~ 12 GPa, InN phase is transmitted from the wurtzite into the rocksalt structure with the space group $Fm\bar{3}m (O_h^5)$ (Ueno, Yoshida, Onodera, Shimomura, & Takemura, 1994).

As mentioned above, group III-nitrides with wurtzite structure are more stable. The crystalline lattice structure of wurtzite group III-nitrides have two kinds of bond named B_1 and B_2 . For example, the schematic diagram of wurtzite AlN structure is shown in Figure 2.1. B_1 is more covalent in nature while B_2 is more ionic, therefore, the formation energy of B_1 is relatively larger than that of B_2 (Kuang et al., 2012c) resulting in easy dissociation of B_2 bond at high growth temperature. The (100) plane is composed of only B_2 bond while the planes of (002), (101) and (103) are consisted of B_1 and B_2 bonds together (Kuang et al., 2012c). Therefore, the energy required for growth particles to be deposited in the planes of (002), (101) and (103) are relatively larger than that needed for (100).

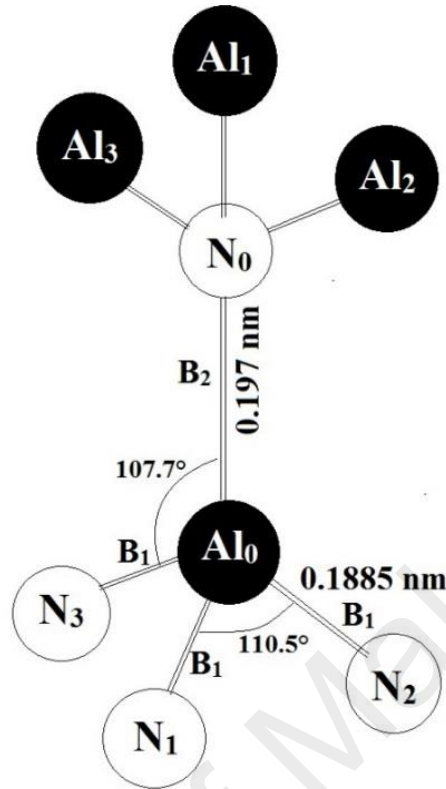


Figure 2.1: Schematic diagram of wurtzite AlN structure (Kuang et al., 2012c).

2.3 Band gap and Band Alignment

InN and AlN are the semiconductors with a remarkable difference in the optical band gap while the lattice constant is almost the same. The band gap energy (E_g) varies from the near-infrared for InN (0.7 eV) to the deep UV for AlN (6.2 eV) that correspond to a wavelength from 1770 to 200 nm. Its direct band gap is suitable for optical devices. Having the very similar lattice constants, it is possible to grow heterojunction systems as well as ternary and quaternary compounds of group III-nitrides which can be utilized in full-color-display application by tuning the band gap and the optical/electrical properties (Z. T. Chen, Tan, Sakai, & Egawa, 2009; Romero et al., 2012).

Long before the revision of the band gap value of InN, many theoretical and experimental investigations has focused on the band offset between group III-nitrides. Since the revision is mainly on the conduction band-filling effect, previous studies and values about valence band offset between InN and other nitrides are still considered to be valid. However, there has been uncertainty on the valence band offset between these semiconductors due to several reasons such as strain, piezoelectric and spontaneous polarization effects (Vurgaftman & Meyer, 2003).

Since 1996, different values have been reported for valence band offset between wurtzite AlN and InN. For instance, on the calculation side 1.25 eV (S. H. Wei & Zunger, 1996), 1.37 eV (Nardelli, Rapcewicz, & Bernholc, 1997) and experimentally 1.52 eV (King et al., 2007) and 1.80 eV (Martin, Botchkarev, Rockett, & Morkoç, 1996) have been reported so far. Recently, Ramón Collazo and Nikolaus Dietz (Ramon Collazo & Dietz, 2013) actively studied Band gap alignments of InN, GaN, AlN and their ternary alloys. The obtained valence band position and offsets for group III-nitrides alloys is shown in Figure 2.2. In their studies the valence band maximum (VBM) of wurtzite InN were found to be ~ 1.2 eV higher than that of AlN whereas the conduction band minimum (CBM) of wurtzite InN was shown to be 5.0 eV lower than that of AlN. For ternary $\text{Al}_x\text{In}_{1-x}\text{N}$, it has been shown that the valence and conduction bands shift linearly and nonlinearly with Al mole fraction (x), respectively, resulting in band gap bowing of the compound (Figure 2.2). The observed behavior of valence and conduction band positions in $\text{Al}_x\text{In}_{1-x}\text{N}$ with different x along with the ability of engineering band gap energy of the semiconductor may offer a promising approach for production of hydrogen fuel using PEC water splitting technique. These properties will be discussed in more detailed in the following section.

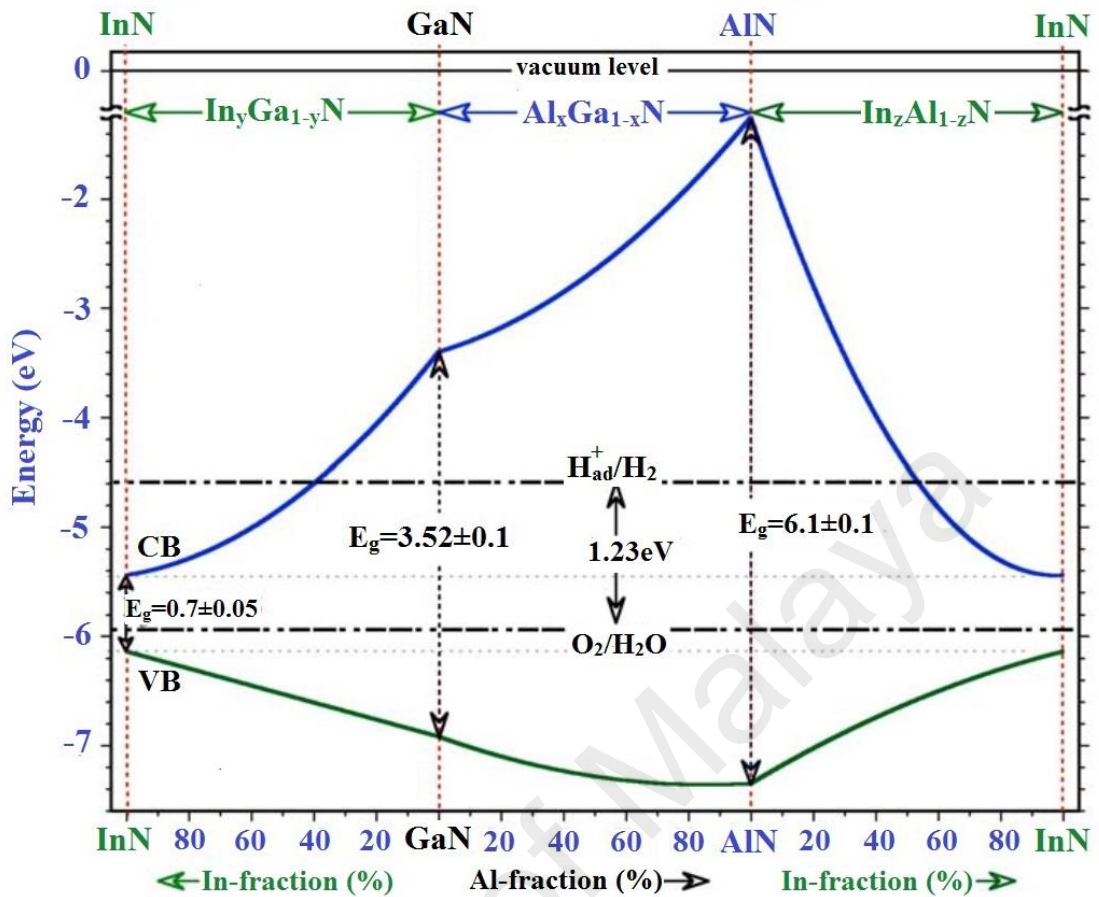


Figure 2.2: Valence band position and offsets for group III-nitrides alloys. From Ref. (Ramon Collazo & Dietz, 2013).

2.4 Photoelectrochemical Water Splitting Application

Energy is a most important factor to drive the life in smooth and neat manner. Rapid industrialization, steep increase in the population growth and world modernization are the crucial factors, which tend to hike the rate of energy consumption in a stipulated manner. The energy has been consumed in the form of commercial, residential, industrial and transportation. The dependence on major fossil fuel associated resources such as, oil and electricity has made the energy a vital component of our daily needs. But, extensive production of energy from fossil fuels causes the emission of anthropogenic CO and CO₂ emission, thus leads to global warming, greenhouse effect and climate changes (Höök & Tang, 2013; Vernon, Thompson, & Cornell, 2011).

Hydrogen gas generated from a clean and renewable source such as solar energy has been considered as a main alternative for the conventional energy carriers including fossil fuels to mitigate financial and environmental problems that associated with fossil fuels consumptions. Recently, hydrogen gas production via photo-assisted electrolysis (photoelectrolysis) of water using a light harvesting semiconductor-based system as a photoelectrochemical (PEC) cell has emerged as one of the most promising methods for the sustainable, carbon-free and affordable energy supply (Ariffin et al., 2015; Tachibana et al., 2012). In fact, the simple procedure of solar energy conversion and storage is photolysis of water with an aid of semiconductor photocatalysts, which act as the light absorber and energy converter and to store solar energy in the simplest chemical bond, hydrogen (Cowan & Durrant, 2013).

In PEC cell, a semiconductor with proper characteristics is immersed in an aqueous electrolyte and illuminated with sunlight. A schematic of PEC water splitting process is shown in Figure 2.3. The principle of PEC hydrogen production is relatively simple, although the underlying fundamental processes are complex and still not well apprehended at the molecular level. Figure 2.3 (a) shows the PEC water splitting based on n-type semiconductor (e.g. TiO_2) electrode. In this PEC system (Ni, Leung, Leung, & Sumathy, 2007), a catalyzed semiconductor photoelectrode is ohmically contacted with a catalytic counter electrode, immersed in an aqueous electrolyte solution. Under light illumination, photo - induced charge transfer takes place that leads to production of hydrogen and oxygen at the counter electrode and semiconductor, respectively. Upon light illumination, the semiconductor absorbs relatively higher energy photons compared to its band gap and subsequently electrons and holes are produced. The photo-excited electrons transfer to a counter electrode (e.g., Pt) through outer circuit which reduce water to hydrogen. Whereas, the holes transfer to the semiconductor surface and oxidize the water to O_2 . In the case of p-type semiconductor materials (Abe, 2010), water is reduced

and oxidized at the semiconductor and counter electrode surfaces, respectively (Figure 2.3 (b)). The other system which is called tandem system consists of an n-type semiconductor electrode with an appropriate p-type semiconductor electrode (Figure 2.3 (c)). There has been numerous investigations on the development of these three systems with a stable photoelectrode semiconductor that functions efficiently for the production of hydrogen gas under visible light illumination.

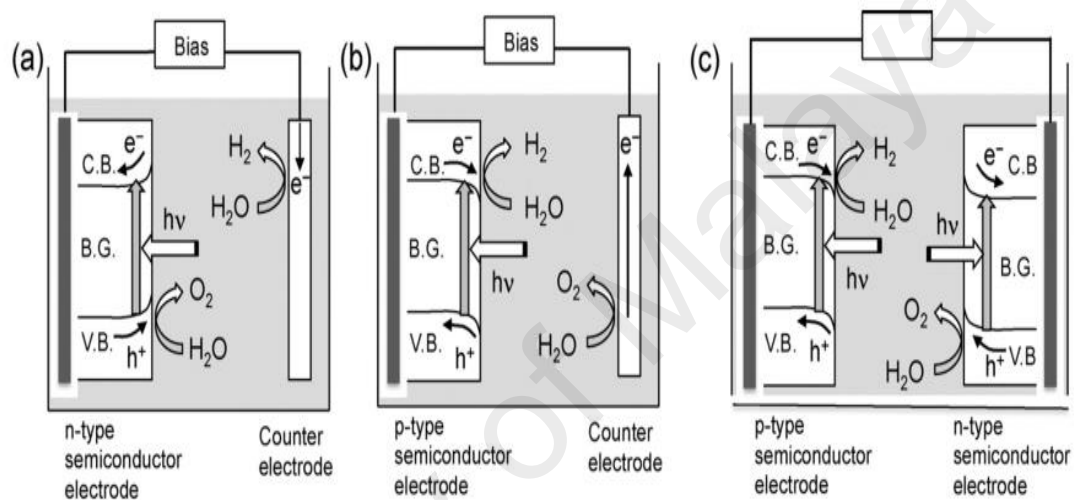
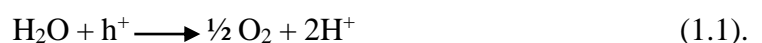


Figure 2.3: Photoelectrochemical water splitting systems using n-type semiconductor photoanode (a), p-type semiconductor photocathode (b), and tandem system (c) (Abe, 2010).

In some cases, only an external bias is applied between the working and the counter electrode to provide charge separation between the electrodes. This system is called electrochemical (EC) water splitting (Wallys, Hoffmann, Furtmayr, Teubert, & Eickhoff, 2012). The applied external bias excites electrons from valence band to conduction band creating holes on the valence band. The H₂O molecules are oxidized at valence band in the following reaction:



The obtained H⁺ ions are reduced by the excited electrons at conduction band:



It should be noted that electron donor density of working electrode is the key factor determining the resultant anodic current in the EC system. This will be explained more detailed in chapter 6 of this thesis.

A semiconductor material must satisfy several criteria to be considered as a PEC water splitter device. (i) Its band gap needs to be a minimum of 1.8 eV to harness visible photons and to provide the required potential for electrolysis in the single-photoelectrode water splitting cell system (Weber & Dignam, 1986). (ii) The electron-accepting and electron-donating states (minority band-edges) and the Fermi level of the material need to “straddle” the hydrogen gas and oxygen gas production potentials. (iii) The material needs to have high level of stability in contact with the electrolyte. (iv) It should has high efficiency to convert energy of acquired photons to separated electron/hole pairs. (v) Charge transfer at the interface of the material needs to be fast enough to avoid carrier accumulation at the surface which may cause to shift the band-edges out of the overlap position.

The suitable band gap for a PEC device is determined by considering two important aspects of the process: 1. maximizing the absorption of solar photons and 2. Generating the required energy for water splitting reactions. The highest level of solar absorption could be attained by narrowing band gap energy of the semiconductor. However, if the E_g value is too small, the photoelectrode cell will not provide the potential necessary for electrolysis reactions. The potential difference between the hydrogen-evolving half reaction (reaction 1.2) and water-oxidation half reaction (reaction 1.1) is 1.229 V. The water-oxidation and the hydrogen-producing half reactions additionally require 0.275 and 0.050 V over-potential, respectively to proceed at an efficient rate (Kocha & Turner, 1995). For a semiconductor as a PEC water splitting cell, the electron-accepting (or

electron-donating) reactions is occurred at Fermi level which is positioned $\sim 0.050 - 0.200$ eV from the band-edge. As a result, the semiconductor band gap needs to be a minimum of 1.8 eV to provide the required potential for electrolysis in the single-photoelectrode water splitting cell system.

Tremendous research works have been reported on metal oxide-based photocatalyst materials (J. Guo & Chen, 2011; Kudo & Miseki, 2009) since the pioneering work by Fujishima and Honda who reported the capability of water splitting using TiO_2/Pt photoelectrochemical cell under UV light irradiation in early 1970s (Fujishima & Honda, 1972). However, band gap energy of the most of metal oxide semiconductors is larger than 3 eV. Therefore it is able to harvest only 4% of light in the solar spectrum. Hence, the use of metal oxides as photocatalyst materials is undesirably limited by narrow range of light absorption in the visible spectrum. In addition, a low energy maximum (around +3 V vs normal hydrogen electrode (NHE) compared to +1.23 V vs NHE for the water-oxidation reaction) has emerged due to the presence of O 2p orbitals in valence band of metal oxide materials resulting in a large potential gap between the valence band and water-oxidation reaction level and, hence, degrades the solar-to-fuel conversion efficiency (Hwang, Wu, Hahn, Jeong, & Yang, 2012).

On the other hand, group III-nitrides compound semiconductors are more promising materials for PEC water splitting due to following reasons: (i) III-nitrides have a wide tunable band gap energy of 0.7– 6.2 eV, which covers the entire solar spectrum and allows harnessing of visible photons. (ii) Valence band of the metal nitrides consists of N 2p orbitals which have smaller ionization energies than O 2p orbitals resulting in less positive valence band maximum potentials than metal oxides (Maeda & Domen, 2007, 2011). (iii) These photoelectrodes have a high level of inherent chemical stability against corrosion in aqueous solutions (Maeda, 2011). Indium gallium nitride ($\text{In}_x\text{Ga}_{1-x}\text{N}$) with the band gap

from 0.7 to 3.4 eV has been proven as a functional photocatalyst for efficient water splitting. Li et al. (J. Li, Lin, & Jiang, 2008) explored the PEC behavior of $\text{In}_x\text{Ga}_{1-x}\text{N}$ epilayers and showed that under white light illumination the photocurrent density strongly depends on indium (In) incorporation of the epilayers. Stable hydrogen gas production from water splitting using multiband $\text{In}_x\text{Ga}_{1-x}\text{N}/\text{GaN}$ nanowire heterostructures under a long-wavelength irradiation (up to 560 nm) were achieved by Kibria et al. (Kibria et al., 2013). Aryal et al. (Aryal, Pantha, Li, Lin, & Jiang, 2010) have observed H_2 generation in biased p-type $\text{In}_x\text{Ga}_{1-x}\text{N}$ ($0 \leq x \leq 0.22$) electrodes under white light illumination and found that the electrodes have an excellent stability in aqueous HBr.

However, very little has been reported so far on electrochemical and photoelectrochemical properties of InN and $\text{Al}_x\text{In}_{1-x}\text{N}$ semiconductors. For InN, this may be due to the fact that the band gap energy of InN is now considered to be 0.7 eV not the previously accepted value of 1.9 eV. Possible reasons for the high band gap value are the Moss–Burstein (MB) shift, presence of oxygen impurity, and other stoichiometry-related defects (K. Butcher et al., 2004; T. Shubina et al., 2005). Presence of oxygen enhances electron donor density on the surface of electrode which is considered as a key factor in EC process. Therefore, unintentional presence of oxygen in the InN thin films with band gap energy of ~ 2.0 eV could merge the material as a competitive candidate for EC water splitting. $\text{Al}_x\text{In}_{1-x}\text{N}$ has a wide tunable band gap of 0.7 to 6.2 eV (V. Yu Davydov et al., 2002) depending on the indium (or aluminum) composition in the structure. Also, from Figure 2.2, it can be seen that band-edge potentials of $\text{Al}_x\text{In}_{1-x}\text{N}$ with minimum aluminum compositions (x) of $\sim 45\%$ ($E_g \sim 1.8$ eV) can straddle the H^+/H_2 and $\text{O}_2/\text{H}_2\text{O}$ redox potentials (Ramón Collazo & Dietz III, 2013) which is another crucial criterion for water splitting performance as mentioned earlier. Therefore, the ability of engineering band gap energy of $\text{Al}_x\text{In}_{1-x}\text{N}$ in the range that meets water splitting requirement (1.8 – 2.4 eV) as

well as suitable band alignments of $\text{Al}_x\text{In}_{1-x}\text{N}$ ($0.45 \leq x \leq 0.60$) alloys, may offer an alternative approach for production of H_2 fuel with PEC water splitting technique.

2.5 Growth Methods of Indium- and Aluminum-Based Nitride Thin Films

As mentioned earlier, various epitaxial growth techniques have been specifically employed for the synthesis of high quality AlN, InN and AlInN semiconductors under controlled conditions. The most common methods are Metalorganic Chemical Vapor Deposition (MOCVD), Molecular Beam Epitaxy (MBE), Pulsed Laser Deposition (PLD), reactive sputtering and Plasma-Enhanced Chemical Vapor Deposition (PECVD). Various substrates have been investigated over the years for the growth or epitaxy of AlN, InN and AlInN thin films. The lattice mismatch between substrate and the epilayer is very important in term of the amount of resulting stress in the epilayer. The thermal expansion coefficient of the substrate is another key factor since a large difference between the thermal expansion coefficient of the substrate and that of the grown thin films may result in mechanical stresses and cracks. Three substrates stand out as the most promising for the growth of III-nitride thin films: sapphire (Al_2O_3), silicon (Si) and silicon carbide (SiC). However, glass and quartz have been also used for optical measurement and devices. Sapphire is most extensively utilized for growth of III-nitride semiconductors (Kuang et al., 2012c; Skuridina et al., 2014; Y. Zhao et al., 2015). The substrate possesses outstanding features including high chemical and thermal stability, high availability and the reasonable cost. However, there are large lattice and thermal mismatch between sapphire substrate and III-nitride thin films which may cause a compressive strain in the epilayer upon cooling. Si is the most available substrate in the semiconductor industry. III-nitride LEDs and LDs are grown on already proceed Si chip to accomplish the integration of the device with Si electronics. Si is the cheapest among the widely used substrate for III-nitride growth. However, the substrate suffers from a poor compatibility with III-nitride crystals and the large lattice mismatch between Si and III-nitrides causes

to low quality of the films grown on Si substrate. 6H-SiC (0001) crystal with silicon-terminated face offers a low lattice mismatch and very close thermal expansion coefficient with III-nitrides resulting in high quality thin films. The band gap energy of 6H-SiC (0001) substrate is wide (3.05 eV) which makes it promising for application in high power electronics. The drawbacks of 6H-SiC (0001) are limited availability and prohibitively high price which undeniably raise the fabrication cost.

In the following sections, a brief explanation on the above-mentioned growth systems and the corresponding processes as well as some examples of the reported works are presented.

2.5.1 Metalorganic Chemical Vapor Deposition (MOCVD)

MOCVD which is also known as metalorganic vapor phase epitaxy (MOVPE) is a widely used technique for depositing thin layers of atoms on a wafer substrate. One of the most substantial advantages of MOCVD is its ability to grow high quality epitaxial layers, each of a precisely controlled thickness, especially for III-V compound semiconductors. The thickness of the grown multilayer structures is sometimes as thin as a few atomic layers. Although the growth process is fast and quality of the MOCVD-grown layers is high, the method has some disadvantages. For example, toxic, volatile and flammable gases are to be handled and it is not an abrupt process due to gas flow issues and memory effects. Additionally, *in situ* observation of films is not possible by using MOCVD process. The MOCVD process is based on the reaction of chemical compounds in the vapor phase in the vicinity of the substrate. Trimethylgallium (TMGa), Trimethylaluminum (TMAI), Trimethylindium (TMIn) and ammonia (NH₃) are used as the Ga, Al, In and N precursors, respectively and hydrogen is the carrier gas. The deposition of III-nitride semiconductors is achieved by decomposing the organic precursors while they are passing over the hot substrate (Çörekçi, Öztürk, Çakmak,

Özçelik, & Özbay, 2012). The substrate temperature depends on the type of growing semiconductor ranging in 500 – 600 °C for InN and 1100 – 1200 °C for AlN.

Chen et al. (Yiren Chen et al., 2014) have studied the effect of the growth temperature of AlN nucleation layer (T_{NL}) grown on sapphire substrate on the AlN template using MOCVD method. Three different T_{NL} of 880 °C, 950 °C and 1020 °C were applied for growth AlN nucleation layer and it was found that high crystalline AlN template with uniform and smooth morphology, small full width at half maximum (FWHM) values in both (0002) and (10–12) planes could be obtained by optimizing the T_{NL} at 950 °C. FWHM of the grown AlN (0002) and (10–12) planes were in the range of 100 – 300 arcsec for (0002) and 650 – 850 arcsec for (10–12) planes. These results were confirmed by D.G. Zhao et al. (D. G. Zhao et al., 2012) who proposed a dual AlN buffer layer structure including an isolated layer (first buffer layer) and a nucleation layer (second buffer layer) for the growth of high quality AlN films by MOCVD. The obtained results indicated that by increasing the thickness of nucleation, layer the quality of AlN film improves. It was additionally found that the thicker the dual AlN buffer layer deposited in the initial stage, the rougher the surface leading to improved lateral growth of the following AlN epilayer and then better structural quality the films.

B. Zhang et al. (B. Zhang et al., 2011) successfully deposited non-polar *a*-plane InN films by a homemade horizontal-type MOCVD system with GaN buffer, with GaN and low-temperature (LT) InN buffers, and without any buffer layer. It was shown that all InN films are in the non-polar (1 1 –2 0) *a*-plane and the crystal quality of the films is improved by increasing the growth temperature of GaN buffer layer from 550 to 800 °C. Furthermore, the author have concluded that the morphology and the crystallography of *a*-plane InN are not affected when the LT-InN layer is added, but the intensity of photoluminescence (PL) spectrum increases significantly. The as-obtained band gap

energy for the InN thin films was about 0.75 eV which is in agreement with the recent reported value.

Numerous works on the growth of AlInN films by MOCVD technique have been reported since 1989. In the most preparation process of the samples, buffer layer was used in order to improve the properties of AlInN films for optical devices. S. Yamaguchi et al. (Yamaguchi et al., 1998) prepared $\text{Al}_{1-x}\text{In}_x\text{N}$ films on GaN which was deposited on AlN-buffered *c*-plane sapphire substrate. Their structural results showed that $\text{Al}_{0.83}\text{In}_{0.17}\text{N}$ has the highest crystallinity due to the lowest lattice mismatch of the films with GaN. The band gap energy of the $\text{Al}_{1-x}\text{In}_x\text{N}$ thin films was tuned between 2 and 3 eV by decreasing the indium incorporation (*x*) from 0.33 to 0.1 respectively. The band gap value of 2 eV for In-rich InAlN is not acceptable nowadays due to the revised band gap value of InN (~ 0.65 eV).

MOCVD system was employed by Sakai et al. (Sakai, Khai, Ichikawa, Egawa, & Jimbo, 2011) for epitaxial growth and characterization of AlInN/GaN structures on AlN templates for high-performance ultra-violet photodiodes. Their objectives are to examine effect of the growth parameters on structural and morphological properties of the structures as well as to fabricate AlInN-based photodiodes. Higher crystallinity of the AlInN layers was obtained at low growth pressure, whereas both flat and low pit density were obtained at the high-temperature growth. By using *I-V* characteristics, their fabricated AlInN-based photodiodes showed a leakage current of 48 nA at a reverse voltage of 5 V and ideality factor of 2.4. Effect of gas flow rate on the structural and morphological properties of MOCVD-grown In-rich AlInN films has been also reported (Kang, Yamamoto, Tanaka, Hashimoto, & Yamamoto, 2009).

Kang et al. (Kang, Yamamoto, et al., 2009) showed that by increasing total MO flow rate or decreasing the distance between the substrate and the MO entrance, the

morphology of AlInN films shifts from a pebble-like structure to a grainy one (see Figure 2.4). It was also found that the corresponding Raman features are broadened as the flow rate increases (Figure 2.5). The author and his co-workers gave a strong experimental support to the two-mode behavior for $A_1(\text{LO})$ phonon in the Raman results of AlInN. As the last example of MOCVD-grown indium and aluminum based nitride nanostructures, W.Y. Weng et al. (Weng et al., 2009) have reported the deposition of AlInN epitaxial layer and the fabrication of AlInN resistive NH_3 gas sensor. A rough surface morphology with quantum dot like nano-islands was found. It was shown that the measured responses to NH_3 gas for the fabricated AlInN sensor (or incremental currents) increase with the increment of NH_3 gas concentration and this responses happened in a short time showing good response speed of the fabricated sensor. The sensor function was explained by considering the role of oxygen sorption in electrical transport properties of AlInN epitaxial layer. It was described that NH_3 molecules reacts with the absorbed reactive oxygen species on AlInN surface resulting in the enhanced conductance of AlInN nano-islands. These results are highly optimistic for application of AlInN alloys for gas sensing.

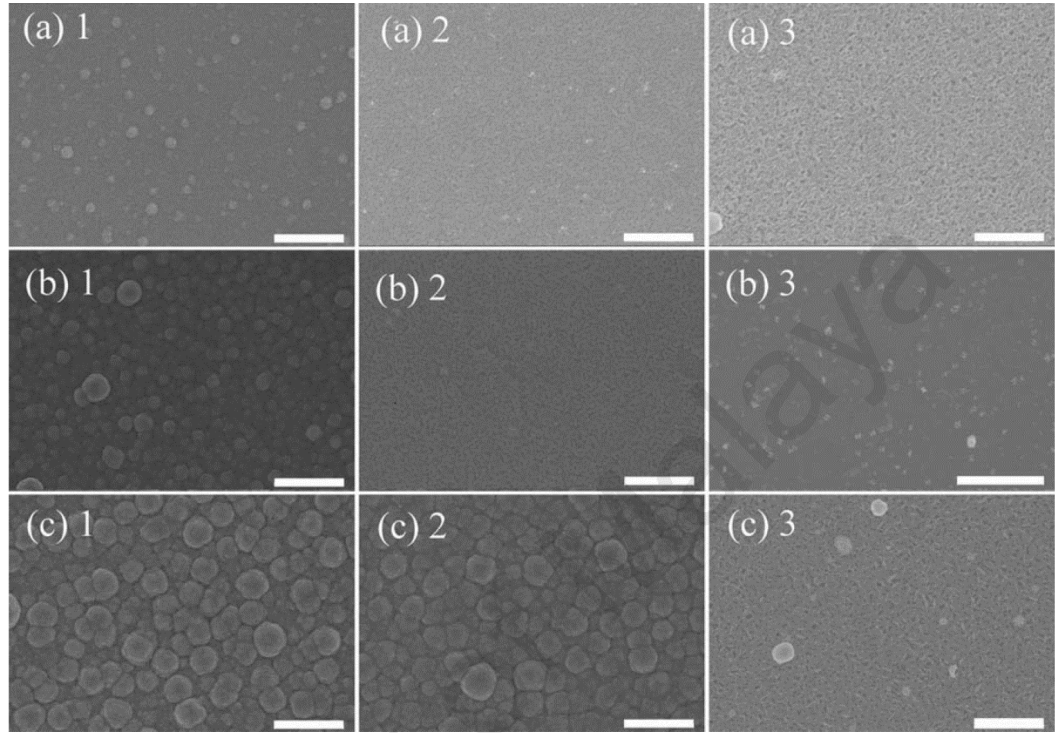


Figure 2.4: The SEM results of AlInN films grown by MOCVD method under various MO gas flow rates of (a) 0.5, (b) 1, and (c) 1.4 standard liters per minute (SLM). The characters 1, 2, and 3 refer to the substrate positions 92, 118, and 144 mm from MO entrance. The length of white scale bar is 5 μm (Kang, Yamamoto, Tanaka, Hashimoto, & Yamamoto, 2009).

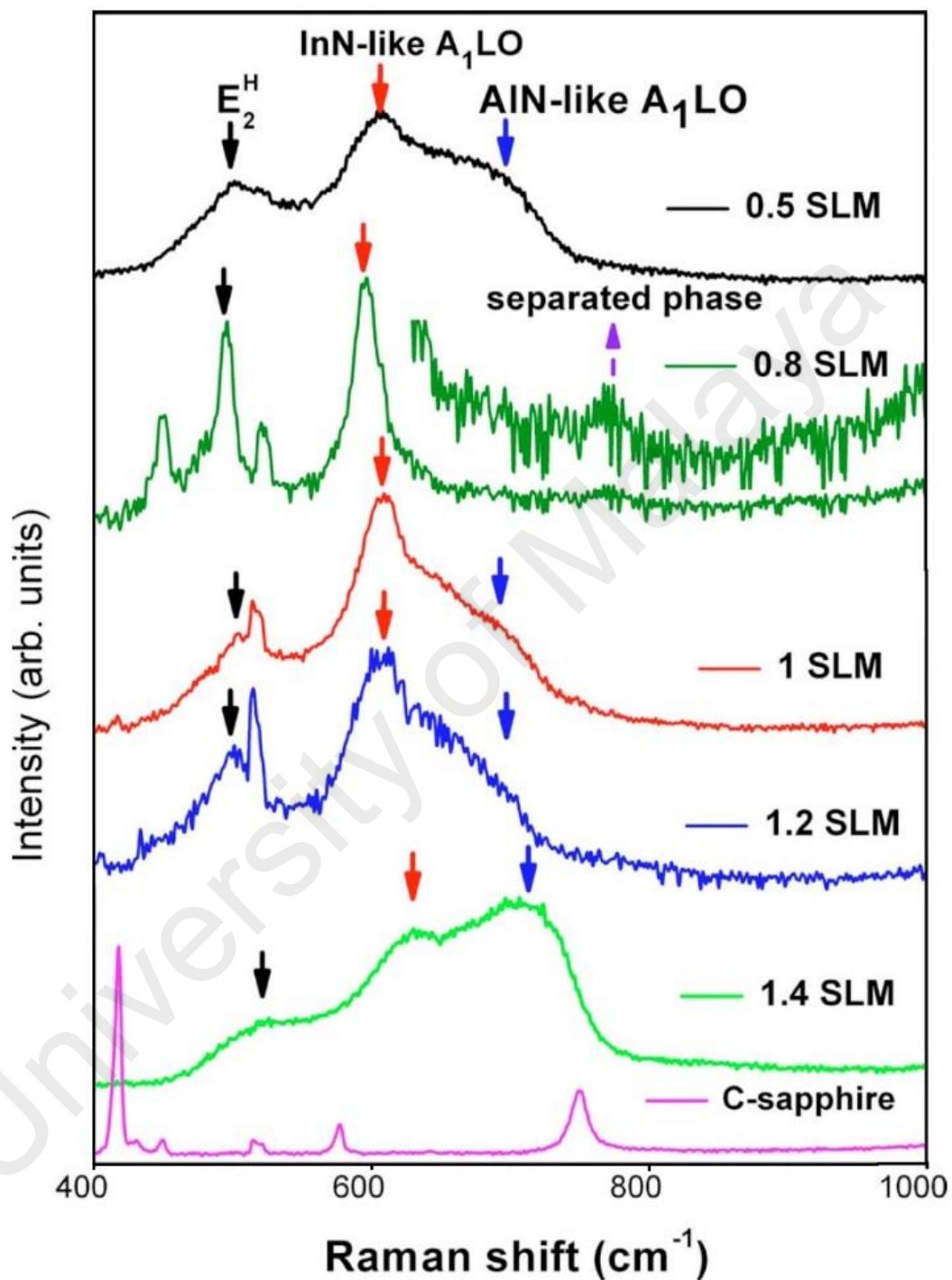


Figure 2.5: Raman spectra AlInN thin films grown by MOCVD at various MO gas flow rates. From Ref. (Kang, Yamamoto, Tanaka, Hashimoto, & Yamamoto, 2009).

2.5.2 Sputtering

Sputtering, a well-known technique of depositing thin films of broad range compositions, is a process whereby atoms are emitted from a solid target (i.e. high quality Al or In disk) onto a substrate under prolonged bombardment of energetic particles (Behrisch & Wittmaack, 1983). The energetic particles can be supplied by a plasma discharge (usually an argon plasma), an ion source, an accelerator, or by a radioactive material emitting alpha particles. The sputter yield which is defined as the average number of atoms sputtered from the target per incident ion, depends on the surface binding energy of atoms in the target, the masses of the ion and target atoms, the energy of the ion, and the ion incident angle. Radio frequency (RF) magnetron sputtering is widely employed for deposition of indium- and aluminum-based nitride thin films. Using this method, the growth of thin films is carried out by deposition of sputtered Al/In adatoms and N^+ ions in N_2/Ar plasma environment.

Many studies have been conducted on the growth of AlN and InN thin films using sputtering-based methods. Kuang et al. (Kuang et al., 2012b) employed RF reactive magnetron sputtering system to study low-temperature growth of AlN films on 6H-SiC substrates under various sputtering pressures. Near-stoichiometric ratio of Al/N (1.13: 1) with few oxygen impurities were found from compositional characterization of the samples. Their two-dimensional X-ray diffraction patterns (2D-XRD) showed that *c*-axis oriented AlN films can be obtained at low working pressures (0.2 – 1.0 Pa). This was confirmed by Wei et al. (Q.-p. Wei et al., 2014) who have showed that the preferential growth of AlN thin films is shifted from (002) to (100) direction as the growth pressure is increased. It was also found that lowering the sputtering pressure is a useful way to minimize the oxygen contamination into the AlN films. By studying effect of the growth temperature on the microstructure and morphology of *c*-axis oriented AlN films, Kuang et al. (Kuang et al., 2012c) also have showed that the films have high purity and increasing

substrate temperature does not have much effect on stoichiometry of the samples, while the film structure and surface morphology are strongly influenced by the growth temperature (30 – 700 °C).

Dependence of preferred orientation and surface morphology of AlN films on RF sputtering powers were investigated by H. Cheng et al. (Hao Cheng & Hing, 2003) and A.V. Singh et al. (Singh, Chandra, & Bose, 2011). In the former, it was shown that low RF powers (≤ 300 W) lead to growth of AlN thin films with mix (100), (002) and (101) orientations, whereas high power (≥ 300 W) is favorable for depositing AlN films with (1 0 1) preferred orientation. Higher deposition rate and a larger grain size were obtained by increasing RF sputtering power resulting a rougher surface compared to the morphology of the films grown at low power. A.V. Singh et al. (Singh et al., 2011) suggested that by increasing RF sputtering power to 300 W highly c-axis orientated AlN films can be prepared on various substrates (glass, Si, oxidized Si, Al–SiO₂–Si, Cr– SiO₂–Si, and Au–Cr–SiO₂–Si) without external substrate heating. The growth of III-nitride thin films without external substrate heating is one of the most outstanding advantages of sputtering method which provides fabrication of devices at reduced cost. The authors also studied the effect of sputtering pressure, ranging from 5 to 20 mTorr, and found that sputtering pressure (in 5 – 20 mTorr range) weakly influences the preferred growth which is in good agreement with the results obtained with Kuang et al. (Kuang et al., 2012a) as mentioned above. The average grain size for different substrates used in the study was 19 – 26 nm which implies that the grown AlN films were smooth and meet the requirements of surface acoustic wave (SAW) and Bulk acoustic wave (BAW) resonators.

The first InN crystal was fabricated by RF sputtering in 1972 (Hovel & Cuomo, 1972) and up to now large number of sputtering works have been devoted to growth of InN thin

films. Most of the works have led to perfect thin films in terms of quality and crystallinity. Despite this, as mentioned earlier, usually larger E_g values for InN (> 0.7 eV) are obtained by sputtering which seems to be one major drawback of this technique, at least in terms of solar cell application because small band gap energies are highly desirable in solar cell devices. Valdueza-Felip et al. (Valdueza-Felip et al., 2012) deposited InN on GaN-buffered sapphire substrate by RF sputtering and the measured band gap energy was 1.7 eV. Dixit et al. (Dixit et al., 2009) and Sasaoka et al. (Sasaoka, Mori, Miyazaki, & Adachi, 2010) obtained the E_g value of around 1.4 eV from rf-magnetron-sputtered InN film on a (0001) sapphire and corning 7059 glass substrates, respectively. The measured absorption edge for sputtered InN thin films reported by Cai et al. (Cai et al., 2009) was observed at around 850 nm which may result in a larger band gap energy than 0.7 eV. Explanations including the formation of oxynitrides ($\text{InO}_y\text{N}_{1-y}$ with y about 0.1) due to low efficiency of nitrogen during the layer growth and the spontaneous formation of needle-like structures upon heteroepitaxial growth of InN (V. Yu Davydov et al., 2002), the difference in crystallinity (Takashi Matsuoka, Okamoto, Nakao, Harima, & Kurimoto, 2002), quantum-size effects in InN nanocrystals and high-carrier-induced Burstein-Moss shift (J. Wu et al., 2004) have been proposed for such a large band gap energy shift. Nevertheless, this is an undeniable disadvantage for sputtering process which limit the sputter-deposited InN devices for solar cell application as the films with narrow band gaps can be considered as the absorbing layer of a solar cell.

As compared to AlN and InN, less works have been reported for sputtering-aided growth of AlInN possibly due to the difficulty of growing AlInN ternary semiconductor. The origin of this difficulty is the large immiscibility and difference in the thermal stability between AlN and InN. The first sputter-deposited AlInN alloy was prepared by Kubota et al. (Kubota et al., 1989) on sapphire substrate in the Al-rich composition regime with substrate temperature of 500 °C. Since then, the optical properties of AlInN films

have been studied by employing both low-temperature and high-temperature sputtering methods (Q. Guo, Tanaka, Nishio, & Ogawa, 2003; He et al., 2010; H. F. Liu et al., 2012; Peng et al., 1997; Yeh, Wu, & Lan, 2008, 2009). Q. Guo et al. (Q. Guo et al., 2003) reported growth of $\text{Al}_x\text{In}_{1-x}\text{N}$ with a wide composition range ($0 \leq x \leq 0.40$) by reactive RF magnetron sputtering. The calculated E_g values were 1.5, 2.0, 2.25 and 2.50 eV for Al compositions (x) 0, 0.05, 0.25 and 0.40, respectively. Large E_g values (much larger than 0.7 eV) for highly textured InN and In-rich AlInN films with rod-like structures were also obtained by He et al. (He et al., 2010) who deposited InN and InAlN films on quartz substrate by magnetron sputtering. The optical results reported by He et al. (He et al., 2010) are shown in Figure 2.6. The author related the large shift of the measured E_g values to high carrier concentration in the films structure. Liu et al. (H. F. Liu et al., 2012) have reported columnar growth of $\text{Al}_{0.278}\text{In}_{0.722}\text{N}$ thin films with no phase separation by radio frequency magnetron sputtering. The room-temperature photoluminescence emission and the optical absorption edge were obtained at 1.875 and 2.102 eV which were larger than the theoretically-predicted band gap energy of the alloy. The deviation of the band gap energy was attributed to the band-filling effect induced by high electron density in the heterostructure.

As mentioned earlier, one common reason reported for the discrepancy in band gap energy of InN is the Burstein–Moss effect by which the band gap energy would be increased with higher carrier concentration (He et al., 2010) according to the following equation:

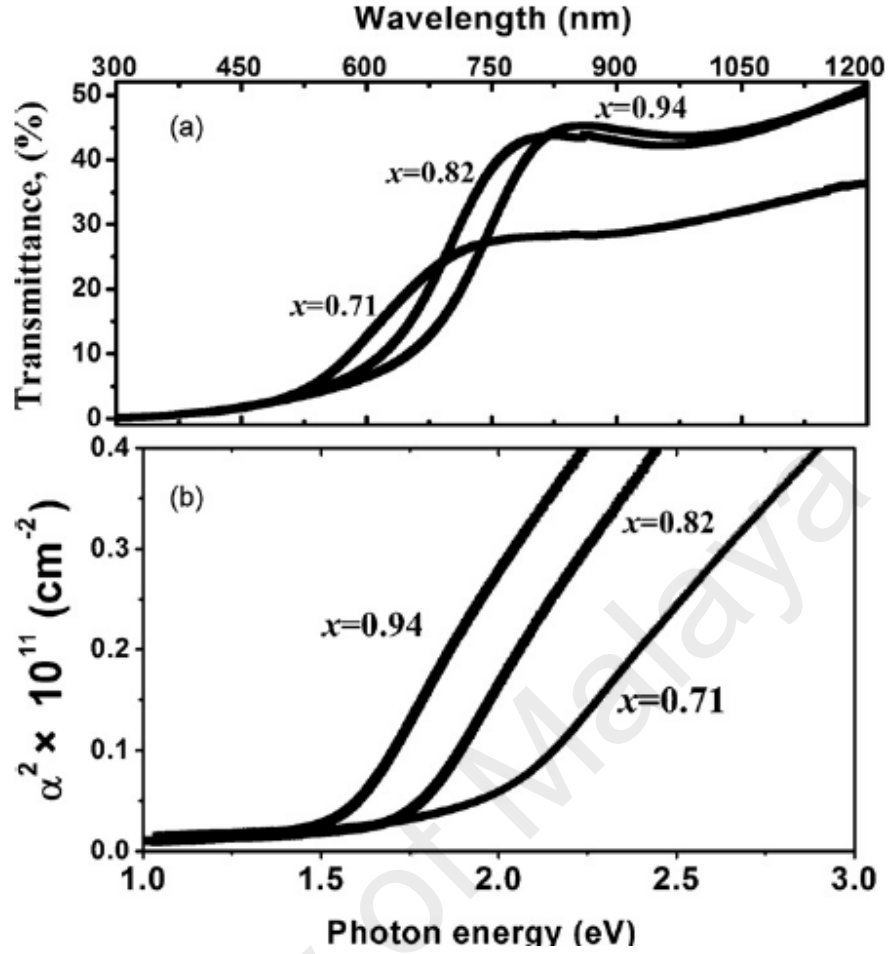


Figure 2.6: Transmittance spectra (a) and squared absorption coefficient (b) of sputtered $\text{In}_x\text{Al}_{1-x}\text{N}$ films with different In content (x). From Ref. (He et al., 2010).

$$\Delta E_g \approx m_e^{*-1} n_e^{2/3} \quad (2.1)$$

where m_e^* and n_e are the effective electron mass and the electron concentration, respectively. The effective electron mass of InN is $0.07m_0$ where m_0 is the free-electron mass. From Hall measurements, He et al. (He et al., 2010) obtained the carrier concentration of the deposited InN and high-In-content InAlN films in the range of 10^{20} - 10^{21} cm^{-3} . However, the author did not mention any scientific reason for such a high electron concentration and further investigation is required. It has been shown that the insertion of a AlN buffer layer can moderate the Burstein–Moss effect on the band gap

energy of InN (Yeh et al., 2008). T.-S. Yeh et al. (Yeh et al., 2008) showed that the carrier concentration of In-rich $\text{Al}_x\text{In}_{1-x}\text{N}/\text{AlN}/\text{glass}$ films with $x = 0.12, 0.26$ and 0.36 were $3 \times 10^{20}, 6 \times 10^{19}$ and 3×10^{18} , respectively.

In another work, both Al-rich ($\text{Al}_{0.55}\text{In}_{0.45}\text{N}$) and In-rich ($\text{Al}_{0.36}\text{In}_{0.64}\text{N}$) films were deposited on glass substrate with and without AlN buffer layer by T.-S. Yeh et al. (Yeh et al., 2009) using pulsed-dc reactive sputtering and the structural and optical properties of the films were investigated at various substrate temperatures. The structural analysis showed that by increasing substrate temperature from 200°C to 400°C , the crystallinity of AlInN films grown directly on the glass substrate improved. However, at high temperature ($\geq 300^\circ\text{C}$) oxygen contamination was detected from XPS analysis of the samples. The author et al. (Yeh et al., 2009) suggested that by using AlN buffer layer not only the crystallinity of AlInN films was considerably improved but also no oxygen contamination was observed. Based on the above-mentioned results, it can be concluded that the lattice-matched buffer layer can play a crucial role in crystallinity, quality, optical and electrical properties of AlInN films.

2.5.3 Molecular Beam Epitaxy (MBE)

Molecular Beam Epitaxy (MBE) combined the knowledge of “surface physics” and “ion propulsion technology” to develop a new method for the deposition of single crystals and was initially employed by A. Y. Cho (A. Y. Cho, 1970) for epitaxial growth of GaAs thin films. Nowadays, this technique is widely utilized in the manufacturing of semiconductor devices such as high-electron-mobility transistors (HEMTs) for cellular phones and WiFi. MBE takes place in a chamber under high vacuum or ultra-high vacuum ($\sim 10^{-10}$ mbar) and without carrier gases. Hence, the highest purity of the grown films is achievable using this method.

In MBE processing, ultra-pure elements such as indium and arsenic are slowly sublimed in separated quasi-Knudsen effusion cells. The gaseous reactants are then ejected to the chamber and condensed on a heated substrate to grow single crystalline InAs films. For the case of indium- and aluminum-based nitride semiconductors, NH₃ (ammonia) is used as the nitrogen source but sometimes MBE is attached to a RF plasma cell to ionize N₂ molecules and generate nitrogen reactants. This system is called plasma-assisted molecular beam epitaxy (PA-MBE). The term “beam” refers to the fact that the reactants are directed separately to the substrate and do not interact with each other until they deposit on the substrate. One of the most substantial advantages of MBE is precise and *in situ* control of the thickness of each layer during the deposition process using reflection high-energy electron diffraction (RHEED) for monitoring the growth of the monolayers. However, this technique has several unavoidable drawbacks. Multi-stage vacuum system is required to provide ultra-high vacuum. The deposition rate is low (around 500 nm per hour) compared to other methods such as MOCVD. Moreover, the maintenance and replacement of the source materials inside the ultra-high vacuum chamber is time-taking and somehow tedious.

Many researchers have reported the growth, characterization and application of AlN films by MBE. Ammonia MBE was employed by V.G. Mansurov et al. (Mansurov et al., 2007) to investigate the effect of sapphire surface nitridation on morphology of the grown AlN. It was shown that modification of nitridated sapphire substrate by depositing 1 – 2 monolayers of Al together with ammonia flux treatment can improve the morphology of the subsequent AlN layers. B. Liu et al. (B. Liu, Gao, Wu, & Liu, 2009) prepared single crystalline AlN thin films on Al₂O₃ at high temperature of 785 °C using RF-MBE and studied the effect of rapid thermal annealing (RTA) on structural and morphological properties of the films for high frequency and high power devices.

The AlN films became smoother with the increase of annealing temperature and the best crystallinity (the minimum FWHM of AlN (002) rocking curve) was found at the annealing temperature of 1000 °C. Mohd Yusoff et al. (Mohd Yusoff et al., 2013) investigated microstructure properties of AlN/GaN/AlN heterostructures by using plasma-assisted MBE and claimed that the crystalline quality of the epilayers was improved compared to previously reported results due to decreased defects of threading dislocations with a screw component. However the reported EDX results showed that the films have high content of Al. C. Flynn and L.W. Sim (Flynn & Sim, 2015) proposed that phosphoric acid (H_3PO_4) is very useful for removing excess Al from the AlN surface. It was shown that if the MBE-grown AlN films are immersed in H_3PO_4 heated to 70 °C for 10 min hexagonal etch pits are formed in the AlN films and the metallic Al particles are removed. The effect of phosphoric acid on the surface morphology of AlN becomes much more important when it was found that excess Al on the surface of the films caused an error of up to 7.6% in the AlN thickness. The study is very promising in improving the quality and morphology of AlN films.

MBE has been also employed by many researchers for growth of InN films. The revised band gap energy of InN (0.7 eV) was obtained by growth of the semiconductor using MBE method in 2003 (J. Wu et al., 2003). Since then, this value has been confirmed by most of the MBE works under different growth conditions. Shih et al. (Shih, Lo, Pang, & Hsieh, 2010) investigated growth of InN thin films on O-polar ZnO substrate under various N/In flow ratios. The author have observed that by decreasing the N/In ratio, surface morphology the PA-MBE-grown films changed from 3D to 2D. From the SEM and TEM imaging it was shown that the formed In_2O_3 buffer layer between ZnO substrate and InN films can significantly improve the morphology of the InN epilayer. However, the obtained threshold energy of optical transmission was around was around 1.9 eV much larger than the recently accepted value of 0.7 eV.

In contrast, M. Kumar et al. (M. Kumar et al., 2012) determined the energy gap of InN/GaN/Si(111) epilayers at 0.74 and 0.76 eV by Photoluminescence (PL) and optical absorption measurement, respectively. The effect of the growth parameters including substrate, indium flux and RF power on the structural and morphological features of the InN layers was studied. It was demonstrated that crystallinity and surface morphology strongly depend on the applied RF power: by increasing RF power FWHM of HRXRD (0 0 2) peak decreases (see Figure 2.7) while the RMS (Root mean square) roughness increases slightly.

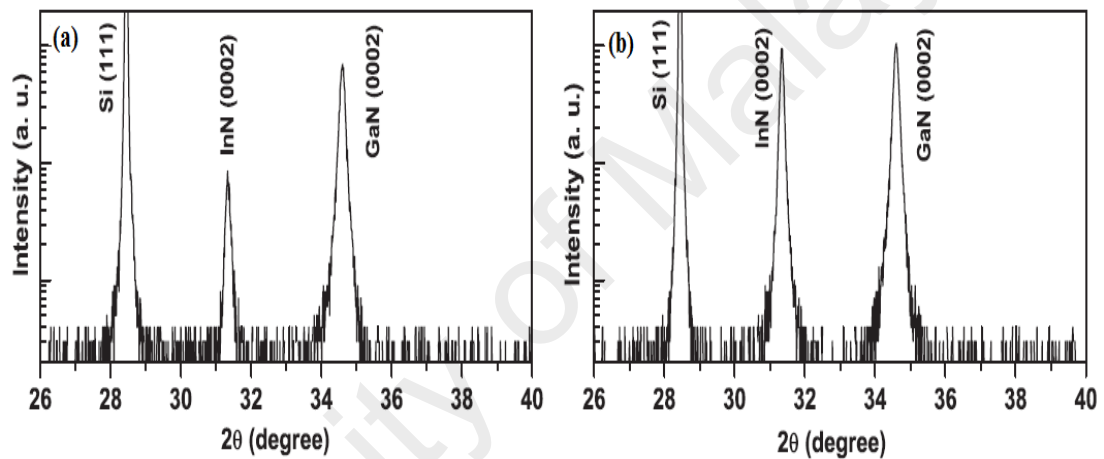


Figure 2.7: HRXRD spectra of InN thin films grown by PA-MBE at the RF powers of (a) 350 W and (b) 450 W. From Ref. (M. Kumar et al., 2012)

By studying the MBE-aided growth of InN films on Si substrate with different buffer layers, M. Kumar et al. (M. Kumar et al., 2011) also showed that the LT-InN/ β -Si₃N₄ double buffer layers (single-crystal β -Si₃N₄ ultrathin layer covered by low-temperature InN buffer layer) not only improve the structural and morphological properties of the InN epilayers but also decreases band gap energy of the films from 0.78 eV (for InN/Si films) to 0.73 eV. This was confirmed by A.O. Ajagunna et al. (Ajagunna et al., 2009) who have deposited InN films on LT-InN and GaN/AlN buffer layers using RF-MBE method.

Numerous works have been devoted to growth of AlInN ternary alloys by PA-MBE and the corresponding optical properties have been investigated. However, the growth of high quality AlInN films is still challenging, due to large differences in bonding energy, lattice constant as well as optimum growth temperature between AlN and InN (Takashi Matsuoka, 1997). Lukitsch et al. (Lukitsch et al., 2001) have obtained epitaxial $\text{Al}_{1-x}\text{In}_x\text{N}$ films with the whole composition range ($0 \leq x \leq 1$) by PA-MBE. However, the measured band gap energy for the In-rich films ($x=0.88$) was around 1.8 eV, very near to the old energy gap of InN. The reason of such a high band gap value probably is that this study was carried out before the confirmation of 0.7 eV for InN band gap energy.

About four years after improvement of InN band gap value from 1.9 to 0.63 eV, W. Terashima et al. (Terashima, Che, Ishitani, & Yoshikawa, 2006) reported deposition of N-polar $\text{Al}_x\text{In}_{1-x}\text{N}$ films with the whole composition range on N-polar GaN substrate at the substrate temperature of 550 °C without any phase separation. The band gap value of the PA-MBE-grown $\text{Al}_{0.12}\text{In}_{0.88}\text{N}$ films was almost half the value obtained by Lukitsch et al. (Lukitsch et al., 2001). The effect of substrate temperature on the structural and compositional properties of $\text{Al}_{0.56}\text{In}_{0.44}\text{N}$ films were also investigated by Terashima et al. (Terashima et al., 2006) and it was shown that by increasing the temperature from 500 °C to 600 °C, the Al incorporation in the films structure decreases by 0.08 and the films become poorly crystalline possibly due to the enhanced phase separation in the alloys prepared at higher temperature. However, the reported compositional behavior was contravened by Fernández-Garrido and his colleagues (Fernández-Garrido, Gačević, & Calleja, 2008) who showed In incorporation into the PA-MBE-grown AlInN films decreases with the substrate temperature. Fernández-Garrido and his co-workers (Fernández-Garrido et al., 2008) explained that the observed behavior is due to thermal InN decomposition while no justification was reported by Terashima et al. (Terashima et al., 2006) for the reverse trend.

By using the grown AlInN alloys as the barrier layer, Terashima et al. (Terashima et al., 2006) could fabricate InN-based multiple quantum wells (MQWs) with different Al compositions. It was suggested that the fabricated MQWs have potential application in inter-subband electron transition (ISBT) optical modulator in the optical communication wavelength. J. Kamimura et al. (Kamimura, Kouno, Ishizawa, Kikuchi, & Kishino, 2007) reported the growth of high-In-content InAlN nanocolumns on dot-like GaN as nanocolumn nucleation seeds on n-type Si (111) substrate. An image of the grown nanocolumns is shown in Figure 2.8. The dependence of shape and density of the columns on the V/III ratio was examined and it was found that only the nanocolumn shape is affected by the V/III ratio. Thus, it was suggested that the dot-like GaN nucleation density is determinant for the column density. From the room temperature PL measurement, it was found that the energy peak of the films shifted from 1.17 to 0.662 eV when indium content is increased from 0.73 to 1.00.

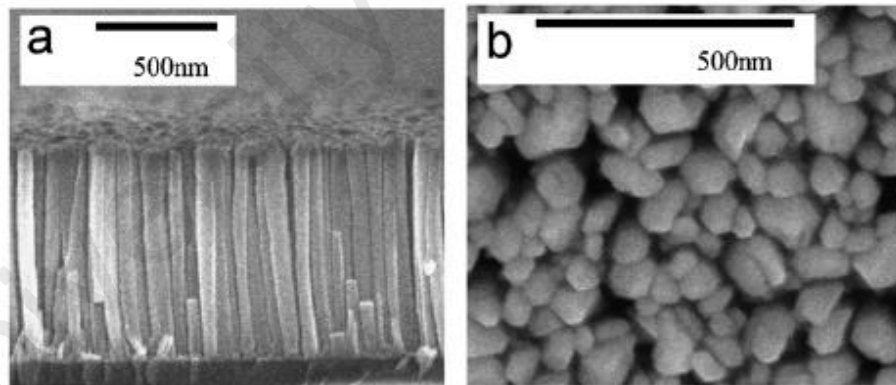


Figure 2.8: The SEM image of cross-section (a) and surface (b) of InN films grown by PA-MB. From Ref. (Kamimura et al., 2007)

Wong et al. (Hoi Wong et al., 2012) have reported the preparation of $\text{In}_{0.18}\text{Al}_{0.82}\text{N}/\text{GaN}$ alloys with homogeneous composition using NH_3 -MBE. High quality InAlN/GaN interface was deduced from high-resolution x-ray diffraction ω - 2θ scans and further confirmed by high angle annular dark field (HAADF) imaging. The author et al. (Hoi

Wong et al., 2012) investigated compositional uniformity of the samples by Energy-dispersive x-ray spectroscopy (EDXS) on parallel to as well as across the InAlN/GaN interface and demonstrated that the deposited films are homogenous in composition. Moreover, the reported atomic force microscopy (AFM) results showed that the thin AlInN has an ultra-smooth hillock-like morphology with the RMS roughness of ~ 2 nm. However, no optical characterization and measurement (e.g. optical band gap energy of the grown Al-rich AlInN films) was provided.

2.5.4 Pulsed Laser Deposition (PLD)

PLD is a thin films growth method where a target of the material is vaporized by a high-power pulsed laser beam in a vacuum or a background gas. For III-nitride cases, pure aluminum/indium and nitrogen are used as the target and background gas, respectively. Although the basic-setup of the technique is simple, the overall process including the physical phenomena occurred during laser-target interaction, dynamic of the developed plasma and nucleation of the deposited adatoms are somehow complicated. In fact, PLD is carried out in following steps: first, the laser pulse is absorbed by the target and its energy is converted into thermal, chemical and mechanical energy leading to ablation and evaporation of the material, ionization of the background gas and formation of plasma ambient. Then, the plasma bulk is spatially distributed over the chamber and in vicinity of the substrate depending on the background pressure. At the third stage, the ablated species are accelerated toward the substrate surface with high energy which may cause to re-sputtering of the deposited particles. The collisions between the ablated species from the target and the re-sputtered particles determine condensation of particles on the substrate surface and as a result growth of the film. Finally, nucleation of the adatoms and growth process of the films are occurred depending on the growth parameters including laser energy and fluency, substrate temperature and background pressure.

Pulsed laser deposition of AlN thin films has been reported by large number of researchers. However, the number of the works is less than MOCVD-, sputtering- and MBE-based works showing that PLD is still on its infant. Nevertheless, the method is surprisingly being developed as most of the PLD-based works have been published in recent years. G. Shukla, A. Khare (Shukla & Khare, 2008) studied effect of the low N₂ pressure regime (5×10^{-2} and 10^{-1} Torr) and the high N₂ pressure regime (10 and 100 Torr) on properties of pulsed laser deposited AlN films and found that the preferred orientation of AlN films changes from (101) at high N₂ pressure to (002) at low N₂ pressure. Accordingly, the films deposited at high N₂ pressure was rougher than that grown at the low pressure regime (see Figure 2.9). By considering the plasma dynamics during the deposition, the authors explained that the more energetic species in low N₂ pressure have enhanced mobility on the substrate surface leading to rearranging of the film surface and filling the voids while increased number of collisions raised from higher nitrogen pressure results in a variation in the growth direction of AlN thin films. At low deposition pressure, the preferred orientation of AlN thin film was (002) while by increasing the N₂ pressure the growth direction of AlN shifted to (101). However, G. Shukla, A. Khare (Shukla & Khare, 2008) mentioned that they could not grow AlN thin films at N₂ pressure below 10^{-2} Torr.

Dependence of surface morphology and crystallinity orientation of pulsed laser deposited AlN films on nitrogen pressure was also confirmed by S. Bakalova et al (Bakalova et al., 2009) and Wang et al. (Z. P. Wang, Morimoto, Kawae, Ito, & Masugata, 2011). The former synthesized AlN films at very low N₂ pressure (7.5×10^{-4} to 7.5×10^{-2} Torr) using bulk AlN as the target. The obtained tendency reported in both works was: by increasing the pressure the size of AlN particles decreases resulting in smooth surface. The reason of this result was correlated with the reduced growth rate at high nitrogen pressure. The influence of target–substrate distance in PLD system on

crystallinity and morphology of AlN films was investigated by Yang et al. (Yang et al., 2015). The reported crystallographic and SEM observation results showed that by increasing the distance from 5 to 8 cm, highly crystalline AlN films with more smooth surface and without interfacial layer in AlN/Si(110) are obtained but further increase of the distance resulted in degraded properties of the films. It was explained that at low target–substrate distances the kinetic energy of the Al adatoms is high due to less collision with nitrogen (Yang et al., 2015). This may destroy the substrate surface.

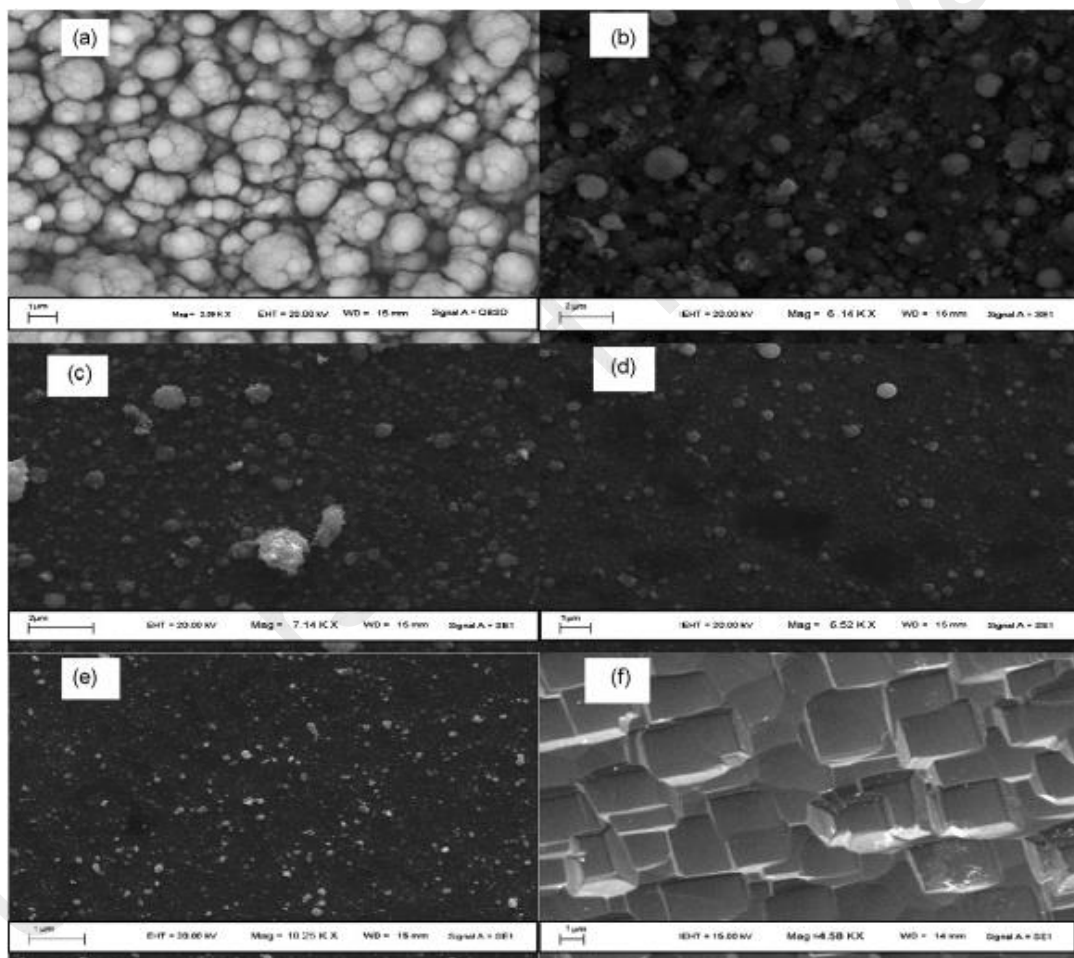


Figure 2.9: SEM image of AlN thin films grown by PLD method at different N₂ pressures; (a) 100 Torr; (b) 50 Torr; (c) 10 Torr; (d) 1 Torr; (e) 10⁻¹ Torr; (f) 5 × 10⁻²Torr. From Ref. (Shukla & Khare, 2008).

On the other hand, at large distances, the kinetic energy of the adatoms is not sufficient for diffusion of the adatoms into their lowest energy nucleation sites. The reported results suggested that there is an optimum target–substrate distance for growth of AlN films using PLD method. Optical properties of PLD-grown AlN films were studied by C. Ristoscu et al. (Ristoscu, Ducu, Socol, Craciunoiu, & Mihailescu, 2005) and F. Chale-Lara et al. (Chale-Lara, Farias, Huerta-Escamilla, & Xiao, 2009). F. Chale-Lara et al. (Chale-Lara et al., 2009) employed PLD system for obtaining high quality AlN thin films under different nitrogen pressure at relatively high temperature. It was suggested that the most influential PLD parameter, especially for optical characterization, is the nitrogen pressure meaning that there is an optimized gas pressure under which the optical properties of AlN films improve significantly. However, there is still lack of information on optical investigation of PLD-grown AlN films.

Successful growth of InN films by PLD method has been also reported, although the number of works is not comparable with MOCVD, sputtering and MBE. Direct deposition of InN films on sapphire (0001) substrate along with the influence of laser intensity and growth temperature on the films properties were examined by K. Mitamura et al. (Mitamura et al., 2009). Based on the obtained results it can be concluded that the buffer-free growth of InN on sapphire by PLD leads to smooth epitaxial films. The optical measurement demonstrated that the band gap energy of the 1.5- μm -thick InN film is about 0.6 eV showing that PLD is promising for growth of InN with small band gap value. Cubic InN with higher and enhanced doping efficiency (if compared to the hexagonal structure) was grown by R. Ohba et al. (Ohba et al., 2009) on MgO (10 0) substrates using a cubic GaN and HfN as the buffer layers. They suggested that the effects of surface migration of the film precursors in PLD process suppresses the formation of nucleation sites for hexagonal phase. F. Stokker-Cheregi et al. (Stokker-Cheregi et al., 2011) employed nitrogen RF-plasma-assisted PLD for growth of InN thin films on Si (111), Si

(100), Al₂O₃ (001) substrates at the substrate temperature of 550 °C. Although all the films were poorly crystalline, the presence of wurtzite InN on cubic-symmetry Si (100) substrate was quite intriguing. It was obtained that the type of substrate plays a major role in evaluation of the films from mixed phases of polycrystalline InN and cubic In₂O₃ to single crystalline InN. However, no PLD-based work has been reported for the growth of ternary AlInN compounds reflecting the fact that PLD fails to overcome the large immiscibility and difference in the thermal stability between AlN and InN for synthesis of AlInN films.

2.5.5 Plasma-Enhanced Chemical Vapor Deposition (PECVD)

Plasma-Enhanced Chemical Vapor Deposition (PECVD) is a process of thin films deposition in which the generated building blocks from a gaseous state (vapor) are condensed on a substrate. Here, it should be noted that the growth process of PECVD system is similar to MOCVD. Only N₂ gas is replaced to NH₃ and dissociation of the N₂ molecules is accrued in plasma ambient. Hence, the PECVD process is sometimes called PEMOCVD. The process is based on several chemical reactions which occur after creation of RF (AC) or DC discharge between two electrodes. The dissociation of precursor N₂ molecules by energetic electrons is a benefit for this process as it provides large yield of building units for the growth stage. Also, all the nanostructures grown on plasma-exposed substrate in fact are assembled in plasma sheath which is formed adjacent to the substrate and controls the dynamic of charge species (radicals, ions and electrons) which are contributing in the growth of nanostructures. Thus, during the process the films surface can be exposed to intensified ion bombardment depending on the potential across the sheath (the floating potential). This bombardment can improve the electrical and mechanical properties of the thin films by removing contaminations from the films structure. However, some disadvantages seem to be unavoidable using PECVD method for growth of indium and aluminum based nitride semiconductors. For instance, toxic and

flammable gases are utilized as Al/In sources (like MOCVD) or high external substrate temperature is required for the deposition.

Only a few works have been reported for growth of AlN and InN thin films by PECVD, while no report on AlInN has been released so far, to the best of our knowledge. AlN thin films was initially prepared by J.-W. Soh et al. (Soh, Jang, Jeong, & Lee, 1996) by using electron cyclotron resonance plasma-enhanced chemical vapor deposition (ECR PECVD) system. The effect of different carrier gases (H_2 and Ar) on crystallinity of *c*-axis orientation of AlN films was investigated and it was suggested that crystallinity of the films improves when hydrogen is used as the carrier gas. According to them, this is due to higher ability of H_2 in removing oxide layer from the substrate surface. The same tendency was also found when the substrate temperature and the microwave power were increased.

A more comprehensive study was conducted by G. Sánchez et al. (Sánchez et al., 2008) who obtained and optimized (100)- and (002)-oriented polycrystalline AlN thin films by varying the parameters of microwave PECVD including the plasma-injector and the injector-substrate distances, RF bias, the substrate temperature, the total pressure, the substrate type and the process time. It was shown that smaller injector-substrate distance, lower deposition pressure and higher substrate temperatures favor the growth of (002)-oriented AlN films, while the reverse conditions support the production of (100) orientation. Moreover, a reduction in the impurity of the films was observed when less negative RF bias, higher substrate temperature and shorter plasma-injector distances were employed. In another work (Sánchez, Tristant, Dublanche-Tixier, Tétard, & Bologna Alles, 2014), the evaluation of AlN microstructure, dependence of the crystallographic orientation on the RF bias applied to the substrate as well as stress measurements of the films were reported by G. Sánchez et al. It was observed that the

intrinsic tensile stress in AlN films was changed to compressive stress by decreasing the floating potential toward negative values. An optimized value of the applied voltage was selected which allowed crystalline development of the films with minimum residual stress.

M. Wintrebert-Fouquet et al. (Wintrebert-Fouquet, Butcher, & Chen, 2004) and Zhi et al. (Zhi et al., 2012) reported the growth of InN films by PECVD and it was claimed that the proposed method is a good alternative for InN deposition. M. Wintrebert-Fouquet et al. (Wintrebert-Fouquet et al., 2004) studied optical and electrical properties of InN films by varying the substrate temperature on Si and sapphire. It was demonstrated that the optical band gap of the thin ($\leq 0.4 \mu\text{m}$) films decreased from 1.8 to 1.1 eV by increasing the substrate temperature from 300 to 500 °C, whereas for the thick films ($>2 \mu\text{m}$) the value was around 1.1 eV for all temperatures which is still far from the real value. Furthermore, the interface layer between the film and the substrate was poor which could result in stress in the microstructure. Zhi et al. (Zhi et al., 2012) reported the growth of highly *c*-axis oriented InN films on glass substrate with an interlayer of *c*-axis oriented (002) AZO (Aluminum-doped Zinc Oxide; ZnO:Al) films and effect of Trimethyl Indium (TMIn) flux on the structural, morphological and optical properties of InN films was investigated. It was demonstrated that by increasing the TMIn flux up to 5.5 sccm, crystallinity of the films are greatly improved whereas surface roughness is significantly decreased. Despite these remarkable achievements, the optical band gap energy of the grown films was 1.54 eV; almost two times higher than the actual E_g of InN.

CHAPTER 3:

SAMPLE PREPARATION AND CHARACTERIZATION TECHNIQUES

3.1 Introduction

Plasma-assisted reactive evaporation technique for the preparation of aluminum and indium-based nitride thin films is described here. One of the most substantial advantages of this method is the high deposition rate which is favorable for low cost and large scale industrial production. As a versatile tool, the hot filament plays a key role in the growth process of these films. It can simultaneously evaporate Al and/or In wires and excite N_2 molecules resulting in the production of energetic N radicals and possibly excited N atoms, as well as thermally heat the growth surface which enhances surface reactions for film growth. The plasma-assisted growth in this technique is needed for the dissociation of N_2 gas into reactive N^+ ions and N radicals, depending on the applied RF power, and to control, transport and deposit the growth species on the substrates.

This chapter is divided into four main sections. In section 3.2, the research methodology adopted in this work is presented. Section 3.3 covers the deposition system configuration, pre-deposition process, the deposition process of AlN, InN, and $Al_xIn_{1-x}N$ thin films as well as the annealing procedure of $Al_xIn_{1-x}N$ thin films. The description of the analytical instrument used in this work as well as the measurement techniques and calculation methods employed to analyze the results are detailed in section 3.4. Finally, in section 3.5 the procedures involved in the electrochemical measurements for the InN and $Al_xIn_{1-x}N$ thin films will be described.

3.2 Research Methodology

In this work, indium- and aluminum-based nitride thin films including AlN, InN and $Al_xIn_{1-x}N$ thin films were deposited by a plasma-assisted reactive evaporation system in

the Low Dimensional Materials Research Centre, Department of Physics, University of Malaya. The aim was to introduce a cost-effective and environmental-friendly method for deposition of indium and aluminum based nitride thin films at low temperatures. The flowchart of the research methodology involved in this work is shown in Figure 3.1. This project started with the growth of AlN thin films at various filament-substrate distances followed by characterization of the grown films using different analytical tools. Next, the deposition and characterization of InN thin films grown at various RF powers were carried out. The results and discussions corresponding to the deposition of AlN and InN thin films are presented in chapter 4. The electrochemical properties of InN thin films were also investigated and are explained in detail in chapter 6.

The parameters used for the growth of AlN and InN were employed for the deposition of $\text{Al}_x\text{In}_{1-x}\text{N}$ thin films, and the first set of $\text{Al}_x\text{In}_{1-x}\text{N}$ alloys was deposited at various AC voltages applied to the filament holding the indium wire. The characterization of the grown $\text{Al}_x\text{In}_{1-x}\text{N}$ thin films showed that Al-rich and In-rich $\text{Al}_x\text{In}_{1-x}\text{N}$ films can be obtained by varying the voltage. In the next step, one sample of Al-rich and In-rich each were selected and the effects of the nitrogen flow rate on the properties of the films were investigated. An annealing study of the In-rich $\text{Al}_x\text{In}_{1-x}\text{N}$ films was performed at various temperatures to examine the stability of the films for potential applications. All the results of the above-mentioned steps on the growth of $\text{Al}_x\text{In}_{1-x}\text{N}$ films are presented and discussed in chapter 5. Finally, the photoelectrochemical behavior of Al-rich $\text{Al}_x\text{In}_{1-x}\text{N}$ films for potential water splitting applications was investigated and the obtained results are presented and discussed in chapter 6.

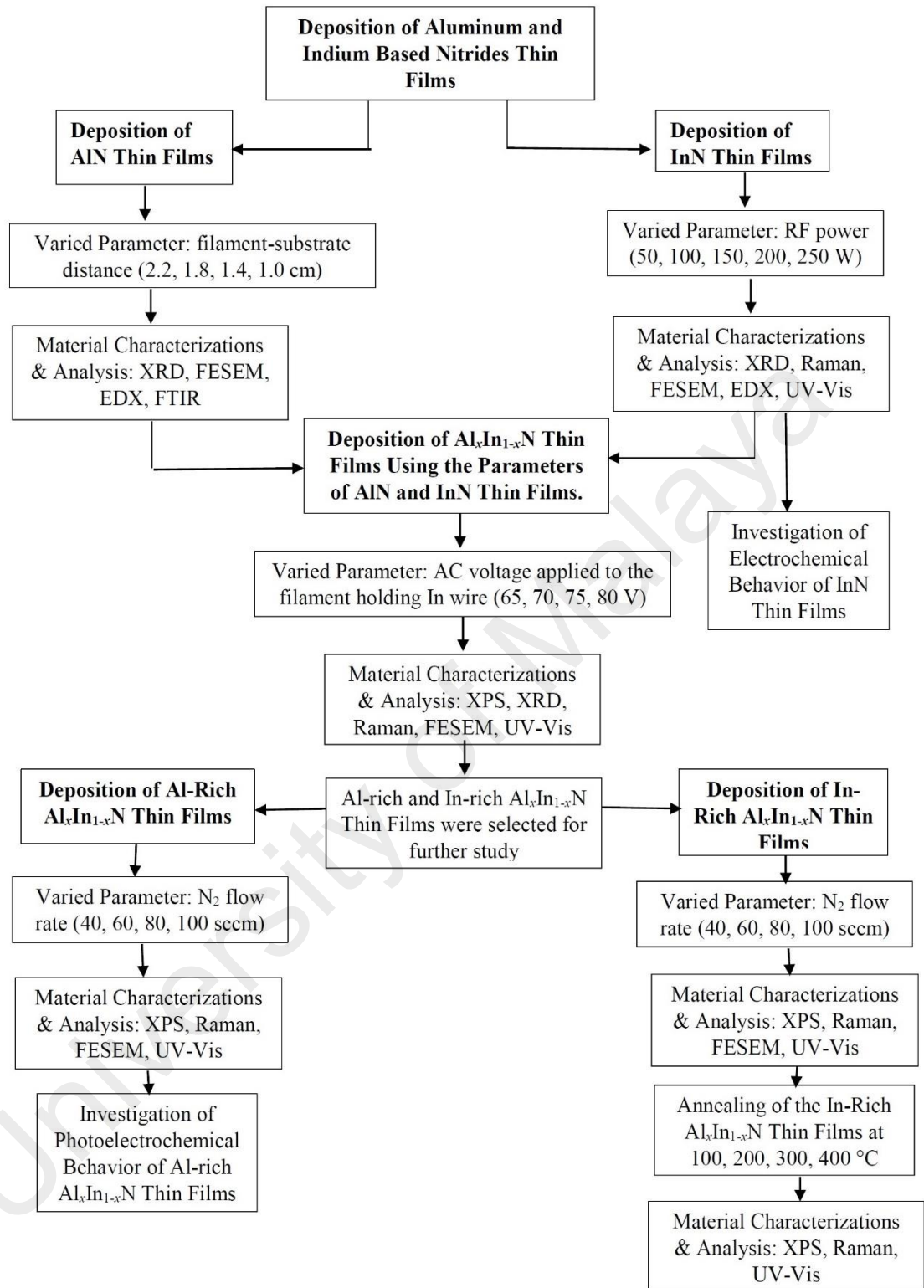


Figure 3.1: Flowchart of research methodology involved in this work.

3.3 Deposition of the Thin Films

3.3.1 Deposition System

A home-built plasma-assisted reactive evaporation system was designed and set up for the deposition of binary and ternary indium- and aluminum-based nitride thin films. An actual photograph of the system is shown in Figure 3.2. The system mainly consisted of four parts: evacuation system, electrical system, reaction chamber, and gas distribution system as shown in Figure 3.2. The evacuation system included two parts, i.e., the rotary and turbomolecular pumps. The turbomolecular pump was backed up with another rotary pump as shown in Figure 3.2. The electrical system consisted of a RF power supply and matching impedance, two hot wire supplies, and temperature controller. The reaction chamber included a top plate, chamber body, and a base plate all of which were made of stainless steel to withstand high temperatures and to provide good vacuum conditions during the growth process.

A schematic diagram of the reaction chamber used for the growth of binary thin films (e.g., AlN and InN) is shown in Figure 3.3. The top plate which has a diameter and thickness of 31.5 and 0.8 cm, respectively, was attached to an air admittance valve, gas inlet, the RF power supply connector, and the hot filament supply connectors. A Teflon block was employed between the gas shower head and the gas inlet to isolate the gas shower and for the establishment of plasma ambient; as such, the shower head also acted as the powered electrode. The RF power was supplied by using an ENI power supply at 13.56 MHz. The hot filament supply connectors were attached to two copper rods connected to copper holders which clamped a tungsten filament between the shower head and the substrate holder inside the chamber body. The tungsten filament was used for evaporation of Al/In wires and labeled as F_{Al}/F_{In} . For the AlInN ternary thin films two separate filaments were clamped perpendicularly to each other (see inset of Figure 3.4)

between the grounded substrate holder and a radio-frequency (RF) - powered stainless steel electrode.

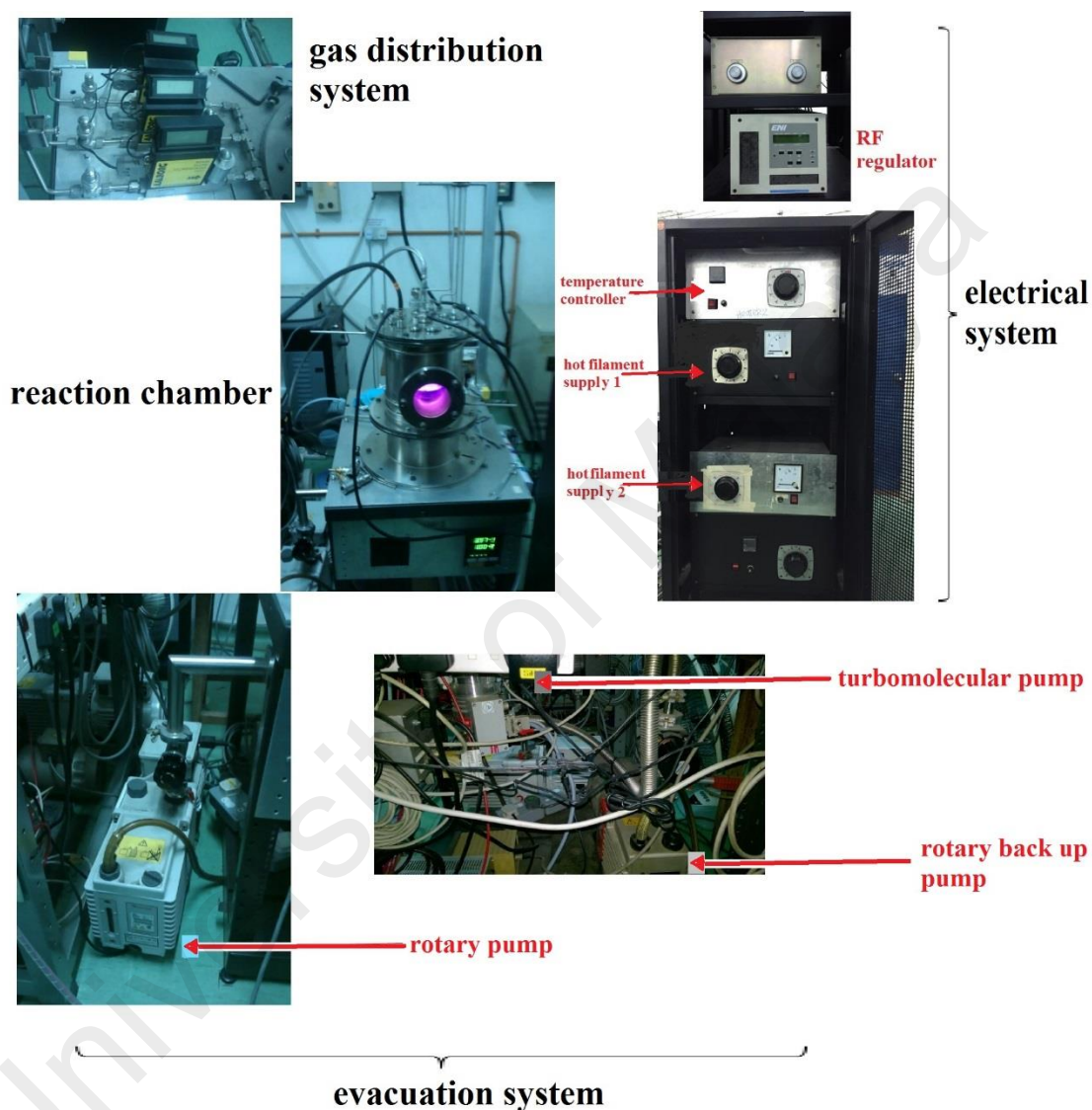


Figure 3.2: A photograph of plasma-assisted reactive evaporation system.

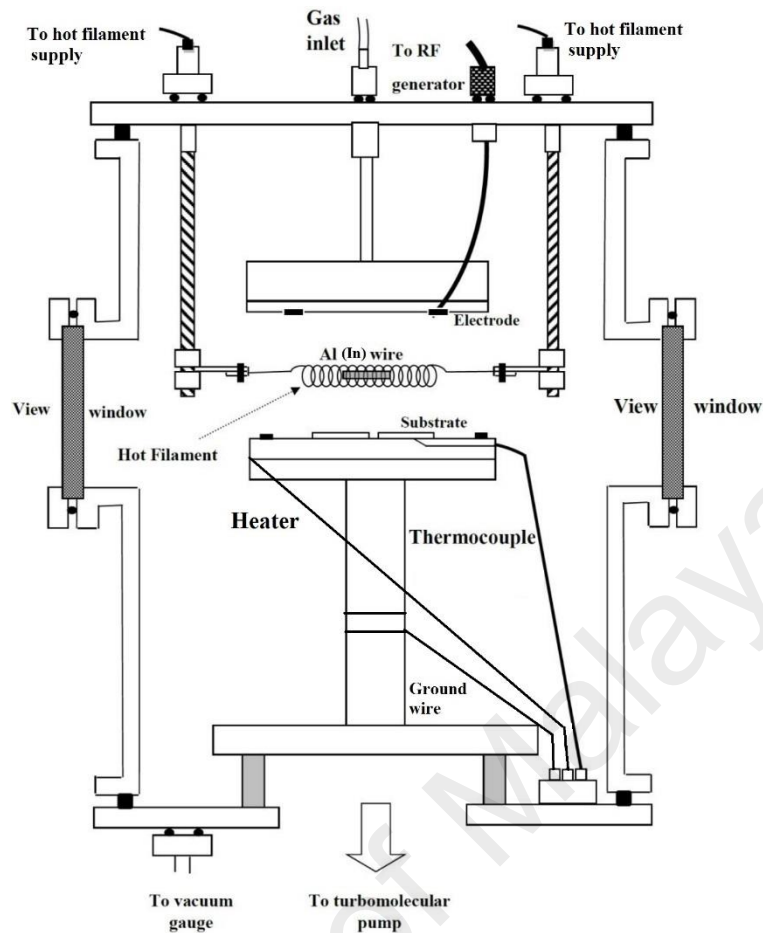


Figure 3.3: Schematic diagram of plasma-assisted reactive evaporation system for growth of AlN and InN thin films. A single tungsten filament holding the In or Al wires are clamped to stainless steel rods filament holders.

The internal diameter, thickness, and height of the body chamber was 20.5, 0.8, 38 cm, respectively and the chamber was equipped with two view windows to monitor the deposition process. The substrate holder having a diameter of 10 cm and thickness of 0.5 cm was positioned inside the chamber and acted as the grounded electrode. A heater rod and thermocouple were inserted through a feed-through beneath the substrate holder. The chamber base was attached to a six-pin electrical feed-throughs which were connected to the thermocouple, heater, and ground wire. The plate was also connected to the turbomolecular and rotary pumps.

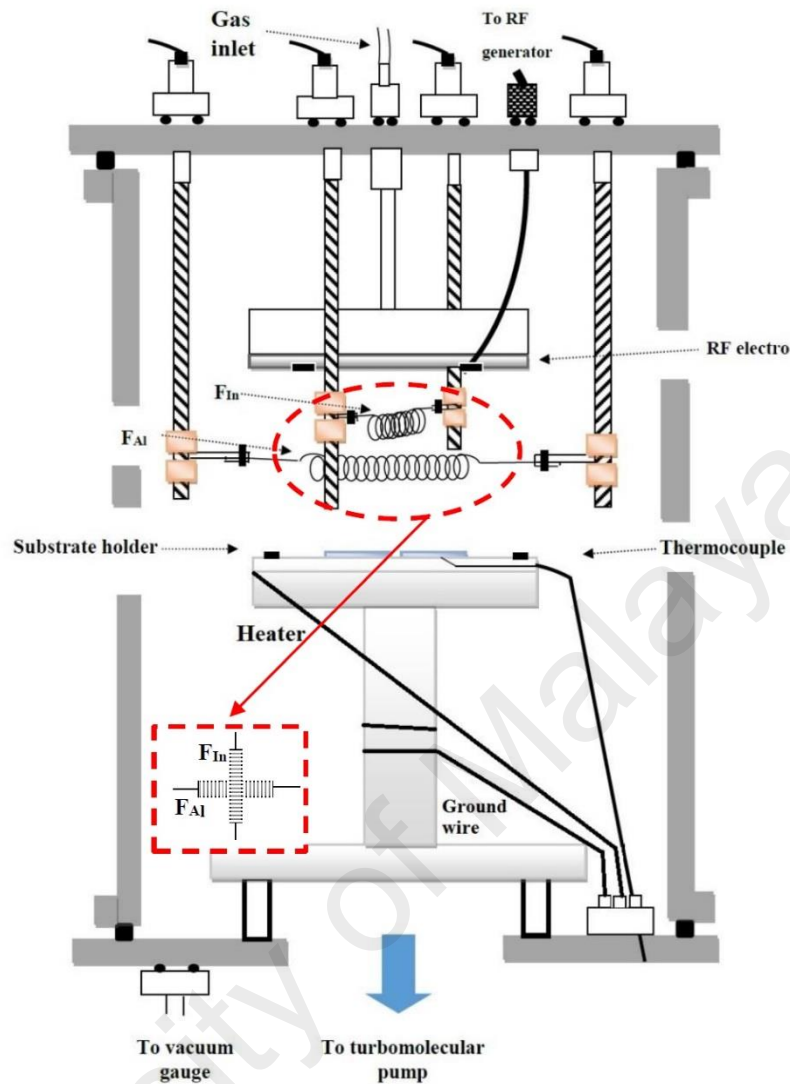


Figure 3.4: Schematic diagram of plasma-assisted reactive evaporation system for growth of $\text{Al}_x\text{In}_{1-x}\text{N}$ thin films. The tungsten filaments holding the In and Al wires are clamped perpendicular to each other (see the inset image) to stainless steel rod filament holders. The former is placed above the latter.

3.3.2 Pre-heating of Filament

Tungsten wire with a purity of 99.95% and diameter of 0.5 mm were coiled and used as the filament for evaporation of Al and/or In wires. Before the filament was employed in the deposition process it was pre-heated to remove potential contaminations. The filament was initially cleaned by acetone and then clamped on two copper rods which were inserted using feed-through on the top plate covering the chamber. The chamber was then tightly screwed. The main rotary pump was switched on and the chamber was

pumped down to a pressure of around 10^{-3} mbar. Then, hydrogen gas with a flow rate of 100 sccm was admitted into the chamber and the filament was heated to around 1800 °C for 10 minutes. Finally, the filament power supply was switched off, the valves admitting the gas were closed and the system cooled down for 2 hours under vacuum condition.

3.3.3 Preparation of Substrates

AlN, InN, and $\text{Al}_x\text{In}_{1-x}\text{N}$ thin films were deposited on silicon and quartz substrates. 625 μm -thick crystal silicon (c-Si) with (111) orientation and quartz glass having a thickness of 1.0 mm were used for deposition of the films. The substrates were cleaved into quadrangular-shaped pieces with dimension of 1.5×1.5 cm and cleaned thoroughly before insertion into the chamber. Each quartz and silicon substrates was cleaned using different procedures.

The Si (111) substrates were initially rinsed with deionized water to remove dust and other particles from the surface and then immersed in $\text{H}_2\text{O}:\text{H}_2\text{O}_2:\text{HCl}$ (at 6: 1: 1 ratio) solution for 5 minutes. Next, the substrates were again rinsed in deionized water for 5 minutes. This was repeated for $\text{H}_2\text{O}:\text{H}_2\text{O}_2:\text{NH}_4\text{OH}$ (at 5: 1: 1 ratio) and with $\text{H}_2\text{O}:\text{HF}$ (at 10: 1 ratio) solutions to remove the oxide layer and other residue contaminants from the surface (Goh, 2012). Finally, the substrates were dried by using compressed nitrogen.

The cleaning procedure for the quartz substrates was somewhat simpler than for the silicon ones. First, they were ultrasonically degreased in decon 90 soap for 30 minutes, then rinsed in deionized water, ethanol, and acetone, and subsequently dried using nitrogen gas (Goh, 2012).

3.3.4 Pre-deposition Process

Prior to the deposition process the substrate holder, filament holder and shower head were thoroughly cleaned by sandpaper to eliminate any contamination and then cleaned

with acetone. The chamber body was wiped with a soft tissue soaked in acetone. The shower head was connected to the RF power supply and the substrate holder was attached to the heater and the thermocouple. The cleaned substrates were placed directly on the substrate holder and the tungsten filament was clamped to the stainless steel rod holders inserted by feed-throughs from the top plate of the deposition chamber. The filament was clamped between the substrates and the shower head. Al (In) wire was placed inside the coils of the filament, the chamber was tightly screwed and all the valves of the system were closed before the evacuation process was commenced.

The evacuation process was done in 3 steps. In the first step, the rotary pump was switched on and the rotary valve slowly opened to its maximum. The pumping process was continuously conducted until the vacuum pressure reached around 10^{-3} mbar. To evacuate any residual gases inside the gas lines, the line valves were opened. Next, the backup rotary pump was switched on and the corresponding valve was opened. This pump acted as the backing for the turbomolecular pump. In the second step, the main rotary pump was closed, the turbomolecular pump switched on for one hour and a minimum pressure, called the base pressure, was obtained. Finally, the turbomolecular pump and the backup rotary pump were switched off and the main rotary pump was opened.

To activate the surface bonds, H₂-plasma treatment was performed on the surface of the substrates for 10 min at a fixed hydrogen gas flow rate of 100 sccm using the mass flow controller (MFC). The RF power during hydrogen treatment process was 15 W. It has been shown that plasma treatment significantly improves the films adhesion on the substrates (Ostrikov, 2005). Upon completion of the treatment the RF power supply was switched off, the MFC was closed, and the residual H₂ pumped out.

3.3.5 Deposition of AlN Thin Films

AlN thin films were deposited using a plasma-assisted single source reactive evaporation system (Figure 3.3). The deposition process for the films was carried out in 2 steps. First, purified nitrogen gas (purity = 99.9999%) was admitted into the chamber and plasma ambient was generated and stabilized for 5 minutes. Then, the tungsten filament was heated to around 1650 °C and the deposition process was performed by evaporating the Al wire under an N₂ plasma environment. During the process the substrate temperature (T_s) increased due to ion bombardment and radiant heat from the plasma and the hot filament, respectively. No external heating was used during the deposition process. However, due to ion bombardment from the plasma and radiant heat from the hot filament the substrate temperature during the deposition process varied from 150 to 200 °C depending on the distance between the filament and substrate. After the deposition process the filament and the plasma supply were switched off and the system cooled down under the flow of N₂ gas until the temperature reached around 50 °C. The effect of the filament-to-substrate distance on the structure, composition, and morphology of AlN thin films was studied. The filament-to-substrate distance (d_{f-s}) was varied in 0.4 cm increments from 1.0 to 2.2 cm and other parameters were fixed during the process. A list of the parameter values for the growth of AlN thin films is summarized in Table 3.1.

3.3.6 Deposition of InN Thin Films

The plasma-assisted single source reactive evaporation system (Figure 3.3) was also employed for growth of InN thin films. Prior to the actual deposition process the substrates were externally heated to 200 °C. The deposition process for InN thin films was carried out in 3 steps. First, purified nitrogen gas (purity = 99.9999%) was admitted into the chamber and plasma ambient generated and stabilized for 5 minutes. Then, the tungsten filament was heated to 1050 °C and the deposition process was performed by evaporating the In wire under N₂ plasma. During the process, the substrate temperature

(T_s) increased due to ion bombardment and radiant heat from the plasma and the hot filament, respectively, and the substrate temperature reached around 350 °C. After the deposition process and before switching off the system the sample was in situ annealed under N_2 plasma ambient (RF= 50 W) and hot filament ($T_f = 950$ °C) for 30 minutes.

The effect of RF power on crystallinity, composition, morphology and optical properties of InN thin films was investigated. The RF power was changed in 50 W increments from 50 to 250 W and other parameters were fixed during the process. A list of the parameter values for growth of InN thin films is summarized in Table 3.1.

3.3.7 Deposition of $Al_xIn_{1-x}N$ Thin Films

The $Al_xIn_{1-x}N$ films were deposited on quartz and Si (111) substrates by the plasma-assisted dual source reactive evaporation system (Figure 3.4). Two separate tungsten wires were used as the hot filaments for evaporation of indium and aluminum wires. The deposition process was conducted in three steps, as follows: 1) N_2 plasma was generated in the chamber and stabilized for 5 min, 2) F_{Al} was heated to the temperature required for evaporation of Al atoms ($T_f \sim 1650$ °C) and then cooled to 1450 °C to avoid high evaporation rates, and 3) an AC voltage was immediately applied to the F_{In} filament and the $Al_xIn_{1-x}N$ film formation was initiated. Conditions for the film growth were maintained under N_2 plasma for 5 min. The substrates were initially heated to 200 °C and, during the deposition process, the final substrate holder temperature was varied from 320 to 360 °C (depending on the AC voltage applied to F_{In} (V_{In})). After the deposition process, the F_{In} was switched off and the F_{Al} temperature was fixed at 1300 °C and the obtained samples were annealed in N_2 plasma (flow rate: 40 sccm, RF power: 50 W) for 30 min.

Three sets of samples were deposited for the $Al_xIn_{1-x}N$ thin films. In the first set, the AC voltage applied to F_{Al} (V_{Al}) was set at 75 V, while that applied to F_{In} (V_{In}) was varied

in 5 V increments from 65 to 80 V in order to obtain $\text{Al}_x\text{In}_{1-x}\text{N}$ films with different Al(In) compositions. One Al-rich (the sample deposited at $V_{\text{in}} = 70$ V) and one In-rich (the sample deposited at $V_{\text{in}} = 80$ V) samples were selected and the effect of the nitrogen gas flow rate during the deposition process was studied for each films (set 2 and 3). The N_2 flow rate was varied in 20 increments from 40 to 100 sccm. The deposition parameters for each set of $\text{Al}_x\text{In}_{1-x}\text{N}$ thin films are summarized in Table. 3.2.

Table 3.1: Deposition parameters used for deposition of AlN and InN thin films. A set of four AlN films was deposited at filament-substrate distances of 2.2, 1.8, 1.4 and 1.0 cm and a set of five InN films was deposited different RF powers of 50, 100, 150, 200 and 250 W.

| Parameter | AlN | InN |
|-----------------------------------|-----------|----------|
| RF power (W) | 250 | 50 – 250 |
| Filament-substrate distance (cm) | 1.0 – 2.2 | 1.0 |
| Filament temperature (°C) | 1650 | 1050 |
| Substrate holder temperature (°C) | 150 – 200 | 350 |
| N_2 flow rate (sccm) | 40 | 80 |
| Deposition time (min) | 8 | 5 |

Table 3.2: Growth parameters used for deposition $\text{Al}_x\text{In}_{1-x}\text{N}$ thin films. A set of four $\text{Al}_x\text{In}_{1-x}\text{N}$ films was initially deposited at various AC voltages applied to the filament holding In wire (set 1). Two sample were selected from set 1 and two sets (set 2&3) of four $\text{Al}_x\text{In}_{1-x}\text{N}$ thin films were deposited at N_2 flow rate of 40, 60, 80, 100 sccm.

| Parameter | Set 1 | Set 2 | Set 3 |
|---|-------------|----------|----------|
| RF power (W) | 250 | 250 | 250 |
| F_{Al} -substrate distance (cm) | 1.0 | 1.0 | 1.0 |
| F_{In} -substrate distance (cm) | 1.5 | 1.5 | 1.5 |
| F_{Al} temperature ($^{\circ}\text{C}$) | 1450 | 1450 | 1450 |
| F_{In} temperature ($^{\circ}\text{C}$) | 1000 – 1100 | 1100 | 1030 |
| Substrate holder temperature ($^{\circ}\text{C}$) | 320 – 360 | 360 | 330 |
| N_2 flow rate (sccm) | 40 | 40 – 100 | 40 – 100 |
| Deposition time (min) | 5 | 5 | 5 |

3.3.8 Annealing Process

Four $\text{Al}_x\text{In}_{1-x}\text{N}$ samples were reproduced under the set 2 conditions (with nitrogen flow rate of 100 sccm) for the annealing study. The annealing process was carried out to investigate the stability of the ternary films at various temperatures and a cylindrical furnace (Thermolyne SM 002672) covering a quartz tube was employed for the process. A photograph of the furnace is shown in Figure 3.5. The sample was placed on a ceramic boat and inserted into the quartz tube, one end of which was connected to an industrial grade nitrogen gas and the other left open. The gas was flown at a rate of 50 sccm for 15 minutes to remove the residual air from the tube. Then, the furnace was switched on and the annealing temperature and rate were set. The annealing rate was set at $15^{\circ}\text{C}/\text{min}$ while the annealing temperature was varied in 100°C increments from 200 to 500°C . Hence, four annealing processes were carried out. When the temperature reached the set figure, the annealing process continued for 1 hour and then the furnace was switched off

and the sample was cooled down under the flow of nitrogen. When the temperature reached around 50°C, the gas was closed, the annealed sample was taken out from the tube and stored for characterization.

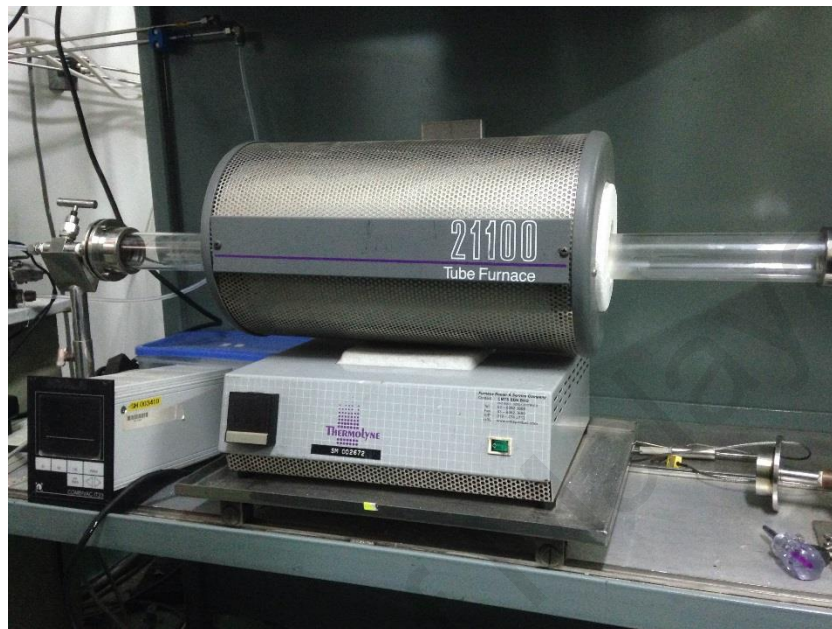


Figure 3.5: A photograph of the tube furnace used for the annealing process.

3.4 Characterization Techniques

Various techniques were employed for the characterization of the thin films. The crystalline structure of the films was investigated by using X-ray diffraction (XRD). Raman spectroscopy was employed to study structural properties of the films. The surface morphology and elemental composition of the thin films were analyzed respectively by field emission scanning electron microscopy and energy-dispersive X-ray spectroscopy attached to the microscope. The compositional uniformity and bonding configuration of the samples were investigated by X-ray photoelectron spectroscopy (XPS). The optical transmittance and reflectance for the fabricated $\text{Al}_x\text{In}_{1-x}\text{N}$ thin films were measured using a ultra-violet visible near-infrared (UV-Vis-NIR) spectrophotometer. The thickness of the films was measured using surface profiler. To examine the chemical bonding in the thin

films Fourier transform infrared spectroscopy (FTIR) was used in the range of 400 – 4000 cm^{-1} .

3.4.1 X-ray Diffraction (XRD)

This versatile technique is able to determine the particle size, the types of chemical bonds, and the atomic-scale differences among various materials. The measurement method is based on the X-ray beam which is scattered from the sample upon exposure to the beam of the incident X-rays. A schematic of XRD principle is shown in Figure 3.6 (a). The incident X-ray beam is generated by heating a cathode filament and thereby creating an emission of electrons. By applying an electrical field, the electrons are then accelerated towards the target material. The kinetic energy of the electron beam is mostly converted to heat and only a small percent (e.g., $\sim 1\%$) of the energy is converted to X-ray photons. In fact, only a limited number of electrons have enough energy to drive away the electrons in the inner shell of the target material and produce X-ray photons. When the incident ray strikes the sample at a certain angle it interacts with the crystal lattice and a constructive interference is produced based on Bragg's Law:

$$n\lambda = 2d\sin\theta \quad (3.1)$$

where n is a positive integer, λ is wavelength of the electromagnetic radiation, d is the interplanar distance. The diffraction only occurs when Bragg's Law is satisfied and the corresponding angles are called Bragg angles.

As mentioned above, XRD measurement is based on recorded diffraction of X-ray beam from the sample upon it is exposed to the beam of incident X-rays. The diffracted beam path in an X-ray diffractometer is schematically shown in Figure 3.6 (b). This configuration was used for XRD measurement of all AlN, InN and $\text{Al}_x\text{In}_{1-x}\text{N}$ samples in this work. The angle (θ) between the incident X-ray beam and the sample surface was fixed at a very small value while the detector was rotated varying the detection angle.

Since the irradiated area on the sample surface is large and intensity of the reflections is insignificant, this configuration is especially suitable for XRD characterization of thin films. This is due to the low penetration of the incident beam in the films as a result of the low incident angle.

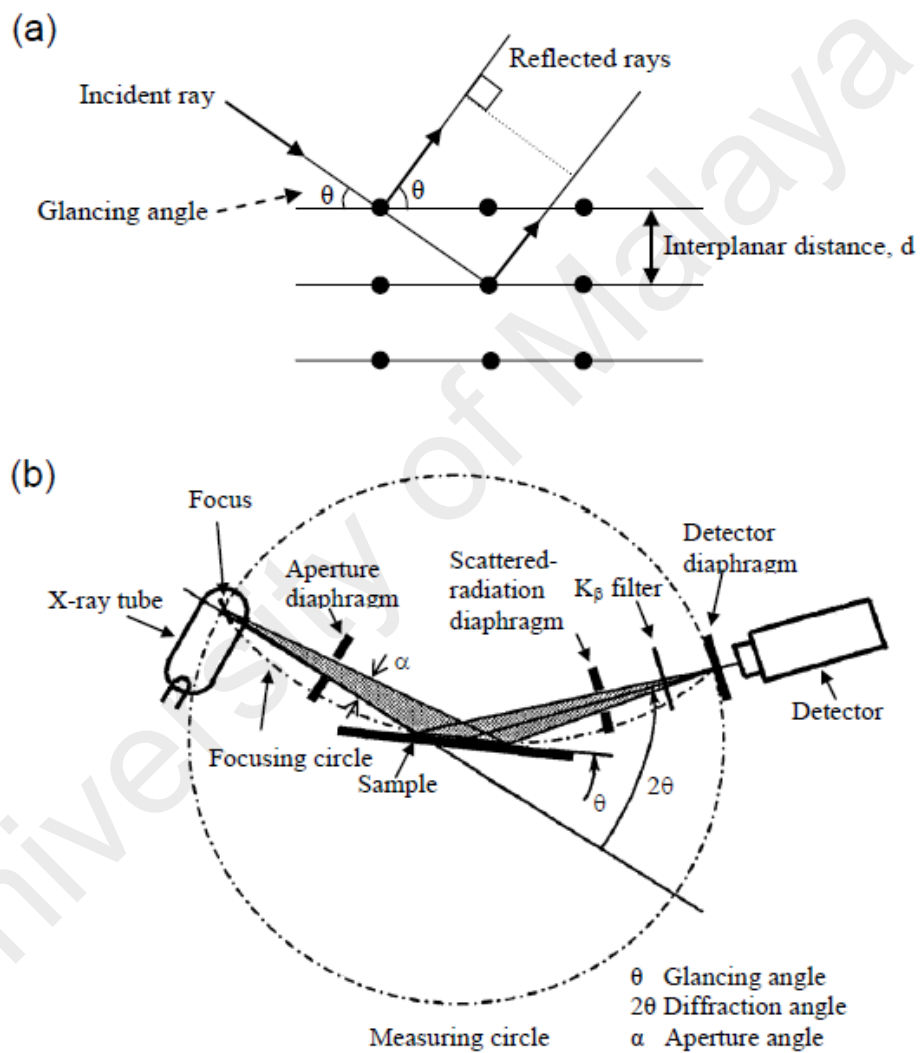


Figure 3.6: (a) The principle of X-ray diffraction and (b) X-ray diffracted beam path in $\theta/2\theta$ mode. From Ref (Goh, 2012).



Figure 3.7: A photograph of SIEMENS D5000 X-ray diffractometer.

XRD measurement was performed by using a SIEMENS D5000 X-ray diffractometer (Figure 3.7) in which copper was used as the target material. The X-ray is Cu K_{α} radiation with a wavelength of $\lambda = 1.54060 \text{ \AA}$. The applied voltage and current were 40 kV and 40 mA, respectively. The incident angle was fixed at 5° . An x-ray detector was employed to detect the interference pattern. The diffraction patterns of the lattice was detected by scanning the sample in 2θ range of 20° to 80° with a step size of 0.05° and a step time of 2 sec.

3.4.2 Fourier Transform Infrared (FTIR) Spectroscopy

Fourier Transform Infrared (FTIR) Spectroscopy is a characterization technique which provides direct information about the local bonding of the constituent atoms in the deposited thin films. In fact, FTIR is used to identify the molecular structure of the material. The measurement involves the passage of a beam of infrared (IR) light through the thin film grown on a substrate which is transparent to IR light. The intensity of the transmitted light through a depth (l) can be obtained from the following equation (Vickerman, 1997):

$$I = I_0 e^{-\mu l} \quad (3.2)$$

where I_0 is the intensity of the incident light on the thin film and μ is the linear attenuation coefficient of the sample. If scattering is insignificant, the linear attenuation coefficient can be equated with the linear absorption coefficient $\frac{I}{I_0}$ which is defined as the transmittance (T). A portion of the incident light is absorbed at a particular wavelength to create an optical phonon mode of the material. As such, the peaks observed at a particular wavelength of the transmittance spectrum provide detailed information about the molecular structure of the thin films.

The FTIR analysis was performed using a Perkin-Elmer System 2000. An image of the employed system is shown in Figure 3.8. The measurement was done in a wavelength range of $400 - 4000 \text{ cm}^{-1}$ after subtraction of FTIR transmittance spectrum of the Si substrate.



Figure 3.8: A photograph of FTIR Perkin-Elmer System 2000.

3.4.3 Micro-Raman Scattering Spectroscopy

Micro-Raman scattering spectroscopy is usually employed to identify low-frequency modes in the thin films. In other words, it is a characterization tool for examining the chemical structure and physical state of the samples. Normally, the sample is illuminated with a laser beam as the photon source in the visible, near-infrared, or near ultra-violet range. The laser beam interacts with the electrons of the bonds of the exposed molecules on the thin film surface. The scattered photons from the sample are detected by a spectrometer through either a notch filter or a band pass filter. During the Raman process, the interaction between the photons and the molecular vibrations or phonons results in a shift in wavelength of the photons to a lower (red shift) or higher (blue shift) values. These shifts provide information on the vibrational modes of the sample. When the incident photon loses its energy to create a phonon it is called Stokes scattering and when it acquires energy from annihilation of a phonon it is called anti-Stokes scattering.

A schematic diagram of Raman principle is displayed in Figure 3.9. As the sample is illuminated with the laser, the light scattered from it passes through the microscope objective, separated into Stokes shift frequency, and then focused onto a CCD array detector. The intensity of each vibrational mode is determined by using an individual pixel on the array. A computer is connected to the CCD to convert the results into a spectrum using a specific software. A Renishaw inVia Raman Microscope (Figure 3.10) with a laser excitation wavelength of 514 nm was used to study the structural properties of the grown AlN, InN, and $\text{Al}_x\text{In}_{1-x}\text{N}$ films. The measurement was carried out by using He-Cd laser (power = 100 %) with exposure time per second of 30 in the wave number range of 100 to 1000 cm^{-1} .

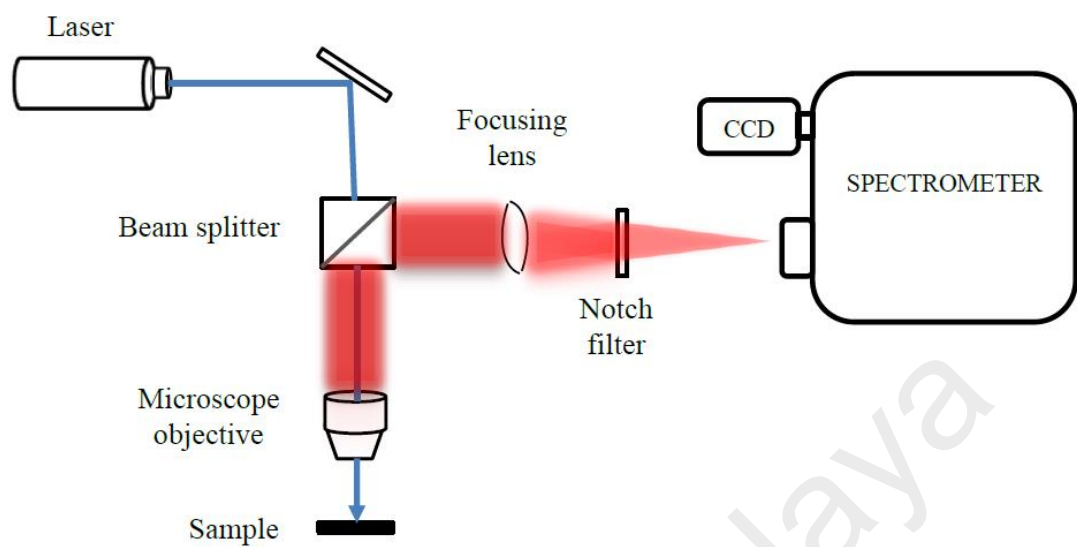


Figure 3.9: Schematic diagram of Raman principle. From Ref. (Othman, 2012).



Figure 3.10: A photograph of Renishaw inVia Raman Microscope.

It is well-known that AlN and InN with wurtzite structure belong to the C_{6v}^4 space group (Q. Guo et al., 2014; Zhu & Pezzotti, 2015). Based on group theory one A_1 , one E_1 , $2E_2$ and $2B_1$ sets of phonon modes are expected. Among these modes, the A_1 , E_1 and E_2 sets are Raman-active while the B_1 modes are silent (Loudon, 1964; Siegle et al., 1997). The A_1 and E_1 modes correspond to the axial and planar vibrations, respectively and split into transversal optical (TO) and longitudinal optical (LO) components. The E_2 symmetry is typically denoted as $E_2(\text{low})$ and $E_2(\text{high})$ Raman modes. Hence, six Raman-active optical modes are allowed for wurtzite AlN and InN (Kallel, Dammak, Wang, & Jadwisienczak, 2014). The allowed optical phonon modes of AlN and InN and their positions are summarized in Table 3.3. It should be noted that the position of the optical phonon modes of $Al_xIn_{1-x}N$ films varies between the positions of the corresponding modes of InN and AlN depending on the alloy composition (x).

Table 3.3: Raman-active optical modes of AlN and InN and their positions (Junqiao Wu, 2009).

| Phonon mode | AlN (cm^{-1}) | InN (cm^{-1}) |
|--------------------|--------------------------|--------------------------|
| $A_1(\text{TO})$ | 611 | 447 |
| $A_1(\text{LO})$ | 890 | 586 |
| $E_1(\text{LO})$ | 912 | 593 |
| $E_1(\text{TO})$ | 671 | 476 |
| $E_2(\text{high})$ | 657 | 488 |
| $E_2(\text{low})$ | 249 | 87 |

3.4.4 Field Emission Scanning Electron Microscopy (FESEM) and Energy-Dispersive X-ray (EDX) Spectroscopy

Field emission scanning electron microscopy was employed to observe the topographical details on the surface of the thin films at magnifications of 10x to 300,000x. In the microscope a field emission source is used to liberate the electrons in a high electrical field gradient which gives rise to the electrons gaining high energy when they travel within the high vacuum column. The energetic electrons (so-called primary electrons) are then condensed by electronic lenses to provide bombardment of the thin films with a narrow scan beam. As a result, secondary electrons are ejected from the surface of the thin films. A detector is used to catch the secondary electrons and to produce electronic signals which are then transduced to a video scan to produce morphology images. Resolution of the images strongly depends on accumulation of the secondary electrons.

Energy-dispersive X-ray spectroscopy (EDX) is an analytical characterization technique that commonly used for elemental composition of a sample. This technique is based on the interaction between a high-energy beam of electrons or a beam of X-rays and a sample. The incident beam is able to excite the inner shell electrons (lower energy shells) and dislodge them from the shell resulting in the formation of electron holes in the shells. The electrons from the outer shells (higher-energy shells) recombine the holes and release energy in form of X-rays. The released energy which is equal to the difference between the energies of the outer and inner shells, is the characteristic of the atomic structure of the emitting element and appears as a peak in the EDX spectrum.

Surface morphology of the InN and $\text{Al}_x\text{In}_{1-x}\text{N}$ thin films were analyzed by JEOL JSM-7600F microscope. The elemental composition of the films were measured by X-Max Oxford Instruments EDX attached to the microscope. A picture of the machine is shown

in Figure 3.11. However, for AlN samples a Hitachi SU 8000 scanning electron microscope and BrukerXFlash6|100 detector attached to the microscope (HIGH-TECH INSTRUMENT SDN BHD, Malaysia) were used for morphology imaging and elemental analysis. Prior to the measurement, the samples were cleaved to a dimension of 1×1 cm and then mounted at a stub using double-sided carbon tape.



Figure 3.11: A photograph of JEOL JSM-7600F microscope.

3.4.5 X-ray Photoelectron Spectroscopy (XPS)

X-ray photoelectron spectroscopy (XPS) is one of the most important characterization technique and was widely used in this work to measure the compositional uniformity and bonding configuration of the samples as well as to analyze the surface chemistry of the grown materials. The function of the XPS system is based on a photoelectric effect where the surface of the thin films is irradiated by an x-ray beam in an ultra-high vacuum leading to the production of photoelectrons. The photoelectrons are ejected from different orbitals (1s, 2s, 2p, etc.) of the atoms and their energy spectrum are determined using a beta-ray spectrometer. The binding energy of the photoelectrons can be obtained from the Einstein equation:

$$E_{BE} = hv - E_{KE} - \varphi \quad (3.3)$$

where E_{BE} is binding energy of the photoelectrons, hv is energy of the incident photons, E_{KE} is kinetic energy of the photoelectrons measured by the spectrometer and φ is work function dependent on both the spectrometer and the material. Since the binding energies of the electron orbitals in atoms are known, the atomic composition of the sample surface is identified from the positions of the peaks in the XPS spectrum. Analyzing the photoelectron peaks using the curve-fitting method allows us to quantitatively determine the composition of the sample.

Three different systems including Shimadzu, Kratos Axis Ultra DLD (Institute of Microengineering and Nanoelectronics (IMEN), Universiti Kebangsaan Malaysia, Malaysia), PHI Quantera II (MIMOS national R&D center, Malaysia) and Thermo VG Scientific, CLAM2 (the Synchrotron Light Research Institute, Thailand) were employed for the XPS characterization of the $Al_xIn_{1-x}N$ thin films. An image of the PHI Quantera II system is shown in Figure 3.12. Since each system has specific calibrations and parameters, all samples of a set were measured by using a single system. For instance, in PHI Quantera II system a monochromatic Al K-alpha (1486.6 eV) at 25 W (15 kV and 3 mA) was used which was incident at 90° to the sample surface under base pressure of 2×10^{-7} Pa. The obtained photoelectrons were collected at a take-off angle of 45° . Narrow high-resolution scans of Al2p, In3d_{5/2}, and N1s photoelectron spectra were run with 0.1 eV steps and 20 ms dwell time. Scans were taken at analyzer pass energy of 112 eV. After measurement all the obtained peaks were calibrated by using the position of C1s peak which is 284.6 eV. Then, Al2p, In3d_{5/2}, and N1s as the main elements of the $Al_xIn_{1-x}N$ thin films were analyzed to identify the bonding configuration of the alloys.



Figure 3.12: A photograph of PHI Quantera II XPS system.

3.4.6 Surface Profilometry

The thickness of the grown AlN, InN, and $\text{Al}_x\text{In}_{1-x}\text{N}$ thin films was calculated by using a KLA-Tencor P-6 surface profiler system (see photograph of the system in Figure 3.13). The system has a contact profilometer, and a diamond stylus is used to touch the surface of the profiled area. For the purpose of thickness measurement, one small slide of quartz or Si was placed on the quartz substrate before the deposition process in such a way that the area beneath remained uncoated. When the stylus shifts from the uncoated area towards the coated films, the displacement was converted into a signal and displayed as a spectrum. The average value is taken as the thickness of the films.

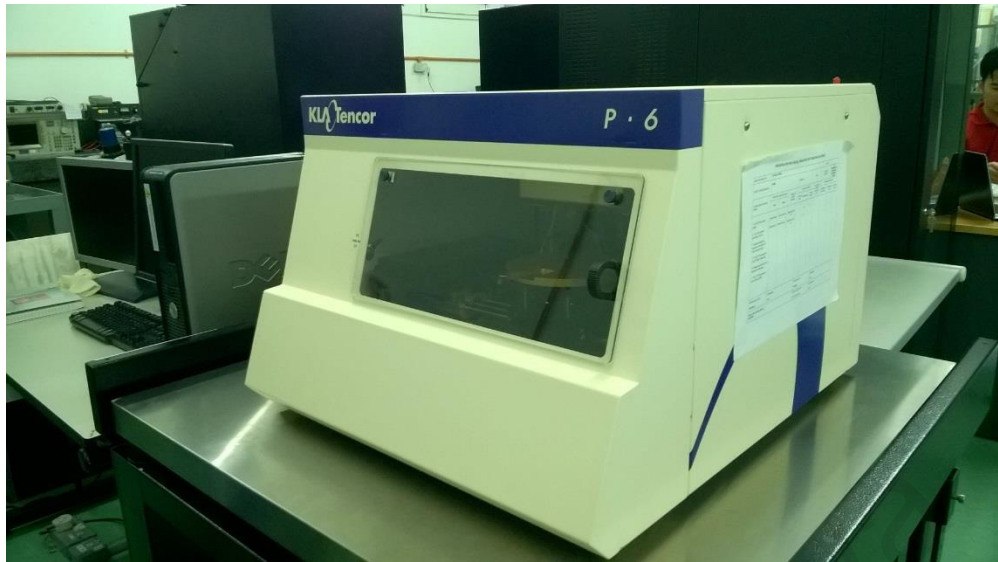


Figure 3.13: A photograph of KLA-Tencor P-6 surface profiler system.

3.4.7 Ultra-Violet Visible Near-Infrared Spectroscopy

The ultra-violet visible near-infrared spectroscopy provides a suitable approach for examining the optical properties of group III-nitride semiconductors. The measurement provides information on the absorption coefficient which determines the optical band gap energy (E_g) of the materials. E_g is the difference in energy between the valance and the conduction bands. A Lambda 750 UV/Vis/NIR spectrometer was used to measure optical transmittance and reflectance of the grown thin films in the wavelength range of 190 to 3300 nm. A photograph of the spectrometer is shown in Figure 3.14. The optical measurements were performed for the films deposited on quartz substrates. D2 lamp (with a wavelength range of 190 – 350 nm) and Halogen lamp (with a wavelength range of 350 – 3300 nm) were used as the sources for UV and Vis - NIR regions, respectively. A bare quartz substrate and a high reflective mirror were used as the references for transmittance and reflectance measurements, respectively. After passing through a monochromator, the light is split into two components using a sector mirror and passes through the film and the reference. Then, the outcome lights reach the detectors and are finally displayed as optical spectra.

The absorption coefficient (α) was calculated for each film with the measured transmittance (T), reflection (R), and film thickness (d) from the following equation (Q. Guo, Tanaka, Nishio, & Ogawa, 2008):

$$\alpha = (1/d)\ln[(1 - R)^2/T] . \quad (3.4)$$

It is known that group III-nitrides have a direct band gap and the squared absorption coefficient of a semiconductor with a direct band gap is a function of photon energy:

$$\alpha^2 = A (hv - E_g)/(hv)^2, \quad (3.5)$$

where A and E_g are the proportional constant and band gap energy, respectively (Peng et al., 1997). Direct band gap of the films is determined by extrapolating the liner part of $(\alpha hv)^2$ vs hv curves down to the energy axis. However, for amorphous films $(\alpha hv)^{1/2}$ vs hv plots are used for calculating band gap energy (Tauc, 1974). This method is also applied for indirect crystalline semiconductors but the transition for amorphous semiconductors is characterized by a “nondirect” as opposed to an “indirect” transition.

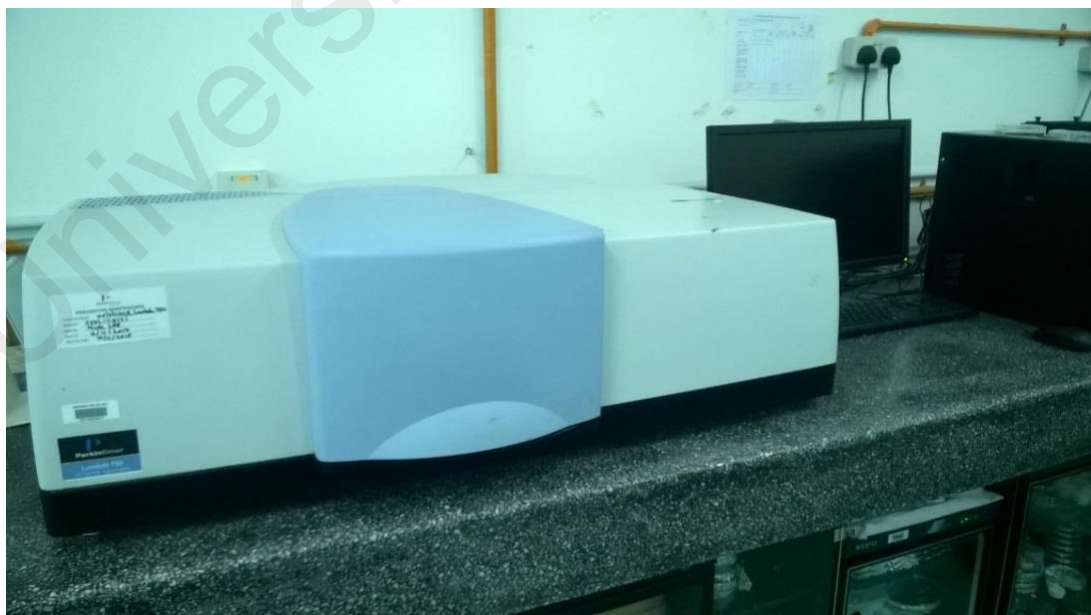


Figure 3.14: A photograph of Lambda 750 UV/Vis/NIR spectrometer.

3.5 Electrochemical Study of $\text{Al}_x\text{In}_{1-x}\text{N}$ and InN Thin Films

3.5.1 Electrochemical Measurement for $\text{Al}_x\text{In}_{1-x}\text{N}$ Thin Films

The electrochemical study of the $\text{Al}_x\text{In}_{1-x}\text{N}$ thin films were performed on a PAR-VersaSTAT 3 electrochemical work station (from Princeton Applied Research) using a conventional three-electrode system. The $\text{Al}_x\text{In}_{1-x}\text{N}$ thin films were used as the working electrode whereas Ag/AgCl and Pt were used as a reference and counter electrode, respectively. A 0.1 M phosphate buffer solution (PBS; $\text{pH}=7.2$) was used as the supporting electrolyte. The photoelectrochemical properties of the ternary alloy was investigated by illumination of the samples with a 150-W Xenon arc lamp (Newport, Model 69907) containing a simulated AM 1.5G filter. The schematic diagram and a photograph of the system is shown in Figures 3.15 and 3.16, respectively. The lamp was used to simulate solar cells throughout the experiments and all the measurements were carried out at room temperature.

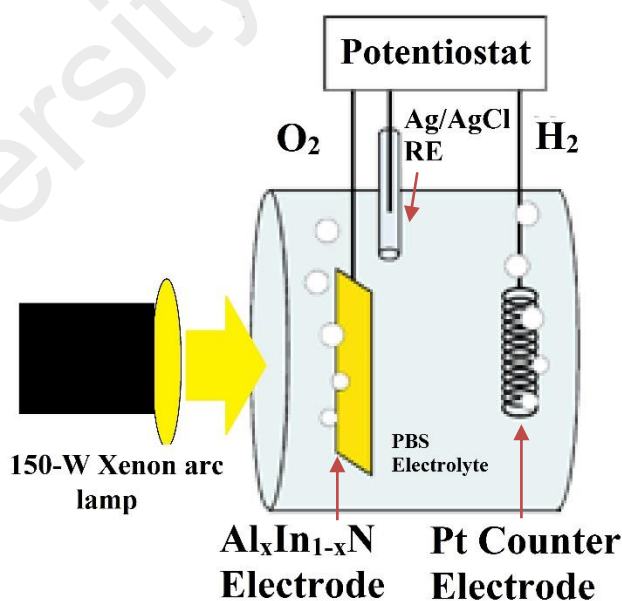


Figure 3.15: Schematic diagram of three-electrode photoelectrochemical cell.

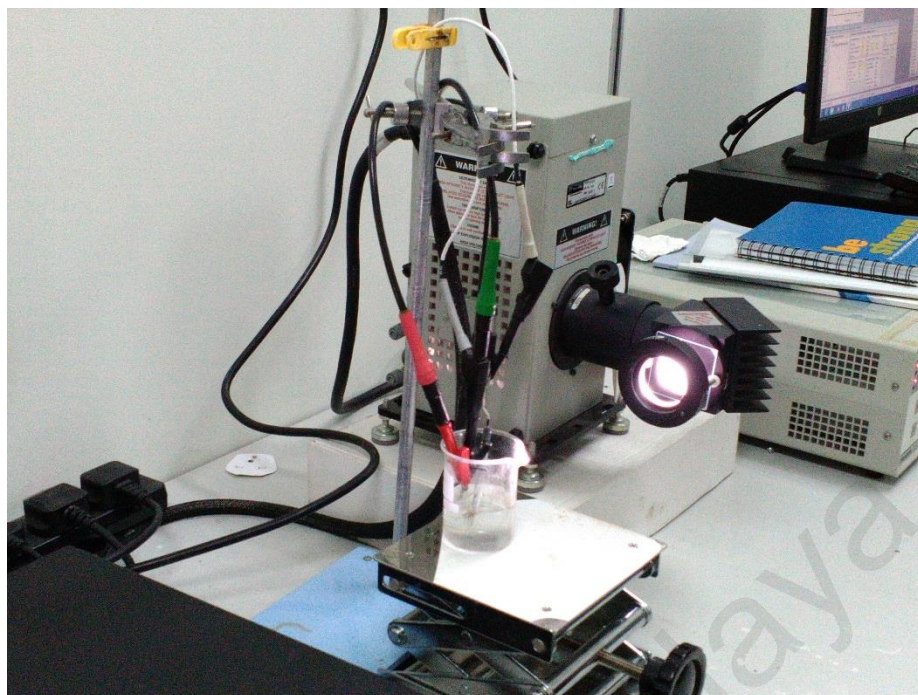


Figure 3.16: A photograph of PAR-VersaSTAT 3 electrochemical work station with 150-W Xenon arc lamp.

3.5.2 Electrochemical Measurement for InN Thin Films

The electrochemical behaviors of the grown InN thin films at different RF power were studied by using a computer-controlled VersaSTAT 4 Electrochemical Work station (Princeton Applied Research, USA). The system was similar to PAR-VersaSTAT 3 system (Figures 3.15 and 3.16) but no light source was used throughout the experiment and all characterizations were performed in dark conditions. The I-V, EIS, and Mott-Schottky characterization were carried out in the presence of 0.1 M KOH using the InN, Ag/AgCl, and Pt electrodes as a working, reference and counter electrodes, respectively. All electrochemical measurements were carried out at room temperature.

CHAPTER 4:

ALUMINUM NITRIDE AND INDIUM NITRIDE THIN FILMS BY PLASMA-ASSISTED REACTIVE EVAPORATION

4.1 Introduction

This chapter discusses two major studies on the effects of key deposition parameters on the properties of aluminum nitride (AlN) and indium nitride (InN) thin films using the plasma-assisted reactive evaporation technique. The first part of the chapter focuses on the synthesis of AlN thin films at different filament-to-substrate distances (d_{f-s}) on Si (111) substrates, where after the structural, compositional, and morphological properties of the grown films will be compared. The structural and bonding characteristics of these films were determined from the XRD and FTIR analysis. The surface morphology and elemental composition of the thin films were analyzed respectively by FESEM and EDX attached to the microscope.

The second part of this chapter studies the effects of plasma radio frequency (RF) power on the properties of InN thin films deposited on Si (111) substrates. The objective is to investigate how the crystallinity, composition, and band gap energy of InN thin films are affected by RF power. The mechanism of changes in the films' properties will be discussed in detail.

4.2 Effects of Filament-to-Substrate Distance on the Structure, Morphology and Optical Properties of Aluminum Nitride Thin Films

Figure 4.1 shows the XRD patterns of AlN thin films deposited at different filament-to-substrate distances (d_{f-s}). The XRD pattern of the films grown at $d_{f-s} = 2.2$ cm exhibits four sharp peaks at $2\theta = 38.45^\circ$, 44.70° , 65.05° and 78.20° , which correspond to the diffraction from the metallic Al (111), (200), (220) and (311) planes. One minor peak is

also observed at 2θ of 43.40° which is assigned to (004) plane of tungsten oxide (WO_3). Furthermore, two minor peaks are detected at $2\theta = 33.35^\circ$ and 35.85° which represents the diffraction from the AlN (100) and (002) planes. These two peaks are indexed based on an AlN hexagonal wurtzite-type structure. The metallic planes shrink significantly when the distance is reduced to 1.8 and 1.4 cm and further decreasing d_{f-s} to 1.0 cm here increased the intensity of the peaks corresponding to the AlN planes. This can be explained by considering crystallography aspect of view. Due to enhanced radiant heat of the filament on the growth surface and less probability of gas-phase reactions, shorter filament-to-substrate distance provides the energy required for formation of AlN plains which is much larger than the metallic ones. As a result, more Al and N adatoms are bonded and form AlN crystalline planes.

In addition to AlN (100) and (002) planes, two more diffraction peaks, centered at 2θ of 37.55° , 59.10° and 71° , are observed from the XRD pattern of AlN films deposited at d_{f-s} of 1.0 cm, which are assigned to the AlN (101), (110) and (200) planes. The peak corresponded to AlN (200) is hardly observed possibly due the high energy required for formation of this plane (L. Guo et al., 2016). Besides, the pattern suggests that the AlN films grown at the shortest filament-substrate distances are preferentially (002) oriented. At the shorter distance, higher surface mobility is imparted to the adatoms. As mentioned in section 2.2, the energy required for growth particles to be deposited in the planes of (002), (101) and (103) are relatively larger than that needed for (100). Hence, the deposition of AlN thin films under shorter d_{f-s} is preferable for the orientation along $\langle 002 \rangle$ direction. The significant decrease in intensity of metallic peaks along with the preferential AlN growth orientation along the c-axis perpendicular to the substrate is evidence of the constructive role of the short filament-to-substrate distance in improving the crystallinity and quality of AlN.

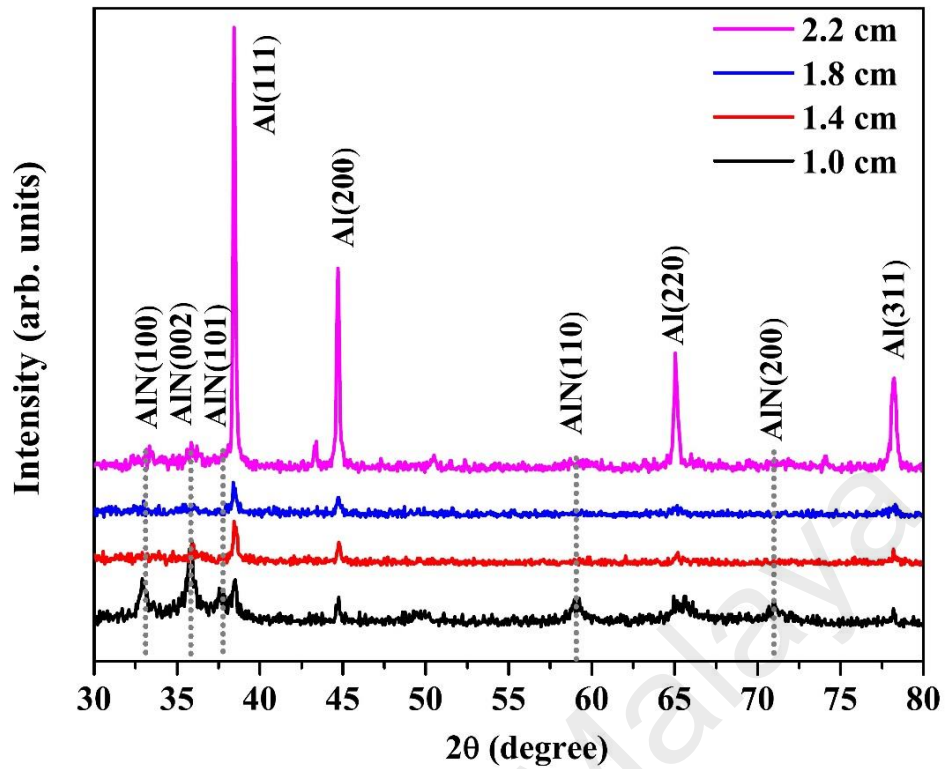


Figure 4.1: The XRD spectra of AlN thin films grown at different filament-substrate distances (d_{f-s}). Decrease in d_{f-s} shows significant decrease of intensity of metallic peaks along with preferential AlN growth orientation along the c-axis perpendicular to the substrate.

Figure 4.2 (a)-(d) show FESEM images of AlN thin films prepared at different filament-to-substrate distances. The surface morphology of the films deposited at d_{f-s} of 2.2 cm (Figure 4.2 (a)) reveals a non-uniform distribution of irregular-shaped particles over the surface. The bright color of the particles confirms that the surface is highly covered with metallic grains. At d_{f-s} of 1.8 cm (Figure 4.2 (b)), the uniformity of the morphology is improved but irregular-shaped grains are still observed. The FESEM image of the films deposited at d_{f-s} of 1.4 cm (Figure 4.2 (c)) shows that the morphology is highly uniform and spherical grains with average size of $\sim 1\mu\text{m}$ are distributed over the whole surface. By further decreasing the distance to d_{f-s} of 1.0 cm (Figure 4.2 (d)), the grains becomes excessively large (around 2 – 3 μm), mainly due to the agglomeration of smaller grains.

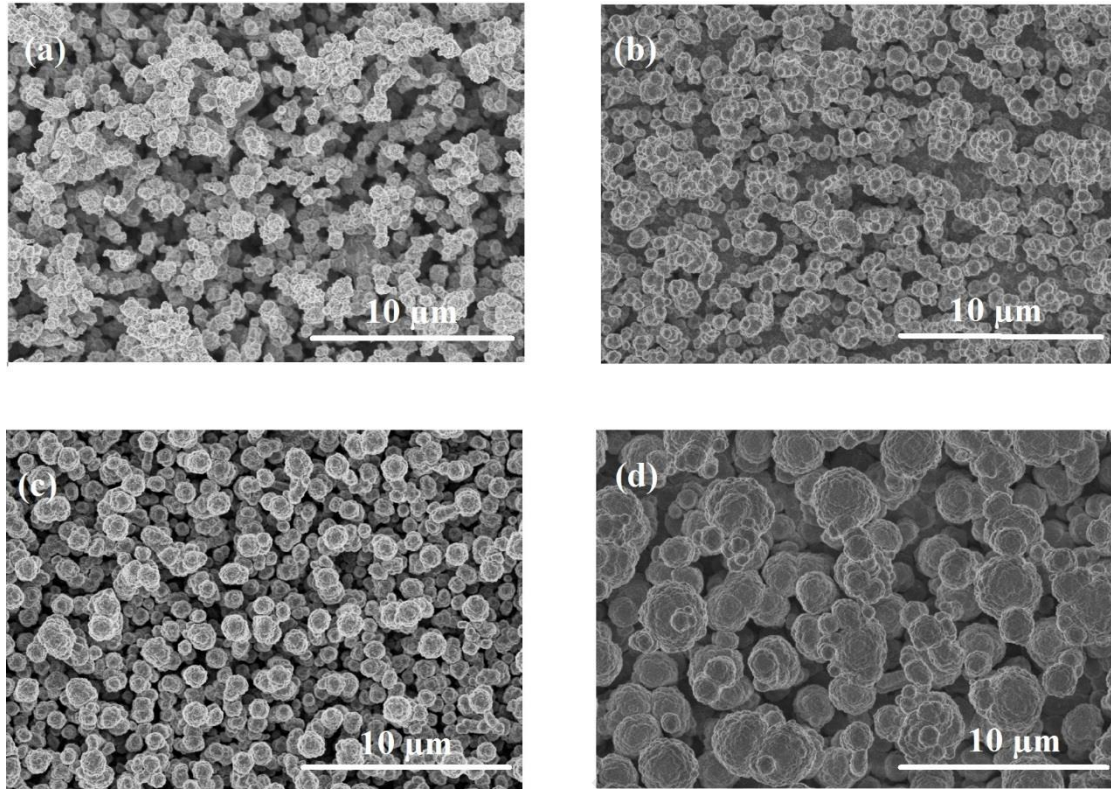


Figure 4.2: FESEM image of AlN films grown at different filament-substrate distances (d_{f-s}) (a) $d_{f-s} = 2.2$, (b) $d_{f-s} = 1.8$, (c) $d_{f-s} = 1.4$ and (d) $d_{f-s} = 1.0$ cm with $\times 5000$ magnification. Decreasing the distance the filament distance results in agglomeration of smaller grains to form cauliflower-shaped grains.

The EDX spectra of AlN thin films deposited at different filament-to-substrate distances are presented in Figure 4.3 (a) - (d). From the qualitative point of view, the spectra of all the samples show the K_{α} peaks of Al, N, O, C, and F. Carbon (C) is background signal and the origin of fluorine may be from Teflon insulating the RF electrode. Decreasing the filament-to-substrate distance from 2.2 to 1.0 cm, increases the intensity of the N peak showing that a narrow filament-substrate distance results in more nitrogen adatoms being incorporated into the grown AlN thin films.

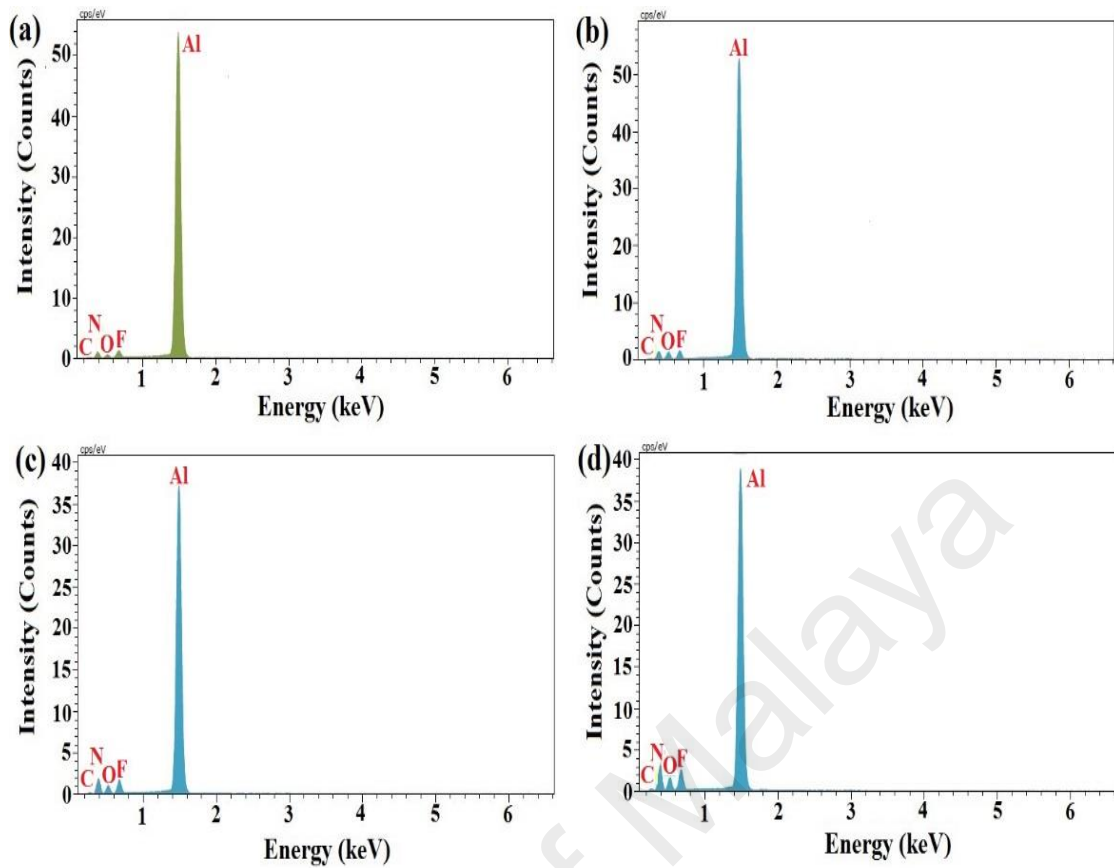


Figure 4.3: EDX spectra of AlN films deposited at different filament-substrate distances (a) $d_{f-s} = 2.2$, (b) $d_{f-s} = 1.8$, (c) $d_{f-s} = 1.4$ and (d) $d_{f-s} = 1.0$ cm. By decreasing d_{f-s} , intensity of Al decreases whereas that of N increases.

The Al to N adatom ratio in the films was obtained from the EDX study. This is of importance for the structural stability and optical properties of the thin film (Reboredo, Pizzagalli, & Galli, 2004). It should be noted that EDX does not provide sufficiently accurate information on the elemental composition and quality of the thin films. However, in this work, the EDX results were employed to compare the elemental content of the films in various growth conditions. The quantitative results are plotted in Figure 4.4 (a) where it can be clearly seen that the atomic concentration of N and Al are greatly affected with respect to d_{f-s} ; as the distance decreases, the atomic percentage of N increases, whereas that of Al declines. The N/Al ratio of the grown samples versus d_{f-s} is presented in Figure 4.4 (b). By narrowing the distance from 2.2 to 1.0 cm, the ratio is noted to be

significantly increased and a balanced composition obtained for the AlN films deposited at $d_{f-s} = 1.0$ cm.

The dependence of atomic percentage of Al and N on d_{f-s} can be related to the energy of the growth species upon reaching the substrate. As a versatile tool, the hot filament plays a key role in the growth process. It can simultaneously produce Al radicals and excited N₂ molecules through the evaporation of Al wires placed on the filament and the excitation of N₂ molecules in the vicinity of the filament, respectively (Chong, Goh, Dee, & Rahman, 2012). The heated filament also contributes to heating the surface of the growing film.

The applied RF power dissociates the excited N₂ molecules producing N radicals and ions depending on the magnitude of the applied RF power. These excited Al and N radicals then will travel towards the substrate surface and upon reaching its growth sites the surface reactions between these radicals and the substrates determine the sticking and diffusing probability of these radicals into the film structure. Narrowing the gap between the filament and substrate increases the radiant heat of the filament on the growth surface and also reduces the probability of gas-phase reactions. Thus, the impact energy of the radicals on the growth surface is increased. This increases the surface temperature and can enhance the growth rate through the higher sticking probability (Chong, Goh, Dee, & Rahman, 2013). However, the high bombardments of the growth surface with excited N atoms or ions can also have the adverse effect of sputtering of atoms on the surface. The higher mobility of the growth species on the surface of the substrate ensures that they reach suitable growth sites for diffusion. As a result, less free metallic Al adatoms are left on the surface of substrate as N atoms are bonded to the Al ones resulting in an increase in the N/Al ratio in the AlN thin films and improving of the films quality and crystallinity.

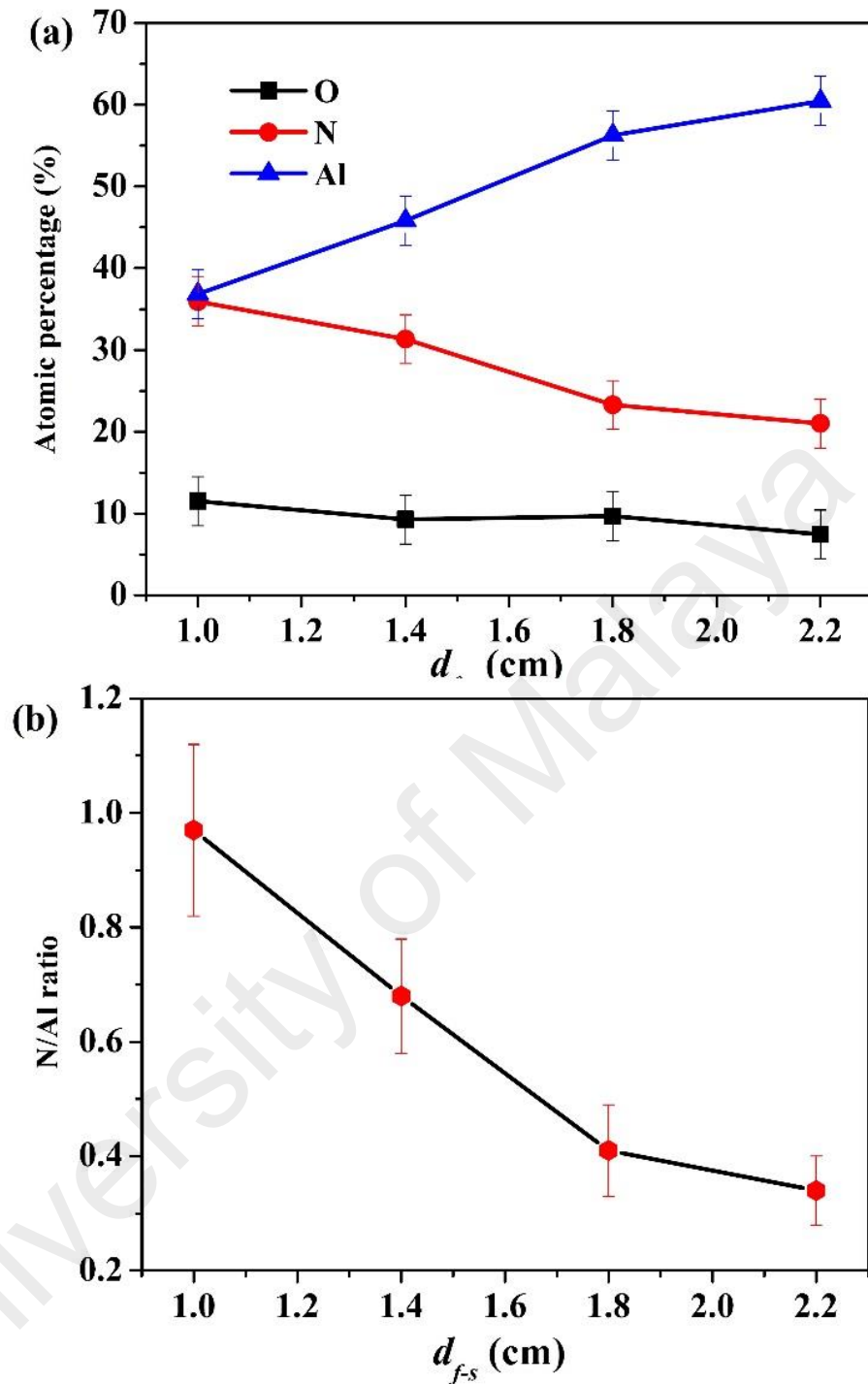


Figure 4.4: (a) Dependence of the elemental percentage of the AlN films on filament-substrate distance (d_{f-s}); (b) dependence of N/Al ratio of AlN films on d_{f-s} . The atomic concentration of N and Al are greatly affected with respect to d_{f-s} ; Decrease in d_{f-s} from 2.2 to 1.0 cm, increases the N/Al ratio to a stoichiometric value of 1. (Note: The lines joining the points are only used as a guide to the eye.)

To examine the characteristic vibration modes of the films lattice, FTIR measurements were carried out on the prepared AlN thin films. AlN has a wurtzite structure and belongs to the C_{6v}^4 space group. As mentioned earlier, based on Group theory, one A_1 , one E_1 , two E_2 , and two B_1 modes are predicted. A_1 , E_1 , and E_2 modes are Raman and infrared-active while B_1 is inactive (H. Cheng et al., 2003; Khan et al., 2013). Due to the polar behavior of the A_1 and E_1 modes, they split into longitudinal optical (LO) and transverse optical (TO) components. It is well-known that the splitting of A_1 and E_1 modes corresponds to the transverse nature of electromagnetic (E.M.) radiation. By using conventional transmission spectroscopy with normal incidence, only the TO mode of vibration interacts with E.M. However, the propagation of E.M. at an oblique angle results in the splitting of A_1 and E_1 modes into their subcomponents. According to the Berreman effect, E.M. radiation interacts perpendicular and parallel to the surface of the film in this case and are able to excite LO and TO phonon modes, respectively (Berreman, 1963). It has been reported that the appearance of the TO mode is a good indicator of the stoichiometry of the films (Singh et al., 2011).

Figure 4.5 presents the FTIR transmittance spectra of the AlN films after subtraction of the FTIR transmittance spectrum of the Si substrate. No clear absorption peak is detected from the FTIR spectrum of the AlN thin film grown at $d_{f-s} = 2.2$ cm. The presence of excessive metallic aluminum in the film's structure (as deduced from XRD (Figure 4.1) and EDX (Figure 4.3) measurements) is perhaps the main reason for such poor absorption. By decreasing the gap to 1.8 cm, a broad absorption peak appears in the range of $400 - 1000 \text{ cm}^{-1}$ and the intensity of this peak increases significantly when the distance is further decreased to 1.4 and 1.0 cm. The observed strong absorption peak was found to be a feature of AlN films.

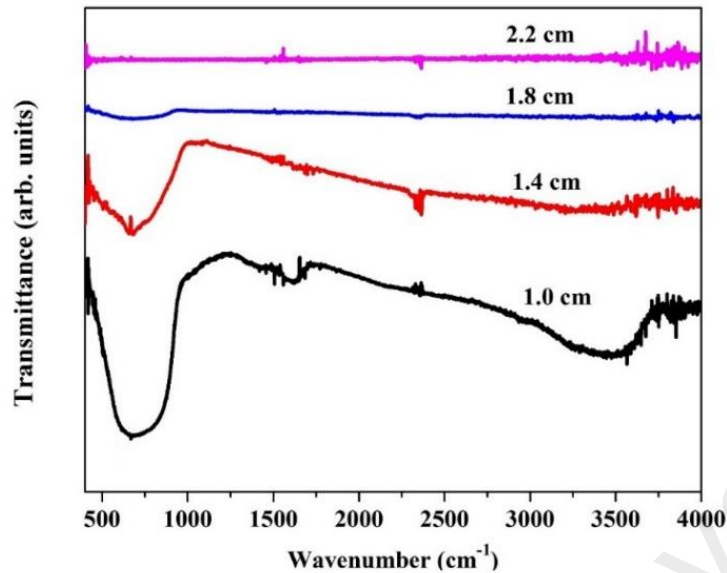


Figure 4.5: FTIR spectra of AlN films grown at various filament-substrate distance (d_{f-s}). A strong absorption peak corresponding to a feature of AlN films is observed at $d_{f-s} = 1.0$ cm.

The broadness of the peak shows that it is composed of few phonon modes. In order to better examine the contribution of the constituent phonon modes in the FTIR spectra, the curve-fitting technique was employed on the observed peaks for the samples deposited at $d_{f-s} = 1.8, 1.4$, and 1.0 cm as shown in Figure 4.6. The FTIR spectra present five main sub-peaks (labeled as 1-5), which are centered at around 590, 665, 745, 855 and 900 cm^{-1} , respectively. The sub-peaks 1, 2, 4, and 5 are attributed to the A_1 (TO), E_1 (TO), A_1 (LO) and E_1 (LO) vibration modes of AlN, respectively (Jagannadham, Sharma, Wei, Kalyanraman, & Narayan, 1998; Ng, Ooi, Lee, Hassan, & Abu Hassan, 2012; Vijayalakshmi & Pillay, 2014). The remaining sub-peak 3 is mainly due to the stretching vibrations of Al–N bonds (Xin et al., 2000). The dependence of absorbance intensity of sub-peak 3 (as a characteristic of AlN) on d_{f-s} is shown in Figure 4.7. By increasing the distance, the intensity of stretching vibration of Al – N bonds decreases dramatically which confirms that at a larger d_{f-s} fewer Al–N bonds are formed due to insufficient energy of adatoms/ions reaching the growth sites for an effective surface reaction to form

AlN. The FTIR spectra are in good agreement with XRD and EDX results showing that a narrow filament-to-substrate distance results in the formation of better quality AlN films by using plasma-assisted reactive evaporation.

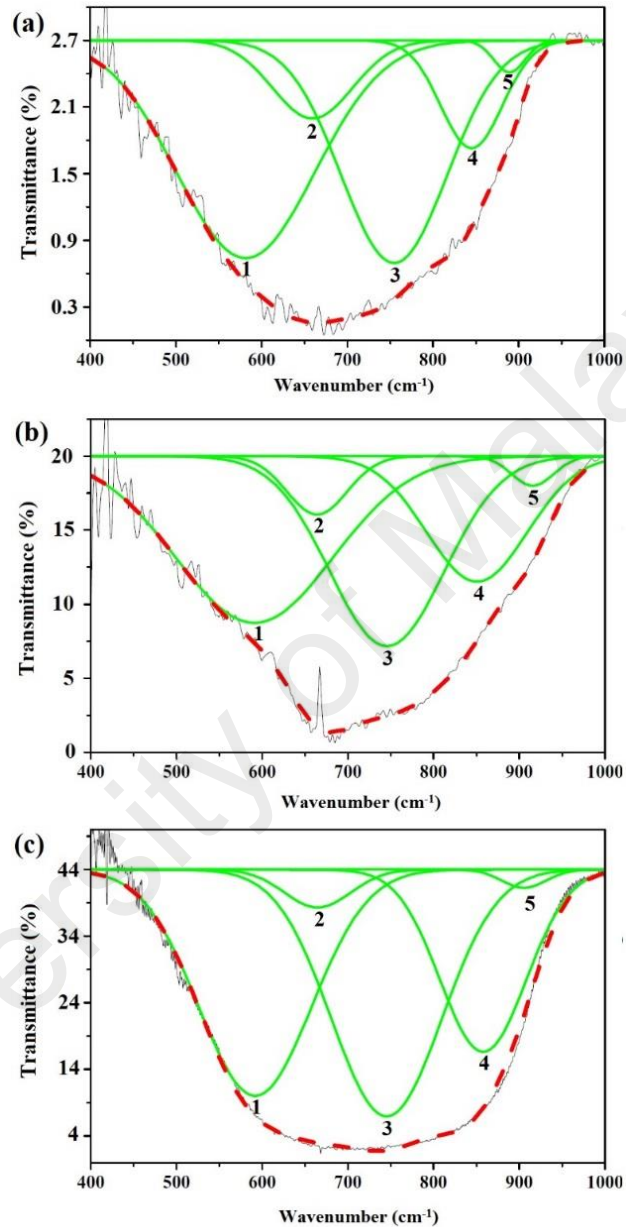


Figure 4.6: Curve-fitting results for the AlN films grown at various filament-substrate distance (a) $d_{f-s} = 1.8$, (b) $d_{f-s} = 1.4$ and (c) $d_{f-s} = 1.0$ cm. The sub-peaks 1, 2, 4, 5 are attributed to $A_1(\text{TO})$, $E_1(\text{TO})$, $A_1(\text{LO})$ and $E_1(\text{LO})$ vibration modes of AlN, respectively. The sub-peak 3 is due to bond stretching vibration of Al–N bonds. The intensity of sub-peak 3 (bond stretching vibration of Al–N bonds) is increased by decreasing d_{f-s} .

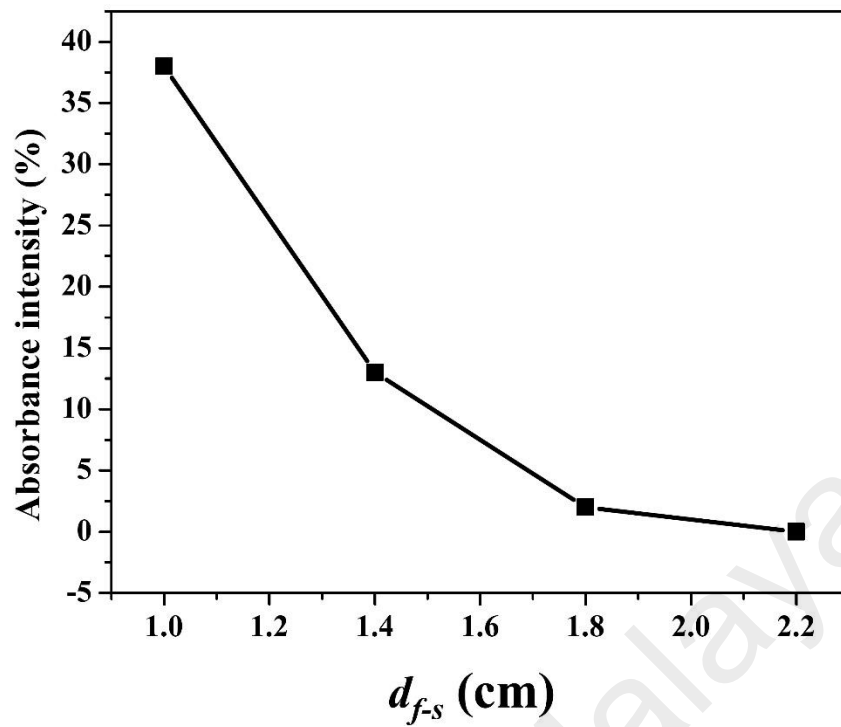


Figure 4.7: Dependence of intensity of bond stretching vibration of Al–N bonds on filament-substrate distance (d_{f-s}). The intensity of bond stretching vibration of Al–N bonds is increased by decreasing d_{f-s} .

4.3 Effects of RF Power on Crystallinity, Morphology, Composition and Optical Properties of Indium Nitride Thin Films

Figure 4.8 shows the XRD patterns of InN samples prepared at different RF powers (50–250 W). Five major peaks are observed from the XRD pattern of the InN films deposited at RF power of 50 W. The peaks centred at $2\theta = 30.50^\circ$, 35.40° , 50.90° and 60.70° are assigned to (222), (400), (440) and (622) planes of cubic indium oxide, respectively (Jothibas et al., 2013). The peak at $2\theta = 33^\circ$ corresponds to (101) plane of InN clearly indicating the existence of nitride- and oxide- phases in the InN film deposited at the RF power of 50 W. The XRD pattern of the samples deposited at the RF powers of 100, 150, 200 and 250 W shows diffraction peaks at $2\theta = 29.10^\circ$, 31.15° , 33° , 43° , 52° , 56.65° , 61.45° and 62.60° that corresponds to the (100), (002), (101), (102), (110), (103), (112) and (201) planes of wurtzite InN, respectively. The peak positions are in

agreement with those reported in the literature (Amirhoseiny, Ng, & Hassan, 2015; Barick & Dhar, 2015; Biju & Jain, 2008; Terziyska, Butcher, Rafailov, & Alexandrov, 2015) and the corresponding miller indexes were labeled near the peaks. The strongest peak, (101), corresponds to the hexagonal InN; hence it can be concluded that most of the films are of hexagonal InN structure. As RF power increases, the (101) plane intensity first increases and reaches a maximum at 200 W and then decreases, possibly due to the effect of elevated re-sputtering rates at high RF power. Therefore, high RF power induces a high sputtering rate which exceeds the growth rate. The high intensity of the diffraction peaks for the film deposited at 200 W indicates higher crystallinity. Higher RF power results in increased kinetic energy of the deposited species upon reaching to the substrate surface. Thus, at this condition local heating of top-most layers of the substrate is enhanced and the primary nuclei are able to move within a certain distance on the substrate surface to find an optimal site that matches its crystal structure resulting in improved crystallinity.

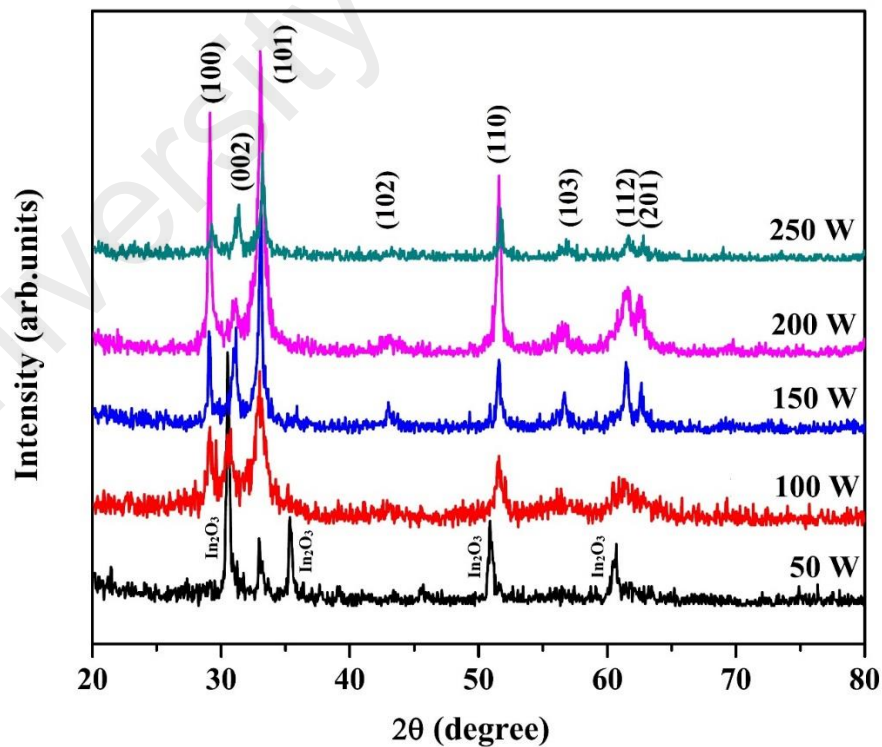


Figure 4.8: XRD patterns of the InN films grown at different RF powers. The crystallinity of InN films is improved by increasing the RF power up to 200 W.

Figure 4.9 shows the micro-Raman spectrum of InN thin films that were deposited at various RF powers in the spectrum range of 100-900 cm^{-1} . For all measurements, the incident beam of the laser is normal to the surface. InN has a wurtzite structure and belongs to the C_{6v}^4 space group. The micro-Raman spectra of all the films deposited at various RF powers reveal a broad peak observed between 170–215 cm^{-1} with a center maximum at 190 cm^{-1} which is assigned to the B_2 (low) phonon mode of InN (Inushima, Shiraishi, & Davydov, 1999; Lee et al., 1998). This region is dominated by the overtones of acoustic phonon modes. In addition, the Raman spectra for all samples show one major peak (at around 570 cm^{-1}) and one shoulder (at around 490 cm^{-1}) that corresponds to the A_1 (LO) and E_2 (high) phonon modes of InN, respectively (Barick & Dhar, 2015). E_2 (High) and A_1 (LO) modes show broadening and almost merge into a single wide mode suggesting the presence of an amorphous state with short-range order.

Lee et al. reported that for InN samples grown at temperatures lower than 400 °C, the structural disorder and sample roughness become more pronounced (Lee et al., 1998). The Raman spectra of all samples are very similar, although the XRD spectrum of the sample deposited at 50 W is quite different from others. This inconsistency can be explained by taking into account the vibrational phonon modes of cubic indium oxide. In–O phonon vibration mode (as a characteristic of cubic In_2O_3) is also at around 490 cm^{-1} (Yunxia Chen, Zhou, Zhao, He, & Gu, 2008). Therefore, the observed shoulder at around 490 cm^{-1} in the Raman spectrum of the films that was deposited at 50 W is possibly due to overlapping of In–O phonon vibration and InN E_2 (high) modes.

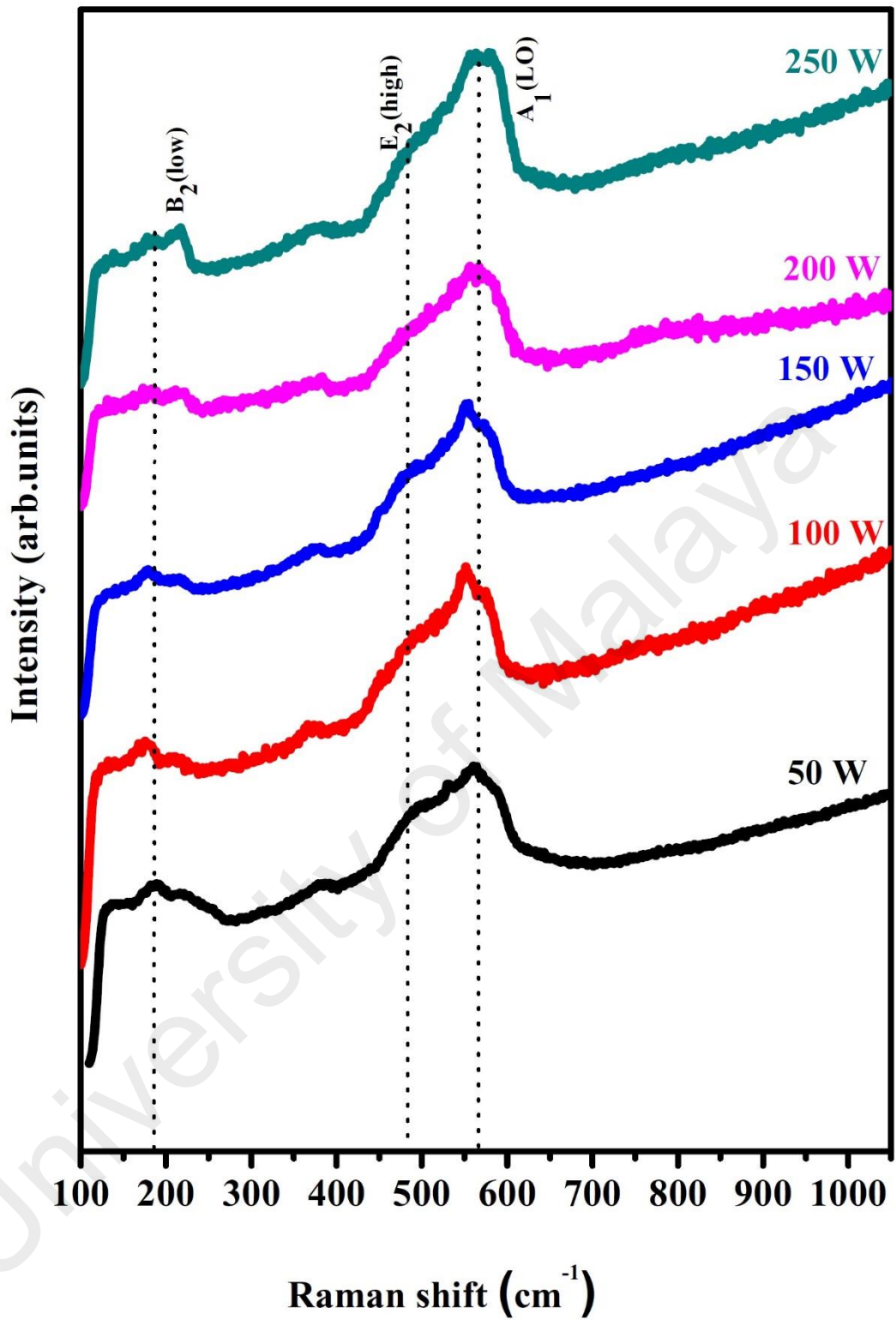


Figure 4.9: Raman spectra of the InN thin films that were deposited at different applied RF powers. $B_2(\text{low})$, $E_2(\text{high})$ and $A_1(\text{LO})$ phonon modes of InN are observed from the Raman spectra.

FESEM results of InN thin films deposited on Si (111) substrate are shown in Figure 4.10 (a)-(e). The results clearly indicate that the surfaces of all the InN films are extremely rough. FESEM results of all the samples show agglomeration of InN grains resulting in the formation of excessively large grains. The film deposited at 50 W (Figure 4.10 (a)) shows irregular-shaped grainy structures with size of 300 – 600 nm. The density of agglomeration is high due to the low surface temperature at low RF power which leads to less kinetic energy of adatoms. Adatoms tend to agglomerate before they find a suitable site for growth because of low kinetic energy. As RF power increases, the films still show agglomeration tendencies but their compactness or density is less than the sample prepared at 50 W due to a higher surface temperature which increases the kinetic energy of adatoms.

The surface morphology of InN thin film prepared at 100 W (Figure 4.10 (b)) shows the formation of grains of uniform size ($\sim 300 - 400$ nm) and shape, whereas the images of the sample prepared at RF power above 100 W (i.e. 150, 200 and 250 W) show clear hexagonal-faceted morphology and the size of the crystals increases when the RF power is increased up to 200 W. The grain size in the films deposited at 150 W (Figure 4.10 (c)) is in the range of 200 – 300 nm. . Due to increase in surface temperatures as a result of the effective bombardment from the plasma environment, the agglomeration effect is significantly enhanced for the sample grown at RF power of 200 W (Figure 4.10 (d)) which results in larger grains of size of 500 – 1000 nm. However, by further increasing RF power to 250 W (Figure 4.10 (e)) the N atom and ion bombardments also induce re-sputtering of the growing film resulting in a decrease in the grain sizes to around 300 – 500 nm. This agrees with the XRD results which show a decrease in the crystallinity of the films prepared at RF power above 200 W.

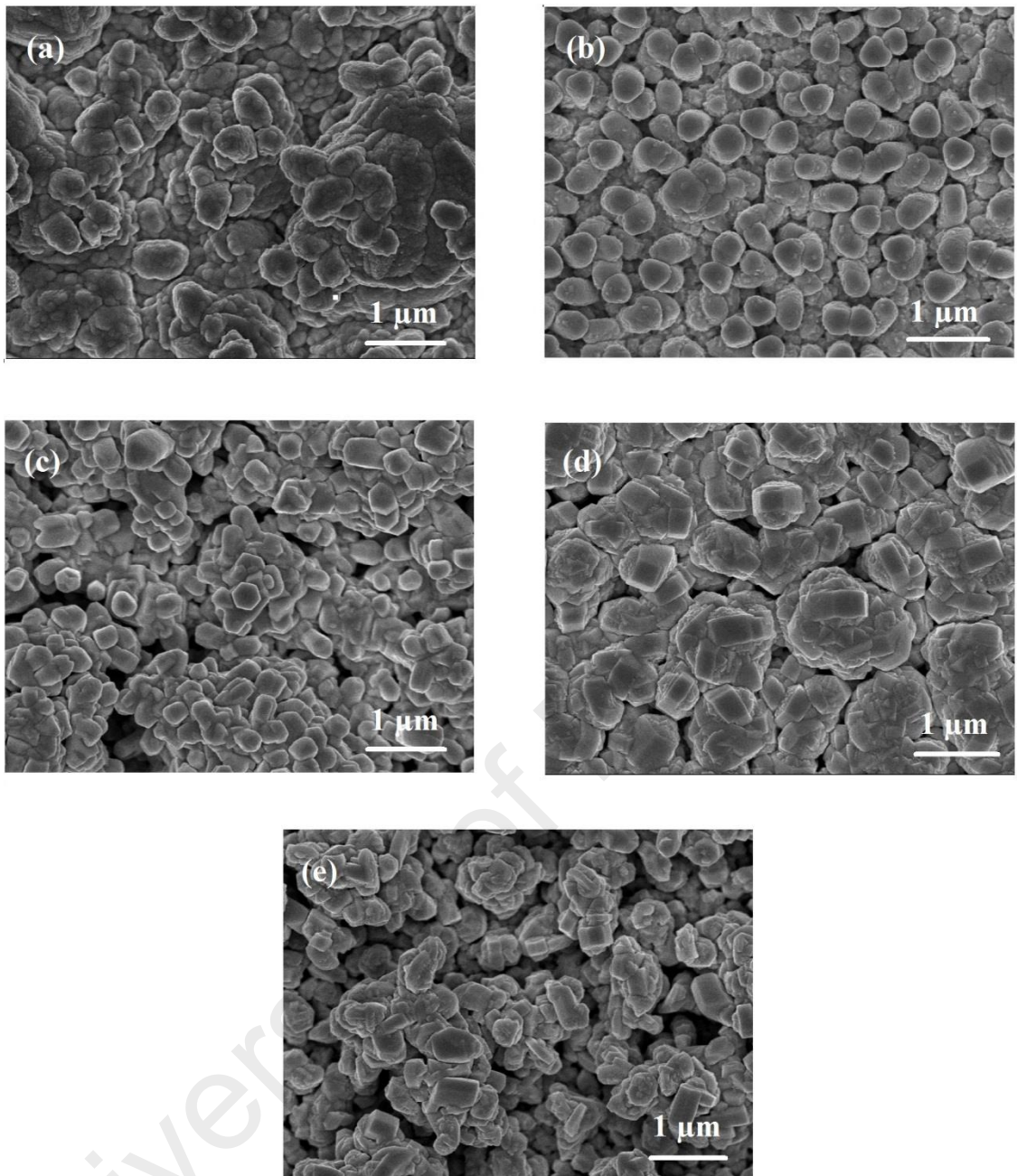


Figure 4.10: FESEM images of the InN thin films grown at the applied RF powers of 50 W (a), 100 W (b), 150 W (c), 200 W (d) and 250 W (e) with $\times 20000$ magnification. FESEM results of all the samples showed agglomeration of InN grains.

Figure 4.11 shows the elemental composition of all the samples determined from the EDX analysis. From the qualitative point of view, the spectra of the samples show the presence of In, N, and O which are the main compositional elements in the film structure. It can be clearly seen that the atomic concentration of N and O are greatly affected in relation to RF power. As the RF power increases, the atomic percentage of N increases while the O percentage decreases. The oxygen concentration in the samples is relatively high and it has been reported that the oxygen mainly resides at the grain boundaries or on the surface (S. Kumar, Li Mo, Motlan, & Tansley, 1996). The increase of RF power leads to a higher dissociation of nitrogen molecules resulting in the formation of InN and also a reduction in oxygen contamination in the grown films. The growth of InN by plasma-assisted reactive evaporation provides control over the nitrogen incorporation into the film structure by controlling the plasma power. The impinging energy of nitrogen ions/atoms reaching the growth surface also increases with the increase of the RF power from 50 to 200 W. This increases the mobility of nitrogen adatoms on the growth surface which ensures that the N adatoms reach favorable growth sites for InN growth. As a result, the probability where bonding of In and O atoms decreases have led to a decrease in O contamination in the film structure.

Biju and Jain (Biju & Jain, 2008) reported an increase in nitrogen incorporation in their InN films that were grown using the modified reactive evaporation (MARE) system where the substrate is placed on the RF-biased cathode. However, further increase of RF power to 250 W slightly increases the oxygen content. The high RF power increases the energy of the nitrogen atoms/ions impinging on the growth surface to a value which increases the sputtering rate of nitrogen atoms from the growth surface. It also reduces the sticking probability of the nitrogen atoms thus leaving the metallic indium atoms free to bond with residual oxygen atoms in the plasma.

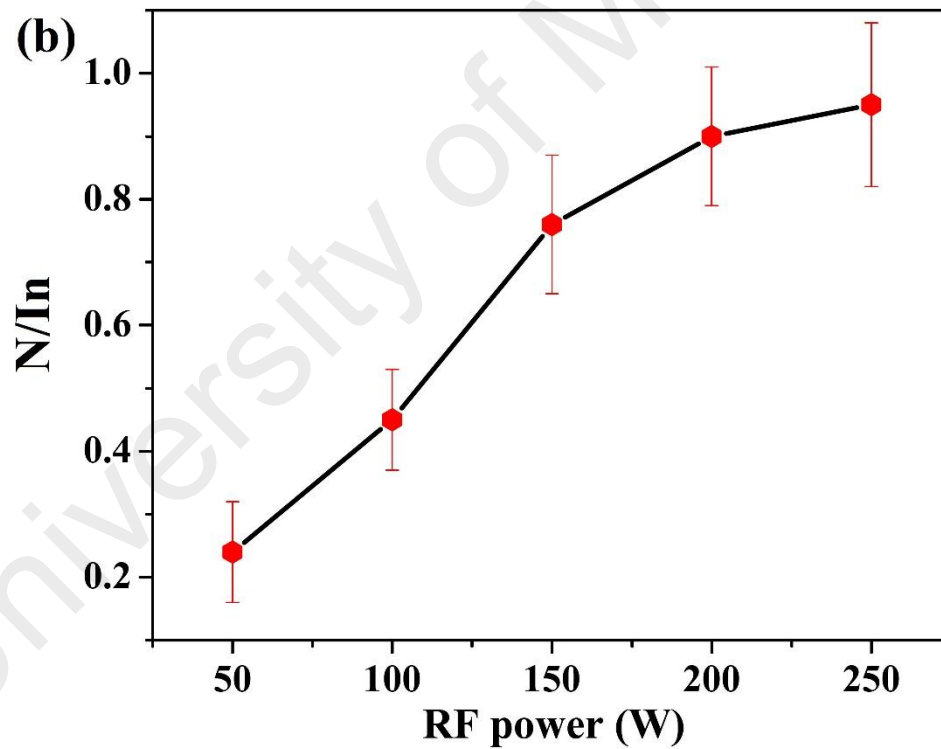
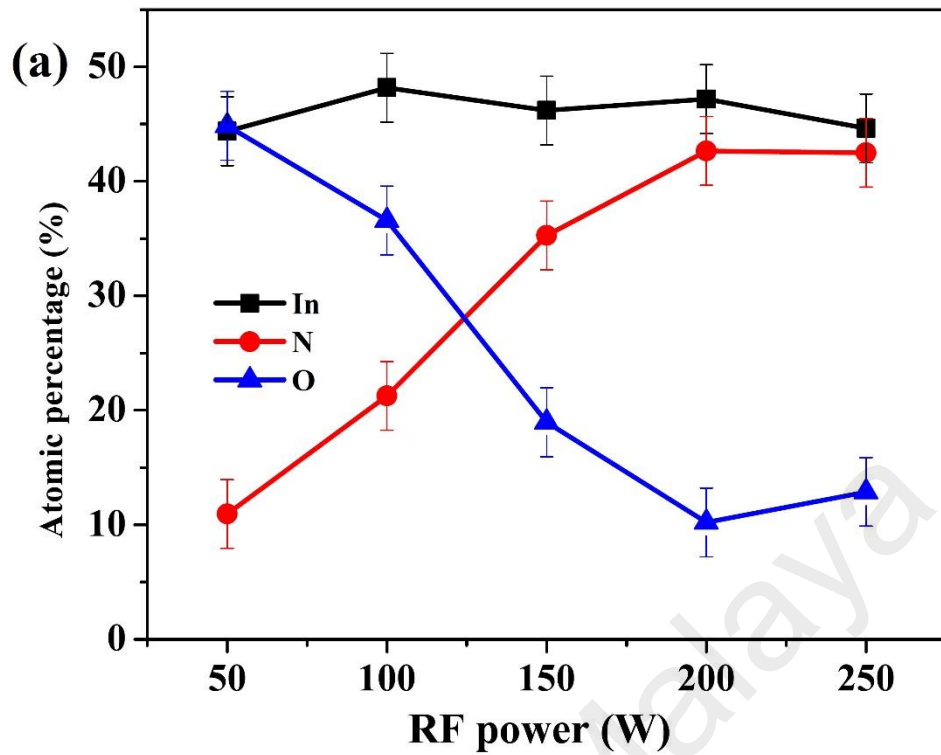


Figure 4.11: (a) Dependence of the elemental percentage of the InN films on RF power; (b) dependence of N/In ratio of AlN films on RF power. The atomic concentration of N and Al are greatly affected with respect to RF power.

Increase in RF power from 50 to 250 W, increases the N/In ratio to a stoichiometric value of 1. (Note: The lines joining the points are only used as a guide to the eye.)

In order to obtain the optical band gap of the InN films, the deposition was performed on quartz substrates. Figure 4.12 displays the plots of $(\alpha hv)^2$ versus photon energy (hv) where α is the absorption coefficient at the specified photon energy. Due to rough surface of the grown films, a very weak reflectance was observed for the films. Hence α was calculated by using the transmission and thickness of the films ($\alpha = -(1/d)\ln[T]$) (Q. Guo et al., 2008). The value of the optical band gap is determined by extrapolating the linear part of the curve to the energy axis in Figure 4.12.

The thickness and obtained band gap energy of each sample are summarized in Table 4.1. The optical band gap energy (E_g) of the films deposited at 100, 150, 200 and 250 W are 2.28, 2.28, 2.18 and 2.13 eV, respectively. These values are close to the E_g of polycrystalline InN as previously reported (K. S. A. Butcher & Tansley, 2005). The obtained values are larger than the recently reported band gap energy value of pure InN (e. g., 0.7 eV). As reported by other researchers, possible reasons for the high band gap value are the Moss-Burstein (MB) shift, the presence of oxygen impurity, and other stoichiometry-related defects (T. Matsuoka et al., 2004; T. V. Shubina et al., 2004; Sundaresan, Vasumathi, Ravichandran, Ravikumar, & Sakthivel, 2012). The sample deposited at 50 W shows largest band gap value which equals to 2.35 eV. This is probably due to the very high oxygen content and formation of oxynitride alloys within the films (Alexandrov, Butcher, & Wintrebert-Fouquet, 2004). Segregated oxygen species could substitute N atoms as InO and form $\text{InO}_y\text{N}_{1-y}$ alloys resulting in the higher band gap values of the films especially for those deposited at the lowest RF power of 50 W, which has the highest oxygen impurities in the film structure.

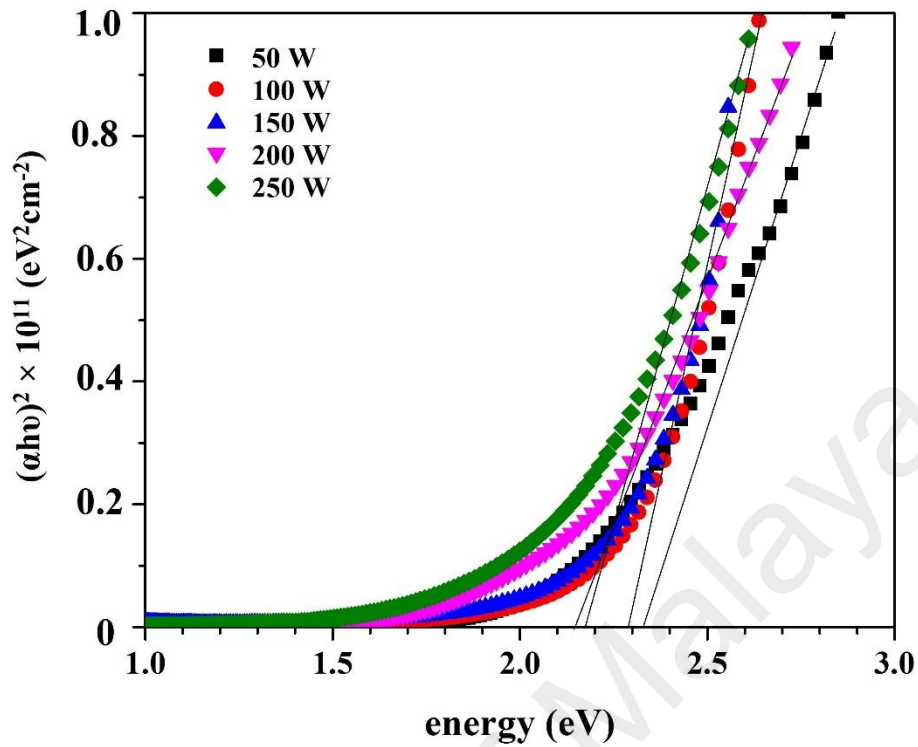


Figure 4.12: Plots of $(\alpha hv)^2$ versus hv for the InN thin films grown at various applied RF powers. The value of the optical band gap is determined by extrapolating the linear part of the curve to energy axis

Table 4.1: The thickness and band gap energy values of InN films deposited at various RF powers. The band gap values (E_g) are close to that of polycrystalline InN.

| RF power | Thickness | Band gap energy |
|----------|-----------|-----------------|
| (W) | (nm) | (eV) |
| 50 | 840 | 2.35 |
| 100 | 710 | 2.28 |
| 150 | 650 | 2.28 |
| 200 | 630 | 2.18 |
| 250 | 580 | 2.13 |

4.4 Summary

In this chapter the results associated with the growth of AlN and InN thin films by plasma-assisted reactive evaporation were presented and discussed. It was shown that filament-to-substrate distance and plasma RF power are the most dominant parameters which have great impacts on the properties of AlN and InN thin films, respectively. The XRD results of AlN thin films showed that by decreasing the distance, the intensity of the peak corresponding to metallic Al decreases while that of AlN increases. EDX results indicated that at lower filament-to-substrate distance, the incorporation of N into the AlN films is enhanced and this was further confirmed by FTIR results. Also, the surface morphology of the AlN thin films grown at the low distance is more uniform. Increasing RF power resulted in the improved crystallinity of the InN films and also reduced the oxygen impurities in the films. Large deviation from the reported value was observed for the band gap energy of the InN films that were grown by plasma-assisted reactive evaporation which was attributed to the Moss-Burstein (MB) shift and the presence of oxygen impurities in the films.

CHAPTER 5:

ALUMINUM INDIUM NITRIDE THIN FILMS: STRUCTURE, MORPHOLOGY AND OPTICAL PROPERTIES

5.1 Introduction

This chapter discusses the results of the studies on aluminum indium nitride ($\text{Al}_x\text{In}_{1-x}\text{N}$) thin films that were deposited by plasma-assisted dual source reactive evaporation. The voltage applied to the filament holding the indium wire (V_{In}) and the nitrogen flow rates appeared to be the most critical parameters in influencing the properties of the produced thin films. In the first part of this chapter, the effects of V_{In} on the properties of $\text{Al}_x\text{In}_{1-x}\text{N}$ thin films are discussed in regard to their structural, compositional, morphological, and optical characteristics. The objective is to establish the role of V_{In} in tuning the Al composition in the films. The second part of this chapter discusses the effects of nitrogen flow rates on the properties of the two sets of films categorized as In-rich and Al-rich $\text{Al}_x\text{In}_{1-x}\text{N}$ thin films selected for the study. The final part of this chapter is devoted to the study of the effects of annealing on the properties of the selected $\text{Al}_x\text{In}_{1-x}\text{N}$ thin films. The objective of this study is to investigate the stability of the properties of the films and the incorporation of oxygen impurity in their structures at elevated temperatures. The results are useful in determining the temperature range which is suitable for application of the $\text{Al}_x\text{In}_{1-x}\text{N}$ thin films deposited by this technique in various opto-electronic devices.

5.2 The Role of Filament Temperature on the Growth of Aluminum Indium Nitride Thin Films

The elemental composition of the $\text{Al}_x\text{In}_{1-x}\text{N}$ films deposited at different applied voltages (V_{In}) was analyzed using x-ray photoelectron spectra (XPS). The $\text{In}3d_{5/2}$ core-level photoelectron spectra of the $\text{Al}_x\text{In}_{1-x}\text{N}$ films prepared at $V_{\text{In}} = 65$ to 80 V are shown

in Figure 5.1. A significant increase in the intensity of the In3d_{5/2} core-level is observed when V_{In} is increased, implying that higher amounts of In adatoms were incorporated into the Al_xIn_{1-x}N film structure at higher voltages. The core-level photoelectron spectra for all samples were deconvoluted into three main sub-peaks centered at 445.3 eV, 444.3 eV and 443.3 eV which are attributed to In–O, In–N and In–In bonds, respectively (A. K. S. Chauhan, Kumar, & Gupta, 2015; Lebedev et al., 2006). The corresponding Al2p core-level photoelectron spectra of Al_xIn_{1-x}N films deposited at V_{In} = 65 to 80 V are presented in the inset of Figure 5.1 (a)-(d). All the spectra were also deconvoluted into three main components at 75 ± 0.2 eV, 74 ± 0.1 eV and 72.6 ± 0.2 eV which are assigned to Al–O, Al–N and Al–Al bonds, respectively (Rosenberger, Baird, McCullen, Auner, & Shreve, 2008; You, Ito, Tu, & Goto, 2013). The appearance of In–In, In–O, Al–Al and Al–O bonds could be due to the higher concentrations of reactive In and Al atoms reaching the growth sites as-compared to the reactive N atoms and the high affinity of the metallic adatoms to oxygen. An analysis on the chemical composition of the films revealed that the estimated Al mole fractions (Al composition) in the Al_xIn_{1-x}N films, *x*, are 0.64, 0.60, 0.18 and 0.10 as determined from the ratio of the area of the Al–N and In–N peaks (Al–N/(Al–N+ In–N)) (Suzuki et al., 2013)) for the films deposited at V_{In} of 65, 70, 75 and 80 V, respectively.

Figure 5.2 displays the dependence of F_{In} temperature and aluminum incorporation into the composition of the films on the applied voltage to F_{In} (V_{In}). A rise from 1010 ± 10 °C to 1105 ± 10 °C was recorded in the F_{In} temperature by increasing V_{In} from 65 to 80 V, which clearly shows that V_{In} controlled the F_{In} temperature. The increase in the F_{In} temperature have resulted in enhanced generation and deposition of reactive indium atoms at the substrate surface and, hence, decreased the aluminum mole fraction (*x*) in the films' composition. Guo *et al.* (Q. X. Guo et al., 2007) reported similar tuning

capability of the Al composition in $\text{Al}_x\text{In}_{1-x}\text{N}$ films by varying the applied RF power to the indium target using the sputtering technique.

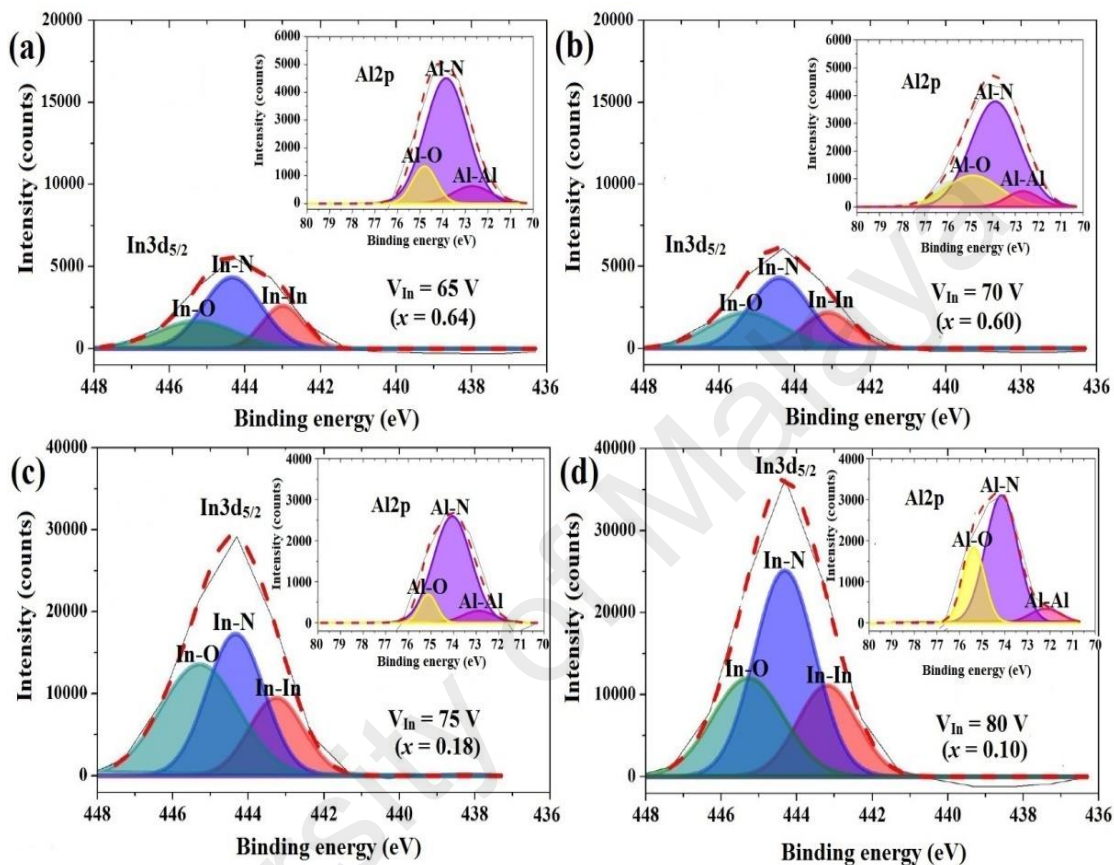


Figure 5.1: $\text{In}3d_{5/2}$ core-level photoelectron spectra of $\text{Al}_x\text{In}_{1-x}\text{N}$ films deposited at $V_{\text{In}} = 65$ (a), 70 (b), 75 (c) and 80 V (d). The inset of (a), (b), (c) and (d) are the corresponding $\text{Al}2p$ core-level photoelectron spectra. A significant increase in the intensity of $\text{In}3d_{5/2}$ core-level is observed when V_{In} is increased.

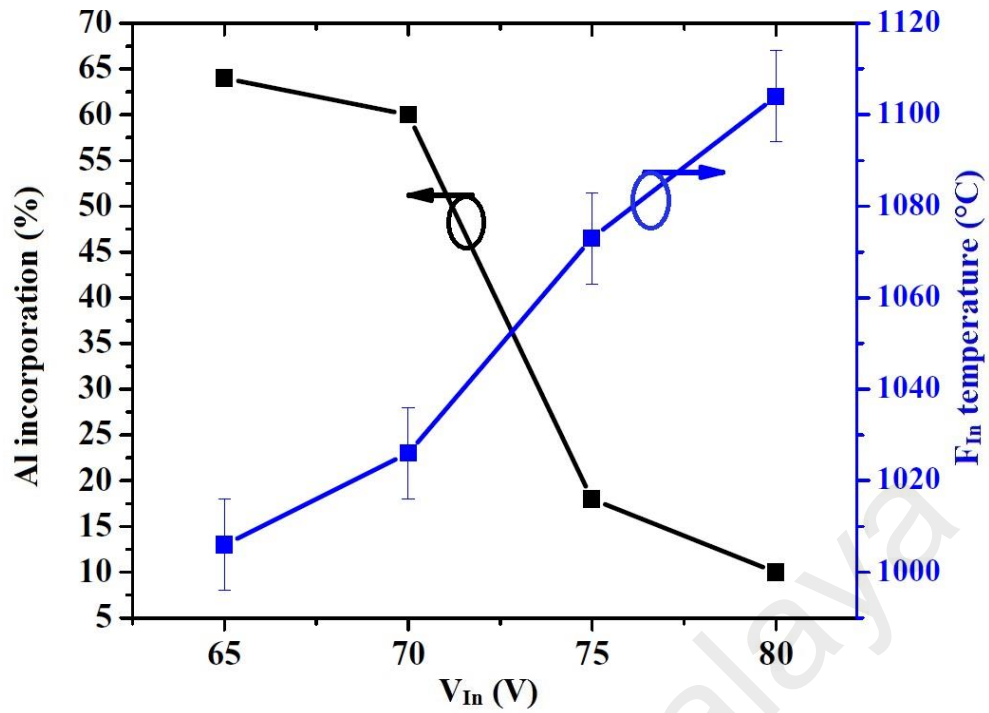


Figure 5.2: Dependence of Al composition in the $Al_xIn_{1-x}N$ films and F_{In} temperature on the applied AC voltage to the filament holding indium wire. The increase in temperature of the filament holding In wire results in decrease in Al incorporation in the $Al_xIn_{1-x}N$ films. (Note: The lines joining the points are only used as a guide to the eye.).

Figure 5.3 shows the X-ray diffraction (XRD) spectra of $Al_xIn_{1-x}N$ films that were deposited at different V_{In} . The spectra of the films grown at $V_{In} = 65, 70,$ and 75 V show no diffraction peaks that can be assigned to the crystalline $Al_xIn_{1-x}N$. The XRD pattern of the films deposited at the highest V_{In} of 80 V shows a small broad peak at $2\theta = 31.30^\circ$ which is very close to the position of the (002) plane of wurtzite $Al_{0.10}In_{0.90}N$ based on Vegard's law:

$$c_{Al_xIn_{1-x}N} = xc_{AlN} + (1 - x)c_{InN}, \quad (5.1)$$

where $c_{AlN} = 5.012 \text{ \AA}$ and $c_{InN} = 5.793 \text{ \AA}$ are the c lattice constants of crystalline AlN and InN, respectively (Angerer et al., 1997; Darakchieva et al., 2008). Interestingly, there is a good agreement between the Al composition (x) calculated from XPS analysis in this work ($x = 0.10$) and that obtained from Vegard's law ($x = 0.11$).

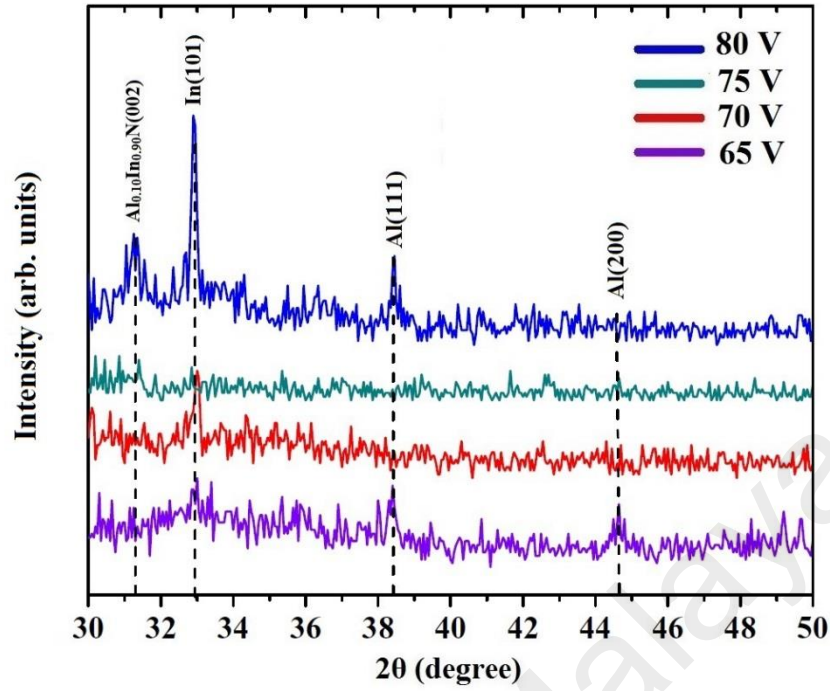


Figure 5.3: XRD pattern of the Al_xIn_{1-x}N thin films grown at different applied AC voltage to the filament holding (V_{In}). No diffraction peaks assigned to crystalline Al_xIn_{1-x}N is observed for the films deposited at V_{In} = 65, 70 and 75 V.

Phases of In- and Al-crystalline grains are observed from XRD spectra of the films grown at V_{In} of 65, 70 and 80 V. The presence of these metallic phases was also deduced from the XPS spectra of the films. Basically, the films studied in this work are amorphous in structure with the presence of In- and Al-crystalline grains scattered within the amorphous matrix of the AlInN structure.

Figure 5.4 (a) shows the Raman spectra for Al_xIn_{1-x}N films with different aluminum mole fractions (*x*). For reference and comparison, the Raman spectrum of the AlN films (grown at V_{In} = 0) is presented in Figure 5.4 (b). Two major peaks centered at 502 and 580 cm⁻¹ are observed in Raman spectrum of Al_{0.10}In_{0.90}N films. These peaks are assigned to E₂(high) and A₁(LO) phonon modes of the In-rich AlInN films (Kang, Hashimoto, & Yamamoto, 2009; H. F. Liu, Li, Ansah Antwi, Chua, & Chi, 2014). The

peaks are slightly blue-shifted when the aluminum incorporation is increased to 0.18. With further increases of the aluminum composition to $x = 0.60$ and 0.64 , the shift becomes more pronounced and the $E_2(\text{high})$ peaks appear at 609 and 617 cm^{-1} , respectively. By taking into account the E_2 (high) phonon mode of the grown AlN films centered at 665 (X. Li et al., 2013) (see Figure 5.4 (b)), it can be seen that the $E_2(\text{high})$ modes of $\text{Al}_{0.60}\text{In}_{0.40}\text{N}$ and $\text{Al}_{0.64}\text{In}_{0.36}\text{N}$ thin films were red-shifted by 56 and 48 cm^{-1} , respectively. Uniquely, the Raman spectra of $\text{Al}_{0.60}\text{In}_{0.40}\text{N}$ and $\text{Al}_{0.64}\text{In}_{0.36}\text{N}$ films reveal one hitherto unknown Raman feature located at around 500 cm^{-1} (labeled as *) which was detected by repeated micro-Raman spectroscopies at various test points. As it was also observed in the Raman spectrum of AlN samples (Figure 5.4 (b)), it cannot be assigned to any $E_2(\text{high})$ mode. This peak does not seem to correspond to the allowed Raman modes of hexagonal AlN based on group theory and may be related to the acoustic phonon modes of AlN (Hobert, Dunken, Meinschien, & Stafast, 1999).

A broad peak at around 800 cm^{-1} was detected from the Raman spectra of the AlInN films with Al compositions of $x = 0.60$ and 0.64 which could have been formed due to the overlapping of some Raman structures. In order to identify each of the contributions, the Raman spectrum of $\text{Al}_{0.64}\text{In}_{0.36}\text{N}$ films was analyzed in the $670 - 900 \text{ cm}^{-1}$ range using the curve-fitting method (Figure 5.4 (c)). The observed broad peak at around 800 cm^{-1} was deconvoluted into two main components at around 740 and 820 cm^{-1} , which are assigned to InN-like $A_1(\text{LO})$ and AlN-like $A_1(\text{LO})$ phonon modes of AlInN, respectively (Jiang, Kong, Shen, & Guo, 2011; Kang, Hashimoto, et al., 2009) as shown in Figure 5.4 (c). Kang *et al.* (Kang, Hashimoto, et al., 2009) and Jiang *et al.* (Jiang et al., 2011) reported similar behavior where the $A_1(\text{LO})$ phonon mode of their $\text{Al}_x\text{In}_{1-x}\text{N}$ films with $x \geq 0.30$ exhibited two-mode behavior. However, the $A_1(\text{LO})$ phonon modes in InGaN and AlGaN wurzite structures have been shown both theoretically (Yu et al., 1998) and experimentally (Demangeot et al., 1998; Q. Guo et al., 2014) to exhibit one-

mode behavior. The different behavior of the $A_1(\text{LO})$ phonon mode in AlInN as compared to those in InGaN and AlGaN can be attributed to various values of A_1 reststrahlen band for InN, AlN and GaN (Kang, Hashimoto, et al., 2009). The A_1 reststrahlen band refers to the phonon frequency region from $A_1(\text{TO})$ to $A_1(\text{LO})$ which is 447–580, 531–734, and 611–880 cm^{-1} for InN, GaN, and AlN, respectively. The A_1 reststrahlen band of GaN is somehow close to that of AlN while the band of InN remarkably overlaps that of GaN but is so narrow that it does not overlap that of AlN. This satisfactorily explains why $A_1(\text{LO})$ obeys a one-mode behavior in AlGaN and InGaN but a two-mode behavior in AlInN.

Figure 5.5 displays the FESEM images of the surface of $\text{Al}_x\text{In}_{1-x}\text{N}$ films with different compositions. It can be clearly seen that the surface morphology of $\text{Al}_x\text{In}_{1-x}\text{N}$ films strongly depends on the Al composition of the films (x). The surface morphology of $\text{Al}_{0.64}\text{In}_{0.36}\text{N}$ thin film (Figure 5.5 (a)) shows a smooth and compact microstructure of nanoparticles with an average size of 50 nm. Agglomeration of these nanoparticles on the surface results in the formation of grains of larger dimension $\sim 100 - 300$ nm. A decrease in the Al composition x to 0.60, enhances the agglomeration of the nanoparticles and a few excessively large grains with the size of $\sim 500 - 800$ nm are formed as a result (see Figure 5.5 (b)). The growth of these grains perpendicular to the surface forms a rough surface. Distribution of pebble-like particles can be observed in the FESEM image of the more Al-diluted $\text{Al}_{0.18}\text{In}_{0.82}\text{N}$ films (Figure 5.5 (c)). However, some relatively large grains are also observed. The surface morphology of $\text{Al}_x\text{In}_{1-x}\text{N}$ with Al composition of $x = 0.10$ (Figure 5.5 (d)) exhibits clusters of near-spherical-shaped nanoparticles over the surface. This kind of morphology is favorable for solar cell applications as the spherical particles are good channels for transporting charge carriers (Miao et al., 2015).

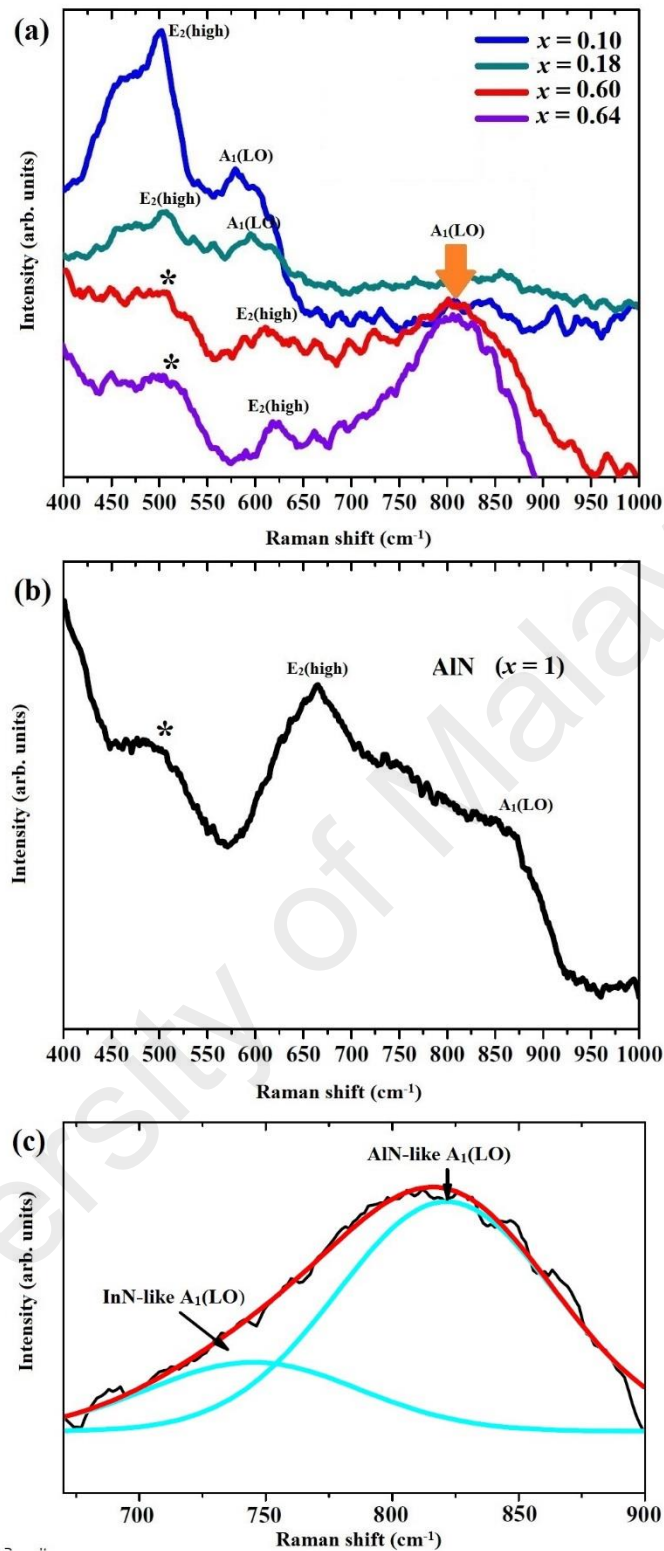


Figure 5.4: Raman spectra of the grown $\text{Al}_x\text{In}_{1-x}\text{N}$ (a) and AlN (b) thin films. (c) Fitted curve of Raman spectrum of $\text{Al}_{0.64}\text{In}_{0.36}\text{N}$ films in the range of $650 - 900 \text{ cm}^{-1}$. The $E_2(\text{high})$ and $A_1(\text{LO})$ phonon modes are blue-shifted when the aluminum incorporation is increased. The $A_1(\text{LO})$ phonon mode of Al-rich $\text{Al}_x\text{In}_{1-x}\text{N}$ films shows two-mode behavior.

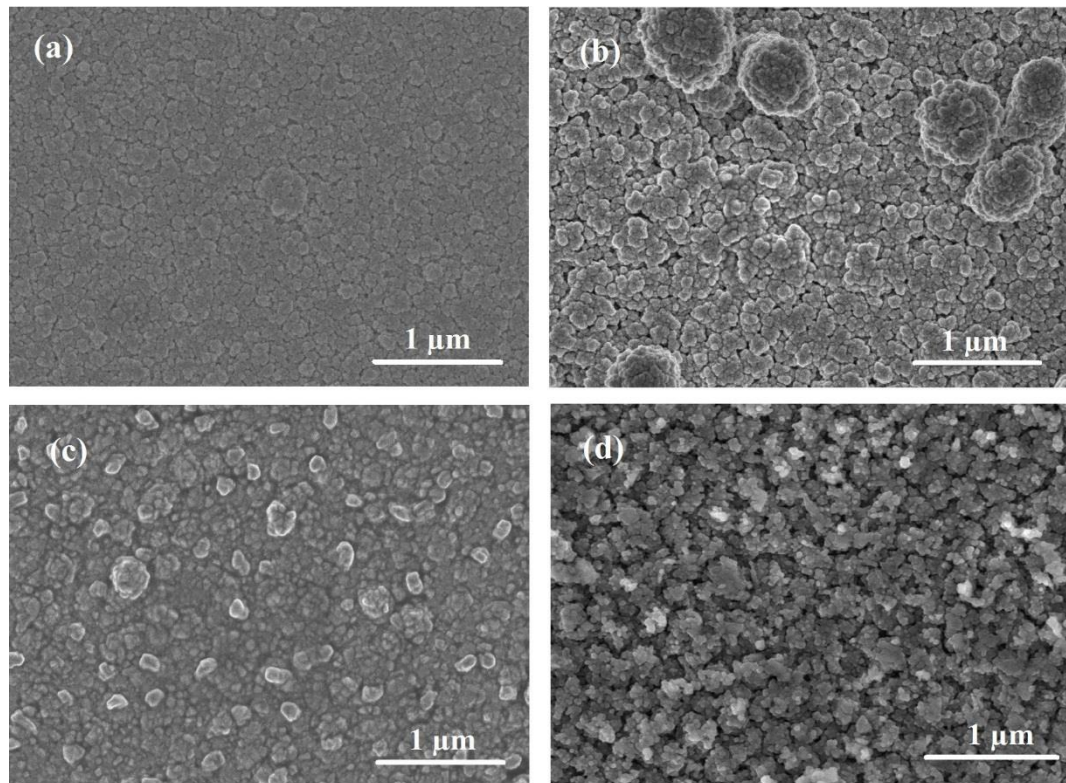


Figure 5.5: FESEM images of the $\text{Al}_x\text{In}_{1-x}\text{N}$ films with Al compositions of $x = 0.64$ (a), 0.60 (b), 0.18 (c) and 0.10 (d) with $\times 30000$ magnification. Agglomeration of grains are observed from the FESEM image of Al-rich $\text{Al}_x\text{In}_{1-x}\text{N}$ films.

The optical properties of $\text{Al}_x\text{In}_{1-x}\text{N}$ films with different compositions were studied by obtaining the transmittance and reflectance spectra of the films. Figure 5.6 (a) displays the transmittance curves of the $\text{Al}_x\text{In}_{1-x}\text{N}$ films with Al compositions of $x = 0.10, 0.18, 0.60,$ and 0.64 . In-rich films ($x = 0.10$ and 0.18) show an absorption in the near-infrared (NIR) region and an insignificant transmittance (e. g., $T \sim 0\%$) in the range of $300 - 1000$ nm. As x is increased towards the Al-rich region, the absorption edge of the films shifts towards a shorter wavelength and the $\text{Al}_x\text{In}_{1-x}\text{N}$ films with a higher Al content become more transparent in the visible and near-infrared (NIR) regions. In order to further clarify the optical results, transmittance of the AlN film was also measured (see inset in Figure 5.6 (a)). The sample was prepared in absence of F_{In} . The absorption edge of the sample occurred at around 200 nm which is in good agreement with the reported

absorption edge wavelength of AlN films (Q. X. Guo, Tanaka, Nishio, & Ogawa, 2006; H. T. Wang et al., 2014). Figure 5.6 (b) depicts the wavelength dependence of the optical reflectance spectra of the AlInN films with different aluminum compositions (x). It can be clearly observed that the minimum reflectance is shifted towards the longer wavelength as x is reduced from 0.64 to 0.10. Since the minimum value of the reflection occurs in the vicinity of the wavelength related to the optical band gap energy, the results in Figure 5.6 (b) show that the band gap value of the AlInN films increases by increasing x . An insignificant reflectance (e. g., $R \sim 3\%$) at around 200 nm is obtained from the optical reflectance spectrum of AlN films (see the inset of Figure 5.6 (b)) which is in good agreement with the corresponding transmittance results shown in the inset of Figure 5.6 (a).

Figure 5.7 shows $(\alpha hv)^2$ vs hv curves for all of the deposited films. The direct band gap of an $\text{Al}_x\text{In}_{1-x}\text{N}$ film was determined by extrapolating the linear part of the curves down to the energy axis. It can be seen that the optical band gap of the $\text{Al}_x\text{In}_{1-x}\text{N}$ film changes with the variation of the Al composition within the film's structure. The optical band gap of grown $\text{Al}_{0.64}\text{In}_{0.36}\text{N}$ thin film is estimated to be 2.50 eV. As x decreases to 0.60, 0.18, and 0.10 the band gap energies of the films are obtained at 2.33, 1.42, and 1.08 eV, respectively. Such controlled tuning of the band gap energy is extremely crucial for the application of AlInN alloys in multi-junction solar technology.

The E_g value of pure AlN as-shown in the inset of Figure 5.7 is estimated to be 5.5 eV, which is smaller than the value of 6.2 eV reported in previous works (Vurgaftman & Meyer, 2003). It has been shown that the band gap of an AlN film decreases due to various factors such as high carrier concentration, nonstoichiometric composition, and impose of residual stresses as well as presence of structural defects and oxygen impurity in the film structure (Persson et al., 2002; Yoshikawa et al., 1999). The AlN band gap energy

obtained in this work is very close to the values reported in other similar works (Jejurikar et al., 2007; H. T. Wang et al., 2014). It is also much larger than the E_g (of AlN films) reported by Cho (S. Cho, 2011) and Wu *et al.* (Y. Wu, Jia, & Zhang, 2012), who prepared the AlN films by reactive magnetron sputtering and laser molecular beam epitaxy method, respectively.

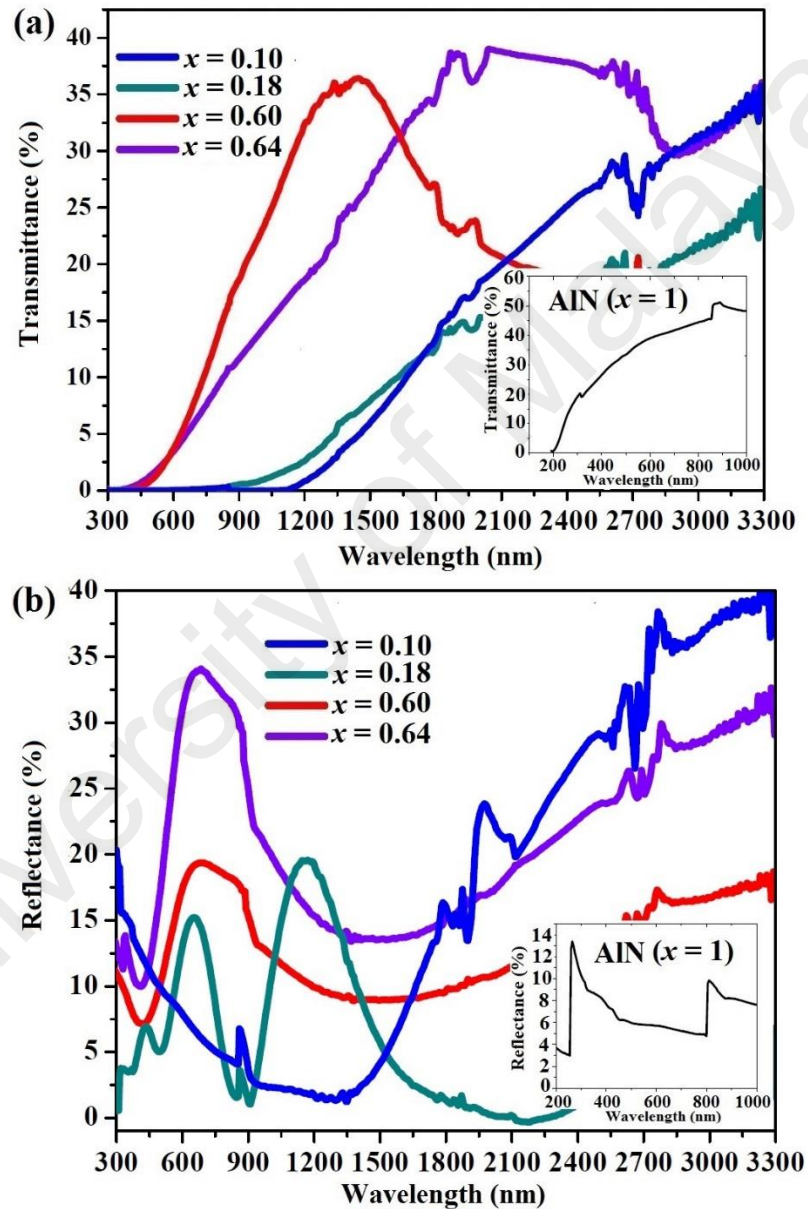


Figure 5.6: Transmittance (a) and Reflectance spectra (b) of $\text{Al}_x\text{In}_{1-x}\text{N}$ films with different Al compositions. The inset of (a) and (b) are transmittance and reflectance spectra of AlN ($x = 1$), respectively. As x is increased toward Al-rich region, the absorption edge and the reflectance minimum of the films shifts toward shorter wavelength

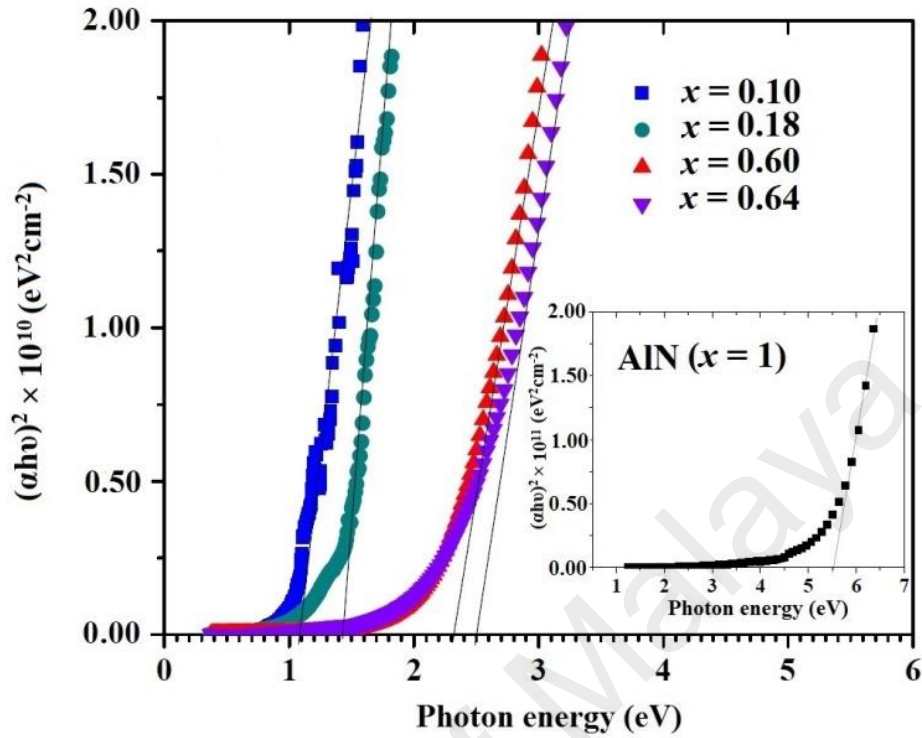


Figure 5.7: Plots of $(\alpha hv)^2$ versus hv for $\text{Al}_x\text{In}_{1-x}\text{N}$ films with different x . The inset is the plot of $(\alpha hv)^2$ versus hv for AlN films. The band gap energy values of the films are shifted from 1.08 to 2.50 as the x is increased from 0.10 to 0.64, respectively.

For optoelectronic applications that envisaged for the $\text{Al}_x\text{In}_{1-x}\text{N}$ film, it is essential to estimate the band gap energy based on the aluminum composition in the film x . Figure 5.8 shows the dependence of E_g values of the $\text{Al}_x\text{In}_{1-x}\text{N}$ films that have been studied in this work on the x . (dotted line). Clearly, the relationship between the obtained band gap values and Al composition is not linear. This phenomenon is named as “bowing effect” which is due to the unstable nature of $\text{Al}_x\text{In}_{1-x}\text{N}$ within the miscibility gap, the charge exchange between forming bonds in a disordered solid solution, and relaxation of the bond length (Voznyy & Deibuk, 2004). The band gap energy of $\text{Al}_x\text{In}_{1-x}\text{N}$ ($E_{g,\text{AlInN}}$) as a function of Al composition (x) was determined using the following equation (Saidi et al., 2015):

$$E_{g,AlInN} = xE_{g,AlN} + (1 - x)E_{g,InN} - bx(1 - x), \quad (5.2)$$

where b is the bowing parameter, $E_{g,AlN}$ and $E_{g,InN}$ are the band gaps of AlN and InN films, respectively. Fitting Eq. 5.2 to the experimental data obtained in this work provides a bowing parameter (b) of 4.3 eV, which is close to the 4.1 and 4.0 eV as reported by Goldhahn *et al.* (Goldhahn et al., 2006) and Yeh *et al.* (Yeh et al., 2008), respectively, and it is much smaller than that of 6.0 eV which are obtained by of Wang *et al.* (K. Wang et al., 2008). By extrapolating the band gap energy curve to the $x = 0$, the band gap of 0.85 eV is obtained for the InN film, which is close to the reported value (0.7 eV) (V. Yu Davydov et al., 2002).

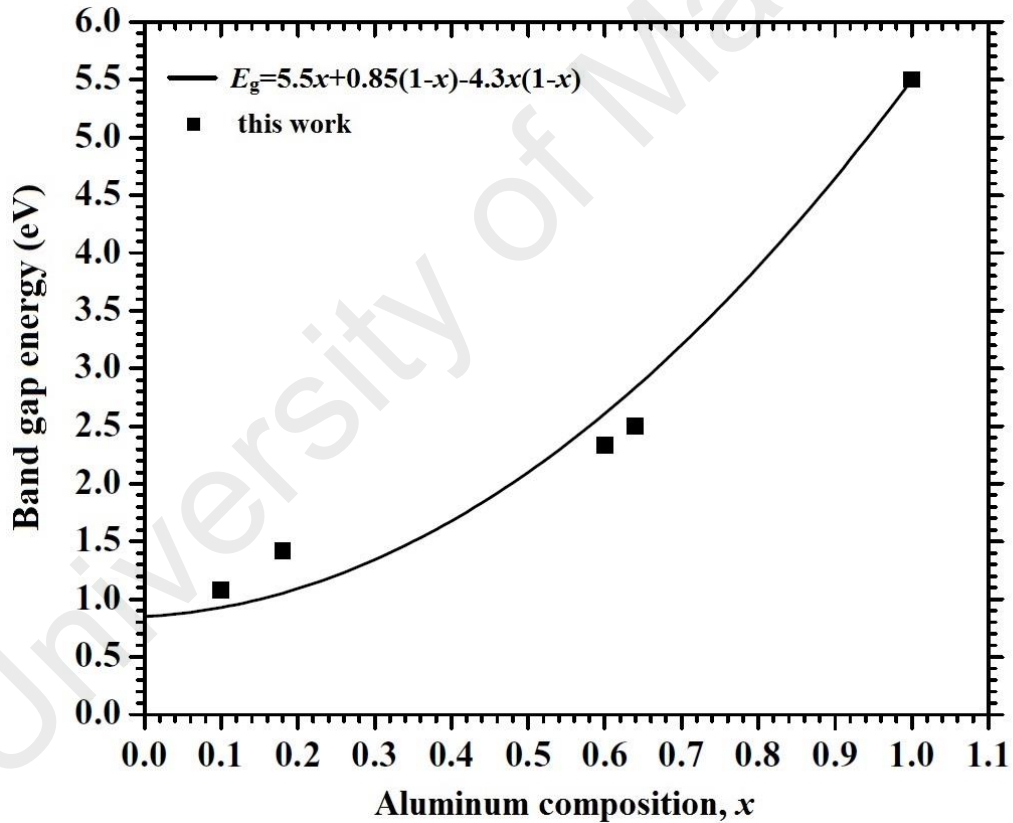


Figure 5.8: Band gap energy of $Al_xIn_{1-x}N$ film as a function of Al composition, x . A bowing parameter of 4.3 was obtained by fitting the obtained band gap values with the theoretical ones.

5.3 Effects of Nitrogen Flow Rate on Structure, Morphology, Composition and Optical Properties of In-rich and Al-rich Aluminum Indium Nitride Thin Films

The previous study on the effects of V_{In} on the aluminum composition of the $\text{Al}_x\text{In}_{1-x}\text{N}$ thin films showed that they can be categorized into two groups: In-rich (with $x = 0.1$ and 0.18) and Al-rich films (with $x = 0.6$ and 0.64). For the study on the effects of N_2 flow rate on the properties of the films, a sample from each category of these films was employed.

XPS analysis was performed to investigate the Al (In) mole fraction in the as-prepared In-rich (on quartz) and Al-rich (on Si(111)) $\text{Al}_x\text{In}_{1-x}\text{N}$ films. Figure 5.9 and 5.10 show the $\text{In}3d_{5/2}$ core-level photoelectron spectra of the In-rich and Al-rich films, respectively deposited at various N_2 flow rates. The core-level photoelectron spectra of the $\text{Al}_x\text{In}_{1-x}\text{N}$ films were deconvoluted into three main sub-peaks centered at 445.4 ± 0.1 , 444.4 ± 0.1 and 443.5 ± 0.1 eV, which are attributed to In–O, In–N and In–In bonds, respectively (A. K. S. Chauhan et al., 2015; Lebedev et al., 2006). The corresponding $\text{Al}2p$ core-level photoelectron spectra of the films are presented in the insets of Figures 5.9 and 5.10. The spectra were deconvoluted into two main components at 75.2 ± 0.2 and 74.25 ± 0.1 eV assigned to Al–O and Al–N bonds, respectively (Rosenberger et al., 2008; You et al., 2013). In addition, the $\text{Al}2p$ core-level photoelectron spectra of some deposited films exhibit a minor bump at the lower bonding energy side (72.8 ± 0.1 eV), which corresponds to the Al–Al bonding within the films (Rosenberger et al., 2008).

The estimated Al mole fractions (x) in the In-rich $\text{Al}_x\text{In}_{1-x}\text{N}$ films were determined to be 0.11, 0.07, 0.05 and 0.03 for the films deposited at the nitrogen flow rates of 40, 60, 80 and 100, respectively. The corresponding x values for the Al-rich $\text{Al}_x\text{In}_{1-x}\text{N}$ thin films

were estimated to be 0.66, 0.58, 0.55 and 0.48, respectively. It can be seen that the Al composition decreases with increase in N_2 flow rate for both In-rich and Al-rich films.

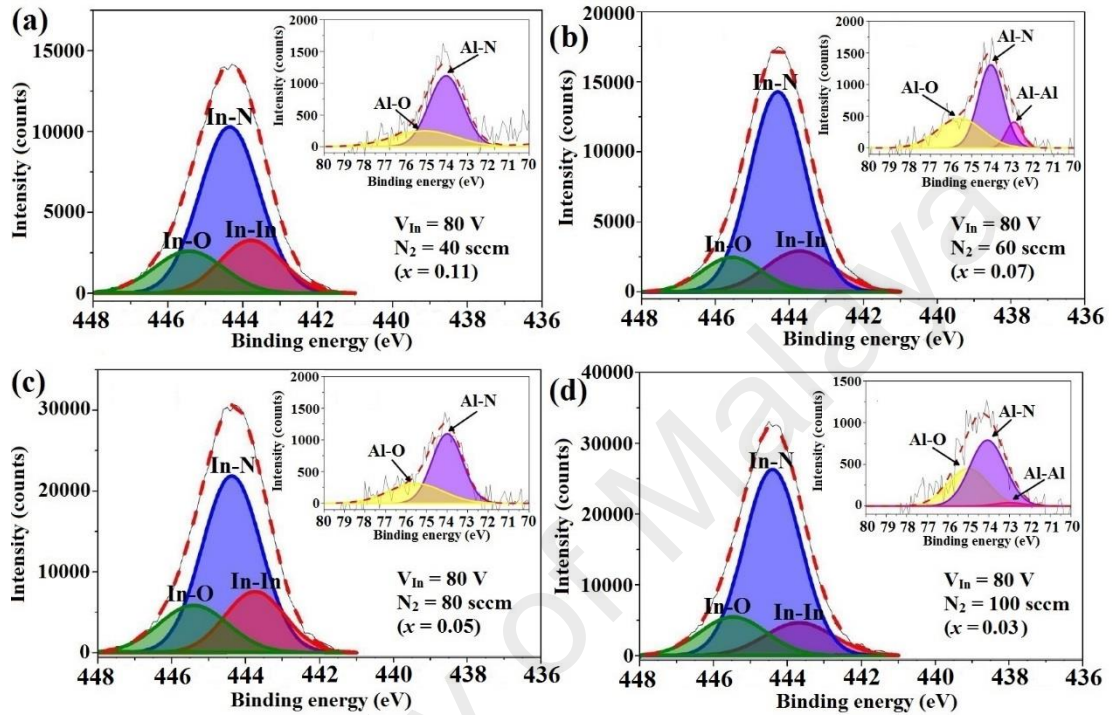


Figure 5.9: $In_{3d_{5/2}}$ core-level photoelectron spectra of the In-rich $Al_xIn_{1-x}N$ films deposited at N_2 flow rate of 40 sccm (a), 60 sccm (b), 80 sccm (c) and 100 sccm (d). The inset of (a), (b), (c) and (d) are the corresponding Al_{2p} core-level photoelectron spectra. The Al incorporation in the In-rich $Al_xIn_{1-x}N$ decreases from 0.11 to 0.03 as the nitrogen flow rate is increased from 40 to 100 sccm.

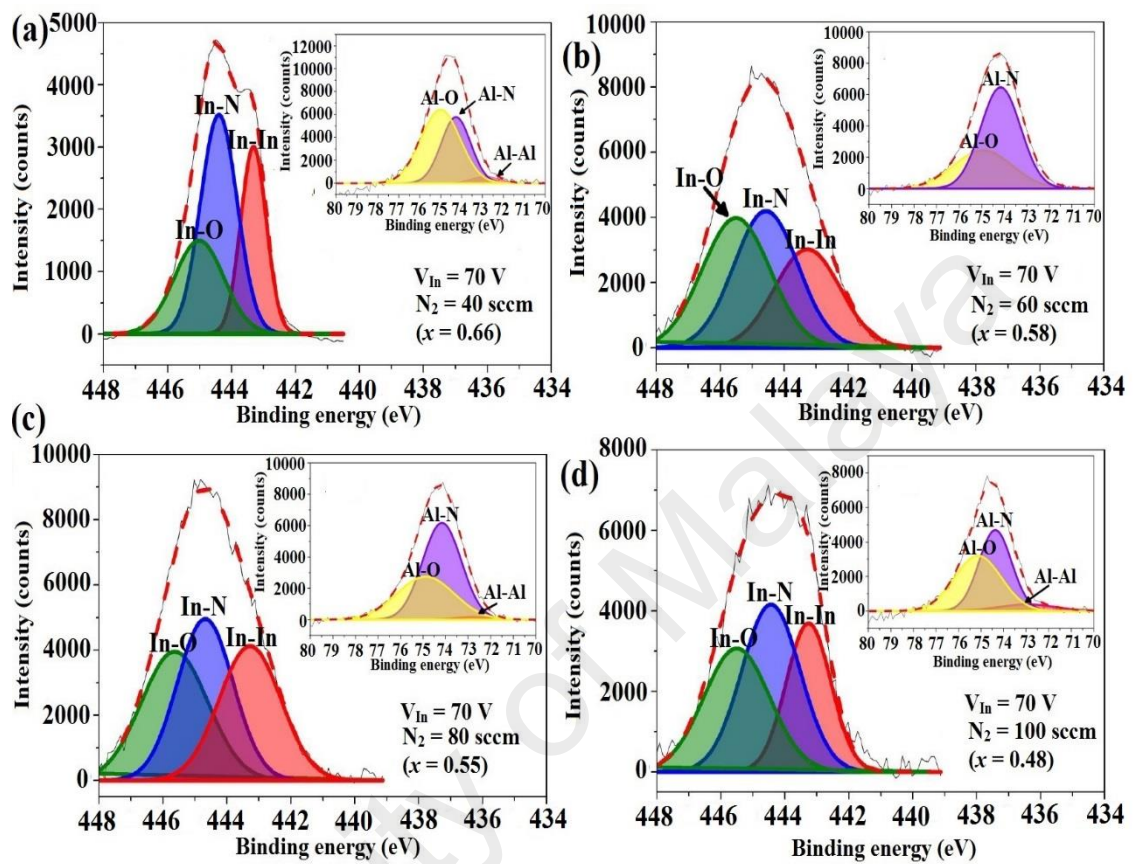


Figure 5.10: $\text{In}3d_{5/2}$ core-level photoelectron spectra of the Al-rich $\text{Al}_x\text{In}_{1-x}\text{N}$ films deposited at N_2 flow rate of 40 sccm (a), 60 sccm (b), 80 sccm (c) and 100 sccm (d). The inset of (a), (b), (c) and (d) are the corresponding $\text{Al}2p$ core-level photoelectron spectra. The Al incorporation in the Al-rich $\text{Al}_x\text{In}_{1-x}\text{N}$ decreases from 0.66 to 0.48 as the nitrogen flow rate is increased from 40 to 100 sccm.

The decrease in x as a result of increment in the flow rate of the nitrogen gas can be explained in terms of plasma dynamics. By increasing the N_2 flow rate, more excited atoms are generated in the plasma and in the vicinity of the hot filament. The increase in N_2 flow rate also results in the presence of more unreacted hot N_2 molecules in the vicinity of the hot filament. More gas-phase reactions occur due to collisions between the excited atoms and molecules. These reactions decrease the kinetic energy of ad-atoms/ions impinging on the growth surface of the film resulting in the lower surface temperature and decreasing their mobility. The bonding energy of Al–N bonds is much larger than that of In–N (Costales, Blanco, Martín Pendás, Kandalam, & Pandey, 2002). Therefore, under a higher nitrogen flow rate ad-atoms/ions with lower energy are energetically favorable for the formation of In–N, rather than Al–N bonds, resulting in a higher InN presence in the $Al_xIn_{1-x}N$ film's structure compared to AlN.

Figures 5.11 and 5.12 show the N1s core-level photoelectron spectra of the In-rich and Al-rich $Al_xIn_{1-x}N$ films, respectively that were grown at various N_2 flow rates. The N1s core-level photoelectron spectra of all samples were deconvoluted into two main sub-peaks centered at 396.1 ± 0.2 and 396.8 ± 0.2 eV which are assigned to the N–In (Shinoda & Mutsukura, 2002) and N–Al (Kuang et al., 2012a) bonds, respectively. The presence of N–In and N–Al components further confirms the growth of the $Al_xIn_{1-x}N$ films. The spectra also exhibit a broad bump at the higher bonding energy side (398.7 ± 0.3 eV) corresponding to N–Al–O bond within grain boundaries of the films (Ozgit, Donmez, Alevli, & Biyikli, 2012). This indicates that the unsatisfied bonds on AlN have higher affinity for O atoms as-compared to those on InN.

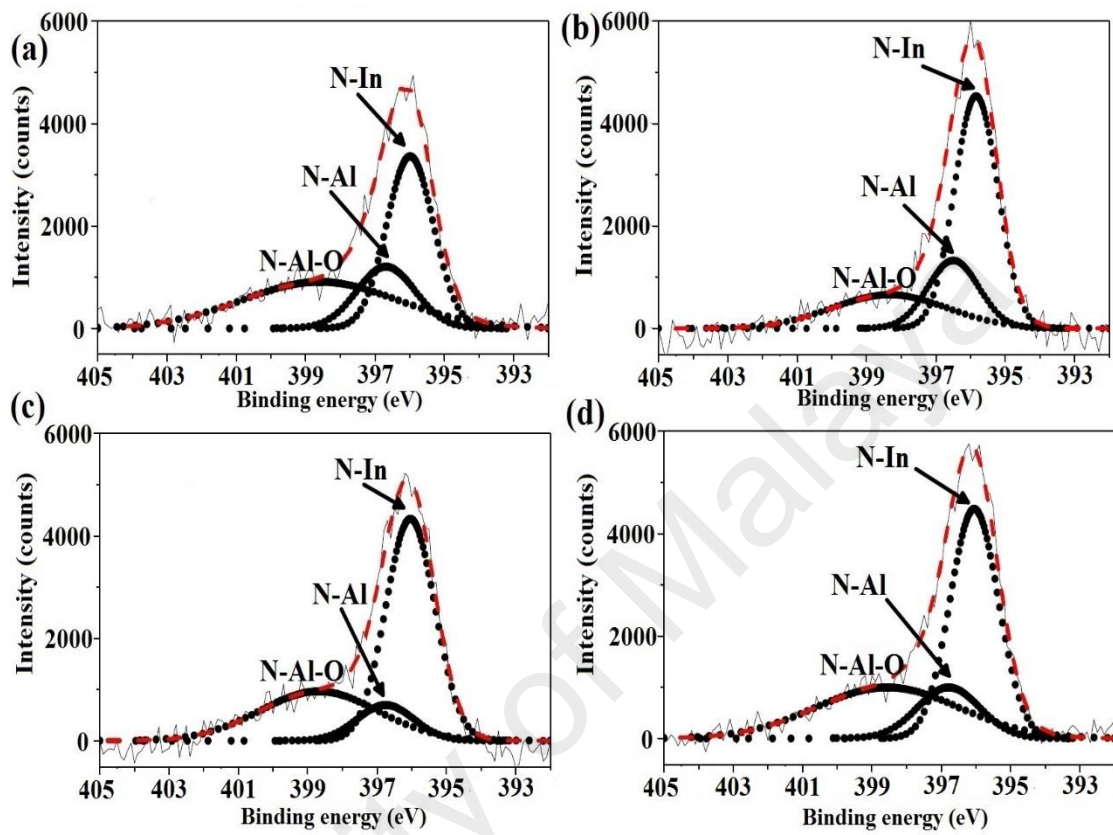


Figure 5.11: N1s core-level photoelectron spectra of the In-rich $\text{Al}_x\text{In}_{1-x}\text{N}$ samples deposited at N_2 flow rate of 40 sccm (a), 60 sccm (b), 80 sccm (c) and 100 sccm (d). The presence of N–In and N–Al components further confirms growth of $\text{Al}_x\text{In}_{1-x}\text{N}$ films.

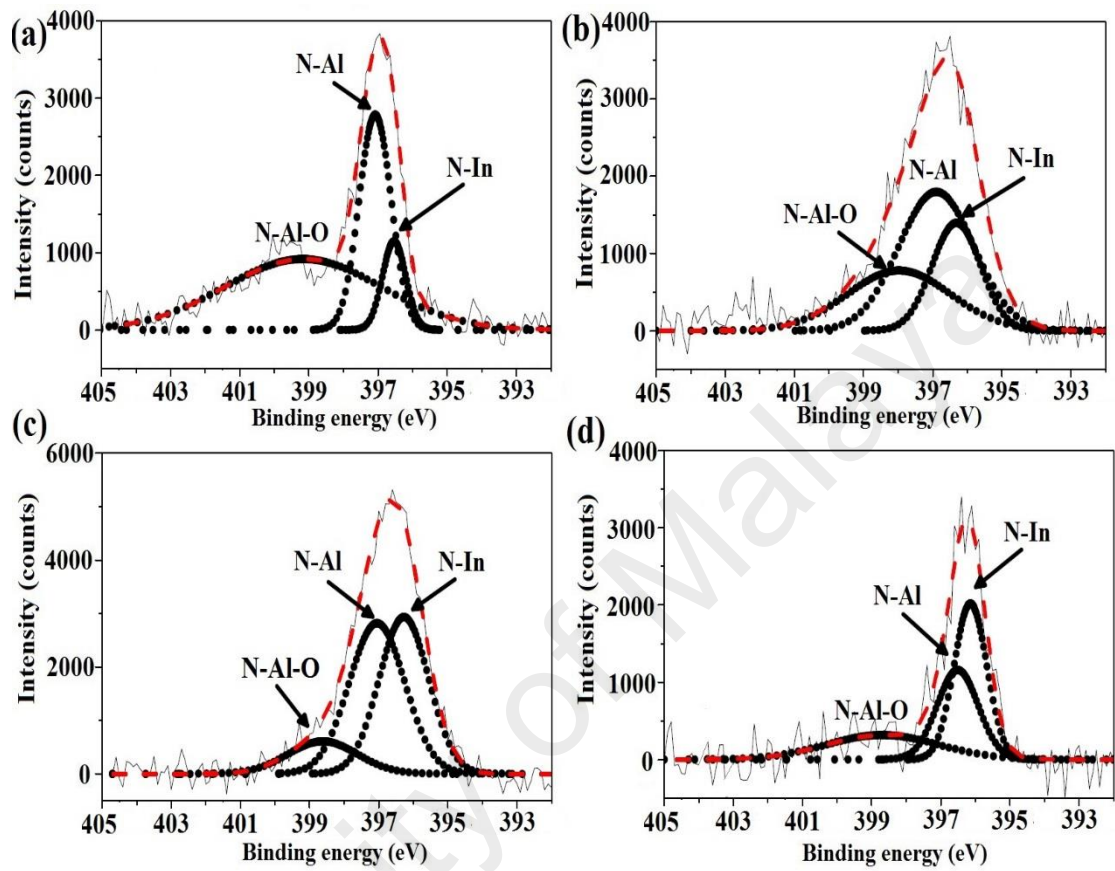


Figure 5.12: N1s core-level photoelectron spectra of the Al-rich $\text{Al}_x\text{In}_{1-x}\text{N}$ samples deposited at N_2 flow rate of 40 sccm (a), 60 sccm (b), 80 sccm (c) and 100 sccm (d). The presence of N–In and N–Al components further confirms growth of $\text{Al}_x\text{In}_{1-x}\text{N}$ films.

Figures 5.13 and 5.14 present the FESEM images of the surface of In-rich and Al-rich $\text{Al}_x\text{In}_{1-x}\text{N}$ films, respectively that were grown at different N_2 flow rates. It is obvious that the surface morphology of the films strongly depends on the gas flow rate. For In-rich films, the surface morphology of sample deposited at 40 sccm (Figure 5.13 (a)) exhibits clusters of near-spherical-shaped nanoparticles over the surface. The FESEM image of $\text{Al}_x\text{In}_{1-x}\text{N}$ films grown at $\text{N}_2 = 60$ sccm (Figure 5.13 (b)) shows that the nanoparticles tend to agglomerate. Further increase in nitrogen flow rate enhances agglomeration of the nanoparticles and a few excessively large grains with the size of $\sim 0.5\text{-}1\ \mu\text{m}$ are formed on the surface of the sample deposited at $\text{N}_2 = 80$ sccm (Figure 5.13 (c)). The FESEM image of the $\text{Al}_x\text{In}_{1-x}\text{N}$ thin films grown at $\text{N}_2 = 100$ sccm (Figure 5.13 (d)) shows cauliflower-shaped clusters with appearance of dark pits.

The surface morphology of the Al-rich $\text{Al}_x\text{In}_{1-x}\text{N}$ films deposited at N_2 flow rate of 40 sccm (Figure 5.14 (a)) exhibits features of pebble-like nanoparticles, which are distributed uniformly between relatively large grains over the surface. As the gas flow rate is increased to 60 and 80 sccm, the cauliflower-like grains with of dimension $\sim 0.5 - 1\ \mu\text{m}$ on surface of the thin films (Figure 5.14 (b) and (c)). Density of the cauliflower-like grains on surface of the films grown at $\text{N}_2 = 80$ sccm seems to be higher compared to $\text{N}_2 = 60$ sccm. Also, the growth of these grains perpendicular to the substrate surface with different rates causes a rougher surface. Further increase in nitrogen flow rate results in fully agglomerated morphology for the films deposited at nitrogen flow rate of 100 sccm and these grains appear to be compressed and flattened (Figure 5.14 (d)). This feature may be formed as a result of the increase in the formation of the InN grains and their stacking on top of each other which flatten the surface and decrease the size of the pits between the grains.

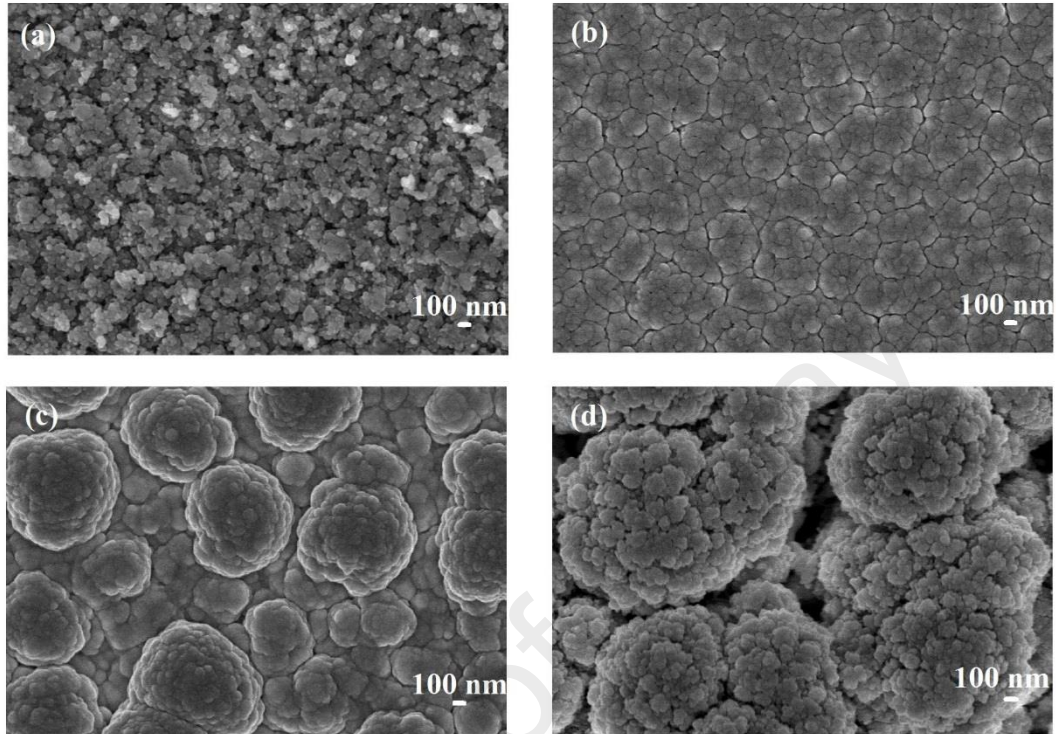


Figure 5.13: FESEM images of the In-rich $\text{Al}_x\text{In}_{1-x}\text{N}$ samples deposited at N_2 flow rate of 40 sccm (a), 60 sccm (b), 80 sccm (c) and 100 sccm (d) with $\times 30000$ magnification. Agglomeration of the grains is enhanced by increasing nitrogen gas flow rate.

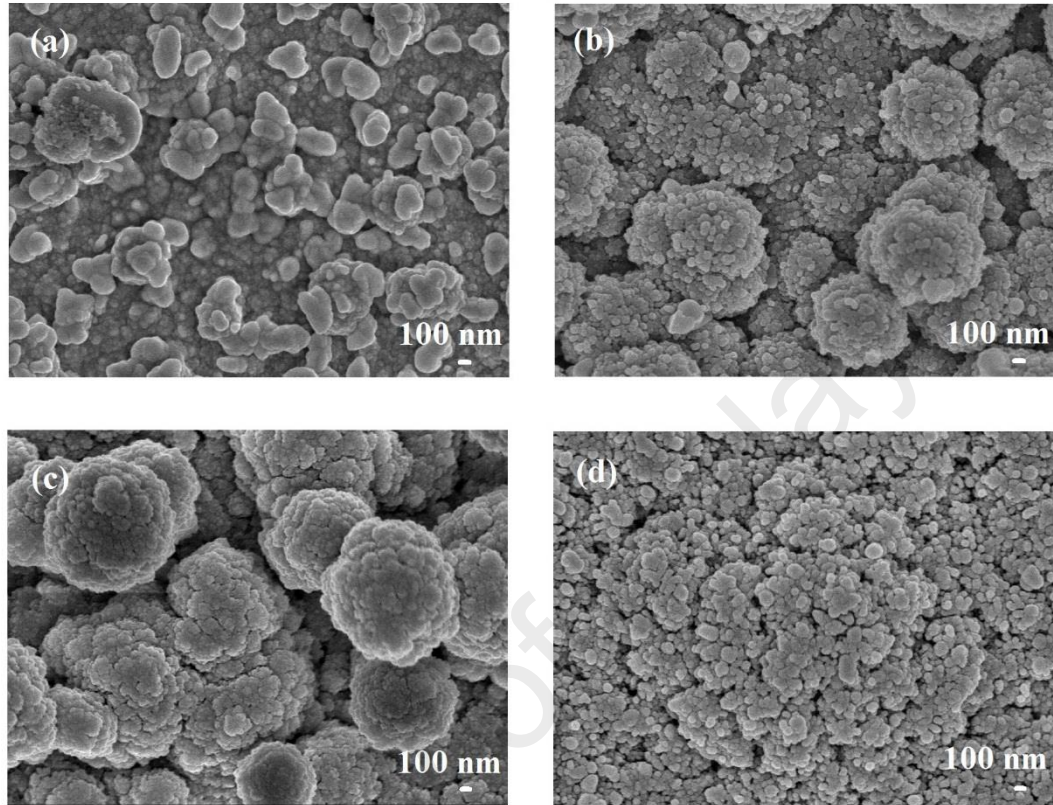


Figure 5.14: FESEM images of the Al-rich $\text{Al}_x\text{In}_{1-x}\text{N}$ films deposited at N_2 flow rate of 40 sccm (a), 60 sccm (b), 80 sccm (c) and 100 sccm (d) with $\times 30000$ magnification. Cauliflower-shaped grains are observed from FESEM image of Al-rich $\text{Al}_x\text{In}_{1-x}\text{N}$ films grown at higher N_2 flow rate.

The dependence of the surface morphology of the $\text{Al}_x\text{In}_{1-x}\text{N}$ thin films on the nitrogen gas flow rate can also be explained in terms of plasma dynamics. As mentioned earlier, at a high N_2 flow rate lower kinetic energy (and hence lower mobility) is imparted to the ad-atoms/ions on the growing surface of the thin film. It is well-known that during the growth process the primary nuclei must move within a certain distance on the substrate surface to find an optimal site that matches its crystal structure. At high N_2 flow rate conditions, and before these atoms or ions have the opportunity to get to the optimal energy site, any congelation of their disorder state has a higher probability of occurring due to the low mobility of the adatoms on the surface. As a result, enhanced agglomeration of particles is observed on the surface of the samples deposited at high nitrogen flow rates.

Figure 5.15 displays the Raman spectra of the In-rich $\text{Al}_x\text{In}_{1-x}\text{N}$ films that are deposited under various nitrogen flow rates. For the films deposited at nitrogen flow rate of 40 sccm, two major peaks centered at 502 and 582 cm^{-1} are observed which are assigned to the $\text{E}_2(\text{high})$ and $\text{A}_1(\text{LO})$ phonon modes of the $\text{Al}_{0.11}\text{In}_{0.89}\text{N}$ films, respectively (Kang, Hashimoto, et al., 2009). Also, one broad peak at around 457 cm^{-1} is seen in the Raman spectra of the film. Since the Al content in the sample is very low it can be easily attributed to the $\text{A}_1(\text{TO})$ mode of the sample that originates from that mode of InN (at 447 cm^{-1} (Terziyska et al., 2015)). In Raman spectrum of $\text{Al}_x\text{In}_{1-x}\text{N}$ films deposited at $\text{N}_2 = 60$ sccm, the $\text{A}_1(\text{TO})$ phonon mode is highly broadened whereas the $\text{A}_1(\text{LO})$ mode experienced a blue shift which is possibly due to an induced residual compressive stress as a result of increased nitrogen flow rate (Watanabe et al., 2013). However, the position of this peak is also close to that of the phonon associated with the bcc-structured In_2O_3 (Yunxia Chen et al., 2008). The $\text{E}_2(\text{high})$ and $\text{A}_1(\text{LO})$ phonon modes of the samples deposited at $\text{N}_2 = 80$ and 100 sccm are very broad showing that the structure of the In-rich $\text{Al}_x\text{In}_{1-x}\text{N}$ thin films tend to turn into an amorphous state at high nitrogen flow rate.

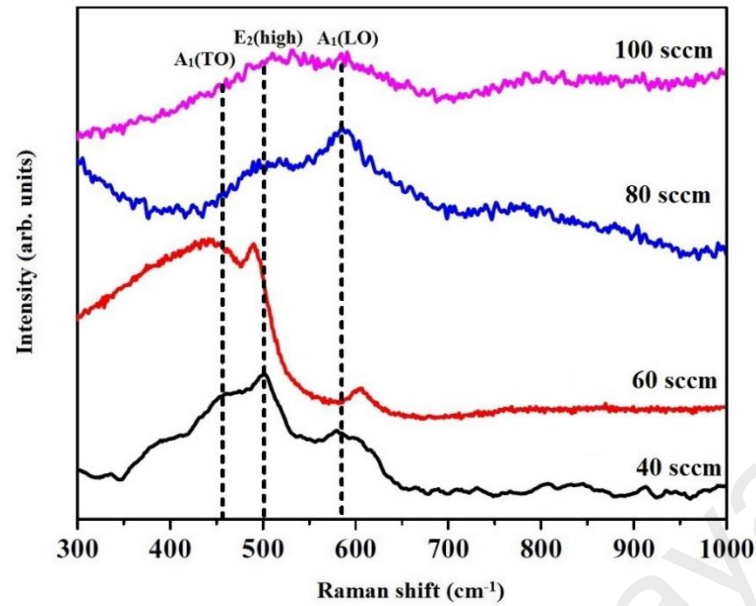


Figure 5.15: Micro-Raman spectra of the In-rich $\text{Al}_x\text{In}_{1-x}\text{N}$ samples. The structure of the In-rich $\text{Al}_x\text{In}_{1-x}\text{N}$ thin films tend to turn into amorphous state at high nitrogen flow rate.

The Raman spectra of the Al-rich $\text{Al}_x\text{In}_{1-x}\text{N}$ samples deposited under various nitrogen flow rates are shown in Figure 5.16. It can be seen that the Raman features of all samples are very broad possibly due to the unstable nature of the $\text{Al}_x\text{In}_{1-x}\text{N}$ thin films in the Al-rich composition range ($x \geq 0.5$) (Q. Guo, Okada, Kidera, Nishio, & Ogawa, 2000). For the sample deposited at $\text{N}_2 = 40$ sccm, two peaks centered at 606 and 810 cm^{-1} are observed, which are assigned to the $\text{E}_2(\text{high})$ and $\text{A}_1(\text{LO})$ phonon modes of the Al-rich $\text{Al}_x\text{In}_{1-x}\text{N}$ films, respectively (Kang, Hashimoto, et al., 2009). By increasing the nitrogen gas flow rate to 60 sccm, the $\text{E}_2(\text{high})$ is significantly broadened while the intensity of the $\text{A}_1(\text{LO})$ mode decreases. The Intensity of the $\text{E}_2(\text{high})$ phonon mode for the films that were grown at $\text{N}_2 = 80$ sccm is remarkably decreased and no $\text{E}_2(\text{high})$ mode is observed for the $\text{Al}_x\text{In}_{1-x}\text{N}$ thin films deposited at the nitrogen gas flow rate of 100 sccm. Also, $\text{E}_2(\text{high})$ phonon modes of the sample obtained at $\text{N}_2 = 60$ and 80 sccm are slightly red-shifted due to the decreased Al mole fraction in the films compositions as shown in the XPS results (Figure 5.10).

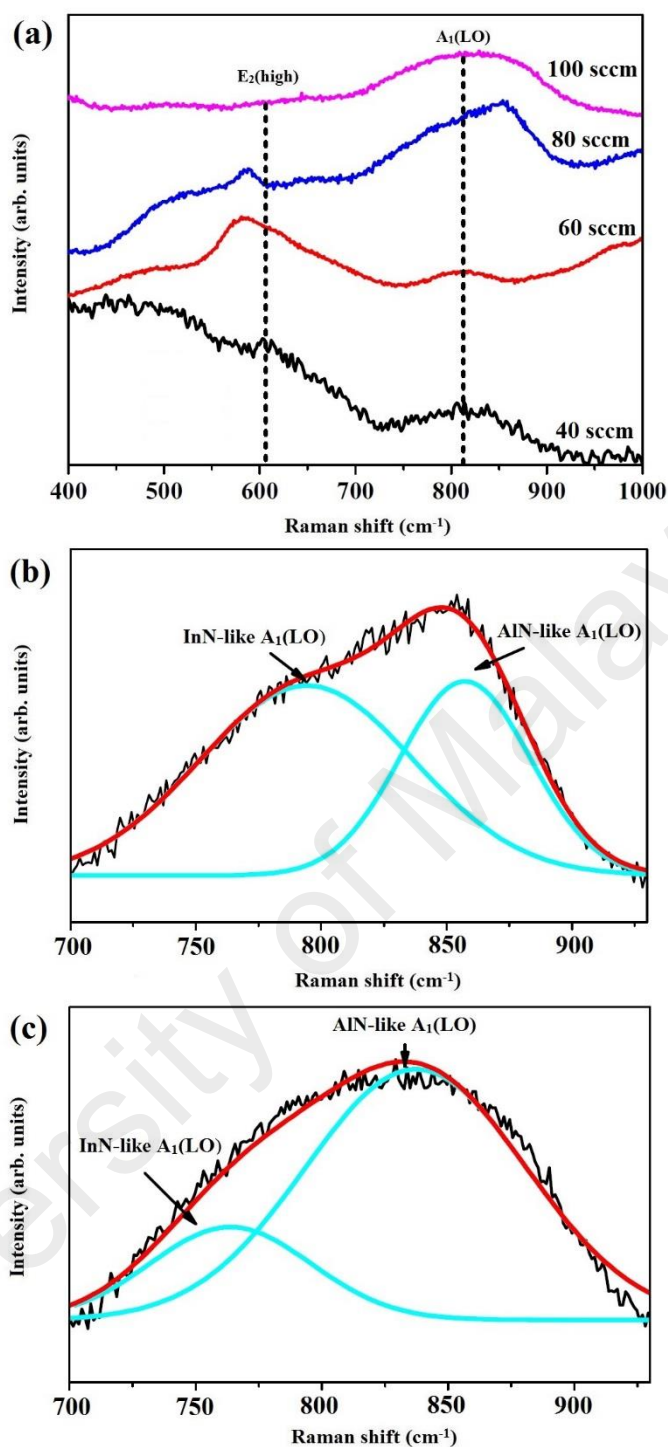


Figure 5.16: (a) Raman spectra of the Al-rich $\text{Al}_x\text{In}_{1-x}\text{N}$ thin films grown at different N_2 flow rates. **(b)** and **(c)** Fitted curves of Raman spectrum of Al-rich $\text{Al}_x\text{In}_{1-x}\text{N}$ films deposited at $\text{N}_2 = 80$ and 100 sccm, respectively in the range of 700 – 950 cm^{-1} . Raman features of all Al-rich $\text{Al}_x\text{In}_{1-x}\text{N}$ are very broad possibly due to unstable nature of $\text{Al}_x\text{In}_{1-x}\text{N}$ thin films in Al-rich composition range.

Similar to the Raman spectra of the Al-rich $\text{Al}_x\text{In}_{1-x}\text{N}$ films that presented in section 5.2, the $A_1(\text{LO})$ phonon modes of the samples grown at 80 and 100 sccm are also very broad showing that the peaks are formed from the overlapping of some Raman phases. In order to identify each of the contributions, the Raman spectra of the $\text{Al}_x\text{In}_{1-x}\text{N}$ films deposited at $\text{N}_2=80$ and 100 sccm were analyzed in $700\text{--}930\text{ cm}^{-1}$ range by using the curve-fitting method (Figure 5.16 (b) and (c)). The observed broad peaks were deconvoluted into two main components at $765\text{--}790$ and $835\text{--}855\text{ cm}^{-1}$ which are assigned to the InN-like $A_1(\text{LO})$ and AlN-like $A_1(\text{LO})$ phonon modes of AlInN, respectively (Jiang et al., 2011; Kang, Hashimoto, et al., 2009).

Figure 5.17 displays $(\alpha hv)^2$ vs hv curves for the In-rich $\text{Al}_x\text{In}_{1-x}\text{N}$ films that were deposited at various nitrogen gas flow ratios. The band gap value of the films deposited at nitrogen flow rate of 40 sccm is estimated to be 1.08 eV while for the samples grown at $\text{N}_2 = 60, 80$ and 100 sccm the E_g value shifts to 0.95, 0.93 and 0.90 eV, respectively. This decline in the band gap can be attributed to the increase in the indium composition of the films as shown in Figure 5.9. However, it may be also related to the degraded crystallinity of the grown films at high nitrogen flow rates. A high N_2 flow rate-induced lattice damage creates defective energy level below the conduction band and as a result the band gap energy decreases (Shah & Mahmood, 2012). The obtained values are around 0.20-0.38 eV higher than new band gap energy (0.70 eV) of InN due to the low concentration of Al incorporated within the film structure forming In-rich $\text{Al}_x\text{In}_{1-x}\text{N}$. It should be noted that the band gap energy of pure InN was obtained at around 2.0 eV by using plasma-assisted single source reactive evaporation (chapter 4). In this part of the work, it was shown that by inclusion small amount of AlN in the film structure and using the dual hot filament for film growth, the band gap energy of In-rich $\text{Al}_x\text{In}_{1-x}\text{N}$ films was further reduced to 0.9 eV.

The direct band gap of the Al-rich $\text{Al}_x\text{In}_{1-x}\text{N}$ films at various growth conditions was also estimated by drawing a tangential line for the $(\alpha h\nu)^2$ versus $(h\nu)$ as shown in Figure 5.18. The optical band gap energy was found to decrease with increase in the nitrogen gas flow rate. The band gap energy of the films deposited at nitrogen flow rate of 40 sccm is estimated to be 2.33 eV. As the flow rate is increased to 60 and 80 sccm, the E_g value decreases to 2.12 eV. Further increase of the N_2 flow rate to 100 sccm, causes a decrease of 0.2 eV in the band gap value. This reduction is due to decrease of the Al mole fraction in the alloy composition as explained in the XPS results (Figure 5.10).

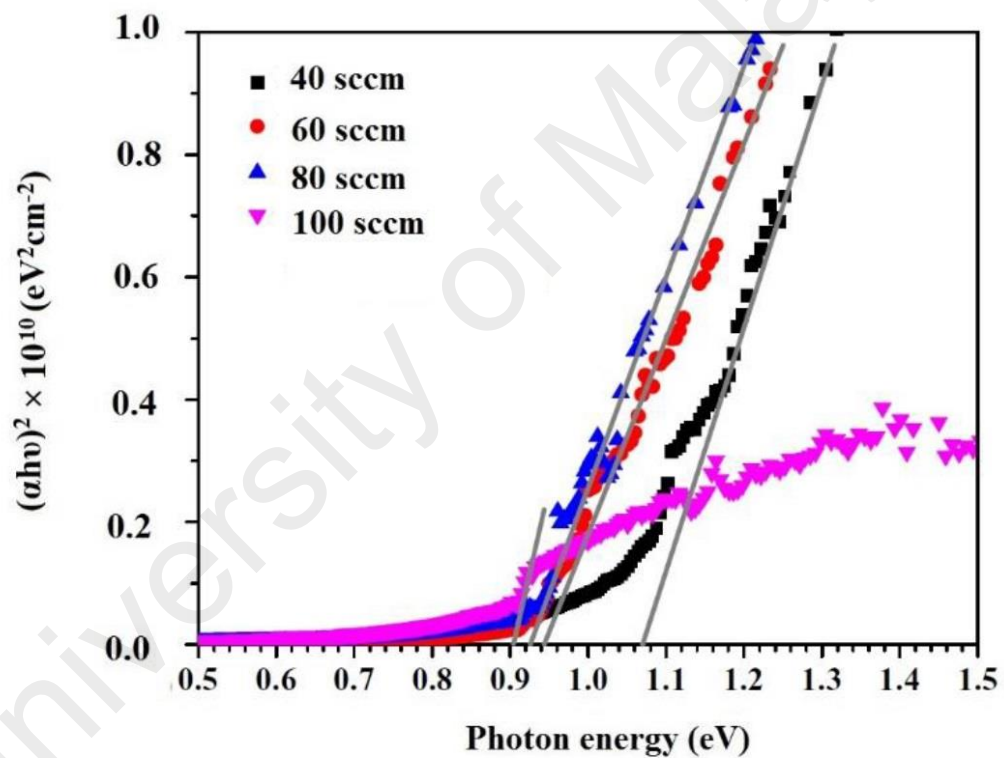


Figure 5.17: Plots of $(\alpha h\nu)^2$ versus $h\nu$ for the In-rich $\text{Al}_x\text{In}_{1-x}\text{N}$ samples grown at various N_2 flow rates. The band gap energy of the films decreases from 1.08 to 0.90 eV as the flow rate is increased from 40 to 100 sccm.

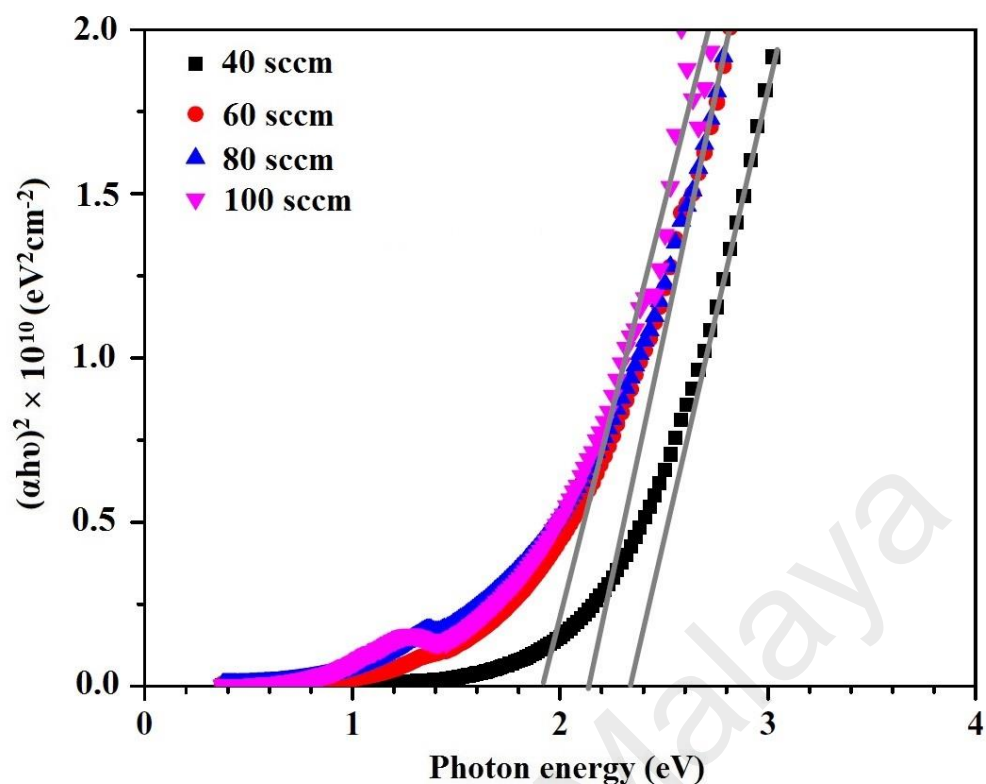


Figure 5.18: Plots of $(\alpha hv)^2$ versus hv for Al-rich $Al_xIn_{1-x}N$ films grown at different N_2 flow rates. The band gap energy of the films decreases from 2.33 to 1.92 eV as the flow rate is increased from 40 to 100 sccm.

5.4 Effects of Annealing Temperature on the Composition, Structure and Optical Properties of Aluminum Indium Nitride Thin Films

Figure 5.19 (a)-(e) shows the $In_{3d_{5/2}}$ core-level photoelectron spectra of the as-grown In-rich $Al_xIn_{1-x}N$ films and the films annealed at various temperatures. As mentioned earlier, the core-level photoelectron spectrum of the as-grown $Al_xIn_{1-x}N$ films (Figure 5.19 (a)) was deconvoluted into three main sub-peaks centered at 445.5, 444.4 and 443.6 eV, which are attributed to In–O, In–N and In–In bonds, respectively (A. K. S. Chauhan et al., 2015; Lebedev et al., 2006). The exact positions with minimum error were applied for the deconvolution of rest of the spectra, to examine them more accurately. It can be clearly seen that for all annealed samples, only In–O and In–N are observed. This is possibly due to high affinity of the metallic indium to the remnant oxygen from the

annealing tube and/or bond transformation of In–In to In–O. At low annealing temperatures (e.g., 200 and 300 °C) the intensity of the In–N bond is higher showing that the InN formation is still dominant (Figure 5.19 (b) and (c)). However, by increasing the annealing temperature to 400 and 500 °C (Figure 5.19 (d) and (e)), the intensity of the In–N bond decreases dramatically while the intensity of the In–O bond becomes increasingly dominant. This may be attributed to dissociation of the In–N bonds followed by the oxidation of the metallic indium. Hence, the elemental compositional studies on the annealed films showed that low-temperature (e.g., ≤ 300 °C) environments should be considered for the application of these $\text{Al}_x\text{In}_{1-x}\text{N}$ films grown by the plasma-assisted reactive evaporation in the devices.

In order to further investigate the stability of the films, the N1s core-level photoelectron spectra of the as-grown and annealed samples were also analyzed (Figure 5.20 (a)-(e)). The N1s core-level photoelectron spectrum of the as-grown (Figure 5.20 (a)) sample was deconvoluted into three main sub-peaks centered at 396, 396.7 and 398.5 eV, which are assigned to N–In, N–Al and N–Al–O bonds, respectively (Kuang et al., 2012a; Ozgit et al., 2012; Shinoda & Mutsukura, 2002). After the annealing process, the N1s spectra of all the samples were eliminated and only the N–In and N–Al–O components are observed from the fitted spectra (Figure 5.20 (b)-(e)). By increasing the annealing temperature from 200 to 500 °C, the intensity of N–In decreases dramatically reflecting the fact that the prepared alloys are unstable at high-temperature environment.

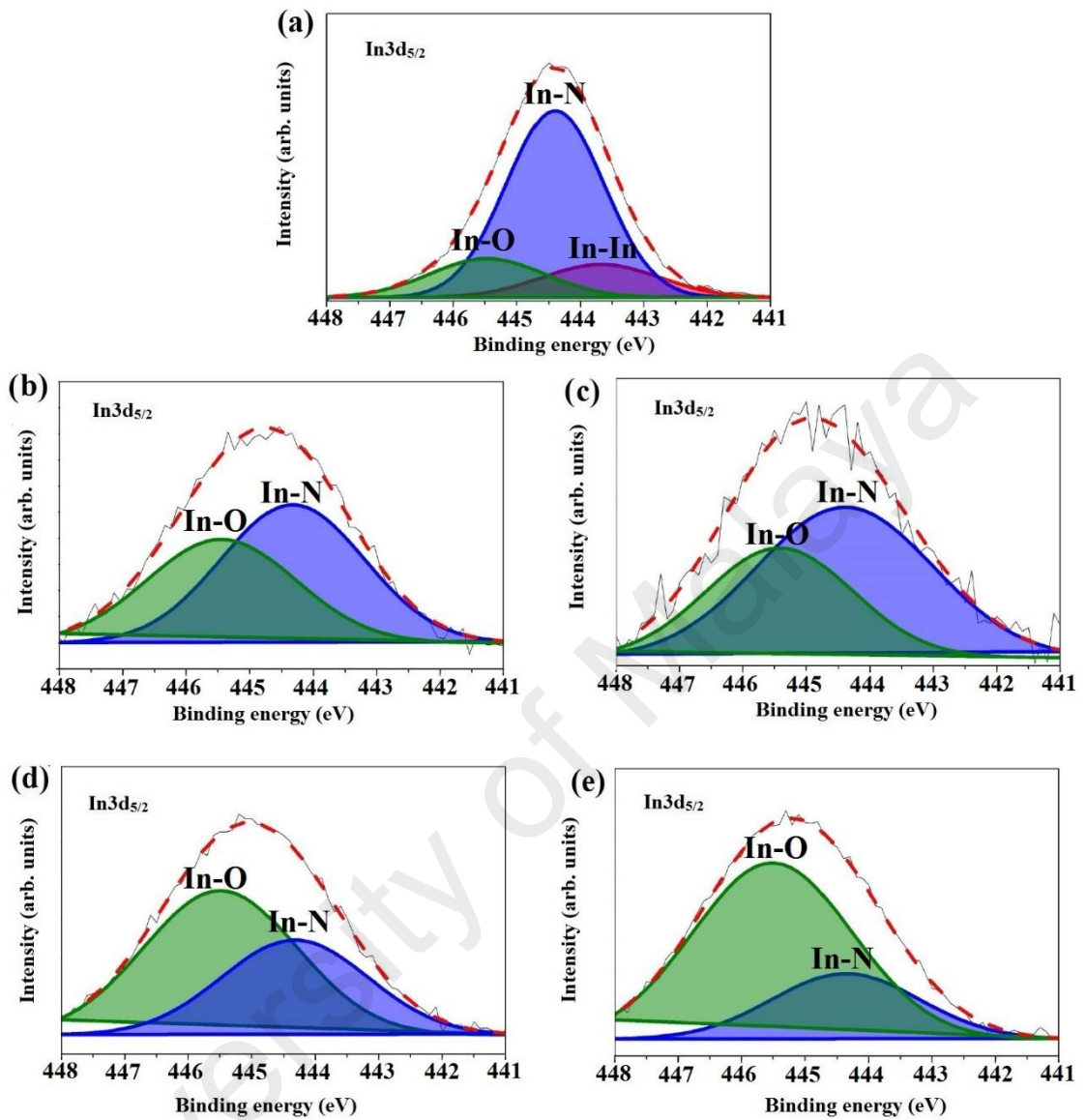


Figure 5.19: $\text{In}3d_{5/2}$ core-level photoelectron spectra of the as-grown In-rich $\text{Al}_x\text{In}_{1-x}\text{N}$ films (a) and the films annealed at 200 °C (b), 300 °C (c), 400 °C (d) and 500 °C (e). Intensity of the peak corresponding to In–O bond increases as the annealing temperature is increased.

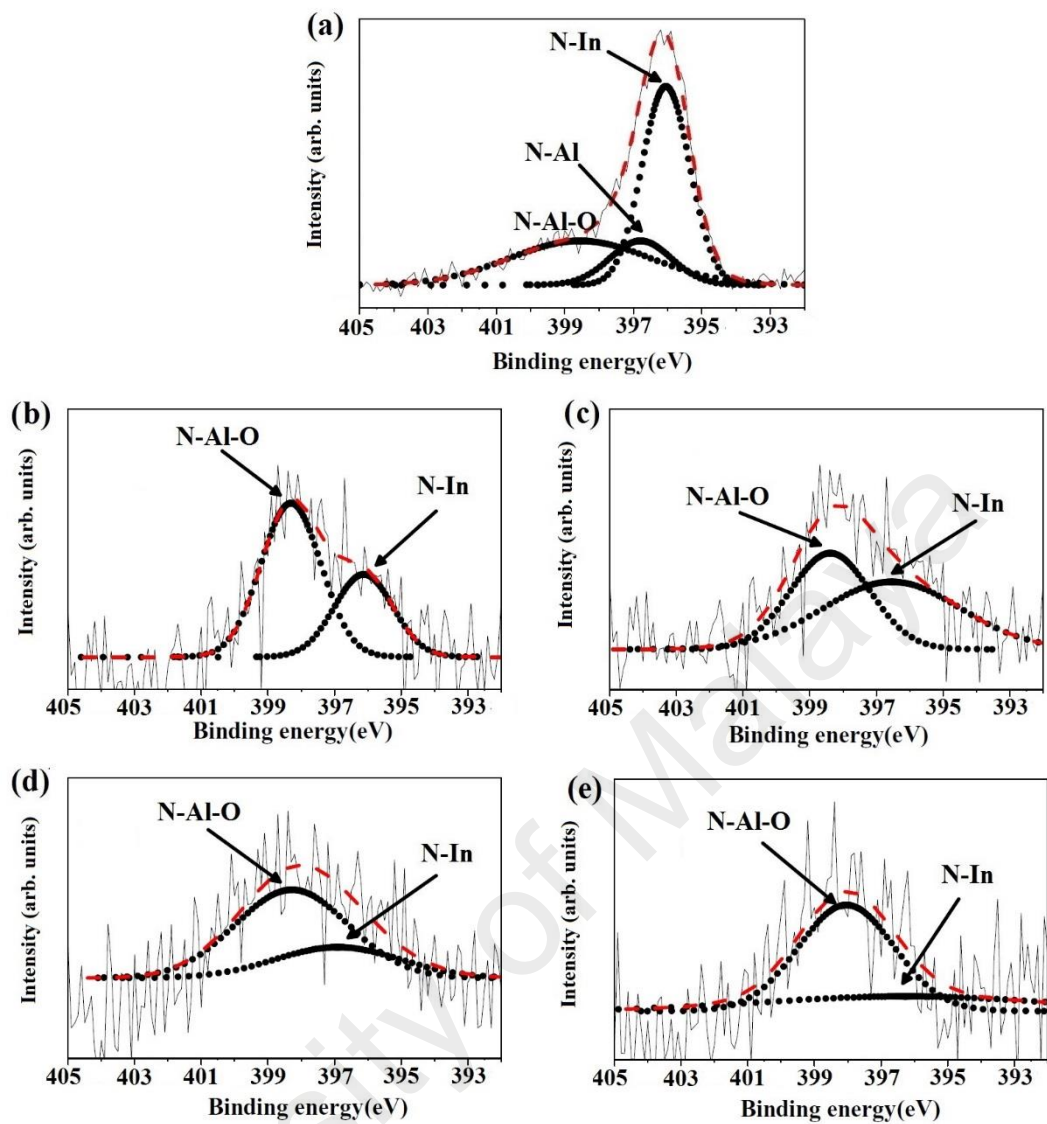


Figure 5.20: N1s core-level photoelectron spectra of the as-grown In-rich $\text{Al}_x\text{In}_{1-x}\text{N}$ films (a) and the films annealed at 200 °C (b), 300 °C (c), 400 °C (d) and 500 °C (e). At all annealing temperatures, the N1s spectra of $\text{Al}_x\text{In}_{1-x}\text{N}$ films are disappeared and the intensity of N–In dramatically decreases.

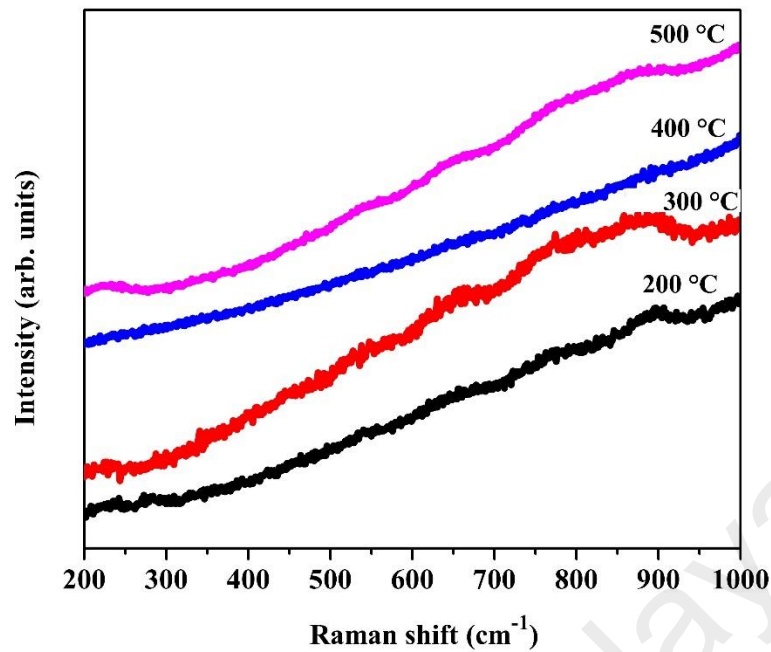


Figure 5.21: Micro-Raman spectra of the $\text{Al}_x\text{In}_{1-x}\text{N}$ samples annealed at various temperatures. The annealing process completely collapses all the films' structures into a totally amorphous state.

Figure 5.21 shows the Raman spectra of the $\text{Al}_x\text{In}_{1-x}\text{N}$ thin films annealed at various temperatures. No clear peak is detected showing that the annealing process completely collapses all the films' structures into a totally amorphous state. The oxygen incorporation from remnant oxygen in the annealing tube may have induced damage to the lattice of the as-grown films and contributes to the total amorphisation in the films.

The band gap energy of the $\text{Al}_x\text{In}_{1-x}\text{N}$ films annealed at various temperatures also estimated by drawing a tangential line for $(\alpha h\nu)^{1/2}$ versus $(h\nu)$ as shown in Figure 5.22. It is known that the $(\alpha h\nu)^{1/2}$ plot is used for calculation of the band gap energy of amorphous materials (Tauc, 1974). This method is also applied for indirect crystalline semiconductors but the transition for the amorphous semiconductor is characterized as “nondirect” transition which is different from “indirect” one. As shown earlier, the band gap energy of the as-grown $\text{Al}_x\text{In}_{1-x}\text{N}$ thin films is estimated to be 0.9 eV (Figure 5.17). After annealing of the sample at 200, 300, 400 and 500 °C, the E_g value increases

to 1.17, 1.40, 1.70 and 1.70 eV, respectively. The deviation is mainly due to the increased concentration of oxygen in the annealed films. Since the In composition in the annealed $\text{Al}_x\text{In}_{1-x}\text{N}$ thin films is very high, the oxidation process may be similar to InN. Alexandrov et al. (Alexandrov et al., 2004) suggested that in the oxidation process segregated oxygen species and these species are substituted into the N sites as InO and form $\text{InO}_y\text{N}_{1-y}$ ($y \sim 0.1$). Also, it has been shown that the oxygen can be trapped at the grain boundaries of the InN films and may result in the formation of amorphous indium oxide or indium oxynitride phases at these areas (Ji, Lau, Yang, & Zhang, 2007). The obtained E_g values for the annealed films are in good agreement with the XPS results showing that increasing oxygen incorporation also elevates the band gap energy.

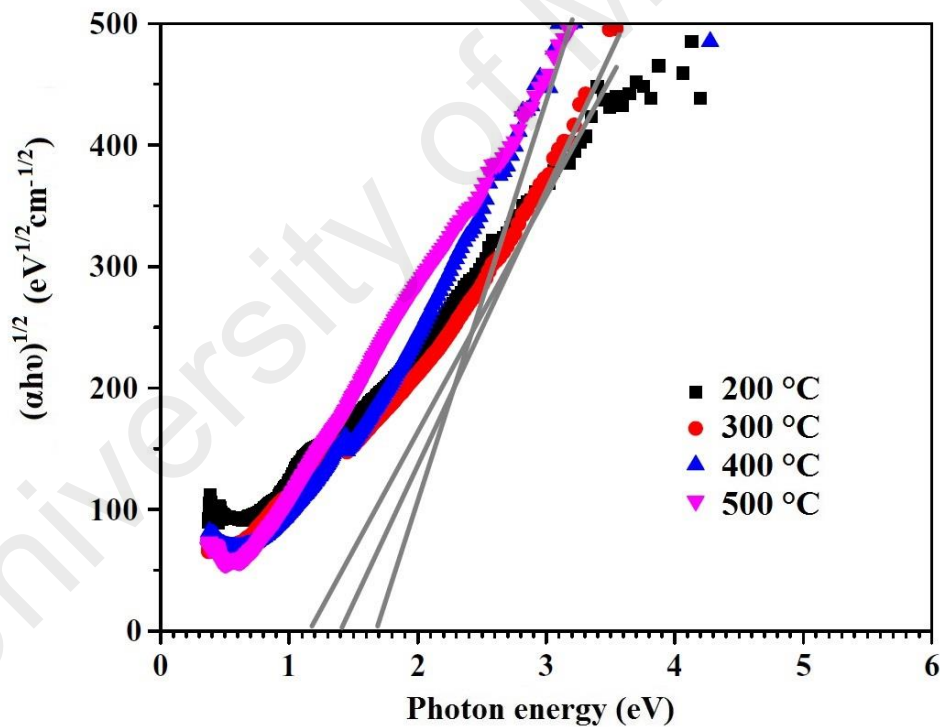


Figure 5.22: Plots of $(\alpha hv)^{1/2}$ versus hv for the $\text{Al}_x\text{In}_{1-x}\text{N}$ samples annealed at various temperature. After the $\text{Al}_x\text{In}_{1-x}\text{N}$ thin film with band gap energy of 0.90 eV was annealed at 200, 300, 400 and 500 °C, the E_g value increases to 1.17, 1.40, 1.70 and 1.70 eV, respectively.

5.5 Summary

In-rich ($x = 0.10$ and 0.18) and Al-rich ($x = 0.60$ and 0.64) $\text{Al}_x\text{In}_{1-x}\text{N}$ thin films were successfully deposited by varying the voltage applied to the indium wire (V_{In}) in plasma-assisted dual source reactive evaporation system. Raman results indicated that $E_2(\text{high})$ and $A_1(\text{LO})$ peaks of the $\text{Al}_x\text{In}_{1-x}\text{N}$ films are considerably blue-shifted by decreasing V_{In} and the $A_1(\text{LO})$ phonon mode of the Al-rich films exhibits two-mode behavior. Optical characterizations showed that the band gap energy of the films increased from 1.08 eV to 2.5 eV as the Al composition is varied from 0.1 to 0.64. A bowing parameter of 4.3 eV was calculated for the grown $\text{Al}_x\text{In}_{1-x}\text{N}$ films and the extrapolated value from the bowing equation was 0.85 eV for band gap energy of for InN. The effect of nitrogen gas flow rate on the structural, morphological and optical properties of In-rich and Al-rich $\text{Al}_x\text{In}_{1-x}\text{N}$ thin films was investigated. It was shown that Al incorporation (x) of both In-rich and Al-rich $\text{Al}_x\text{In}_{1-x}\text{N}$ thin films decreases as the N_2 flow rate is increased. FESEM images of the $\text{Al}_x\text{In}_{1-x}\text{N}$ films reflects that by increasing the N_2 flow rate agglomeration of grains is enhanced. Optical characterizations showed that the band gap energy of the In-rich and Al-rich films decreased by 0.18 eV and 0.41 eV, respectively, as the N_2 flow rate is increased from 40 to 100 sccm. Annealing studies shows that low-temperature (e.g., ≤ 300 °C) environments should be considered for application of these $\text{Al}_x\text{In}_{1-x}\text{N}$ films in the devices.

CHAPTER 6:

ELECTROCHEMICAL BEHAVIOR OF INDIUM- AND ALUMINUM-BASED NITRIDE THIN FILMS GROWN BY PLASMA-ASSISTED REACTIVE EVAPORATION

6.1 Introduction

This chapter discusses the electrochemical (EC) and photoelectrochemical (PEC) behaviors of the grown InN and Al-rich $\text{Al}_x\text{In}_{1-x}\text{N}$ thin films, respectively. It will be shown that the EC and PEC properties of the films are affected by the growth conditions. In chapter 4 it was shown that plasma RF power has a significant effect on structural and compositional properties of InN thin films. The first part of this chapter is devoted to the corresponding variations in donor density and the charge transfer dynamics between the InN thin film and electrolyte interfaces during the EC process. In chapter 5 the effects of nitrogen gas flow rates on the morphology and optical properties of Al-rich $\text{Al}_x\text{In}_{1-x}\text{N}$ films were presented. The second part of this chapter explores the effects of the studied growth parameter on the EC and PEC properties of the $\text{Al}_x\text{In}_{1-x}\text{N}$ films targeted for water splitting reactions. It will be shown that surface morphology as well as the elemental composition of the alloys are key factors in PEC surface reactions and electron transfer across the electrode-electrolyte interface.

6.2 Effects of RF Power on the Electrochemical Properties of Indium Nitride Thin Films

Electrolyte-based capacitance-voltage measurements were used to evaluate the surface charge of InN thin films grown at different RF power and were recorded by the Mott-Schottky (MS) plots capacitance method (D. Chauhan, Dass, & Shrivastav; Shinar & Kennedy, 1982) as a function of applied potential at a frequency of 1 kHz in 0.1 M KOH (Figure 6.1).

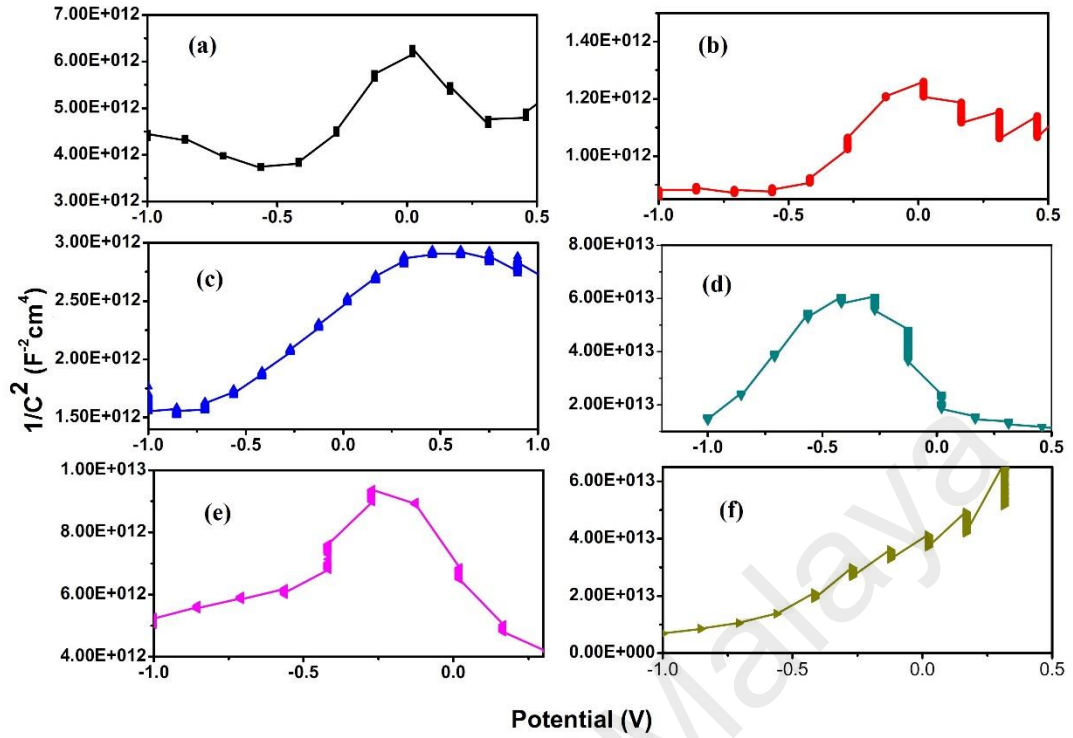


Figure 6.1: Mott–Schottky plots of the measured capacitance of the Si substrate (a) and the InN thin films grown at RF powers of 50 W (b), 100 W (c), 150 W (d), 200 W (e) and 250 W (f).

It is clear from the MS plots that all films show negative slopes at a lower bias which reflects the depletion of the surface accumulation (Ager et al., 2007; Ager et al., 2008). The donor density and the flat band potential for the InN thin films can be calculated by using the following Mott–Schottky equations (D. Chauhan et al.):

$$\frac{1}{C^2} = \frac{2}{qAN_d\epsilon\epsilon_0} \left[V_{bias} - V_{fb} \frac{KT}{q} \right], \quad (6.1)$$

where N_d is the donor density of InN thin films, C is the capacitance of the space charge region, ϵ is the static dielectric constant of InN, ϵ_0 is the permittivity of free space, q is the elementary electron charge, A is the interfacial area, K is Boltzmann's constant, T is the absolute temperature, V_{bias} is the applied potential and V_{fb} and is the flat band

potential. The N_d of each InN thin films was calculated from slope of linear part of the $1/C^2$ curves vs. V_{bias} in equation (6-1):

$$\text{Slope of } \left(\frac{1}{C^2}\right) \text{ vs. } (V_{bias}) = \frac{2}{qAN_d \epsilon \epsilon_0}. \quad (6.2)$$

The V_{fb} of the InN films was estimated by drawing the linear part of $1/C^2$ curves down to V_{bias} axis. The N_d and V_{fb} of InN thin films that calculated from MS equations were plotted as a function of the applied RF power in Figure 6.2. The N_d of the InN thin film decreases steeply with the increase in RF power from 50 to 150 W but decreases slowly with the increase in RF power to 200 W. This effect is due to the similar decreasing trend in the oxygen atomic percentage in the film as shown in Figure 4.11. A further increase in RF power to 250 W led to a slight increase in the oxygen concentrations (Figure 4.11). As explained in chapter 4, the high RF power results in the sputtering of N atoms from the growth surface. The energetic ions break up InN bonds and the unsatisfied bonds left by the N atoms are replaced by the O atoms. This produces a slight increase in donor concentration (from 1.1×10^{15} to $2.2 \times 10^{15} \text{ cm}^{-3}$).

As a matter of point, the EC properties of the grown thin films are attributed to oxynitride phase with a large electron density that screens the underlying ions and inhibits the oxidation reaction. Oxygen is the most common impurity and is mostly present on the surface of the nitride films, thus resulting in free charge accumulations (F. Zhang et al., 2012). The anodic current in the InN thin films deposited at lower RF power is larger due to the improved charge separation at the semiconductor-electrolyte interface as a result of higher presence of oxygen in the films composition. The V_{fb} of the InN thin films also shows a similar trend with respect to RF power (Figure 6.2). Thus, it can be concluded that the V_{fb} behavior is due to the presence of oxygen donor atoms in the film structure which causes the band bending at the InN thin film/electrolyte interface.

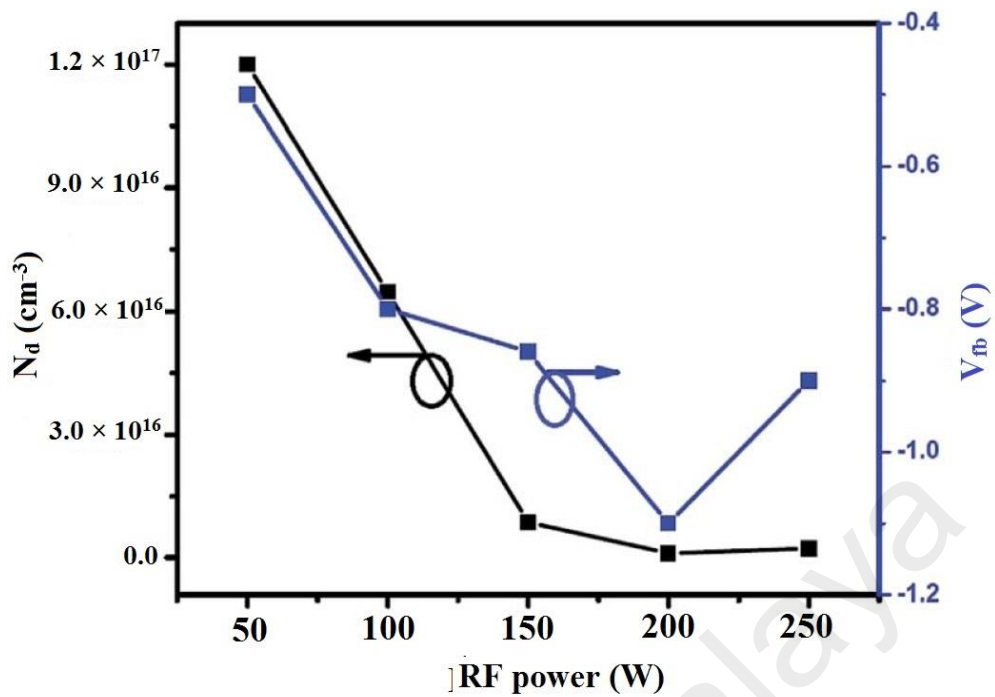


Figure 6.2: Dependence of donor density (N_d) and flat band potential (V_{fb}) of the InN thin films on the applied RF power. At lower RF powers the N_d of the films is higher while the V_{fb} is more negative at higher RF power. (Note: The lines joining the points are only used as a guide to the eye.).

The linear sweep voltammogram (LSV) of InN thin films were recorded in the presence of 0.1 M KOH and the results are shown in Figure 6.3. It can be seen that, after 0 V, the anodic current increases with the increment of applied bias for all the InN thin films. The bare Si substrate shows a negligible anodic current due to the absence of electroactive species on the surface. By increasing RF power during the growth of InN thin films from 50 to 200 W, the anodic current decreases. A further increase in the RF power to 250 W results in a slight increase of the anodic current. This may be due to the decrease in donor density in the InN thin film as a result of the increase in RF power as (Figure 6.2). Hence, the observed anodic oxidation current is due to the oxygen evolution reaction on the electrode surface in the presence of KOH (S. Chen & Qiao, 2013).

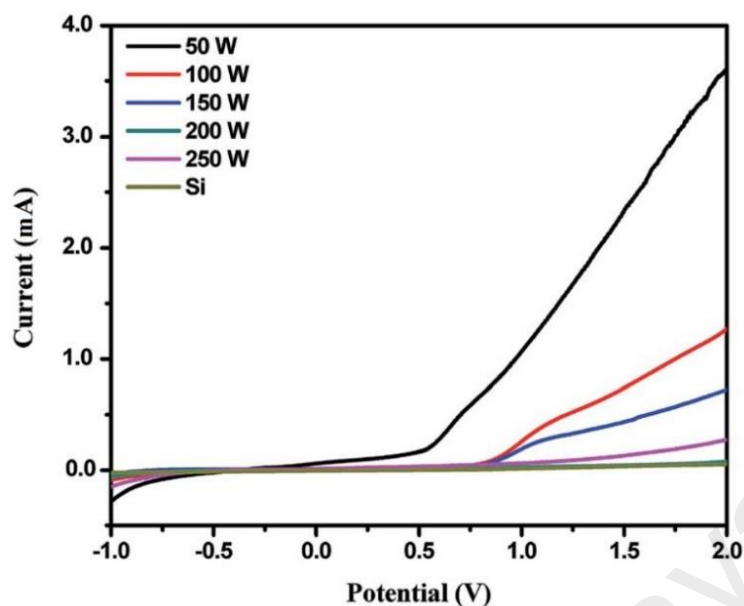


Figure 6.3: Linear sweep voltammograms of the InN thin films grown at different RF powers. The films grown at lower RF power show higher anodic current.

Furthermore, the onset of anodic potentials is slowly shifted to a more positive region by increasing RF power. Avasarala et al. (Avasarala & Haldar, 2010) concluded that the oxidation current of TiN in the potential range of 1–1.2 V is low due to the corrosion resistance behavior of the semiconductor. As such, the decrease in the anodic current could be also due to the increase in the nitrogen content in the film which results in corrosion resistance (Avasarala & Haldar, 2010).

Also, it has been shown that the photoelectrodes with less defects shows higher resistance against corrosion (Deutsch, Koval, & Turner, 2006). From XRD results (Figure 4.8) it can be seen that by increasing the RF power from 50 to 200 W, InN thin films with additional nitrogen content and higher crystallinity (less defects) are obtained. Higher presence of oxygen contamination in the InN films grown at low RF power results in large lattice mismatch in the films and less resistance of them against corrosion. Again for the InN thin film grown at 250 W (Figure 6.2), the onset potential is shifted back towards a lower potential due to a slight decrease in the nitrogen content of the film.

Electrochemical impedance spectroscopy (EIS) was performed for the InN thin films to investigate the charge transfer dynamics between the film/electrolyte interfaces during the electrochemical process. Nyquist plots showed that the bare Si substrate showed a large semicircle due to very poor conductivity as-compared to the InN deposited on the Si substrate (Figure 6.4 (a)). By increasing the RF power from 50 to 200 W, the semicircle diameter increases and then decreases at 250 W (Figure 6.4 (b)-(f)).

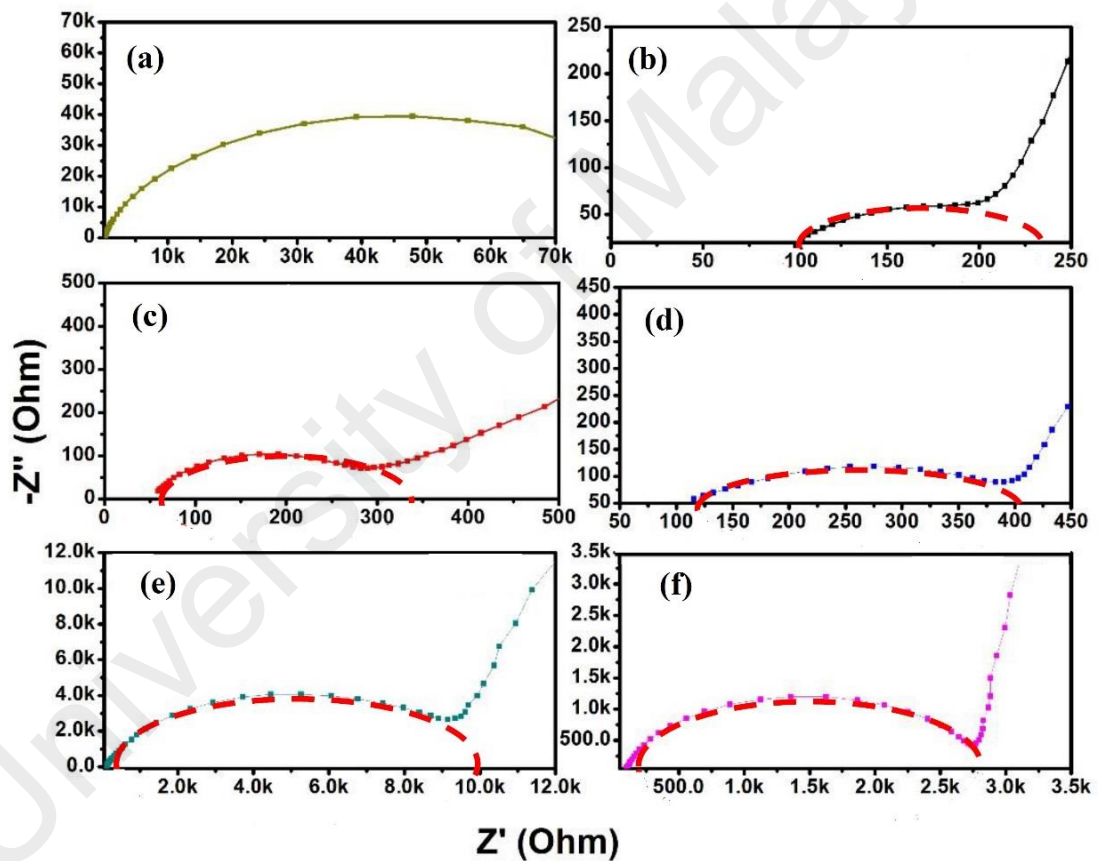


Figure 6.4: Nyquist plots of the Si substrate (a) and the InN thin films deposited at the RF powers of 50 W (b), 100 W (c), 150 W (d), 200 W (e) and 250 W (f).

The observed semicircle is due to the charge-transfer resistance (R_{ct}) that took place at the electrode/electrolyte interface. According to Figure 6.5, increasing the RF power up to 200 W have resulted in an increase in the R_{ct} value but a further increase to 250 W led to a significant decrease in R_{ct} value (Figure 6.5). The observed R_{ct} vs RF power trend shows that the EIS data are in good agreement with the LSV results. Both sets of results show direct correspondence with the RF power-induced variation of donor density in the InN thin film. A decrease in the R_{ct} value leads to an increase in the conductivity and the anodic current of the InN thin films grown at a lower RF power (Figure 6.5).

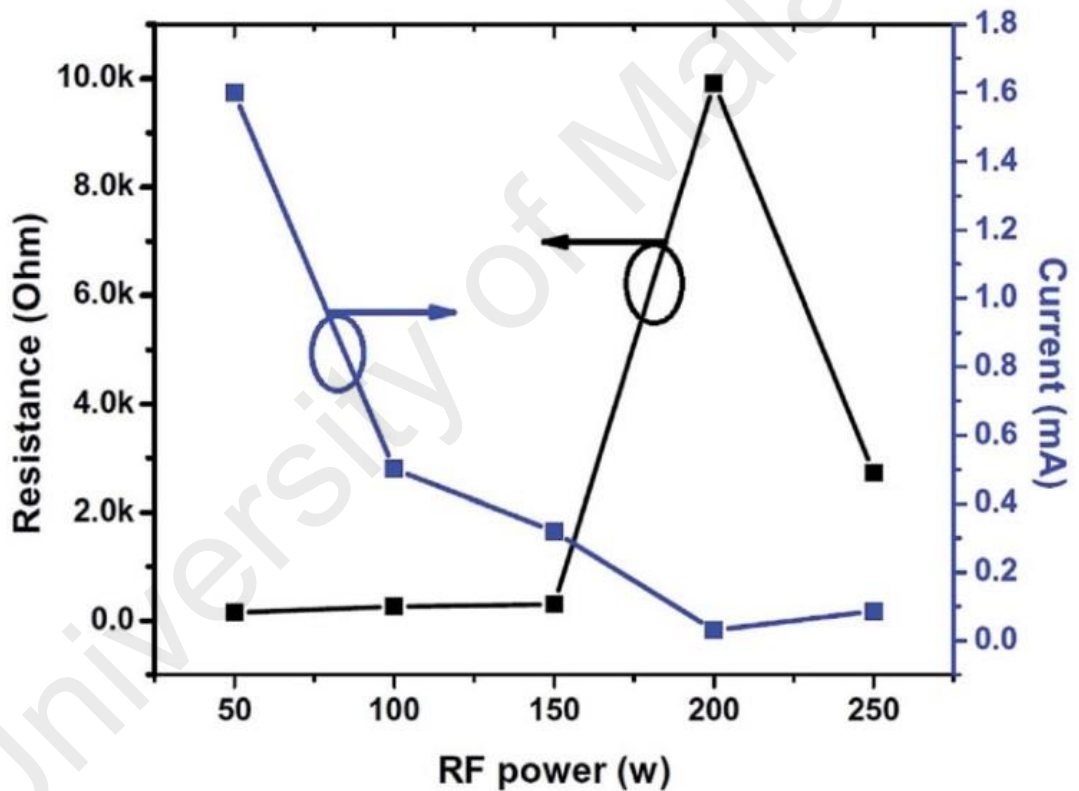


Figure 6.5: Dependence of current and resistance of the InN thin films on the applied RF powers. By increasing the power to a certain value the resistance increases while the current decreases. (Note: The lines joining the points are only used as a guide to the eye.).

The Bode phase plots were also recorded to provide detailed understanding of charge-transfer resistance of the InN thin films as shown in Figure 6.6. The bare Si substrate shows a broad and indefinite peak in the frequency region of 10 Hz-10 kHz due to the larger charge-transfer resistance at the electrode/electrolyte interface and the lack of availability of electroactive species on the bare Si substrate. After the deposition of the InN thin film on the surface of the Si substrate, a well-resolved peak in the frequency region of 10 Hz–10 kHz appears due to a decrease in the charge-transfer resistance.

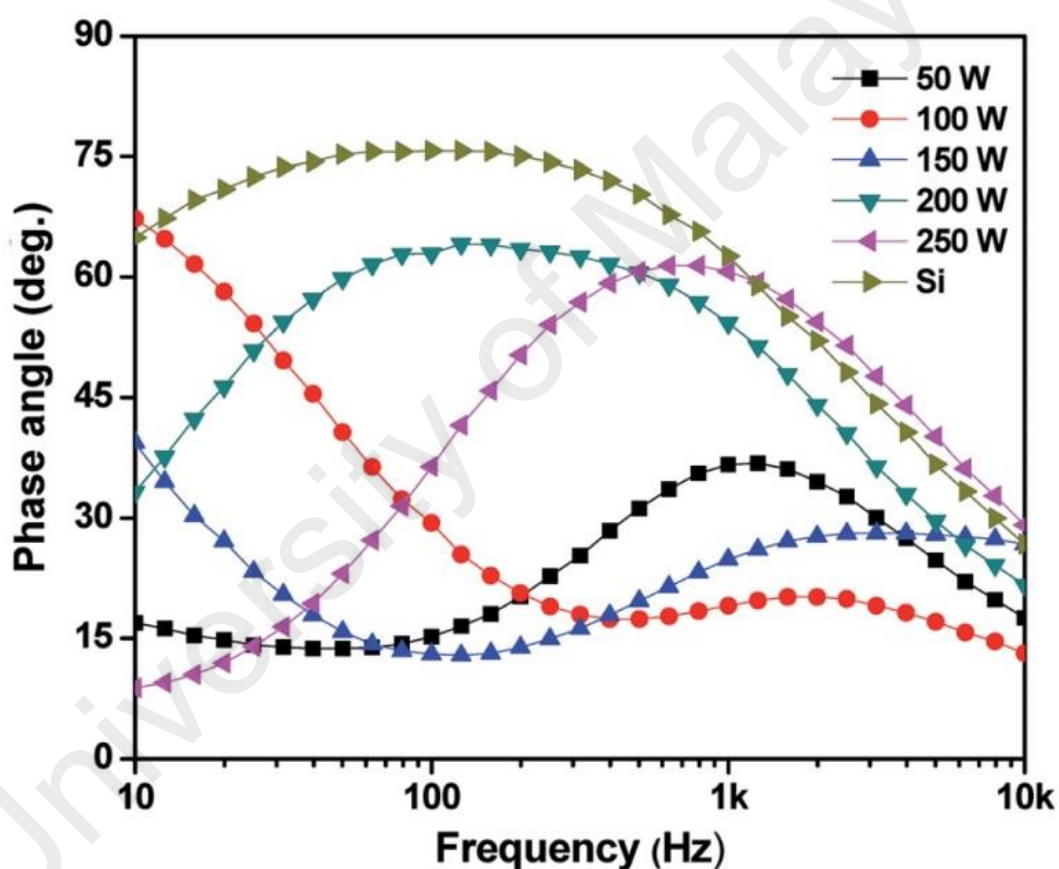


Figure 6.6: Bode angle phase plots of the InN thin films grown at different RF power in the presence of 0.1 M KOH. The phase angles for the InN thin films grown at different RF powers are all less than 90°.

The dependence of the Bode phase angle of the InN thin films on the RF power is shown in Figure 6.7. The angle initially decreases with the increment of power from 50 to 100 W and it increases as the power is ramped up to 200 W and then decreases marginally at 250 W. Matemadombo and Nyokong (Matemadombo & Nyokong, 2007) have reported that when the phase angle is greater than or equal to 90°, the electrode behaves like an ideal capacitor and if it is less than 90°, the electrode is permeable to solution ions. From Figure 6.7 it is clear that the phase angles for the InN thin films grown at different RF powers are all less than 90°, which indicates that these thin films can easily permeate OH⁻ ions. Hence, the low Bode phase angles for the films deposited at RF powers of 100 and 150 W indicate higher permeability to OH⁻ ions, which results in lower resistivity. These results demonstrate that the Bode phase angle trend only corresponds to the atomic N percentage for the films deposited at RF powers of 100 to 250 W. In the other words, the high O atomic percentage makes the Bode plot not sensitive to the N content in the film structure as shown by the film deposited at RF power of 50 W.

Moreover, the electron recombination lifetime for each sample (τ_n) can be measured from the corresponding characteristic frequency peak (f_{max}) using the following equation:

$$\tau_n = 1/2\pi f_{max}. \quad (6.3)$$

The dependence of τ_n values of the InN thin films on the RF power is shown in Figure 6.7. It can be seen that for the RF power from 50 to 150 W, the τ_n remains almost constant and increasing the power to 200 W significantly increases the τ_n . Further increase in RF to 250 W leads to a sharp shift in the τ_n value. The results show that the high τ_n values of InN thin films grown at higher RF power could effectively reduce the electron recombination and thereby enhance electrochemical performance. Also, it seems

that the τ_n of the InN films deposited at various RF powers is independent of the N percentage, conductivity and resistance of the films as different behaviors are observed for these parameters at the various growth conditions.

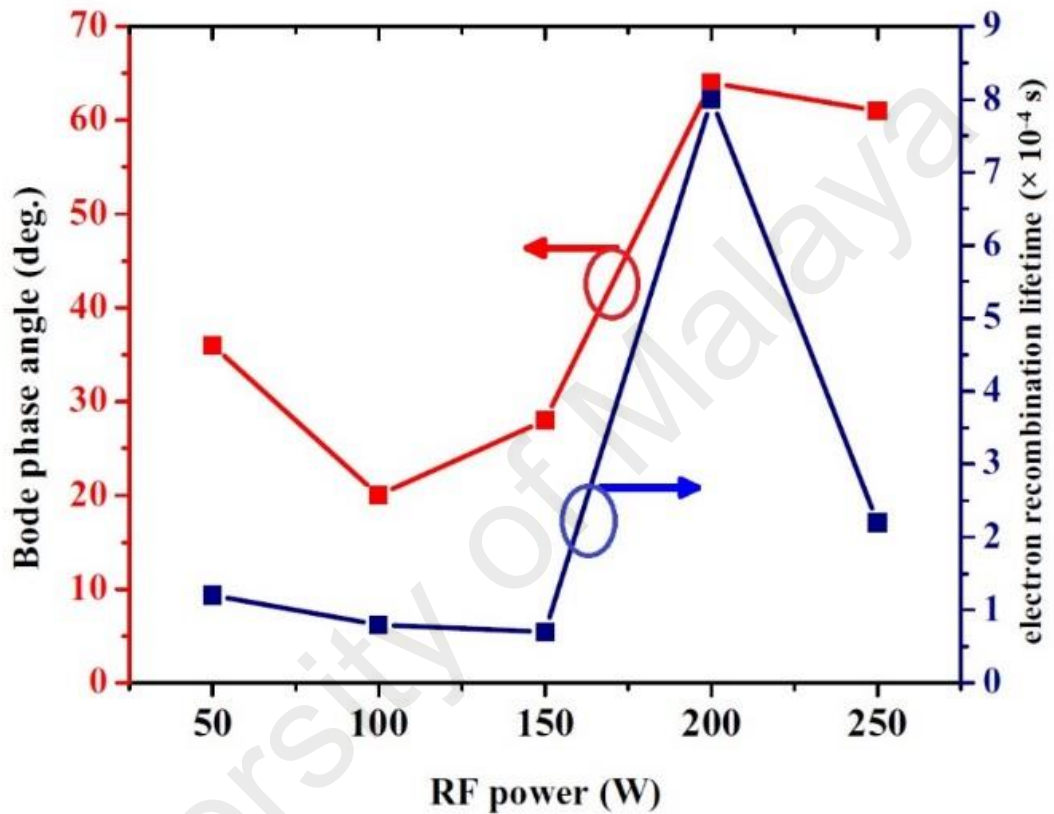


Figure 6.7: Dependence of Bode phase angle and electron recombination lifetime (τ_n) of the InN thin films on the applied RF powers. (Note: The lines joining the points are only used as a guide to the eye.).

6.3 Electrochemical and Photoelectrochemical Behaviors of Aluminum Indium Nitride Thin Films Grown by Plasma-Assisted Dual Source Reactive Evaporation

The photoelectrochemical performance of the $\text{Al}_x\text{In}_{1-x}\text{N}$ thin films grown at various N_2 flow rates was investigated for water splitting by using LSV techniques under simulated solar AM 1.5 G irradiation in the presence of 0.1 M PBS (pH 7.2) at a scan rate of 50 mV/s. Figures 6.8(a) and (b) show the LSV of the samples in the absence and presence of simulated solar irradiation, respectively. It can be seen that under both conditions, after 0 V, the anodic current increases with the increment in the applied bias for all the $\text{Al}_x\text{In}_{1-x}\text{N}$ thin films. Also, by increasing the N_2 flow rate from 40 to 80 sccm during the growth of $\text{Al}_x\text{In}_{1-x}\text{N}$ thin films, the anodic current (in both dark and light conditions) significantly increases and then decreases for the thin film grown at the N_2 flow rate of 100 sccm.

The EC and PEC behaviors of the $\text{Al}_x\text{In}_{1-x}\text{N}$ thin films can be explained by taking into account the dependence of the alloys morphology on N_2 flow rate during the deposition process. From Figure 5.14 it was observed that excessively large grains cover the whole surface of the AlInN films deposited at $\text{N}_2 = 60$ and 80 sccm. These large-sized grains with porous morphology act as an effective channel for electron transfer, enhance surface reaction rates and facilitate the interfacial electron transfer process due to the large electrode-electrolyte interfacial contact area. This has been proven to be crucial for improvement of the electronic interactions and interfacial electron transfer at the electrode/electrolyte interface (Manivasakan, Ramasamy, & Kim, 2014).

More interestingly, Figure 6.8 (a) and (b) show that the anodic current significantly increases when the simulated solar AM 1.5 G is illuminated onto the samples, especially for those grown at nitrogen flow rates of 60 and 80 sccm. For instance, at 1.23 V the current increases from 0.09 mA to 0.8 mA upon the $\text{Al}_x\text{In}_{1-x}\text{N}$ sample grown at $\text{N}_2 =$

80 sccm being exposed to the light. This could be attributed to the band gap values and the band alignments of $\text{Al}_x\text{In}_{1-x}\text{N}$ alloys with different Al(In) compositions which have been reported to be crucial in photoelectrochemical water splitting reactions, as explained in chapter 2. The results in Section 5.2 of this thesis showed that the films deposited at the N_2 flow rate of 60 and 80 sccm has a band gap energy of 2.12 eV and the Al composition of 58% and 55%, respectively. The Al composition and band gap energy values are consistent with the values reported by Collazo and Dietz (Ramón Collazo & Dietz III, 2013), who showed that $\text{Al}_x\text{In}_{1-x}\text{N}$ with Al composition of ~55% possesses suitable band alignment and band gap (2.2 eV) for photoelectrochemical water splitting. They reported that at higher Al composition (e.g., $\geq 65\%$) the corresponding maximum potential of the valence band is more positive whereas at lower Al composition (e.g., $\leq 50\%$) the band-edge potentials of the alloy do not properly straddle the H^+/H_2 and $\text{O}_2/\text{H}_2\text{O}$ redox potentials (Ramón Collazo & Dietz III, 2013). Hence, the photocurrent enhancement of the $\text{Al}_x\text{In}_{1-x}\text{N}$ films deposited at $\text{N}_2 = 60$ and 80 sccm could be due to the composition and the band gap energy of the samples. The band alignment and band gap of the films are similar to those of $\text{In}_x\text{Ga}_{1-x}\text{N}$ alloy with ~25% – 30% indium composition which has been widely reported as an efficient photocatalyst material for overall water splitting (AlOtaibi et al., 2013).

The time dependence of the photocurrent was measured for the $\text{Al}_x\text{In}_{1-x}\text{N}$ thin films grown at nitrogen gas flow rate of 80 sccm under simulated AM 1.5 G illumination (Figure 6.9). Measurements were also performed for the other films grown at the N_2 flow rates of 40, 60 and 100 sccm. No significant photo-response was observed for the films grown at N_2 flow rates of 40 and 100 sccm and the photo-response of the films grown at N_2 flow rate of 60 sccm (not shown here) was quite similar to that of the film grown at N_2 flow rate of 80 sccm.

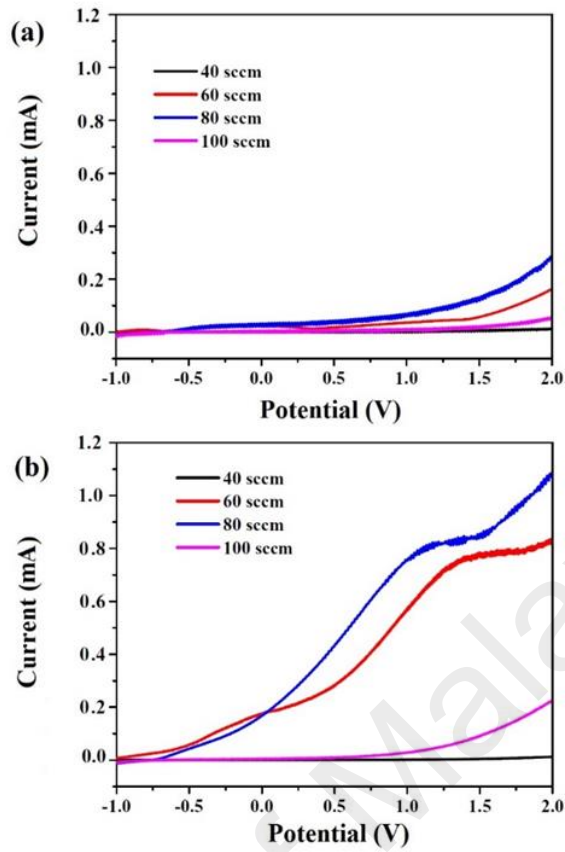


Figure 6.8: Linear sweep voltammograms (LSV) of the $\text{Al}_x\text{In}_{1-x}\text{N}$ thin films grown at different N_2 flow rates without (a) and under (b) simulated AM 1.5 G illumination. The films grown at the N_2 flow rates of 60 and 80 sccm show significant photocurrent.

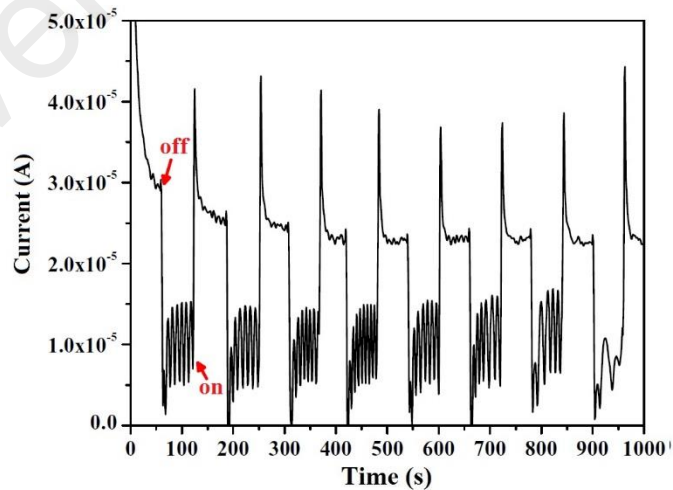


Figure 6.9: Amperometric $i-t$ curve of the $\text{Al}_x\text{In}_{1-x}\text{N}$ thin films grown at nitrogen flow rate of 80 sccm under simulated AM 1.5 G illumination. A rapid rise in the current upon illumination is seen from the cycles confirming considerable PEC behavior of the sample.

Eight cycles of “on-and-off” lighting were performed during measurement, as shown in Figure 6.9. A rapid rise in the current upon illumination can be seen from the cycles and this confirms considerable PEC behavior of the sample. The rise and fall in the photocurrent is due to the photo-induced charge separation. Upon illumination, the electrons in the valence band of the $\text{Al}_x\text{In}_{1-x}\text{N}$ thin films are excited to the conduction band leaving holes in the valence band. These electrons are separated from the interface and are consumed to generate H_2 at the counter electrode. The holes produced in the valence band at the interface are consumed to oxidize the water to produce O_2 . When the light was turned off, this process stopped resulting in the drop in the photocurrent.

The obtained photocurrent and photo-response for the $\text{Al}_x\text{In}_{1-x}\text{N}$ thin films grown by plasma-assisted reactive evaporation is lower than those for $\text{In}_x\text{Ga}_{1-x}\text{N}$ deposited by well-established MOCVD technique (Juodkazytė et al., 2014; S.-Y. Liu et al., 2013) possibly due to the lower presence of oxygen contamination in the later. However, it should be noticed that the investigation of photoelectrochemical behavior of $\text{Al}_x\text{In}_{1-x}\text{N}$ thin films deposited by plasma-assisted reactive evaporation is in early stage and further studies may result in improved photocurrent and photo-response for the $\text{Al}_x\text{In}_{1-x}\text{N}$ photoelectrodes.

Electrochemical impedance spectroscopic (ELS) analysis was performed to examine further insights into the electrochemical characteristics of $\text{Al}_x\text{In}_{1-x}\text{N}$ thin films. The Nyquist plots produced from measurements in 0.1 M PBS are displayed in Figure 6.10 (a)-(d). It can be observed that all the plots exhibit a quartercircle-like curve, which is attributed to the charge-transfer resistance (R_{ct}) that has taken place at the electrode/electrolyte interface.

The R_{ct} values for each sample are estimated from diameter of the curves and are summarized in Table 6.1. It can be clearly seen that the value decreases with an increase

in nitrogen gas flow rate from 40 to 80 sccm and then increases for 100 sccm. The decrease in R_{ct} value with increase in N_2 flow rate from 40 to 80 sccm is consistent with the LSV results presented earlier where an increase in the anodic current was recorded with the increase in N_2 flow rate in this range. This behavior of the R_{ct} value could be related to the interconnection between particles at the surface of the alloys. By increasing the nitrogen flow rate from 40 to 80 sccm for the growth of $Al_xIn_{1-x}N$ thin films, constituent particles of the films become highly agglomerated and the surface roughness of the films increases (Figure 5.14).

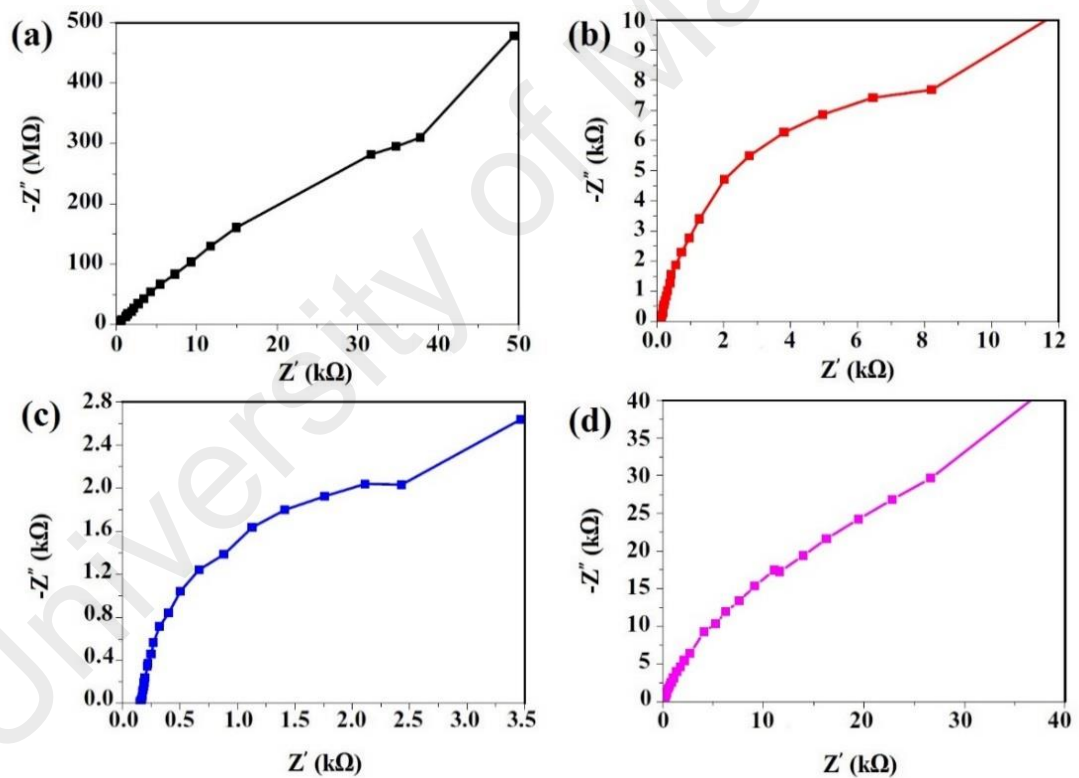


Figure 6.10: Nyquist plots of the $Al_xIn_{1-x}N$ thin films deposited at the N_2 flow rates of 40 sccm (a), 60 sccm (b), 80 sccm (c) and 100 sccm (d). The film deposited $N_2 = 80$ sccm shows the lowest quartercircle-like diameter (the lowest resistance).

For the films that have been deposited at nitrogen gas flow rates of $N_2 = 60$ and 80 sccm the particles show highly agglomerated particles with cauliflower-shaped grains separated by channels resulting in a porous film structure. The R_{ct} value appears to decrease with the increase in grain size due to the higher interconnectivity between particles and the increase in the channel width joining the grains. In the case of the $Al_xIn_{1-x}N$ thin film grown at $N_2 = 100$ sccm, the grain sizes and the channel widths are reduced and the inter-particle connectivity is not uniform, thus leading to higher R_{ct} . It can be deduced that the R_{ct} value is dependent on the grain size and the porosity of the film. Increase in the channel width increases the porosity of the film and results in higher interconnectivity between the grains and the permeation of electrolyte into the film results in a more efficient charge-transfer across the electrode-electrolyte interface. Thus reducing the possibility of charge recombination and enhancing the photocurrent response against water oxidation.

Table 6.1: Calculated compositional, optical and electrical values of $Al_xIn_{1-x}N$ films grown at various N_2 flow rates.

| N_2 flow rate (sccm) | Al ratio, x | Band gap (eV) | Electrical properties | | | |
|---------------------------|---------------|---------------|------------------------|---------------|--------------|----------------------|
| | | | R_{ct} (k Ω) | τ_n (ms) | V_{fb} (V) | N_d (cm $^{-3}$) |
| 40 | 0.66 | 2.33 | 92.3 | 1 | -0.84 | 1.9×10^{17} |
| 60 | 0.58 | 2.12 | 16.1 | 4 | -1.35 | 1.1×10^{17} |
| 80 | 0.55 | 2.12 | 3.9 | 10 | -1.37 | 8×10^{16} |
| 100 | 0.48 | 1.92 | 66.4 | 5 | -1.30 | 1.3×10^{17} |

Figure 6.11 shows the Bode phase plots that were obtained for the $Al_xIn_{1-x}N$ thin films grown at various N_2 flow rates. The sample deposited at $N_2 = 40$ sccm shows a broad and indefinite peak in the frequency region of 10 Hz–10 kHz due to the large charge-transfer resistance at the electrode/electrolyte interface and lack of availability of electroactive species. As the flow rate is increased from 40 to 100 sccm, a well-resolved peak in the frequency region of 10 Hz–10 kHz is observed for all films due to a decrease

in the charge-transfer resistance. The characteristic frequency peaks were obtained at the frequencies of 143, 40, 15 and 33 Hz for AlInN thin films grown at nitrogen gas flow rates of 40, 60, 80 and 100 sccm, respectively. The corresponding Bode phase angles are 79° , 67° , 76° and 74° for $N_2 = 40, 60, 80$ and 100 sccm, respectively. As mentioned earlier, when the phase angle is greater than or equal to 90° , the electrode behaves like an ideal capacitor, whereas if it is less than 90° the electrode is permeable to the constituent ions of the solution (Matemadombo & Nyokong, 2007). Here, the obtained Bode phase angles of all $Al_xIn_{1-x}N$ films are less than 90° suggesting that these thin films can be easily permeated by ions.

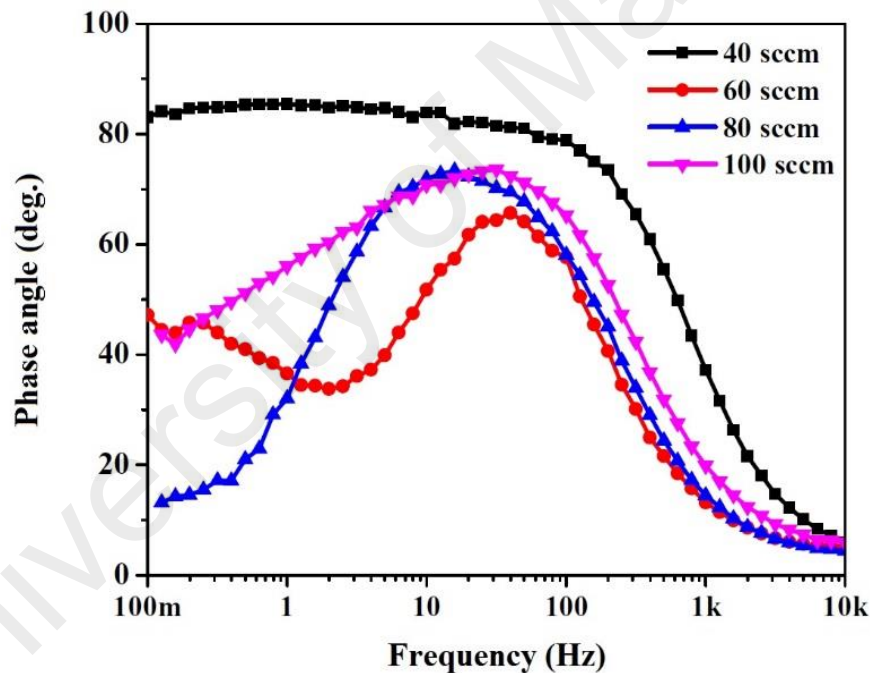


Figure 6.11: Bode angle phase plots of the $Al_xIn_{1-x}N$ thin films grown at different N_2 flow rates in the presence of 0.1 M PBS. The obtained Bode phase angles of all $Al_xIn_{1-x}N$ films are less than 90° suggesting that these thin films can be easily permeated by ions.

Moreover, the electron recombination lifetime of each sample, τ_n , can be measured from Equation 6.3. The calculated τ_n values of the films deposited at different nitrogen gas flow rates are shown in Table 6.1 for comparison purposes. It is noteworthy that the τ_n value for the photo-generated charge carriers over the ternary $\text{Al}_x\text{In}_{1-x}\text{N}$ alloy grown at $\text{N}_2 = 80$ sccm is the highest, which could effectively reduce the electron recombination and thereby enhance photoelectrochemical performance. Hence, the significant decrease in the Bode phase angle value towards zero and the shift to a lower peak frequency enhance the permeability of the ions and contribute to the enhancement of the electrochemical performance.

Electrolyte-based capacitance–voltage measurements were performed to investigate the variations in electronic properties of the $\text{Al}_x\text{In}_{1-x}\text{N}$ thin films by using Mott-Schottky (MS) plots, in which $1/(\text{Capacitance})^2$ is a function of the applied potential at a frequency of 1 kHz in 0.1 M PBS under dark conditions (Fig. 6.12). The MS plots of all samples clearly show a positive slope which reflects the n-type properties of the $\text{Al}_x\text{In}_{1-x}\text{N}$ films.

The donor densities (N_d) and flat band potentials (V_{fb}) that were calculated from Equations (6.1) and (6.2) for the $\text{Al}_x\text{In}_{1-x}\text{N}$ thin films are summarized in Table. 6.1. It can be seen that there is a shift in V_{fb} toward negative values from -0.84 to -1.37 V when the N_2 flow rate is increased from 40 to 80 sccm, respectively. Further increase in the N_2 flow rate to 100 sccm, shifts the flat band potential back to -1.30 V. It is well-known that semiconductor materials with a more negative flat band potential have a better ability to facilitate charge transport in PEC applications (Rai et al., 2014; Yusoff et al., 2015). This indicates that $\text{Al}_x\text{In}_{1-x}\text{N}$ thin films deposited at nitrogen gas flow rate of 80 sccm has a significant photoelectrochemical performance which is in good agreement with LSV results (Figure 6.8). Furthermore, N_d decreases as the flow rate increase from 40 to

80 sccm and then increases for the films grown at $N_2 = 100$ sccm. The observed behavior of N_d corresponds to the inclusion of oxygen impurity within structure of the $Al_xIn_{1-x}N$ thin films grown at various N_2 flow rates (Figure 5. 12).

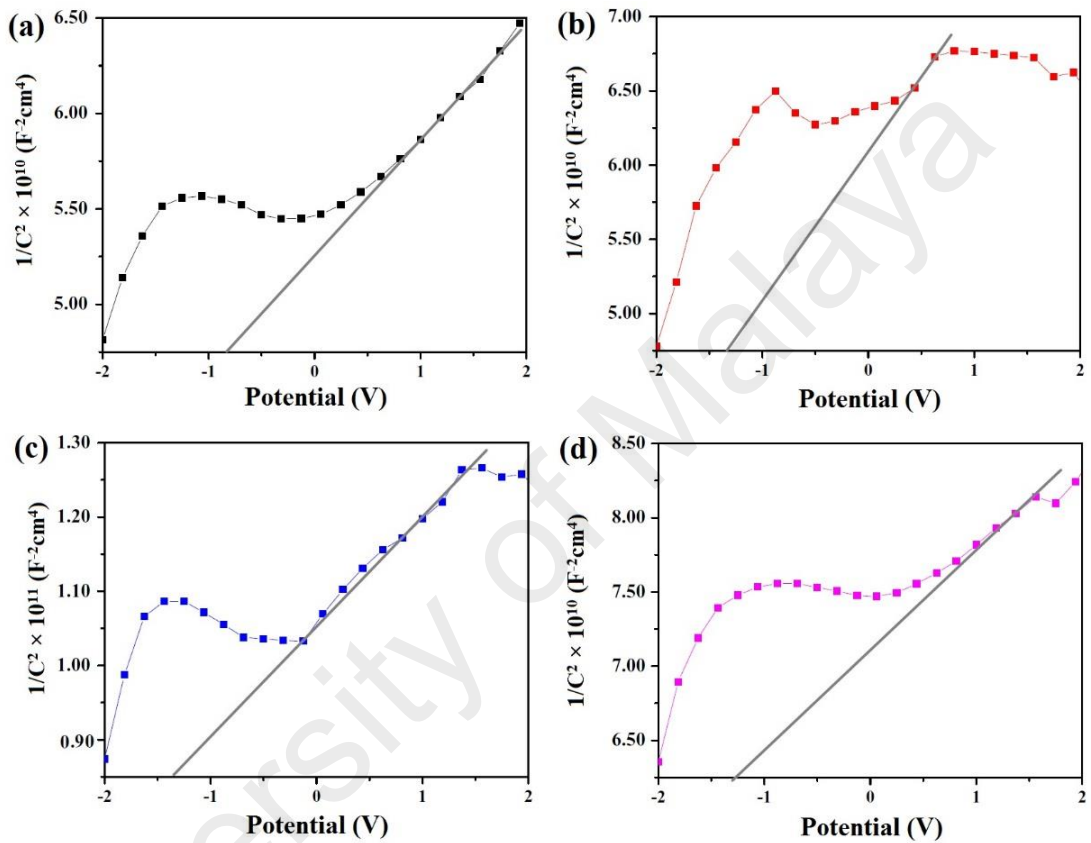


Figure 6.12: Mott–Schottky plots of the measured capacitance of the $Al_xIn_{1-x}N$ thin films grown at N_2 flow rates of 40 sccm (a), 60 sccm (b), 80 sccm (c) and 100 sccm (d). Donor densities (N_d) and flat band potentials (V_{fb}) of all the films were calculated using this plots and Equations (6.1) and (6.2).

6.4 Summary

The electrochemical properties of InN thin films were investigated in terms of their water splitting ability in the presence of 0.1 M KOH. Changes in donor density and flat band potentials with respect to RF power were observed from MS plots. The LSV data revealed a decrease in the anodic current with increases in nitrogen gas content in the InN thin films. EIS studies showed that an increase of R_{ct} value with RF power leads to increased resistivity. Bode phase plots suggest that these thin films can be easily permeable to OH^- ions at the InN thin film/electrolyte interface. The good electrochemical behavior of InN thin films showed that this material could be a potential candidate for water splitting application. The photoelectrochemical properties of $\text{Al}_x\text{In}_{1-x}\text{N}$ ($0.48 \leq x \leq 0.66$) thin films were investigated for water splitting capability in the presence of 0.1 M PBS. The PEC results of $\text{Al}_x\text{In}_{1-x}\text{N}$ thin films indicated that the photocurrent for the $\text{Al}_x\text{In}_{1-x}\text{N}$ thin film grown at N_2 flow rate of 80 sccm is ~ 10 -fold higher than the dark current. EIS results revealed that the R_{ct} value of $\text{Al}_x\text{In}_{1-x}\text{N}$ thin film decreases as the N_2 flow rate is increased from 40 to 80 sccm. From the Mott-Schottky (MS) plots it was deduced that by increasing N_2 flow rate up to 80 sccm, the flat band potential shifts toward more negative values. The good PEC behavior of $\text{Al}_x\text{In}_{1-x}\text{N}$ thin films grown by plasma-assisted dual source reactive evaporation showed their promising potential in PEC water splitting application.

CHAPTER 7:

CONCLUSION AND SUGGESTIONS FOR FUTURE WORKS

7.1 Overview

This thesis presents the research that was focused on the growth of indium- and aluminum-based nitride thin films by plasma-assisted reactive evaporation, which to the best of the author's knowledge has not been reported by other researchers. The structure, morphology, optical and electrochemical properties of AlN, InN and $\text{Al}_x\text{In}_{1-x}\text{N}$ thin films deposited by this technique using a deposition system specifically developed for this work have been investigated. The most influential growth parameters on specific properties of each of these films have been investigated in great details to achieve the objectives of this work as-highlighted in Chapter 1. This work is divided into four important parts in order to achieve the objectives.

The first part of this work involved the investigations on the structure, composition and morphology of AlN thin films grown on Si(111) substrate at different filament-substrate distances. The second part of this work is focused on studying the morphology, crystallinity, composition and optical properties of InN thin films deposited on Si(111) and quartz substrates at the different RF powers. The main aim of carrying out these two parts is to determine the optimized filament-substrate distances and RF power for the growth of $\text{Al}_x\text{In}_{1-x}\text{N}$ thin films, which is done in the third part of this work. The third part of this work is divided into three steps. The AC voltages applied to the filament holding the indium wire were varied in the first step of this part to obtain $\text{Al}_x\text{In}_{1-x}\text{N}$ thin films with a wide range of elemental compositions covering both In-rich and Al-rich films. The second step involved studying the effects of nitrogen flow rate on the properties of the selected Al-rich and In-rich $\text{Al}_x\text{In}_{1-x}\text{N}$ thin films. The last step was performed to study the stability of the grown $\text{Al}_x\text{In}_{1-x}\text{N}$ alloys at various annealing temperatures. XRD,

Raman spectroscopy, FESEM and UV-VIS-NIR spectroscopy techniques were used for the characterization of the films grown in these three parts of the work. The last part of this work was conducted to study the electrochemical properties of selected InN and Al-rich $\text{Al}_x\text{In}_{1-x}\text{N}$ thin films that have been grown in the second and third part of this work. The aim of this study is to investigate electrochemical (EC) and photoelectrochemical (PEC) characteristics on the deposited InN and Al-rich $\text{Al}_x\text{In}_{1-x}\text{N}$ thin films, respectively. The electrochemical behaviors of the InN thin films were investigated in 0.1 M KOH electrolyte, while for the $\text{Al}_x\text{In}_{1-x}\text{N}$ thin films 0.1 M PBS electrolyte was used. Linear sweep voltammograms (LSV), electrochemical impedance spectroscopy (EIS), Bode phase plots, Electrolyte-based capacitance–voltage measurements and cyclic voltammograms were utilized for electrochemical study of the thin films.

7.2 Conclusion

This work has been successfully carried out and the major findings obtained are highlighted below:

- A simple, cost-effective and environmental-friendly home-built plasma-assisted reactive evaporation system has been successfully developed for controlled growth of AlN, InN and AlInN thin films with tunable optical and electrochemical properties. This deposition system was able to grow the above-mentioned thin films at high deposition rate.
- The filament-to-substrate distance and RF power were shown to have strong influence on the structure, morphology and composition of AlN and InN thin films, respectively. The enhancement in surface reaction as a result of reduced filament-to-substrate distance have led to the growth AlN thin films with lower presence of metallic phase. Increasing the RF power to a certain threshold value resulted in highly crystalline InN thin films with

higher nitrogen incorporation and lower oxygen contamination due to the controlled impinging energy of the nitrogen adatoms on the growth sites.

- The obtained band gap energy (E_g) values of InN thin films grown at various RF power were fell in the range of 2.0 – 2.5 eV, which is much higher than reported E_g values for InN due to unavoidable presence of oxygen impurity in the film structure.
- $\text{Al}_x\text{In}_{1-x}\text{N}$ thin films with different Al (In) mole fractions were obtained by simply varying the AC voltage that is applied to the filament heating the In wire. In this work, Al-rich ($x=0.64$ and 0.60) and In-rich ($x=0.18$ and 0.10) $\text{Al}_x\text{In}_{1-x}\text{N}$ thin films were deposited by varying this voltage.
- The Raman results established that the $A_1(\text{LO})$ phonon mode of the Al-rich $\text{Al}_x\text{In}_{1-x}\text{N}$ films deposited by plasma-assisted reactive evaporation exhibit a two-mode behavior. The obtained result confirmed that this is a characteristic behavior of Al-rich $\text{Al}_x\text{In}_{1-x}\text{N}$ films.
- The band gap energy of $\text{Al}_x\text{In}_{1-x}\text{N}$ films deposited by plasma-assisted reactive evaporation can be tuned within a wide range of energy from 0.9 eV to 2.5 eV by varying specific growth parameters.
- The bowing parameter of $\text{Al}_x\text{In}_{1-x}\text{N}$ films that had been deposited in this work was determined to be 4.3 eV which is close to the values reported in literature for this type of film grown using various other conventional techniques.
- Nitrogen flow rate was shown to have significant effect on the structure, morphology and optical properties of In-rich and Al-rich $\text{Al}_x\text{In}_{1-x}\text{N}$ thin films. Al incorporation (x) into the structure of both In-rich and Al-rich $\text{Al}_x\text{In}_{1-x}\text{N}$ thin films was decreased with increase in N_2 flow rate. Enhanced

gas-phase reactions decreased the energy of adatoms reaching on the growth sites which contributed to the low Al incorporation.

- The inclusion of AlN in InN films (In-rich $\text{Al}_x\text{In}_{1-x}\text{N}$ films) that were grown by reactive evaporation of In and Al wires using dual heated filaments in N_2 plasma ambient resulted in films with band gap energy of 0.9 eV which is close to the reported band gap energy of InN (0.7 eV);
- Annealing studies showed that the optical and structural properties of $\text{Al}_x\text{In}_{1-x}\text{N}$ films grown by plasma-assisted reactive evaporation are stable at temperatures below 300 °C for applications in opto-electronic devices.
- Unavoidable presence of oxygen impurities in InN thin films was shown to have favorable effects on the electrochemical properties of the films. It was shown that the donor density (N_d) of the films grown at different RF power contain strong dependence on the oxygen content in the thin film. The nitrogen content in the InN thin films on the other hand, influenced the anodic current measured by linear sweep voltammogram (LSV).
- The photoelectrochemical (PEC) results obtained for $\text{Al}_x\text{In}_{1-x}\text{N}$ thin films with band gap energy of 2.12 eV showed 10-fold enhancement in the photocurrent compared to the dark current. The Mott-Schottky (MS) plot of these films showed that the flat band potential had large negative values indicating higher ability to facilitate charge transport in PEC applications;
- The electrochemical behavior of the InN and $\text{Al}_x\text{In}_{1-x}\text{N}$ thin films grown by plasma-assisted reactive evaporation technique showed that these films are promising for EC and PEC water splitting applications, respectively. Both InN and $\text{Al}_x\text{In}_{1-x}\text{N}$ ($0.48 \leq x \leq 0.66$) thin films showed easy permeability to ions at the film/electrolyte interface during EC process.

7.3 Suggestions for Future Work

The results presented here have created a path towards a cost-effective and non-toxic technique of growing aluminum and indium based nitrides thin films by plasma-assisted reactive evaporation. However, precise control of the growth parameters, especially control of the evaporation rate to remove the metallic phase from the films structure is needed. Investigations on the post-treatment effects on the deposited thin films by using acidic solutions is strongly recommended for removing the metallic phase from the grown films. Moreover, for InN and AlN thin films, more precise/detailed analysis techniques such as XPS and XRF in the bulk form with identical scanning parameters should be planned for further improve the confidence level of the nitrogen content in the films.

The most serious research problem faced in this work was incorporation of Al atoms into the $\text{Al}_x\text{In}_{1-x}\text{N}$ structure in a controlled and precise manner due the flash evaporation behaviour of Al when it reaches melting point. This results in inclusion of Al metal into the film structure and can be considered as a serious weakness in using this growth technique. Suggestions for future work is combination of sputtering with the current growth system where the Al and In atoms are incorporated into the film structure by sputtering of Al target and evaporation of In wire, respectively.

In situ gas-phase diagnostics techniques such as optical emission spectroscopy (OES), mass spectroscopy and diode laser absorption (DLA) make it possible to measure the density of reactive species in the steady state of plasma and may strengthen the existing model on the growth kinetics of these materials. The concentration of ionic species that is measured during the various steps of the growth process with respect to the studied deposition parameters will enable precise control of the parameters for growth of the studied materials with higher quality.

Since the EC and PEC studies of the InN and AlInN thin films done in this work is only preliminary, further investigations are required to improve the corresponding EC and PEC behaviors of the grown films. The evaluation of the stability of the grown thin films is strongly suggested by taking into account the recyclability/reusability of the thin films during the EC and PEC processes. Effects of the film structure on the EC and PEC behavior properties are interesting investigations to be pursued for future work. Investigations in improving the PEC performance with introduction of sacrificial electron donor such as oxalic acid, methanol and formic acid into the PEC cells can be another possible future work. Another possible study to be pursued is to introduce some noble metal dopants on the surface of the AlInN thin films to improve the visible light absorption and interfacial charge-transfer process which can result in enhancement of the PEC efficiency.

REFERENCES

- Abe, R. (2010). Recent progress on photocatalytic and photoelectrochemical water splitting under visible light irradiation. *Journal of Photochemistry and Photobiology C: Photochemistry Reviews*, 11(4), 179-209.
- Ager, J. W., Jones, R. E., Yamaguchi, D. M., Yu, K. M., Walukiewicz, W., Li, S. X., Haller, E. E., Lu, H., & Schaff, W. J. (2007). p-type InN and In-rich InGaN. *physica status solidi (b)*, 244(6), 1820-1824.
- Ager, J. W., Miller, N., Jones, R. E., Yu, K. M., Wu, J., Schaff, W. J., & Walukiewicz, W. (2008). Mg-doped InN and InGaN – Photoluminescence, capacitance–voltage and thermopower measurements. *physica status solidi (b)*, 245(5), 873-877.
- Ajagunna, A. O., Adikimenakis, A., Iliopoulos, E., Tsagaraki, K., Androulidaki, M., & Georgakilas, A. (2009). InN films and nanostructures grown on Si (1 1 1) by RF-MBE. *Journal of Crystal Growth*, 311(7), 2058-2062.
- Akasaki, I., Amano, H., Sota, S., Sakai, H., Tanaka, T., & Koike, M. (1995). Stimulated Emission by Current Injection from an AlGaIn/GaN/GaInN Quantum Well Device. *Japanese Journal of Applied Physics*, 34(11B), L1517-L1519.
- Alexandrov, D., Butcher, K. S. A., & Wintrebert-Fouquet, M. (2004). Absorption and photoluminescence features caused by defects in InN. *Journal of Crystal Growth*, 269(1), 77-86.
- AlOtaibi, B., Nguyen, H., Zhao, S., Kibria, M., Fan, S., & Mi, Z. (2013). Highly stable photoelectrochemical water splitting and hydrogen generation using a double-band InGaIn/GaN core/shell nanowire photoanode. *Nano Letters*, 13(9), 4356-4361.
- Amirhoseiny, M., Ng, S. S., & Hassan, Z. (2015). Effect of deposition conditions on properties of nitrogen rich-InN nanostructures grown on anisotropic Si (110). *Materials Science in Semiconductor Processing*, 35, 216-221.
- Angerer, H., Brunner, D., Freudenberg, F., Ambacher, O., Stutzmann, M., Höppler, R., Metzger, T., Born, E., Dollinger, G., Bergmaier, A., Karsch, S., & Körner, H.-J. (1997). Determination of the Al mole fraction and the band gap bowing of epitaxial Al_xGa_{1-x}N films. *Applied Physics Letters*, 71(11), 1504-1506.
- Ariffin, S., Lim, H., Talib, Z., Pandikumar, A., & Huang, N. (2015). Aerosol-assisted chemical vapor deposition of metal oxide thin films for photoelectrochemical water splitting. *International Journal of Hydrogen Energy*, 40(5), 2115-2131.
- Aryal, K., Pantha, B., Li, J., Lin, J., & Jiang, H. (2010). Hydrogen generation by solar water splitting using p-InGaIn photoelectrochemical cells. *Applied Physics Letter* 96, 052110-3.
- Avasarala, B., & Haldar, P. (2010). Electrochemical oxidation behavior of titanium nitride based electrocatalysts under PEM fuel cell conditions. *Electrochimica Acta*, 55(28), 9024-9034.

- Bakalova, S., Szekeres, A., Huhn, G., Havancsak, K., Grigorescu, S., Socol, G., Ristoscu, C., & Mihailescu, I. N. (2009). Surface morphology of AlN films synthesized by pulsed laser deposition. *Vacuum*, 84(1), 155-157.
- Barick, B. K., & Dhar, S. (2015). Surface and bulk electronic properties of low temperature synthesized InN microcrystals. *Journal of Crystal Growth*, 416, 154-158.
- Bechstedt, F., Furthmüller, J., Ferhat, M., Teles, L. K., Scolfaro, L. M. R., Leite, J. R., Davydov, V. Yu, Ambacher, O., & Goldhahn, R. (2003). Energy gap and optical properties of $\text{In}_x\text{Ga}_{1-x}\text{N}$. *physica status solidi (a)*, 195(3), 628-633.
- Behrisch, R., & Wittmaack, K. (1983). *Sputtering by particle bombardment* (Vol. 3): Springer Berlin.
- Berger, C., Dadgar, A., Bläsing, J., & Krost, A. (2013). In-situ growth monitoring of AlInN/AlGaIn distributed Bragg reflectors for the UV-spectral range. *Journal of Crystal Growth*, 370, 87-91.
- Berreman, D. W. (1963). Infrared Absorption at Longitudinal Optic Frequency in Cubic Crystal Films. *Physical Review*, 130(6), 2193-2198.
- Bhuiyan, A. G., Hashimoto, A., & Yamamoto, A. (2003). Indium nitride (InN): A review on growth, characterization, and properties. *Journal of Applied Physics*, 94(5), 2779-2808.
- Biju, K. P., & Jain, M. K. (2008). The effect of rf power on the growth of InN films by modified activated reactive evaporation. *Applied Surface Science*, 254(22), 7259-7265.
- Butcher, K., Wintrebert-Fouquet, M., Chen, P.-T., Tansley, T., Dou, H., Shrestha, S., Timmers, H., Kuball, M., Prince, K. E., & Bradby, J. (2004). Nitrogen-rich indium nitride. *Journal of Applied Physics*, 95(11), 6124-6128.
- Butcher, K. S. A., & Tansley, T. L. (2005). InN, latest development and a review of the band-gap controversy. *Superlattices and Microstructures*, 38(1), 1-37.
- Cai, X.-M., Ye, F., Hao, Y.-Q., Zhang, D.-P., Zhang, Z.-H., & Fan, P. (2009). The properties of direct current sputtering deposited InN thin films under different gas flow rates. *Journal of Alloys and Compounds*, 484(1-2), 677-681.
- Chale-Lara, F., Farias, M. H., Huerta-Escamilla, C., & Xiao, M. (2009). Optical properties of pulse laser deposited AlN thin films on silicon. *Materials Letters*, 63(24-25), 2093-2096.
- Chauhan, A. K. S., Kumar, M., & Gupta, G. (2015). Catalyst free self-assembled growth of InN nanorings on stepped Si (5 5 3) surface. *Applied Surface Science*, 345, 156-161.
- Chauhan, D., Dass, S., & Shrivastav, R. Preparation and characterization of nanostructured CuO thin films for photoelectrochemical splitting of water. *Bulletin of Materials Science*, 29 (7) 709-716.

- Chen, S., & Qiao, S.-Z. (2013). Hierarchically Porous Nitrogen-Doped Graphene–NiCo₂O₄ Hybrid Paper as an Advanced Electrocatalytic Water-Splitting Material. *ACS Nano*, 7(11), 10190-10196.
- Chen, Y., Song, H., Li, D., Sun, X., Jiang, H., Li, Z., Miao, G., Zhang, Z., & Zhou, Y. (2014). Influence of the growth temperature of AlN nucleation layer on AlN template grown by high-temperature MOCVD. *Materials Letters*, 114, 26-28.
- Chen, Y., Zhou, X., Zhao, X., He, X., & Gu, X. (2008). Crystallite structure, surface morphology and optical properties of In₂O₃–TiO₂ composite thin films by sol–gel method. *Materials Science and Engineering: B*, 151(2), 179-186.
- Chen, Z. T., Tan, S. X., Sakai, Y., & Egawa, T. (2009). Improved performance of InAlN-based Schottky solar-blind photodiodes. *Applied Physics Letters*, 94(21), 213504-3.
- Cheng, H., & Hing, P. (2003). The evolution of preferred orientation and morphology of AlN films under various RF sputtering powers. *Surface and Coatings Technology*, 167(2–3), 297-301.
- Cheng, H., Sun, Y., Zhang, J. X., Zhang, Y. B., Yuan, S., & Hing, P. (2003). AlN films deposited under various nitrogen concentrations by RF reactive sputtering. *Journal of Crystal Growth*, 254(1–2), 46-54.
- Cho, A. Y. (1970). Morphology of Epitaxial Growth of GaAs by a Molecular Beam Method: The Observation of Surface Structures. *Journal of Applied Physics*, 41(7), 2780-2786.
- Cho, S. (2011). Effect of nitrogen flow ratio on the structural and optical properties of aluminum nitride thin films. *Journal of Crystal Growth*, 326(1), 179-182.
- Chong, S. K., Goh, B. T., Dee, C. F., & Rahman, S. A. (2012). Study on the role of filament temperature on growth of indium-catalyzed silicon nanowires by the hot-wire chemical vapor deposition technique. *Materials Chemistry and Physics*, 135(2–3), 635-643.
- Chong, S. K., Goh, B. T., Dee, C. F., & Rahman, S. A. (2013). Effect of substrate to filament distance on formation and photoluminescence properties of indium catalyzed silicon nanowires using hot-wire chemical vapor deposition. *Thin Solid Films*, 529, 153-158.
- Collazo, R., & Dietz III, N. (2013). *The group III-nitride material class: From preparation to perspectives in photoelectrocatalysis*: RSC Publishing.
- Collazo, R., & Dietz, N. (2013). CHAPTER 8 The Group III-Nitride Material Class: from Preparation to Perspectives in Photoelectrocatalysis *Photoelectrochemical Water Splitting: Materials, Processes and Architectures* (pp. 193-222): The Royal Society of Chemistry.
- Çörekçi, S., Öztürk, M. K., Çakmak, M., Özçelik, S., & Özbay, E. (2012). The influence of thickness and ammonia flow rate on the properties of AlN layers. *Materials Science in Semiconductor Processing*, 15(1), 32-36.

- Costales, A., Blanco, M. A., Martín Pendás, Á., Kandalam, A. K., & Pandey, R. (2002). Chemical Bonding in Group III Nitrides. *Journal of the American Chemical Society*, 124(15), 4116-4123.
- Cowan, A. J., & Durrant, J. R. (2013). Long-lived charge separated states in nanostructured semiconductor photoelectrodes for the production of solar fuels. *Chemical Society Reviews*, 42(6), 2281-2293.
- Darakchieva, V., Xie, M.-Y., Tasnádi, F., Abrikosov, I. A., Hultman, L., Monemar, B., Kamimura, J., & Kishino, K. (2008). Lattice parameters, deviations from Vegard's rule, and E2 phonons in InAlN. *Applied Physics Letters*, 93(26), 261908-3.
- Daudin, B., Rouvière, J. L., & Arlery, M. (1996). Polarity determination of GaN films by ion channeling and convergent beam electron diffraction. *Applied Physics Letters*, 69(17), 2480-2482.
- Davydov, V. Y., Klochikhin, A., Seisyan, R., Emtsev, V., Ivanov, S., Bechstedt, F., Furthmüller, J., Harima, H., Mudryi, A. V., & Aderhold, J. (2002). Absorption and emission of hexagonal InN. Evidence of narrow fundamental band gap. *physica status solidi (b)*, 229(3), r1-r3.
- Davydov, V. Y., Klochikhin, A. A., Seisyan, R. P., Emtsev, V. V., Ivanov, S. V., Bechstedt, F., Furthmüller, J., Harima, H., Mudryi, A. V., Aderhold, J., Semchinova, O., & Graul, J. (2002). Absorption and Emission of Hexagonal InN. Evidence of Narrow Fundamental Band Gap. *physica status solidi (b)*, 229(3), r1-r3.
- Demangeot, F., Groenen, J., Frandon, J., Renucci, M. A., Briot, O., Clur, S., & Aulombard, R. L. (1998). Coupling of GaN- and AlN-like longitudinal optic phonons in Ga_{1-x}Al_xN solid solutions. *Applied Physics Letters*, 72(21), 2674-2676.
- Deutsch, T. G., Koval, C. A., & Turner, J. A. (2006). III-V Nitride Epilayers for Photoelectrochemical Water Splitting: GaPN and GaAsPN. *The Journal of Physical Chemistry B*, 110(50), 25297-25307.
- Dixit, A., Sudakar, C., Thakur, J. S., Padmanabhan, K., Kumar, S., Naik, R., Naik, V. M., & Lawes, G. (2009). Strong plasmon absorption in InN thin films. *Journal of Applied Physics*, 105(5), 053104-5.
- Ferhat, M., & Bechstedt, F. (2002). First-principles calculations of gap bowing in In_xGa_{1-x}N and In_xAl_{1-x}N alloys: Relation to structural and thermodynamic properties. *Physical Review B*, 65(7), 075213-7.
- Fernández-Garrido, S., Gačević, Ž., & Calleja, E. (2008). A comprehensive diagram to grow InAlN alloys by plasma-assisted molecular beam epitaxy. *Applied Physics Letters*, 93(19), 191907-3.
- Fichter, F. (1907). Über Aluminiumnitrid. *Zeitschrift für anorganische Chemie*, 54(1), 322-327.

- Flynn, C., & Sim, L. W. (2015). Effects of phosphoric acid on the surface morphology and reflectance of AlN grown by MBE under Al-rich conditions. *Thin Solid Films*, 589, 338-343.
- Fujishima, A., & Honda, K. (1972). Electrochemical Photolysis of Water at a Semiconductor Electrode. *Nature*, 238(5358), 37-38.
- García-Gancedo, L., Zhu, Z., Iborra, E., Clement, M., Olivares, J., Flewitt, A. J., Milne, W. I., Ashley, G. M., Luo, J. K., Zhao, X. B., & Lu, J. R. (2011). AlN-based BAW resonators with CNT electrodes for gravimetric biosensing. *Sensors and Actuators B: Chemical*, 160(1), 1386-1393.
- Goh, B. T. (2012). *Layer-by-layer plasma enhanced chemical vapour deposition of nanocrystalline silicon thin films/Goh Boon Tong*. University of Malaya.
- Goldhahn, R., Schley, P., Winzer, A. T., Gobsch, G., Cimalla, V., Ambacher, O., Rakel, M., Cobet, C., Esser, N., Lu, H., & Schaff, W. J. (2006). Detailed analysis of the dielectric function for wurtzite InN and In-rich InAlN alloys. *physica status solidi (a)*, 203(1), 42-49.
- Guo, J., & Chen, X. (2011). *Solar hydrogen generation: transition metal oxides in water photoelectrolysis*: McGraw Hill Professional.
- Guo, L., Yang, J., Feng, Y., Qiu, T., Chen, B., & Wan, W. (2016). Preparation and properties of AlN ceramic suspension for non-aqueous gel casting. *Ceramics International*, 42(7), 8066-8071.
- Guo, L. a., Chen, G., Zhu, Y., Duan, X., & Ye, H. (2015). The growth of Sea-urchin-like AlN nanostructures by modified CVD and their Field Emission properties. *Journal of Crystal Growth*, 426, 49-53.
- Guo, Q., Nakao, T., Ushijima, T., Shi, W., Liu, F., Saito, K., Tanaka, T., & Nishio, M. (2014). Growth of InGaN layers on (1 1 1) silicon substrates by reactive sputtering. *Journal of Alloys and Compounds*, 587, 217-221.
- Guo, Q., Okada, A., Kidera, H., Nishio, M., & Ogawa, H. (2000). Growth of AlInN on (111)GaAs Substrates. *Japanese Journal of Applied Physics*, 39(11B), L1143-L1145.
- Guo, Q., Tanaka, T., Nishio, M., & Ogawa, H. (2003). Optical Bandgap Energy of Wurtzite In-Rich AlInN Alloys. *Japanese Journal of Applied Physics*, 42(2B), L141-L143.
- Guo, Q., Tanaka, T., Nishio, M., & Ogawa, H. (2008). Structural and Optical Properties of AlInN Films Grown on Sapphire Substrates. *Japanese Journal of Applied Physics*, 47(1S), 612-615.
- Guo, Q. X., Okazaki, Y., Kume, Y., Tanaka, T., Nishio, M., & Ogawa, H. (2007). Reactive sputter deposition of AlInN thin films. *Journal of Crystal Growth*, 300(1), 151-154.

- Guo, Q. X., Tanaka, T., Nishio, M., & Ogawa, H. (2006). Growth properties of AlN films on sapphire substrates by reactive sputtering. *Vacuum*, 80(7), 716-718.
- He, H., Cao, Y., Fu, R., Guo, W., Huang, Z., Wang, M., Huang, C., Huang, J., & Wang, H. (2010). Band gap energy and bowing parameter of In-rich InAlN films grown by magnetron sputtering. *Applied Surface Science*, 256(6), 1812-1816.
- Hobert, H., Dunken, H. H., Meinschien, J., & Stafast, H. (1999). Infrared and Raman spectroscopic investigation of thin films of AlN and SiC on Si substrates. *Vibrational Spectroscopy*, 19(2), 205-211.
- Hoi Wong, M., Wu, F., Hurni, C. A., Choi, S., Speck, J. S., & Mishra, U. K. (2012). Molecular beam epitaxy of InAlN lattice-matched to GaN with homogeneous composition using ammonia as nitrogen source. *Applied Physics Letters*, 100(7), 072107-3.
- Höök, M., & Tang, X. (2013). Depletion of fossil fuels and anthropogenic climate change—A review. *Energy Policy*, 52, 797-809.
- Hovel, H. J., & Cuomo, J. J. (1972). Electrical and Optical Properties of rf-Sputtered GaN and InN. *Applied Physics Letters*, 20(2), 71-73.
- Hwang, Y. J., Wu, C. H., Hahn, C., Jeong, H. E., & Yang, P. (2012). Si/InGaN Core/Shell Hierarchical Nanowire Arrays and their Photoelectrochemical Properties. *Nano Letters*, 12(3), 1678-1682.
- Inushima, T., Shiraishi, T., & Davydov, V. Y. (1999). Phonon structure of InN grown by atomic layer epitaxy. *Solid State Communications*, 110(9), 491-495.
- Ivanov, S. V., Shubina, T. V., Komissarova, T. A., & Jmerik, V. N. (2014). Metastable nature of InN and In-rich InGaN alloys. *Journal of Crystal Growth*, 403, 83-89.
- Jagannadham, K., Sharma, A. K., Wei, Q., Kalyanraman, R., & Narayan, J. (1998). Structural characteristics of AlN films deposited by pulsed laser deposition and reactive magnetron sputtering: A comparative study. *Journal of Vacuum Science & Technology A*, 16(5), 2804-2815.
- Jejurikar, S. M., Banpurkar, A. G., Bankar, D. N., Adhi, K. P., Kukreja, L. M., & Sathe, V. G. (2007). Growth temperature and N₂ ambient pressure-dependent crystalline orientations and band gaps of pulsed laser-deposited AlN/(0 0 0 1) sapphire thin films. *Journal of Crystal Growth*, 304(1), 257-263.
- Jeong, M. W., Jeon, S. W., Lee, S. H., & Kim, Y. (2015). Effective heat dissipation and geometric optimization in an LED module with aluminum nitride (AlN) insulation plate. *Applied Thermal Engineering*, 76, 212-219.
- Ji, X. H., Lau, S. P., Yang, H. Y., & Zhang, Q. Y. (2007). Structural and optical properties of wurtzite InN grown on Si(111). *Thin Solid Films*, 515(11), 4619-4623.
- Jiang, L. F., Kong, J. F., Shen, W. Z., & Guo, Q. X. (2011). Temperature dependence of Raman scattering in AlInN. *Journal of Applied Physics*, 109(11), 113514-5.

- Johnson, W. C., & Parsons, J. B. (1931). Nitrogen Compounds of Gallium. I, II. *The Journal of Physical Chemistry*, 36(10), 2588-2594.
- Jothibas, M., Manoharan, C., Ramalingam, S., Dhanapandian, S., Johnson Jeyakumar, S., & Bououdina, M. (2013). Preparation, characterization, spectroscopic (FT-IR, FT-Raman, UV and visible) studies, optical properties and Kubo gap analysis of In₂O₃ thin films. *Journal of Molecular Structure*, 1049(0), 239-249.
- Juodkazytė, J., Šebeka, B., Savickaja, I., Kadys, A., Jelmakas, E., Grinys, T., Juodkazis, S., Juodkazis, K., Malinauskas, T. (2014). In_xGa_{1-x}N performance as a band-gap-tunable photo-electrode in acidic and basic solutions. *Solar Energy Materials and Solar Cells*, 130, 36-41.
- Kallel, T., Dammak, M., Wang, J., & Jadwisienczak, W. M. (2014). Raman characterization and stress analysis of AlN:Er³⁺ epilayers grown on sapphire and silicon substrates. *Materials Science and Engineering: B*, 187, 46-52.
- Kamimura, J., Kouno, T., Ishizawa, S., Kikuchi, A., & Kishino, K. (2007). Growth of high-In-content InAlN nanocolumns on Si (1 1 1) by RF-plasma-assisted molecular-beam epitaxy. *Journal of Crystal Growth*, 300(1), 160-163.
- Kang, T.-T., Hashimoto, A., & Yamamoto, A. (2009). Raman scattering of indium-rich Al_xIn_{1-x}N : Unexpected two-mode behavior of A₁(LO) . *Physical Review B*, 79(3), 033301-4.
- Kang, T.-T., Yamamoto, M., Tanaka, M., Hashimoto, A., & Yamamoto, A. (2009). Effect of gas flow on the growth of In-rich AlInN films by metal-organic chemical vapor deposition. *Journal of Applied Physics*, 106(5), 053525-4.
- Kelekci, O., Tasli, P., Cetin, S. S., Kasap, M., Ozcelik, S., & Ozbay, E. (2012). Investigation of AlInN HEMT structures with different AlGaIn buffer layers grown on sapphire substrates by MOCVD. *Current Applied Physics*, 12(6), 1600-1605.
- Khan, S., Mehmood, M., Saeed, S., Khan, T. M., Sadiq, G., & Ahmed, I. (2013). Effect of substrate biasing and temperature on AlN thin film deposited by cathodic arc ion. *Materials Science in Semiconductor Processing*, 16(3), 640-646.
- Kibria, M. G., Nguyen, H. P., Cui, K., Zhao, S., Liu, D., Guo, H., Trudeau, M. L., Paradis, S., Hakima, A. R., & Mi, Z. (2013). One-step overall water splitting under visible light using multiband InGaIn/GaN nanowire heterostructures. *ACS Nano*, 7(9), 7886-7893.
- King, P. D. C., Veal, T. D., Jefferson, P. H., McConville, C. F., Wang, T., Parbrook, P. J., Lu, H., & Schaff, W. J. (2007). Valence band offset of InN/AlN heterojunctions measured by x-ray photoelectron spectroscopy. *Applied Physics Letters*, 90(13), 132105-3.
- Kocha, S. S., & Turner, J. A. (1995). Displacement of the Bandedges of GaInP₂ in Aqueous Electrolytes Induced by Surface Modification. *Journal of The Electrochemical Society*, 142(8), 2625-2630.

- Kuang, X.-P., Zhang, H.-Y., Wang, G.-G., Cui, L., Zhu, C., Jin, L., Sun, R., & Han, J.-C. (2012a). AlN films prepared on 6H-SiC substrates under various sputtering pressures by RF reactive magnetron sputtering. *Applied Surface Science*, 263, 62-68.
- Kuang, X.-P., Zhang, H.-Y., Wang, G.-G., Cui, L., Zhu, C., Jin, L., Sun, R., & Han, J.-C. (2012b). AlN films prepared on 6H-SiC substrates under various sputtering pressures by RF reactive magnetron sputtering. *Applied Surface Science*, 263(0), 62-68.
- Kuang, X.-P., Zhang, H.-Y., Wang, G.-G., Cui, L., Zhu, C., Jin, L., Sun, R., & Han, J.-C. (2012c). Effect of deposition temperature on the microstructure and surface morphology of c-axis oriented AlN films deposited on sapphire substrate by RF reactive magnetron sputtering. *Superlattices and Microstructures*, 52(5), 931-940.
- Kubota, K., Kobayashi, Y., & Fujimoto, K. (1989). Preparation and properties of III-V nitride thin films. *Journal of Applied Physics*, 66(7), 2984-2988.
- Kucera, M., Wistrela, E., Pfusterschmied, G., Ruiz-Díez, V., Manzaneque, T., Hernando-García, J., Sánchez-Rojas, J. L., Jachimowicz, A., Schalko, J., Bittner, A., & Schmid, U. (2014). Design-dependent performance of self-actuated and self-sensing piezoelectric-AlN cantilevers in liquid media oscillating in the fundamental in-plane bending mode. *Sensors and Actuators B: Chemical*, 200, 235-244.
- Kudo, A., & Miseki, Y. (2009). Heterogeneous photocatalyst materials for water splitting. *Chemical Society Reviews*, 38(1), 253-278.
- Kumar, M., Bhat, T. N., Rajpalke, M. K., Roul, B., Kalghatgi, A. T., & Krupanidhi, S. B. (2012). Indium flux, growth temperature and RF power induced effects in InN layers grown on GaN/Si substrate by plasma-assisted MBE. *Journal of Alloys and Compounds*, 513, 6-9.
- Kumar, M., Rajpalke, M. K., Bhat, T. N., Roul, B., Sinha, N., Kalghatgi, A. T., & Krupanidhi, S. B. (2011). Growth of InN layers on Si (111) using ultra thin silicon nitride buffer layer by NPA-MBE. *Materials Letters*, 65(9), 1396-1399.
- Kumar, S., Li Mo, Motlan, & Tansley, Trevor L. (1996). Elemental Composition of Reactively Sputtered Indium Nitride Thin Films. *Japanese Journal of Applied Physics*, 35(4R), 2261-2265.
- Lebedev, V., Morales, F. M., Cimalla, V., Lozano, J. G., González, D., Himmerlich, M., Krischok, S., Schaefer, J. A., & Ambacher, O. (2006). Correlation between structural and electrical properties of InN thin films prepared by molecular beam epitaxy. *Superlattices and Microstructures*, 40(4-6), 289-294.
- Lee, M.-C., Lin, H.-C., Pan, Y.-C., Shu, C.-K., Ou, J., Chen, W.-H., & Chen, W.-K. (1998). Raman and x-ray studies of InN films grown by metalorganic vapor phase epitaxy. *Applied Physics Letters*, 73(18), 2606-2608.

- Li, G., Wang, W., Yang, W., & Wang, H. (2015). Epitaxial growth of group III-nitride films by pulsed laser deposition and their use in the development of LED devices. *Surface Science Reports*, 70(3), 380-423.
- Li, J., Lin, J., & Jiang, H. (2008). Direct hydrogen gas generation by using InGaN epilayers as working electrodes. *Applied Physics Letters*, 93(16), 162107-3.
- Li, X., Kong, L., Shen, L., Yang, J., Gao, M., Hu, T., Wu, X., & Li, M. (2013). Synthesis and in situ high pressure Raman spectroscopy study of AlN dendritic crystal. *Materials Research Bulletin*, 48(9), 3310-3314.
- Liu, B., Gao, J., Wu, K. M., & Liu, C. (2009). Preparation and rapid thermal annealing of AlN thin films grown by molecular beam epitaxy. *Solid State Communications*, 149(17-18), 715-717.
- Liu, H. F., Li, C. G., Ansah Antwi, K. K., Chua, S. J., & Chi, D. Z. (2014). Electron-beam-induced carbon deposition on high-indium-content AlInN thin films grown on Si by sputtering at elevated temperature. *Materials Letters*, 128(0), 344-348.
- Liu, H. F., Tan, C. C., Dalapati, G. K., & Chi, D. Z. (2012). Magnetron-sputter deposition of high-indium-content n-AlInN thin film on p-Si(001) substrate for photovoltaic applications. *Journal of Applied Physics*, 112(6), 063114-5.
- Liu, S.-Y., Sheu, J. K., Lin, Y.-C., Chen, Y.-T., Tu, S. J., Lee, M. L., & Lai, W. C. (2013). InGaN working electrodes with assisted bias generated from GaAs solar cells for efficient water splitting. *Optics Express*, 21(S6), A991-A996.
- Loudon, R. (1964). The Raman effect in crystals. *Advances in Physics*, 13(52), 423-482.
- Lukitsch, M. J., Danylyuk, Y. V., Naik, V. M., Huang, C., Auner, G. W., Rimai, L., & Naik, R. (2001). Optical and electrical properties of Al_{1-x}In_xN films grown by plasma source molecular-beam epitaxy. *Applied Physics Letters*, 79(5), 632-634.
- Maeda, K. (2011). Photocatalytic water splitting using semiconductor particles: history and recent developments. *Journal of Photochemistry and Photobiology C: Photochemistry Reviews*, 12(4), 237-268.
- Maeda, K., & Domen, K. (2007). New non-oxide photocatalysts designed for overall water splitting under visible light. *The Journal of Physical Chemistry C*, 111(22), 7851-7861.
- Maeda, K., & Domen, K. (2011). Oxynitride materials for solar water splitting. *MRS bulletin*, 36(01), 25-31.
- Manasevit, H. M., Erdmann, F. M., & Simpson, W. I. (1971). The Use of Metalorganics in the Preparation of Semiconductor Materials: IV . The Nitrides of Aluminum and Gallium. *Journal of The Electrochemical Society*, 118(11), 1864-1868.
- Manivasakan, P., Ramasamy, P., & Kim, J. (2014). Use of urchin-like Ni_x Co_{3-x}O₄ hierarchical nanostructures based on non-precious metals as bifunctional electrocatalysts for anion-exchange membrane alkaline alcohol fuel cells. *Nanoscale*, 6(16), 9665-9672.

- Mansurov, V. G., Nikitin, A. Y., Galitsyn, Y. G., Svitashva, S. N., Zhuravlev, K. S., Osvath, Z., Dobos, L., Horvath, Z. E., & Pecz, B. (2007). AlN growth on sapphire substrate by ammonia MBE. *Journal of Crystal Growth*, 300(1), 145-150.
- Martin, G., Botchkarev, A., Rockett, A., & Morkoç, H. (1996). Valence-band discontinuities of wurtzite GaN, AlN, and InN heterojunctions measured by x-ray photoemission spectroscopy. *Applied Physics Letters*, 68(18), 2541-2543.
- Maruska, H. P., & Tietjen, J. J. (1969). THE PREPARATION AND PROPERTIES OF VAPOR-DEPOSITED SINGLE-CRYSTAL-LINE GaN. *Applied Physics Letters*, 15(10), 327-329.
- Matemadombo, F., & Nyokong, T. (2007). Characterization of self-assembled monolayers of iron and cobalt octaalkylthiosubstituted phthalocyanines and their use in nitrite electrocatalytic oxidation. *Electrochimica Acta*, 52(24), 6856-6864.
- Matsuoka, T. (1997). Calculation of unstable mixing region in wurtzite $\text{In}_{1-x-y}\text{Ga}_x\text{Al}_y\text{N}$. *Applied Physics Letters*, 71(1), 105-106.
- Matsuoka, T., Okamoto, H., Nakao, M., Harima, H., & Kurimoto, E. (2002). Optical bandgap energy of wurtzite InN. *Applied Physics Letters*, 81(7), 1246-1248.
- Matsuoka, T., Okamoto, H., Takahata, H., Mitate, T., Mizuno, S., Uchiyama, Y., & Makimoto, T. (2004). MOVPE growth and photoluminescence of wurtzite InN. *Journal of Crystal Growth*, 269(1), 139-144.
- Medjdoub, F., Carlin, J. F., Gonschorek, M., Feltin, E., Py, M. A., Ducatteau, D., Gaquiere, C., Grandjean, N., & Kohn, E. (2006, 11-13 Dec. 2006). *Can InAlN/GaN be an alternative to high power / high temperature AlGaIn/GaN devices?* Paper presented at the Electron Devices Meeting, 2006. IEDM '06. International, page 1-4, IEEE.
- Miao, H., Ji, R., Hu, X., Han, L., Hao, Y., Sun, Q., Zhang, D., Fan, J., Bai, J., & Hou, X. (2015). $\text{Y}_2\text{O}_3: \text{Eu}^{3+}, \text{Tb}^{3+}$ spherical particles based anti-reflection and wavelength conversion bi-functional films: Synthesis and application to solar cells. *Journal of Alloys and Compounds*, 629, 74-79.
- Mitamura, K., Honke, T., Ohta, J., Kobayashi, A., Fujioka, H., & Oshima, M. (2009). Characteristics of InN grown directly on Al_2O_3 (0 0 0 1) substrates by pulsed laser deposition. *Journal of Crystal Growth*, 311(5), 1316-1320.
- Mohd Yusoff, M. Z., Mahyuddin, A., Hassan, Z., Yusof, Y., Ahmad, M. A., Chin, C. W., Hassan, H. A., & Abdullah, M. J. (2013). Plasma-assisted MBE growth of AlN/GaN/AlN heterostructures on Si (1 1 1) substrate. *Superlattices and Microstructures*, 60, 500-507.
- Monemar, B., Paskov, P. P., & Kasic, A. (2005). Optical properties of InN—the bandgap question. *Superlattices and Microstructures*, 38(1), 38-56.
- Nardelli, M. B., Rapcewicz, K., & Bernholc, J. (1997). Strain effects on the interface properties of nitride semiconductors. *Physical Review B*, 55(12), R7323-R7326.

- Naveed ul Hassan, A., Paul, E. D. S. R., Victor, J. G., Praveen, K., Magnus, W., & Richard, N. (2013). Highly Sensitive and Fast Anion-Selective InN Quantum Dot Electrochemical Sensors. *Applied Physics Express*, 6(11), 115201-4.
- Ng, S. S., Ooi, P. K., Lee, S. C., Hassan, Z., & Abu Hassan, H. (2012). Surface phonon polariton of wurtzite AlN thin film grown on sapphire. *Materials Chemistry and Physics*, 134(1), 493-498.
- Ni, M., Leung, M. K., Leung, D. Y., & Sumathy, K. (2007). A review and recent developments in photocatalytic water-splitting using TiO₂ for hydrogen production. *Renewable and Sustainable Energy Reviews*, 11(3), 401-425.
- Ohba, R., Mitamura, K., Shimomoto, K., Fujii, T., Kawano, S., Ohta, J., Fujioka, & H., Oshima, M. (2009). Growth of cubic InN films with high phase purity by pulsed laser deposition. *Journal of Crystal Growth*, 311(11), 3130-3132.
- Ooi, P. K., Lee, S. C., Ng, S. S., Hassan, Z., Abu Hassan, H., & Chen, W. L. (2011). Polarized infrared reflectance studies for wurtzite InN epilayers on Si(111) grown by molecular beam epitaxy. *Thin Solid Films*, 520(2), 739-742.
- Ostrikov, K. (2005). Colloquium: Reactive plasmas as a versatile nanofabrication tool. *Reviews of Modern Physics*, 77(2), 489-511.
- Othman, M. (2012). *Plasma enhanced chemical vapour deposition of carbon nitride films from ethane and nitrogen gas mixtures/Maisara binti Othman*. University Malaya.
- Ozgit, C., Donmez, I., Alevli, M., & Biyikli, N. (2012). Self-limiting low-temperature growth of crystalline AlN thin films by plasma-enhanced atomic layer deposition. *Thin Solid Films*, 520(7), 2750-2755.
- Pearnton, S. J., Zolper, J. C., Shul, R. J., & Ren, F. (1999). GaN: Processing, defects, and devices. *Journal of Applied Physics*, 86(1), 1-78.
- Peng, T., Piprek, J., Qiu, G., Olowolafe, J. O., Unruh, K. M., Swann, C. P., & Schubert, E. F. (1997). Band gap bowing and refractive index spectra of polycrystalline Al_xIn_{1-x}N films deposited by sputtering. *Applied Physics Letters*, 71(17), 2439-2441.
- Persson, C., Sernelius, B. E., Ferreira da Silva, A., Araújo, C. M., Ahuja, R., & Johansson, B. (2002). Optical and reduced band gap in n- and p-type GaN and AlN. *Journal of Applied Physics*, 92(6), 3207-3216.
- Rai, S., Ikram, A., Sahai, S., Dass, S., Shrivastav, R., & Satsangi, V. R. (2014). Morphological, optical and photoelectrochemical properties of Fe₂O₃-GNP composite thin films. *RSC Advances*, 4(34), 17671-17679.
- Reboredo, F. A., Pizzagalli, L., & Galli, G. (2004). Computational Engineering of the Stability and Optical Gaps of SiC Quantum Dots. *Nano Letters*, 4(5), 801-804.
- Ristoscu, C., Ducu, C., Socol, G., Craciunoiu, F., & Mihailescu, I. N. (2005). Structural and optical characterization of AlN films grown by pulsed laser deposition. *Applied Surface Science*, 248(1-4), 411-415.

- Rodríguez-Madrid, J. G., Iriarte, G. F., Araujo, D., Villar, M. P., Williams, O. A., Müller-Sebert, W., & Calle, F. (2012). Optimization of AlN thin layers on diamond substrates for high frequency SAW resonators. *Materials Letters*, 66(1), 339-342.
- Romero, M. F., Feneberg, M., Moser, P., Berger, C., Bläsing, J., Dadgar, A., Krost, A., Sakalauskas, E., & Goldhahn, R. (2012). Luminescence from two-dimensional electron gases in InAlN/GaN heterostructures with different In content. *Applied Physics Letters*, 100(21), 212101-3.
- Rosenberger, L., Baird, R., McCullen, E., Auner, G., & Shreve, G. (2008). XPS analysis of aluminum nitride films deposited by plasma source molecular beam epitaxy. *Surface and Interface Analysis*, 40(9), 1254-1261.
- Saidi, I., Mejri, H., Baira, M., & Maaref, H. (2015). Electronic and transport properties of AlInN/AlN/GaN high electron mobility transistors. *Superlattices and Microstructures*, 84, 113-125.
- Sakai, Y., Khai, P. C., Ichikawa, J., Egawa, T., & Jimbo, T. (2011). Characterization of AlInN/GaN structures on AlN templates for high-performance ultraviolet photodiodes. *Journal of Applied Physics*, 109(3), 033512-6.
- Sánchez, G., Tristant, P., Dublanche-Tixier, C., Tétard, F., & Bologna Alles, A. (2014). Effect of low RF bias potential on AlN films obtained by Microwave Plasma Enhanced Chemical Vapor Deposition. *Surface and Coatings Technology*, 256, 3-8.
- Sánchez, G., Wu, A., Tristant, P., Tixier, C., Soulestin, B., Desmaison, J., & Bologna Alles, A. (2008). Polycrystalline AlN films with preferential orientation by plasma enhanced chemical vapor deposition. *Thin Solid Films*, 516(15), 4868-4875.
- Sasaoka, T., Mori, M., Miyazaki, T., & Adachi, S. (2010). Room-temperature infrared photoluminescence from sputter-deposited InN films. *Journal of Applied Physics*, 108(6), 063538-5.
- Schmidt, T. J., Yang, X. H., Shan, W., Song, J. J., Salvador, A., Kim, W., Aktas, Ö., Botchkarev, A., & Morkoç, H. (1996). Room-temperature stimulated emission in GaN/AlGaIn separate confinement heterostructures grown by molecular beam epitaxy. *Applied Physics Letters*, 68(13), 1820-1822.
- Shah, A., & Mahmood, A. (2012). Effect of Cr implantation on structural and optical properties of AlN thin films. *Physica B: Condensed Matter*, 407(19), 3987-3991.
- Shih, C.-H., Lo, I., Pang, W.-Y., & Hsieh, C.-H. (2010). Growth of InN thin films on ZnO substrate by plasma-assisted molecular beam epitaxy. *Journal of Physics and Chemistry of Solids*, 71(12), 1664-1668.
- Shinar, R., & Kennedy, J. H. (1982). Photoactivity of doped α -Fe₂O₃ electrodes. *Solar Energy Materials*, 6(3), 323-335.

- Shinoda, H., & Mutsukura, N. (2002). Deposition of an InN thin film by a r.f. plasma-assisted reactive ion-beam sputtering deposition (R-IBSD) technique. *Diamond and Related Materials*, 11(3–6), 896-900.
- Shubina, T., Ivanov, S., Jmerik, V., Solnyshkov, D., Vekshin, V., Kop'ev, P., Vasson, A., Leymarie, J., Kavokin, A., & Amano, H. (2005). Erratum: Mie Resonances, Infrared Emission, and the Band Gap of InN [Phys. Rev. Lett. 92, 117407 (2004)]. *Physical Review Letters*, 95(20), 209901-1.
- Shubina, T. V., Ivanov, S. V., Jmerik, V. N., Solnyshkov, D. D., Vekshin, V. A., Kop'ev, P. S., Vasson, A., Leymarie, J., Kavokin, A., Amano, H., Shimono, K., Kasic, A., & Monemar, B. (2004). Mie Resonances, Infrared Emission, and the Band Gap of InN. *Physical Review Letters*, 92(11), 117407-4.
- Shukla, G., & Khare, A. (2008). Dependence of N₂ pressure on the crystal structure and surface quality of AlN thin films deposited via pulsed laser deposition technique at room temperature. *Applied Surface Science*, 255(5, Part 1), 2057-2062.
- Siegle, H., Kaczmarczyk, G., Filippidis, L., Litvinchuk, A. P., Hoffmann, A., & Thomsen, C. (1997). Zone-boundary phonons in hexagonal and cubic GaN. *Physical Review B*, 55(11), 7000-7004.
- Singh, A. V., Chandra, S., & Bose, G. (2011). Deposition and characterization of c-axis oriented aluminum nitride films by radio frequency magnetron sputtering without external substrate heating. *Thin Solid Films*, 519(18), 5846-5853.
- Skuridina, D., Dinh, D. V., Pristovsek, M., Lacroix, B., Chauvat, M. P., Ruterana, P., Kneissl, M., & Vogt, P. (2014). Surface and crystal structure of nitridated sapphire substrates and their effect on polar InN layers. *Applied Surface Science*, 307, 461-467.
- Sofikiti, N., Chaniotakis, N., Grandal, J., Utrera, M., Sánchez-García, M. A., & Calleja, E. (2010). GaN and InN nanocolumns as electrochemical sensing elements: Potentiometric response to KCl, pH and urea. *Materials Letters*, 64(12), 1332-1335.
- Soh, J.-W., Jang, S.-S., Jeong, I.-S., & Lee, W.-J. (1996). C-axis orientation of AlN films prepared by ECR PECVD. *Thin Solid Films*, 279(1–2), 17-22.
- Stokker-Cheregi, F., Nedelcea, A., Filipescu, M., Moldovan, A., Colceag, D., Ion, V., Bîrjega, R., & Dinescu, M. (2011). High temperature growth of InN on various substrates by plasma-assisted pulsed laser deposition. *Applied Surface Science*, 257(12), 5312-5314.
- Sumitani, K., Ohtani, R., Yoshida, T., Nakagawa, Y., Mohri, S., & Yoshitake, T. (2010). Influences of repetition rate of laser pulses on growth of crystalline AlN films on sapphire(0001) substrates by pulsed laser deposition. *Diamond and Related Materials*, 19(5–6), 618-620.
- Sundaresan, B., Vasumathi, A., Ravichandran, K., Ravikumar, P., & Sakthivel, B. (2012). Annealing effect on physical properties of spin coated ZnO films. *Surface Engineering*, 28(5), 323-328.

- Suzuki, T., Hibino, S., Katayama, R., Kato, Y., Ohashi, F., Itoh, T., & Nonomura, S. (2013). Effects of Substrate Temperature on Properties of Amorphous $\text{In}_x\text{Ga}_{1-x}\text{N}$ Films Deposited by Reactive Radio Frequency Sputtering. *Japanese Journal of Applied Physics*, 52(11S), 11NG05-4.
- Tachibana, Y., Vayssieres, L., & Durrant, J. R. (2012). Artificial photosynthesis for solar water-splitting. *Nature Photonics*, 6(8), 511-518.
- Tauc, J. (1974). *Amorphous and liquid semiconductors*, edited by J. Tauc. London, New York: Plenum.
- Terashima, W., Che, S.-B., Ishitani, Y., & Yoshikawa, A. (2006). Growth and Characterization of AlInN Ternary Alloys in Whole Composition Range and Fabrication of InN/AlInN Multiple Quantum Wells by RF Molecular Beam Epitaxy. *Japanese Journal of Applied Physics*, 45(6L), L539-L542.
- Terziyska, P. T., Butcher, K. S. A., Rafailov, P., & Alexandrov, D. (2015). Growth of vertically oriented InN nanorods from In-rich conditions on unintentionally patterned sapphire substrates. *Applied Surface Science*, 353, 103-105.
- Tran, A. T., Wunnicke, O., Pandraud, G., Nguyen, M. D., Schellevis, H., & Sarro, P. M. (2013). Slender piezoelectric cantilevers of high quality AlN layers sputtered on Ti thin film for MEMS actuators. *Sensors and Actuators A: Physical*, 202, 118-123.
- Ueno, M., Yoshida, M., Onodera, A., Shimomura, O., & Takemura, K. (1994). Stability of the wurtzite-type structure under high pressure: GaN and InN. *Physical Review B*, 49(1), 14-21.
- Valdúeza-Felip, S., Ibáñez, J., Monroy, E., González-Herráez, M., Artús, L., & Naranjo, F. B. (2012). Improvement of InN layers deposited on Si(111) by RF sputtering using a low-growth-rate InN buffer layer. *Thin Solid Films*, 520(7), 2805-2809.
- Vernon, C., Thompson, E., & Cornell, S. (2011). Carbon dioxide emission scenarios: limitations of the fossil fuel resource. *Procedia Environmental Sciences*, 6, 206-215.
- Vickerman, J. (1997). *Surface Analysis: Techniques and Applications*: Wiley.
- Vijayalakshmi, K., & Pillay, V. V. (2014). Influence of deposition time on the microstructure and dielectric properties of AlN/Si thin films for enhanced hydrogen sensing application. *Microelectronic Engineering*, 113, 29-34.
- Voznyy, A. V., & Deibuk, V. G. (2004). The role of alloying effects in the formation of electronic structure of unordered Group III nitride solid solutions. *Semiconductors*, 38(3), 304-309.
- Vurgaftman, I., & Meyer, J. R. (2003). Band parameters for nitrogen-containing semiconductors. *Journal of Applied Physics*, 94(6), 3675-3696.

- Wallys, J., Hoffmann, S., Furtmayr, F., Teubert, J., & Eickhoff, M. (2012). Electrochemical properties of GaN nanowire electrodes—influence of doping and control by external bias. *Nanotechnology*, 23(16), 165701-7.
- Wang, H. T., Jia, C. H., Xu, J. K., Chen, Y. H., Chen, X. W., & Zhang, W. F. (2014). Epitaxial growth of non-polar m-plane AlN film on bare and ZnO buffered m-sapphire. *Journal of Crystal Growth*, 391(0), 111-115.
- Wang, K., Martin, R. W., Amabile, D., Edwards, P. R., Hernandez, S., Nogales, E., O'Donnell, K. P., Lorenz, K., Alves, E., Matias, V., Vantomme, A., Wolverson, D., & Watson, I. M. (2008). Optical energies of AlInN epilayers. *Journal of Applied Physics*, 103(7), 073510-3.
- Wang, X., & Yoshikawa, A. (2004). Molecular beam epitaxy growth of GaN, AlN and InN. *Progress in Crystal Growth and Characterization of Materials*, 48–49, 42-103.
- Wang, Z. P., Morimoto, A., Kawae, T., Ito, H., & Masugata, K. (2011). Growth of preferentially-oriented AlN films on amorphous substrate by pulsed laser deposition. *Physics Letters A*, 375(33), 3007-3011.
- Watanabe, M., Brauns, C., Komatsu, M., Kuroda, S., Gärtner, F., Klassen, T., & Katanoda, H. (2013). Effect of nitrogen flow rate on microstructures and mechanical properties of metallic coatings by warm spray deposition. *Surface and Coatings Technology*, 232(0), 587-599.
- Watson, I. M., Liu, C., Gu, E., Dawson, M. D., Edwards, P. R., & Martin, R. W. (2005). Use of AlInN layers in optical monitoring of growth of GaN-based structures on free-standing GaN substrates. *Applied Physics Letters*, 87(15), 151901-3.
- Weber, M. F., & Dignam, M. J. (1986). Splitting water with semiconducting photoelectrodes—Efficiency considerations. *International Journal of Hydrogen Energy*, 11(4), 225-232.
- Wei, Q.-p., Zhang, X.-w., Liu, D.-y., Li, J., Zhou, K.-c., Zhang, D., & Yu, Z.-m. (2014). Effects of sputtering pressure on nanostructure and nanomechanical properties of AlN films prepared by RF reactive sputtering. *Transactions of Nonferrous Metals Society of China*, 24(9), 2845-2855.
- Wei, S. H., & Zunger, A. (1996). Valence band splittings and band offsets of AlN, GaN, and InN. *Applied Physics Letters*, 69(18), 2719-2721.
- Weng, W. Y., Chang, S. J., Hsueh, T. J., Hsu, C. L., Li, M. J., & Lai, W. C. (2009). AlInN resistive ammonia gas sensors. *Sensors and Actuators B: Chemical*, 140(1), 139-142.
- Wintrebart-Fouquet, M., Butcher, K. S. A., & Chen, P. P. T. (2004). InN grown by remote plasma-enhanced chemical vapor deposition. *Journal of Crystal Growth*, 269(1), 134-138.
- Wu, J. (2009). When group-III nitrides go infrared: New properties and perspectives. *Journal of Applied Physics*, 106(1), 011101-5.

- Wu, J., Walukiewicz, W., Li, S. X., Armitage, R., Ho, J. C., Weber, E. R., Haller, E. E., Lu, H., Schaff, W. J., Barcz, A., & Jakiela, R. (2004). Effects of electron concentration on the optical absorption edge of InN. *Applied Physics Letters*, 84(15), 2805-2807.
- Wu, J., Walukiewicz, W., Shan, W., Yu, K. M., Ager, J. W., Li, S. X., Haller, E. E., Lu, H., & Schaff, W. J. (2003). Temperature dependence of the fundamental band gap of InN. *Journal of Applied Physics*, 94(7), 4457-4460.
- Wu, J., Walukiewicz, W., Yu, K. M., Ager, J. W., Haller, E. E., Lu, H., Schaff, W. J., Saito, Y., & Nanishi, Y. (2002). Unusual properties of the fundamental band gap of InN. *Applied Physics Letters*, 80(21), 3967-3969.
- Wu, Y., Jia, C. H., & Zhang, W. F. (2012). Growth of conductive and insulative highly-orientated aluminum nitride thin films using laser molecular beam epitaxy. *Diamond and Related Materials*, 25(0), 139-143.
- Xin, H.-W., Tian, L.-H., Pan, J.-D., He, Q., Xu, Z., & Zhang, Z.-M. (2000). Synthesis of aluminum nitride films by activated reactive ion plating with a cathodic arc source. *Surface and Coatings Technology*, 131(1-3), 167-170.
- Xu, K., & Yoshikawa, A. (2003). Effects of film polarities on InN growth by molecular-beam epitaxy. *Applied Physics Letters*, 83(2), 251-253.
- Yalavarthi, K., Gaddipati, V., & Ahmed, S. (2011). Internal fields in InN/GaN quantum dots: Geometry dependence and competing effects on the electronic structure. *Physica E: Low-dimensional Systems and Nanostructures*, 43(6), 1235-1239.
- Yamaguchi, S., Kariya, M., Nitta, S., Kato, H., Takeuchi, T., Wetzel, C., Amano, H., & Akasaki, I. (1998). Structural and optical properties of AlInN and AlGaInN on GaN grown by metalorganic vapor phase epitaxy. *Journal of Crystal Growth*, 195(1-4), 309-313.
- Yamamoto, A., Islam, M. R., Kang, T.-T., & Hashimoto, A. (2010). Recent advances in InN-based solar cells: status and challenges in InGaN and InAlN solar cells. *physica status solidi (c)*, 7(5), 1309-1316.
- Yang, W., Wang, W., Lin, Y., Liu, Z., Zhou, S., Qian, H., Gao, F., Zhang, S., & Li, G. (2014). Deposition of nonpolar m-plane InGaN/GaN multiple quantum wells on LiGaO₂ (100) substrates. *Journal of Materials Chemistry C*, 2(5), 801-805.
- Yang, W., Wang, W., Lin, Y., Zhou, S., Liu, Y., & Li, G. (2015). Effect of target-substrate distance on the quality of AlN films grown on Si(110) substrates by pulsed laser deposition. *Materials Letters*, 160, 20-23.
- Yeh, T.-S., Wu, J.-M., & Lan, W.-H. (2008). Electrical properties and optical bandgaps of AlInN films by reactive sputtering. *Journal of Crystal Growth*, 310(24), 5308-5311.
- Yeh, T.-S., Wu, J.-M., & Lan, W.-H. (2009). The effect of AlN buffer layer on properties of Al_xIn_{1-x}N films on glass substrates. *Thin Solid Films*, 517(11), 3204-3207.

- Yoshida, S., Misawa, S., & Itoh, A. (1975). Epitaxial growth of aluminum nitride films on sapphire by reactive evaporation. *Applied Physics Letters*, 26(8), 461-462.
- Yoshikawa, M., Kunzer, M., Wagner, J., Obloh, H., Schlotter, P., Schmidt, R., Herres, N., & Kaufmann, U. (1999). Band-gap renormalization and band filling in Si-doped GaN films studied by photoluminescence spectroscopy. *Journal of Applied Physics*, 86(8), 4400-4402.
- You, Y., Ito, A., Tu, R., & Goto, T. (2013). Effects of laser power on the growth of polycrystalline AlN films by laser chemical vapor deposition method. *Surface and Coatings Technology*, 232(0), 1-5.
- Yu, S., Kim, K. W., Bergman, L., Dutta, M., Stroscio, M. A., & Zavada, J. M. (1998). Long-wavelength optical phonons in ternary nitride-based crystals. *Physical Review B*, 58(23), 15283-15287.
- Yusoff, N., Kumar, S. V., Pandikumar, A., Huang, N. M., Marlinda, A. R., & An'amt, M. N. (2015). Core-shell Fe₃O₄-ZnO nanoparticles decorated on reduced graphene oxide for enhanced photoelectrochemical water splitting. *Ceramics International*, 41(3, Part B), 5117-5128.
- Zhang, B., Song, H., Wang, J., Jia, C., Liu, J., Xu, X., Liu, X., Yang, S., Zhu, Q., & Wang, Z. (2011). MOCVD growth of a-plane InN films on r-Al₂O₃ with different buffer layers. *Journal of Crystal Growth*, 319(1), 114-117.
- Zhang, F., Wu, Q., Zhang, Y., Zhu, J., Liu, N., Yang, J., Wang, X., & Hu, Z. (2012). Chemical vapor deposition growth of InN nanostructures: Morphology regulation and field emission properties. *Applied Surface Science*, 258(24), 9701-9705.
- Zhang, H. Y., He, X. H., Shih, Y. H., Schurman, M., Feng, Z. C., & Stall, R. A. (1996). Study of nonlinear optical effects in GaN:Mg epitaxial film. *Applied Physics Letters*, 69(20), 2953-2955.
- Zhao, D. G., Jiang, D. S., Wu, L. L., Le, L. C., Li, L., Chen, P., Liu, Z. S., Zhu, J. J., Wang, H., Zhang, S. M., & Yang, H. (2012). Effect of dual buffer layer structure on the epitaxial growth of AlN on sapphire. *Journal of Alloys and Compounds*, 544, 94-98.
- Zhao, Y., Wang, H., Yang, H., Wu, G., Jing, Q., Gao, F., Li, W., Zhang, B., & Du, G. (2015). Growth temperature induced physical property variation of InN films grown on nitrated sapphire substrate by PAMBE. *Vacuum*, 112, 55-58.
- Zhi, A.-B., Qin, F.-W., Zhang, D., Bian, J.-m., Yu, B., Zhou, Z.-F., & Jiang, X. (2012). Low-temperature growth of highly c-oriented InN films on glass substrates with ECR-PEMOCVD. *Vacuum*, 86(8), 1102-1106.
- Zhu, W., & Pezzotti, G. (2015). Raman spectroscopic assessments of structural orientation and residual stress in wurtzitic AlN film deposited on (0 0 1) Si. *Microelectronics Reliability*, 55(1), 66-73.

LIST OF PUBLICATIONS AND PAPERS PRESENTED

Publications:

1. Plasma-assisted hot filament chemical vapor deposition of AlN thin films on ZnO buffer layer: toward highly c-axis-oriented, uniform, insulative films;
M. Alizadeh*, H. Mehdipour, V. Ganesh, A. N. Ameera, B. T. Goh, A. Shuhaimi, S. A. Rahman*, *Applied Physics A: Materials Science & processing*, **117** (2014) 2217–2224.
2. Structural ordering, morphology and optical properties of amorphous Al_xIn_{1-x}N thin films grown by plasma-assisted dual source reactive evaporation;
M. Alizadeh*, V. Ganesh, H. Mehdipour, N.F.F. Nazarudin, B.T. Goh, A. Shuhaimi, S.A. Rahman*, *Journal of Alloys and Compounds*, **632** (2015) 741–747.
3. Investigation of the electrochemical behavior of indium nitride thin films by plasma-assisted reactive evaporation;
Vattikondala Ganesh,* Mahdi Alizadeh,* Ahamad Shuhaimi, Alagarsamy Pandikumar, Boon Tong Goh, Nay Ming Huang and Saadah Abdul Rahman, *RSC Advances*, **5** (2015) 17325-17335.
4. Photoelectrochemical behavior of Al_xIn_{1-x}N thin films grown by plasma-assisted dual source reactive evaporation;
M. Alizadeh*, V. Ganesh, A. Pandikumar, B.T. Goh, S. Azianty, N.M. Huang, S.A. Rahman*, *Journal of Alloys and Compounds*, **670** (2016) 229-238.
5. Effect of nitrogen flow rate on structural, morphological and optical properties of In-rich In_xAl_{1-x}N thin films grown by plasma-assisted dual source reactive evaporation;
M. Alizadeh*, V. Ganesh, B.T. Goh, C.F. Dee, A.R. Mohmad, S.A. Rahman*,

Conference presentation:

1. Deposition of InAlN thin films by plasma assisted- hot filament chemical vapor deposition on quartz substrate;

M. Alizadeh, V. Ganesh, N.F.F Nazarudin, B.T. Goh, S.A. Rahman, THIN FILMS CONFERENCE, CHONGQING, CHINA (2014).

University of Malaysia